



HAL
open science

Reconfigurable transmitarrays for beam-steering and beam -forming at millimeter-waves

Fatimata Diaby

► **To cite this version:**

Fatimata Diaby. Reconfigurable transmitarrays for beam-steering and beam -forming at millimeter-waves. Optics / Photonic. Université Grenoble Alpes, 2018. English. NNT : 2018GREAT125 . tel-02183145

HAL Id: tel-02183145

<https://theses.hal.science/tel-02183145>

Submitted on 15 Jul 2019

HAL is a multi-disciplinary open access archive for the deposit and dissemination of scientific research documents, whether they are published or not. The documents may come from teaching and research institutions in France or abroad, or from public or private research centers.

L'archive ouverte pluridisciplinaire **HAL**, est destinée au dépôt et à la diffusion de documents scientifiques de niveau recherche, publiés ou non, émanant des établissements d'enseignement et de recherche français ou étrangers, des laboratoires publics ou privés.



THÈSE

Pour obtenir le grade de

DOCTEUR DE LA COMMUNAUTÉ UNIVERSITÉ GRENOBLE ALPES

Spécialité : OPTIQUE ET RADIOFREQUENCES

Arrêté ministériel : 25 mai 2016

Présentée par

Fatimata DIABY

Thèse dirigée par **Laurent DUSSOPT**, Ingénieur chercheur, CEA

préparée au sein du **Laboratoire CEA/LETI**
dans l'**École Doctorale Electronique, Electrotechnique,
Automatique, Traitement du Signal (EEATS)**

**Réseaux transmetteurs reconfigurables pour
le dépointage et la formation de faisceau en
bande millimétrique.**

**Reconfigurable transmitarrays for beam-
steering and beam -forming at millimeter-
waves.**

Thèse soutenue publiquement le **14 décembre 2018**,
devant le jury composé de :

Monsieur LAURENT DUSSOPT

INGENIEUR DE RECHERCHE, CEA GRENOBLE, Directeur de thèse

Madame CLAIRE MIGLIACCIO

PROFESSEUR, UNIVERSITE NICESOPHIA- ANTIPOLIS, Rapporteur

Monsieur SYLVAIN BOLIOLI

INGENIEUR, ONERA CENTRE MIDI-PYRENEES, Rapporteur

Madame PAOLA PIRINOLI

PROFESSEUR, UNIVERSITE POLYTECHNIQUE TURIN - ITALIE,
Examineur

Monsieur HERVE AUBERT

PROFESSEUR, INSTITUT NATIONAL POLYTECHNIQUE TOULOUSE,
Président

Monsieur RONAN SAULEAU

PROFESSEUR, UNIVERSITE RENNES 1, Examineur

Monsieur LAURENT PETIT

INGENIEUR DE RECHERCHE, RADIAL CENTR'ALP VOREPPE,
Examineur

Monsieur ANTONIO CLEMENTE

Ingénieur de Recherche, CEA GRENOBLE, Examineur

Contents

Acknowledgments.....	iii
List of Tables.....	iv
List of Figures	vi
Résumé en français.....	xvi
Abstract	xxii
General introduction.....	1
Chapter I. Introduction	5
1.1. Millimeter-wave applications and emerging technologies.....	5
1.1.1. 5 th generation communications networks	7
1.1.2. SatCom systems.....	12
1.2. Transmitarray antennas	23
1.2.1. Transmitarray working principle	23
1.2.2. Analysis of a unit-cell.....	24
1.2.3. Simulation techniques of a transmitarray antenna.....	25
1.2.4. State of the art on transmitarray antennas.....	28
1.3. Conclusion.....	50
Chapter II. Theoretical analysis of transmitarray antennas	56
2.1. Impact of the phase compensation method on transmitarray performances	56
2.1.1. Impact on the bandwidth	58
2.1.2. Impact on the radiation pattern in the broadside direction	59
2.1.3. Impact on the beam scanning capability.....	60
2.2. Faceted transmitarray	63
2.2.1. Design methodology of a faceted transmitarray	64
2.2.2. Simulation of a 400-element 3-facet transmitarray	67
2.2.3. Numerical simulation of 3-facet transmitarrays of different sizes.....	68
2.3. Conclusion.....	73
Chapter III. Design and optimization of passive unit-cells and fixed-beam transmitarray antennas	76
3.1. Linearly-polarized unit-cells	76
3.1.1. Passive unit-cell based on a simple microstrip patch antenna	76
3.1.2. Broadband passive unit-cells with 1-bit of phase resolution	80
3.1.3. Broadband passive unit-cells with 3-bit of phase resolution	84
3.2. Fixed-beam linearly-polarized transmitarray with 3 bits of phase resolution.....	86
3.3. Circularly-polarized unit-cells.....	87
3.3.1. Unit-cell architecture	88
3.3.2. Full-wave simulation of the proposed 3-bit unit-cell.....	89
3.4. Fixed-beam circularly-polarized transmitarrays with 3 bits of phase resolution	90

CONTENTS

3.4.1. Simulation of the 400-element transmitarray	91
3.4.2. Impact of phase quantization on the circularly-polarized transmitarray	92
3.4.3. Fixed quad-beam transmitarray with 3 bits of phase quantization	95
3.5. Prototyping and characterization of fixed-beam transmitarrays	96
3.5.1. Measurements of the 1600-element single-beam transmitarray	96
3.5.2. Measurement of the quad-beam transmitarray	100
3.6. Conclusion.....	102
Chapter IV. Design and optimization of active unit-cells for electronically reconfigurable transmitarrays	105
4.1. Design and optimization of an active linearly-polarized unit-cell with 2 bits of phase resolution.....	106
4.1.1. Architecture	106
4.1.2. Simulation results	109
4.1.3. Impact of bias lines.....	110
4.1.4. Waveguide setup.....	112
4.2. Experimental results	114
4.2.1. Fabricated unit-cell with two bias lines	115
4.2.2. Fabricated unit-cell with more than two bias lines	118
4.2.3. Sensitivity analysis of the 2-bit linearly-polarized unit-cell	120
4.3. Design and optimization of an active circularly-polarized unit-cell with 2 bits of phase resolution.....	123
4.3.1. Architecture of the proposed unit-cell.....	123
4.3.2. Simulated frequency response	125
4.4. Conclusion.....	128
Chapter V. Linearly-polarized electronically reconfigurable transmitarray antenna with 2-bit phase resolution in Ka-band	130
5.1. Design and optimization of the active linearly-polarized transmitarray	130
5.2. Architecture of the prototype board	133
5.3. Experimental results	136
5.4. Conclusion.....	144
General conclusion and perspectives.....	147
Appendix A - Scattering parameters in circular polarization of a unit-cell with periodic boundary conditions.....	151
Appendix B - Description of electronic control boards for reconfigurable transmitarray antenna	153
Bibliography	155
List of Publications.....	165

Acknowledgments

This thesis took place at the CEA-LETI (Laboratory of Electronics and Information Technology) within the Laboratory of Antenna, Propagation and Inductive Coupling.

I would like to express my deep gratitude to all of those who, from near and far, have contributed to the carrying out of this thesis.

First of all, I would like to express my gratitude and deep thanks to Dr. Laurent Dussopt, Senior Research Engineer at CEA-Leti, for agreeing to lead my research, to trust me during the thesis. Your knowledge-sharing and advices were essential for the success of the thesis.

I would like to also address my thankful to my supervisor Dr. Antonio Clemente, Research Engineer at CEA-Leti. Throughout this work, he has provided me constant support, great availability and listening. Thanks for your constructive criticism and advices which are guided me throughout this thesis. I am aware of having benefited from high quality scientific supervision.

I am also very thankful to Prof. Ronan Sauleau, Professor at the University of Rennes for your precious comments and suggestions which have guided this work to the end. I would like to express my gratitude to having accepted to be a part of the jury.

I would like to address my acknowledgment to Dr. Christophe Delaveaud (Head of Laboratory Antenna, Propagation and Inductive Coupling), Fabien Clermidy (head of Wireless Technologies Services), and Sébastien Dauve (head of the Department DSYS), for welcoming me during the three years of this thesis, for allowing me to work in very good conditions and putting at my disposal all the means necessary for the smooth running of my thesis.

I acknowledge the members of my thesis jury for having accepted to examine this thesis, Prof. Claire Migliaccio, Dr. Sylvain Bolioli, Prof. Paola Pirinoli, Prof Hervé Aubert, and Dr. Laurent Petit.

I would also like to thank all the members of the LAPCI for their availability and sympathy.

Finally, I could not finish these thanks without thinking of my family whose affection, constant love, support and encouragement have been a great comfort to me and have contributed to the completion of this work.

List of Tables

Table I-1: IEEE radar-frequency letter band definition.	5
Table I-2: Antenna main specifications for automotive radars.	7
Table I.3: Key system parameters of the mm-wave beamforming prototypes [13].	9
Table I.4: Impact of phase quantization on the TA performances.	28
Table I.5: Performances of existing fixed beam transmitarrays.	52
Table I.6: Performances of existing switched beam transmitarrays.	53
Table I.7: Performances of existing electronically beam transmitarrays.	54
Table II-1: Impact of phase quantization on the TA performances.	60
Table II-2: Performance of the TA when the beam points at 30°	62
Table II-3: Performance of the TA when the beam points at 60°	62
Table II-4: Maximum gain of the 3-facet TA as function of the desired scan angle.	68
Table II-5: Maximum gain of the 3-facet TA as a function of the desired scan angle: config. 1 (30×20 elements).	72
Table II-6: Maximum gain of the 3-facet TA as a function of the desired scan angle: config. 2 (40×40 elements).	72
Table II-7: Maximum gain of the 3-facet TA as a function of the desired scan angle: config 3 (50×20 elements).	73
Table III-1: Main features of the 1-bit simple patch unit-cell.	77
Table III-2: Performance of the proposed linearly-polarized transmitarray at 29 GHz.	86
Table III-3: Geometrical dimensions of the proposed unit-cell.	89
Table III-4: Effect of phase quantization on the 1600-element circularly-polarized transmitarray.	93
Table III-5: Measured performances of the proposed 1600-element fixed-beam transmitarray.	98
Table IV-1: Dimensions of the proposed 2-bit unit-cell (Figure IV-1(a)).	109
Table IV-2: Different combinations of the reception and transmission layers corresponding to the four phase states.	109
Table IV-3: Simulated performances of the 2-bit linearly-polarized unit-cell.	110
Table IV-4: Measured and simulated performances in the waveguide of the 2-bit linearly-polarized unit-cell.	118
Table IV-5: Simulated performances of the 2-bit circularly-polarized unit-cell.	124
Table IV-6: Summary of the 2-bit circularly-polarized unit-cell performances.	127
Table V-1: Summary of the 2-bit electronically reconfigurable transmitarray performances in E plane at 29 GHz.	141
Table V-2: Summary of the 2-bit electronically reconfigurable transmitarray performances in H plane at 29GHz.	142
Table V-3: Summary of the 2-bit electronically reconfigurable transmitarray performances at broadside (Measurement, theoretical results with and without errors).	145

LIST OF TABLES

List of Figures

Figure 1 : Réseau transmetteur à 3 facettes : (a) vue schématique, (b) diagrammes de rayonnement (simulé et théorique) à 29 GHz sur le plan E.	xvii
Figure 2 : Réseau transmetteur à faisceau collimaté : (a) gain et (b) rapport axial en fonction de la fréquence.	xviii
Figure 3 : Diagrammes de rayonnement (polarisation circulaire gauche) simulés et mesurés du réseau transmetteur à quatre faisceaux dans les (a) plan horizontal (29 GHz) et plan vertical (29 GHz).	xix
Figure 4 : Diagrammes de rayonnement mesurés du réseau transmetteur électroniquement reconfigurable dans les plans E (a) et H (b) à 29 GHz) en fonction de l'angle de l'angle de dépointage de $\pm 60^\circ$	xx
Figure I-1: D-RAN and C-RAN 5G network architectures with backhaul and fronthaul [9]....	8
Figure I-2: Configuration of the mm-wave beamforming prototype [13].	9
Figure I-3: 28 GHz phased array transceiver. (a) Measurement setup. (b) E plane radiation pattern at 29.5 GHz.	10
Figure I-4: Single layer polarization independent reflectarray antenna. (a) Top view of the unit-cell. (b) Radiation patterns in E-plane.	10
Figure I-5: (a) 3-D view and (b) radiation patterns in E-plane of the proposed folded reflectarray antenna at 38 GHz.	11
Figure I-6: Measured normalized radiation patterns in E-, and H-plane at 60 GHz with ETSI masks: (a) polarization in x-direction, (b) polarization in y-direction.	11
Figure I-7: Co-polar (solid line) and cross-polar (dotted line) components radiation masks of the ETSI 302 217 in the frequency band (a) 24 – 30 GHz, and (b) 30 – 47 GHz.	12
Figure I-8: Alternative radiation masks of the Class 3 antenna defined by of the ETSI 302 217 in the frequency band 30 – 47 GHz. (a) Class 3B and (b) class 3C.	12
Figure I-9: The main building blocks of a satellite communication system.	13
Figure I-10: ThinKom's agile, ThinAir® Falcon-Ka2517 antenna for broadband air flight connectivity [19].	14
Figure I-11: 70cm Ku-band MSAT beam patterns vs. scan angle [20].	14
Figure I-12: (a) 51 cm diameter Ku-band Variable Inclination Continuous Transverse Stub (VICTS) array. (b) Measured elevation-plane pattern for the 51 cm VICTS array at 12.5 GHz (scanned to 63 degrees) [21].	15
Figure I-13: Prototype of an 8x8-element aperture (1) and two stacked waveguide networks for horizontal (2) and vertical polarization (3) for achieving arbitrary polarization control, and broadside radiation patterns.	15
Figure I-14: X/Ka Commander Integrated Antenna/Terminal Subsystem.	16
Figure I-15: K/Ka band array antenna for Office-in-the-Air Connectivity.	16
Figure I-16: Simulated and measured directivity patterns of the FSS-backed reflectarray antenna in transverse plane at 20 GHz (left) and 29.8 GHz (right).	17

LIST OF FIGURES

Figure I-17: Prototype of the proposed Ka-band reflectarray antenna integrated with solar cells (left) and measured gain within the operating frequency band (right).	17
Figure I-18: 3-D view of the folded reflectarray antenna for SatCom applications at Ka-band (left), and radiation patterns (calculated and measured) at 60° in $\phi = 0^\circ$ cut plane (right).	18
Figure I-19: Reflectarray prototype (left), and measured versus simulated gain in Ku/Ka bands for H-polarization (right).	19
Figure I-20: Frequency band allocations for SatCom applications according to ITU.	20
Figure I-21: Ka-band SatCom coverage. (a) Ka-Sat coverage [31]. (b) Launch of satellites offering lower cost per bit Ku/Ka-bands capability [32]. (c) Satellite interface in Inmarsat Global Xpress [33], (d) Terminal characteristics for Inmarsat Global Xpress [33].	21
Figure I-22: Power mask of recommendations ETSI EN 301 360 and ETSI EN 301 459 in the case of one Earth Terminal.	22
Figure I-23: Radiation mask of recommendation ITU S.465-6.	22
Figure I-24: Power mask of recommendation FCC 25.138. The masks are calculated considering one earth terminal (TDMA carriers with bandwidth > 40 kHz).	22
Figure I-25: Power mask of recommendation ETSI EN 303 978. The masks are calculated considering one Earth Terminal (TDMA carriers with bandwidth > 40 kHz).	23
Figure I-26: (a) Schematic view of a transmitarray antenna. (b) Full power budget of a TA.	24
Figure I-27: Full-wave electromagnetic simulation setup of a unit-cell using periodic boundary conditions and Floquet port excitation.	25
Figure I-28: (a) Prototype of the proposed bidirectional high gain array. (b) Simulated and measured transmitted (TA) and reflected (RA) gains of the Bi-HGA versus frequency [54].	29
Figure I-29: High-efficiency wideband transmitarray antenna. (a) Fabricated prototype, (b) measured and simulated realized gain and aperture efficiency of the proposed transmitarray antenna.	29
Figure I-30: Simulated and measured co- and cross-polar radiation patterns in E-plane (a) 11 GHz, and (b) 12.5 GHz.	30
Figure I-31: (a) Fabricated wideband transmitarray under measurement. (b) Measured and simulated gains as a function of frequency [57].	31
Figure I-32: 20 GHz double-layer linearly-polarized transmitarray antenna using Malta crosses with vias [58].	31
Figure I-33: Circularly-polarized transmitarray with sequential rotation at 30 GHz [41]. (a) 3-D exploded view of the unit-cell. (b) Simulated and measured radiation patterns in horizontal plane.	32
Figure I-34: Ultra low profile transmitarray using multifolded ray tracing principle [59]. (a) 3-D exploded view of the unit-cell. (b) Simulated and measured radiations patterns.	33
Figure I-35: Circularly-polarized transmitarray based on linearly-polarized unit-cell [60]. (a) Architecture of the unit-cell. (b) Axial ratio as a function of frequency.	33
Figure I-36: Dual-band circularly-polarized transmitarray for SOTM systems [61]. (a) Perspective view of the unit-cell. (b) Broadside radiation pattern at 20 GHz and 30 GHz.	34
Figure I-37: Dual-band transmitarray at Ka-band with the capability of forming independent linearly-polarized beams [62]. (a) Beam directions of the proposed prototypes. Theoretical and measured gain as a function of frequency in (b) up link and (c) down link bands.	35
Figure I-38: (a) Phase delay (PD) unit-cell. (b) Phase rotation (PR) unit-cell. Performances of both TA types [63].	36
Figure I-39: 60 GHz linearly-polarized transmitarray for backhauling [64]. (a) Prototype of the TA. (b) Measured and simulated gain as a function of frequency. (c) Co-, and cross-	

LIST OF FIGURES

polarization radiation patterns of the TA for different frequencies (57 GHz, 61.5 GHz, and 66 GHz) compared to ETSI masks.....	37
Figure I-40: Fabricated 140 GHz high gain LTCC-integrated transmitarray (left); simulated and measured gain and corresponding efficiency within the frequency band of interest (right) [65].	37
Figure I-41: Prototype and frequency response (gain as a function of frequency) of the two-layer transmitarray [66].	38
Figure I-42: High-gain dual band-beam steering transmitarray at Ka-band. (a) Unit-cell configuration. Measured radiation patterns at (b) 20 GHz and (c) 30 GHz [67].	39
Figure I-43: Prototype of the proposed lens with seven-element feeding antenna (left), and measured scanned beam at 28 GHz (right) [68].	39
Figure I-44: Switched-beam transmitarray at V-band [69]. (a) Principle. (b) Experimental radiation patterns in H-plane at 61 GHz.....	40
Figure I-45: Coplanar transmitarray with four SIW slot primary feeds at 76.5GHz [70].....	40
Figure I-46: 36-element reconfigurable transmitarray based on varactors at 5 GHz [71]. (a) Unit cell design. (b) Prototype of the TA. Measured radiation patterns (c) E-plane, (d) H-plane.	42
Figure I-47: Reconfigurable transmitarray with beam-steering and polarization conversion capabilities [72]. (a) Architecture of the proposed unit-cell. (b) Far-field radiation patterns in E-plane at 5.4 GHz.	43
Figure I-48: Circularly-polarized reconfigurable transmitarray antenna [73]: (a) architecture of the unit-cell, (b) far-field radiation pattern in the diagonal plane at 4.8 GHz.....	43
Figure I-49: Electronically-reconfigurable transmitarray with integrated leaky-wave feed [74]. (a) Exploded model of the proposed TA. (b) Measured and simulated co-polarized realized gain at 4.8 GHz in the diagonal plane.	44
Figure I-50: Measured radiation patterns at 5.2 GHz for different steering angles in azimuth (left) and elevation (right) planes [75].	44
Figure I-51: (a) Schematic model of the amplifying unit-cell with electronically reflection-type phase shifter. Measured frequency responses: (b) transmission coefficient, (c) phase tuning range [76].	45
Figure I-52: Electronically reconfigurable transmitarray in X-band [77]. (a) Schematic view of the TA. (b) H-plane beam scanning capability.	45
Figure I-53: Electronically reconfigurable circularly-polarized transmitarray in X-band [78]. (a) Schematic view of the unit-cell. (b) Measured transmission characteristics of the fabricated transmitarray.....	46
Figure I-54: Dual linearly polarized unit-cell with 1-bit phase resolution in X-band [79].	47
Figure I-55: Circularly-polarized reconfigurable transmitarray unit cell based on microfluidics at X band [80].	47
Figure I-56: A Ku-band 1-bit reconfigurable transmitarray: architecture of the proposed unit-cell (left), and radiation patterns (right) [81].	48
Figure I-57: K-band linearly-polarized reconfigurable transmitarray: fabricated prototype (left), and radiations patterns (right) [82].	48
Figure I-58: 2-bit electronically reconfigurable transmitarray based on RF-MEMS switched unit-cells [84].	49
Figure I-59: (a) Prototype of a Ka-band 400-element circularly polarized transmitarray, (b) simulated and measured frequency response (broadside) [85].	49

LIST OF FIGURES

Figure I-60: (a) Active dual-band TA and realized module. Measured and simulated radiation patterns: (b) Receive antenna at 20 GHz, (c) Transmit antenna at 30 GHz [86]. 50

Figure II-1: TA peak gain at broadside for three different TAs and for both phase compensation techniques as a function of the normalized frequency f/f_0 59

Figure II-2: Phase distribution of the 40×40 TA when TTD phase compensation technique is used for the normalized frequencies f/f_0 59

Figure II-3: (a) Radiation patterns (E-plane) of the 40×40 TA for three different frequencies using constant phase-shift compensation, (b) A zoom on the main beam for elevation angle θ_0 ranging from -10° to 10° 60

Figure II-4: (a) Radiation patterns (E-plane) of the 40×40 TA for three different frequencies using true-time delay compensation, (b) A zoom on the beam for elevation angle θ_0 ranging from -10° to 10° 60

Figure II-5: Radiation patterns of the 40×40 TA steered at 30° in E-plane. (a) Constant phase-shift compensation. (b) TTD compensation. 61

Figure II-6: (a) Radiation patterns of the 40×40 TA steered at 60° in E-plane. (a) Constant phase-shift compensation. (b) TTD compensation. 61

Figure II-7: (a) Radiation patterns (E-plane) of the 40×40 TA for three different frequencies using constant phase-shift compensation when the beam is steered at 60° , (b) zoom on the beam for elevation angle θ_0 ranging from 50° to 70° 63

Figure II-8: (a) Radiation patterns (E-plane) of the 40×40 TA for three different frequencies using TTD compensation when the beam is steered at 60° , (b) zoom on the beam for elevation angle θ_0 ranging from 50° to 70° 63

Figure II-9: Three elementary rotations. (a) Around z-axis. (b) Around y-axis. (c) Around x-axis. 64

Figure II-10: Different shapes of transmitarray. (a) Flat shape. (b) 2-facets. (c) 3-facets. 65

Figure II-11: Schematic view of a 3-facet TA (left) and unit-cells used for full-wave simulations (right). 66

Figure II-12: Normalized gain versus frequency of the 3-facet TA; comparison of the theoretical model with a full-wave simulation. 67

Figure II-13: : Normalized gain versus frequency of the planar and 3-facet TAs. 67

Figure II-14: Schematic view of the 3-facet TAs for the three configurations : (a) *config. 1* (30×20), (b) *config. 2* (40×20), and (c) *config. 3* (50×20). 69

Figure II-15: Gain versus focal ratio for the three configurations of the 3-facet TAs. 69

Figure II-16: (a) Radiation patterns of the three configurations of the 3-facet TA when the lateral panels are tilted at $\alpha = 0^\circ$ (i.e. case of a planar array), (b) zoom on the beam for elevation angle θ_0 ranging from 70° to 88° 70

Figure II-17: (a) Radiation patterns of the three configurations of the 3-facet TA when the lateral panels are tilted at $\alpha = 10^\circ$, (b) zoom on the beam for elevation angle θ_0 ranging from 70° to 88° 70

Figure II-18: (a) Radiation patterns of the thee configurations of the 3-facet TA when the lateral panels are tilted at $\alpha = 30^\circ$, (b) zoom on the beam for elevation angle θ_0 ranging from 70° to 88° 70

Figure II-19: (a) Radiation patterns of the three configurations of the 3-facet TA when the lateral panels are tilted at $\alpha = 70^\circ$, (b) zoom on the beam for elevation angle θ_0 ranging from 70° to 88° 71

Figure II-20: Phase distribution of the 3-facet TA with $\alpha = 70^\circ$ in the config. 1 (5×20 , 20×20 , 5×20 panels). The beam is steered at $\theta_0 = 80^\circ$ 71

LIST OF FIGURES

Figure II-21: Phase distribution of the 3-facet TA with $\alpha = 70^\circ$ in the config. 2 (10×20, 20×20, 10×20 panels). The beam is steered at $\theta_0 = 80^\circ$.	71
Figure II-22: Phase distribution of the 3-facet TA with $\alpha = 70^\circ$ in the config. 3 (15×20, 20×20, 15×20 panels). The beam is steered at $\theta_0 = 80^\circ$.	72
Figure III-1: Proposed simple patch unit-cell with 1-bit phase resolution. (a) 3-D exploded view. (b) Top view.	77
Figure III-2: Simulated results of the simple patch unit-cell. (a) and (b) Magnitude of the reflection S_{11} and transmission S_{21} coefficients. (c) Transmission phase. (d) Differential phase-shift.	78
Figure III-3: Impact of typical fabrication errors for the patch width on the S-parameters. (a) Reflection, (b) transmission coefficients.	79
Figure III-4: Impact of typical fabrication errors for the patch length on the S-parameters. (a) Reflection, and (b) transmission coefficients.	79
Figure III-5: Impact of the feed location on the S-parameters. (a) Reflection, and (b) transmission coefficients.	80
Figure III-6: Impact of the ground-plane hole diameter on the S-parameters. (a) Reflection, and (b) transmission coefficients.	80
Figure III-7: Broadband unit-cell based on simple patches. (a) Top view. (b) Parameters values.	81
Figure III-8: Simulated S-parameters of the broadband unit-cell based on simple patch antennas. Magnitude of the (a) reflection S_{11} and (b) transmission S_{21} coefficients.	82
Figure III-9: (a) Top view and (b) main features of the proposed U-shaped slot unit-cell.	82
Figure III-10: Simulated S-parameters of the U-shaped slot unit-cell. Magnitude of the (a) reflection S_{11} and (b) transmission S_{21} coefficients.	82
Figure III-11: (a) Top view and (b) main features of the proposed O-shaped slot unit-cell.	83
Figure III-12: Simulated S-parameters of the O-shaped slot unit-cell. Magnitude of the (a) reflection S_{11} and (b) transmission S_{21} coefficients.	83
Figure III-13: (a) Top view and (b) main features of the proposed capacitively-coupled unit-cell.	84
Figure III-14: Simulated S-parameters of the capacitively-coupled unit-cell. Magnitude of the (a) reflection S_{11} and (b) transmission S_{21} coefficients.	84
Figure III-15: Scheme of the eight unit-cells with 3 bits of phase quantization (top view).	85
Figure III-16: S-parameters of the 0° , 45° , 90° , 135° , 180° , 225° , 270° and 315° unit-cells. Magnitude of the (a) reflection S_{11} , and (b) transmission S_{21} coefficients. (c) Transmission phase. (d) Phase-shift between the 0° unit-cell and the other states.	85
Figure III-17: 20×20-element transmitarray with 3 bits of phase quantization. (a) Schematic view and phase distribution. (b) Gain as a function of frequency.	87
Figure III-18: Theoretical and full-wave simulated radiation patterns at 29 GHz in E-plane: (a) co-, (b) cross-polarizations.	87
Figure III-19: Theoretical and full-wave simulated radiation patterns at 29 GHz in H-plane: (a) Co-, (b) Cross-polarizations.	87
Figure III-20: Proposed 3-bit circularly-polarized unit-cell. (a) 3-D exploded view. (b) Transmitting and receiving layers.	88
Figure III-21: S-parameters of 3-bit circularly-polarized unit-cells. Magnitude of the (a) reflection coefficients referred to the (a) receiving (S_{11}) and (b) transmitting (S_{22}) layers. (c) Transmission coefficient S_{21} .	90

LIST OF FIGURES

Figure III-22: (a) Transmission phase and (b) phase-shift between the 0° unit-cell and the other states.	90
Figure III-23: Theoretical and simulated frequency responses of the 20×20 -element circularly-polarized transmitarray: (a) broadside gain, and (b) axial ratio.	91
Figure III-24: 20×20 -element circularly-polarized transmitarray: LHCP and RHCP radiation patterns in the 0° plane.	92
Figure III-25: 20×20 -element circularly-polarized transmitarray: LHCP and RHCP radiation patterns in the 90° plane.	92
Figure III-26: Phase distribution of the 1-, 2-, and 3-bit transmitarray for a broadside beam.	93
Figure III-27: (a) Theoretical broadside gain, (b) and axial ratio as a function of frequency for the 3 transmitarrays.	94
Figure III-28: Comparison between the (a) co-, and (b) cross polarization radiation patterns of the 1-, 2-, 3-bit transmitarray and the ETSI masks.	94
Figure III-29: Theoretical and simulated radiation patterns in the 0° plane at 29 GHz: (a) LHCP, (b) RHCP.	94
Figure III-30: Theoretical and simulated radiation patterns in the 90° plane at 29 GHz: (a) LHCP, (b) RHCP.	95
Figure III-31: Circularly-polarized quad-beam transmitarray: (a) 3-D scheme, (b) 3-bit phase distribution optimized at 29 GHz.	95
Figure III-32: Theoretical and simulated LHCP and RHCP radiation patterns of the proposed quad-beam transmitarray in (a) vertical and (b) horizontal planes.	96
Figure III-33: Far-field measurement setup of the 1600-element single-beam circularly-polarized TA in (a) vertical and (b) diagonal planes.	97
Figure III-34: Theoretical and simulated frequency responses of the 1600-element single-beam circularly-polarized transmitarray: (a) broadside gain and (b) axial ratio.	97
Figure III-35: Simulated and measured radiation patterns of the 1600-element single-beam circularly-polarized transmitarray antenna: (a) vertical and (b) horizontal planes.	98
Figure III-36: Measured gain as a function of the frequency and elevation angle in the vertical plane: (a) LHCP, (b) RHCP.	99
Figure III-37: Measured radiation patterns (LHCP and RHCP) in the vertical, diagonal and horizontal planes at 27 GHz.	99
Figure III-38: Measured radiation patterns (LHCP and RHCP) in the vertical, diagonal and horizontal planes at 29 GHz.	99
Figure III-39: Measured radiation patterns (LHCP and RHCP) in the vertical, diagonal and horizontal planes at 32 GHz.	100
Figure III-40: Far-field measurement setup of the 489-element quad-beam transmitarray: (a) vertical, and horizontal planes.	100
Figure III-41: Theoretical, simulated, and measured frequency responses of the quad-beam transmitarray.	101
Figure III-42: Simulated and measured radiation patterns in the vertical plane at 29 GHz: (a) LHCP, (b) RHCP.	101
Figure III-43: Simulated and measured radiation patterns in the horizontal plane at 29 GHz: (a) LHCP, (b) RHCP.	101
Figure III-44: Measured gain as a function of the frequency and elevation angle in the vertical plane.	102
Figure III-45: Measured gain as a function of the frequency and elevation angle in the horizontal plane.	102

LIST OF FIGURES

Figure IV-1: Proposed 2-bit linearly-polarized unit-cell: (a) Schematic view, (b) transmitting layer, (c) biasing layer of the transmission side, (d) DC connection to the ground layer, (e) ground plane, (f) biasing layer of the receive side, and (g) receiving layer.....	107
Figure IV-2: Equivalent lumped-element models of the PIN diode (MA4GFCP907) in the <i>ON</i> , and <i>OFF</i> states.....	108
Figure IV-3: Surface current distribution: (a) and (b) on Tx layer, (c) and (d) on Rx layer..	108
Figure IV-4: Frequency responses of the proposed 2-bit linearly-polarized unit-cell. Magnitude of the (a) reflection and (b) transmission coefficients. (c) Transmission phase. (d) Phase-shift between the 0° state and the other states.	110
Figure IV-5: Bias lines arrangement of the 2-bit unit-cell: (a) transmitting <i>Tx</i> , (b) <i>Tx</i> biasing network, (c), receiving <i>Rx</i> , and (d) <i>Rx</i> biasing network layers.	111
Figure IV-6: Impact of bias lines on the performances of the proposed 2-bit linearly-polarized unit-cell: (a) 0° , (b) 90° , (c) 180° , and (d) 270° states.	112
Figure IV-7: Scheme of the waveguide setup to test the unit-cell.	112
Figure IV-8: Scattering-parameters of the 2-bit linearly-polarized unit-cell performed with a waveguide simulator and Floquet ports under oblique incidence : (a) 0° , (b) 90° , (c) 180° , and (d) 270° states.....	114
Figure IV-9: (a) Transmission phase and (b) phase-shift between the 0° state and the other states performed in waveguide simulator.	114
Figure IV-10: Prototype of the proposed 2-bit linearly-polarized unit-cells: transmitting, and receiving layers on left and right, respectively.	115
Figure IV-11: Fabricated unit-cells with (a) bias wires and (b) placed in the waveguide.	115
Figure IV-12: Measured (in WR-28 waveguide) and simulated scattering parameters magnitudes in the 0° state: (a) reflection (S_{11}) and (b) transmission (S_{21}) coefficients.....	116
Figure IV-13: Measured (in WR-28 waveguide) and simulated scattering parameters magnitudes in the 90° state: (a) reflection (S_{11}) and (b) transmission (S_{21}) coefficients.....	116
Figure IV-14: Measured (in WR-28 waveguide) and simulated scattering parameters magnitudes in the 180° state: (a) reflection (S_{11}) and (b) transmission (S_{21}) coefficients...	116
Figure IV-15: Measured (in WR-28 waveguide) and simulated scattering parameters magnitudes in the 270° state: (a) reflection (S_{11}) and (b) transmission (S_{21}) coefficients.	117
Figure IV-16: (a) Measured transmission phase of the four states of the proposed 2-bit unit-cell and (b) phase-shift between the 0° state and the other states.	118
Figure IV-17: Impact of bias lines on the measured scattering parameters magnitudes in the waveguide in the 0° state: (a) reflection (S_{11}) and (b) transmission (S_{21}) coefficients.	119
Figure IV-18 Impact of bias lines on the measured scattering parameters magnitudes in the waveguide in the 90° state: (a) reflection (S_{11}) and (b) transmission (S_{21}) coefficients.	119
Figure IV-19: Impact of bias lines on the measured scattering parameters magnitudes in the waveguide in the 180° state: (a) reflection (S_{11}) and (b) transmission (S_{21}) coefficients.	119
Figure IV-20: Impact of bias lines on the measured scattering parameters magnitudes in the waveguide in the 270° state: (a) reflection (S_{11}) and (b) transmission (S_{21}) coefficients.	119
Figure IV-21: Holes positioning error for the measurement of the active unit-cell in the waveguide.....	120
Figure IV-22: Measured and simulated scattering parameters magnitudes in the waveguide (taking into account holes positioning errors) in the (a) 0° , (b) 90° , (c) 180° , and (d) 270° states.....	121
Figure IV-23: Impact of typical fabrication errors for the transmission patch length on the S-parameters: (a) 0° and (b) 90° states.	121

LIST OF FIGURES

Figure IV-24: Impact of typical fabrication errors for the receiving patch length on the S-parameters: (a) 0° and (b) 90° states.	122
Figure IV-25: Impact of typical fabrication errors for the transmission bonding film thickness on the S-parameters: (a) 0° and (b) 90° states.	122
Figure IV-26: Impact of typical fabrication errors for the receiving bonding film thickness on the S-parameters: (a) 0° and (b) 90° states.	122
Figure IV-27: Impact of typical fabrication errors for the diameter of the metallized via on the S-parameters: (a) 0° and (b) 90° states.	123
Figure IV-28: Proposed circularly-polarized unit-cell: (a) Schematic view, (b) transmitting layer, (c) biasing layer of the transmit side, (d) ground plane, (e) DC connection to the ground layer, (f) biasing layer of the receive side, and (g) receiving layer.	125
Figure IV-29: Reflection coefficient (a) S_{11} and (b) S_{22} referred to the Rx and Tx sides, respectively, of the proposed 2-bit circularly polarized unit-cell.	126
Figure IV-30: Magnitude of the transmission coefficients associated to the (a) right-, and (b) left-handed circular polarization.	127
Figure IV-31: (a) Transmission phase and (b) phase-shift between the 0° state and the other states.	127
Figure V-1: Optimization of the proposed 196-element transmitarray. (a) Directivity and gain as a function of the focal ratio (F/D). (b) Optimal phase distribution for a broadside beam.	130
Figure V-2: Theoretical and full-wave simulated broadside gain of the 2-bit transmitarray as a function of frequency.	131
Figure V-3: Theoretical and simulated radiation patterns of the 196-element transmitarray at 29 GHz: (a) E, and H planes.	131
Figure V-4: Co-polarized radiation patterns computed at 29 GHz for a beam scanned from -60° to $+60^\circ$ in (a) E, and (b) H planes.	132
Figure V-5: Optimal phase distributions computed at 29 GHz for a beam pointing at (a) 20° , 40° , and 60° in E plane.	132
Figure V-6: Optimal phase distributions computed at 29 GHz for a beam pointing at (a) 20° , 40° , and 60° in H plane.	132
Figure V-7: Arrangement of the bias lines in the external layer for diodes on the transmission patches: (a,b) sub-array of 7×7 unit-cells, (c,d) a line of 7 unit-cells of the sub-array.	134
Figure V-8: Arrangement of the bias lines in the external layer for diodes on the receiving patches: (a,b) sub-array of 7×7 unit-cells, (c,d) a line of 7 unit-cells of the sub-array.	134
Figure V-9: Prototype of the 2-bit electronically reconfigurable transmitarray: top view (transmitting layer).	135
Figure V-10: Prototype of the 2-bit electronically reconfigurable transmitarray: bottom view (receiving layer).	136
Figure V-11: Setup of the TA prototype mounted in the anechoic chamber for characterization.	136
Figure V-12: Broadside gain: theoretical simulation (solid line), full-wave simulation (dashed line), and measurement in vertical (dot line) and horizontal polarization (dash-dot line).	137
Figure V-13: Normalized radiation patterns computed at 29 GHz in (a) E and (b) H planes. Measured results (solid lines) and simulated results (dash lines).	137
Figure V-14: Location of the faulty unit-cells (in cross) in the prototype: (a) Top and (b) bottom views.	138
Figure V-15: Measured gain as a function of frequency in E (dash lines), and H (dash-dot lines) planes of the prototype compared to the full-wave and theoretical results.	138

LIST OF FIGURES

Figure V-16: (a) Co-, and (b) cross-polarized measured radiation patterns at 29 GHz in E plane for different steering angles from -60° to $+60^\circ$	139
Figure V-17: (a) Co-, and (b) cross-polarized measured radiation patterns at 29 GHz in H plane for different steering angles from -60° to $+60^\circ$	139
Figure V-18: Measured and simulated radiation patterns at 29 GHz in (a) E and (b) H planes for a steering angle of -40°	140
Figure V-19: Measured and simulated radiation patterns at 29 GHz in (a) E and (b) H planes for a steering angle of -20°	140
Figure V-20: Measured and simulated radiation patterns at 29 GHz in (a) E and (b) H planes at broadside.	140
Figure V-21: Measured and simulated radiation patterns at 29 GHz in (a) E and (b) H planes for a steering angle of 20°	141
Figure V-22: Measured and simulated radiation patterns at 29 GHz in (a) E and (b) H planes for a steering angle of 40°	141
Figure V-23: Measured gain as a function of the frequency and elevation angle at broadside in (a) E and (b) H planes.	142
Figure V-24: Measured gain as a function of the frequency and elevation angle for a steering angle of -20° in (a) E and (b) H planes.	143
Figure V-25: Measured gain as a function of the frequency and elevation angle for a steering angle of 20° in (a) E and (b) H planes.	143
Figure V-26: Measured gain as a function of the frequency and elevation angle for a steering angle of -40° in (a) E and (b) H planes.	143
Figure V-27: Measured gain as a function of the frequency and elevation angle for a steering angle of 40° in (a) E and (b) H planes.	143
Figure V-28: Measured gain as a function of the frequency and elevation angle for a steering angle of -60° in (a) E and (b) H planes.	144
Figure V-29: Measured gain as a function of the frequency and elevation angle for a steering angle of 60° in (a) E and (b) H planes.	144
Figure B-1: The 2-bit linearly-polarized transmitarray with the four control boards.	153
Figure B-2: Description of the architecture of the control board.	154

LIST OF FIGURES

Résumé en français

De nos jours, les antennes à réseaux transmetteurs présentent un grand intérêt pour de nombreuses applications civiles et militaires aux bandes de fréquence comprises entre 10 et 110 GHz (réseaux 5G, communications point à point, radars, etc.).

Cette technologie antennaire est composée d'un ensemble de cellules élémentaires illuminé par une ou plusieurs sources focales. Chaque cellule élémentaire comporte deux antennes, l'une fonctionnant en mode réception (Rx) et l'autre en mode transmission (Tx). Ces deux antennes sont connectées par un circuit de compensation de phase afin de focaliser le faisceau dans la direction désirée ou de synthétiser un diagramme de rayonnement spécifique. La phase de l'onde transmise peut être contrôlée électroniquement par l'intégration de dispositifs actifs tels que les diodes varactors, les diodes p-i-n, les commutateurs MEMS ou des matériaux accordables.

Les réseaux transmetteurs sont assez compacts avec un important gain. Par ailleurs, ils ne souffrent pas d'effet de blocage de la source focale (contrairement aux réseaux réflecteurs), ce qui facilite leur intégration dans diverses plateformes (bâtiments, trains, bateaux, véhicules, avions, drones, etc.).

L'objectif général de ce travail de thèse est d'apporter des innovations dans la modélisation et la conception d'antennes à réseaux transmetteurs pour répondre aux spécifications techniques requises pour les applications en bande millimétrique, particulièrement celles en bande Ka (28 - 40 GHz).

Plus précisément, les travaux ont porté sur le développement d'outils numériques pour l'analyse et l'optimisation théoriques des réseaux transmetteurs, la conception et la démonstration de plusieurs prototypes avec des fonctionnalités avancées, telles que des réseaux transmetteurs passifs (larges bandes ou à multifaisceaux) et actifs (à reconfiguration électronique). Les grandes étapes de développement sont décrites dans la suite de cette section.

L'étude théorique des réseaux transmetteurs a concerné deux grandes thématiques à savoir le facétage (pour réduire l'encombrement spatial) ou la compensation par ligne à retard (pour corriger les erreurs de dépointage et augmenter la bande passante).

Dans un premier temps, l'impact de la méthode de compensation de phase sur les performances des réseaux transmetteurs est étudié. La loi de compensation de phase de l'onde quasi-sphérique incidente sur l'ouverture du réseau transmetteur est calculée en utilisant deux méthodes nommées compensation à phase constante et compensation par ligne à retard. Les réseaux d'antennes à ligne à retard fournissent un retard temporel pour compenser correctement les différences de chemins entre la source focale et l'ouverture du réseau. Dans ce cas, le déphasage varie linéairement en fonction de la fréquence. Nous montrons que cette méthode permet d'augmenter la bande passante du réseau transmetteur et de corriger les erreurs de dépointage du faisceau.

Dans un second temps, la faisabilité de réseaux transmetteurs facettés a été analysée au travers de modélisations théoriques sous Matlab (réseaux transmetteurs à deux et trois facettes). Les simulations numériques ont été validées par des simulations électromagnétiques 3-D. Le réseau comprend deux panneaux latéraux (6×20 cellules élémentaires) inclinés d'un angle $\theta = 10^\circ$ et d'un panneau central de 8×20 éléments rayonnants (Figure 1). Pour un certain angle d'inclinaison, nous démontrons que la bande passante et la capacité de dépointage du réseau transmetteur sont améliorées au détriment du gain.

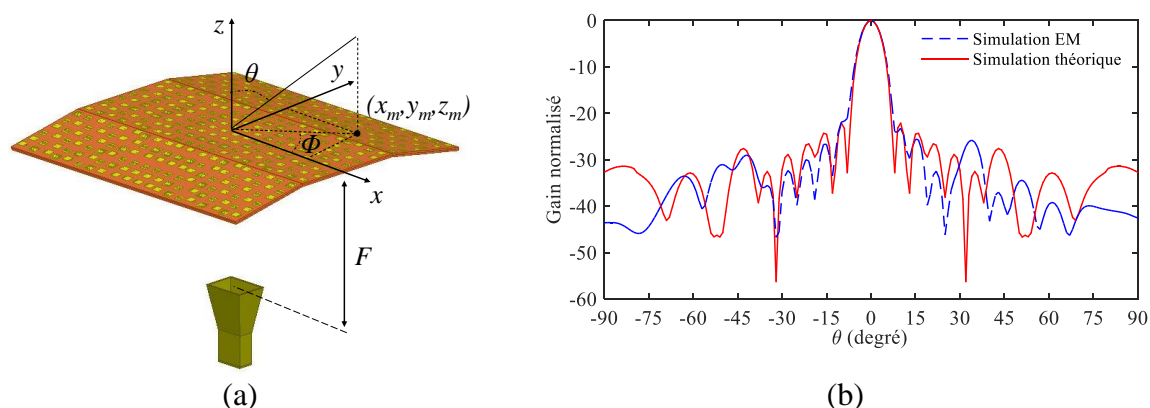


Figure 1 : Réseau transmetteur à 3 facettes : (a) vue schématique, (b) diagrammes de rayonnement (simulé et théorique) à 29 GHz sur le plan E.

La suite des travaux a porté sur la conception et le prototypage de deux réseaux transmetteurs passifs, dont l'un à faisceau collimaté et très large bande, et l'autre à quatre faisceaux fixes. Les deux réseaux transmetteurs sont basés sur une cellule élémentaire à 3 bits de quantification de phase. Cette dernière assure une double fonction à savoir la compensation de phase et la conversion de la polarisation linéaire en circulaire.

La cellule élémentaire est composée de trois couches métalliques imprimées sur deux substrats de type Rogers RT / Duroid 6002. Ces derniers sont liés à l'aide du film de collage CuClad 6700 et séparés par un plan de masse. Des antennes patch rectangulaires chargées par

une fente en U sont imprimées sur les deux couches externes de la cellule. L'élément rayonnant en mode réception est en polarisation linéaire, et celui en mode transmission est polarisé circulairement (les coins du patch sont tronqués). Les deux patches sont connectés à l'aide d'un via métallisé. Les 8 états de phase requis pour une quantification 3 bits sont obtenus par rotation de l'élément rayonnant en mode transmission de 0° à 315° par pas de 45° .

La topologie de la cellule passive ainsi proposée a été optimisée, en utilisant le simulateur commercial Ansys HFSS. Elle présente une bande passante en transmission à -3 dB supérieure ou égale à 15,9% pour tous les états de phase. De plus, le coefficient de réflexion reste inférieur à -10 dB entre 27 et 32 GHz (soit 17,2% autour de la fréquence d'optimisation de 29 GHz).

Le réseau passif à faisceau collimaté, basé sur 1600 cellules élémentaires, a été réalisé et caractérisé. Il est illuminé par une source focale de type cornet en polarisation linéaire avec un gain nominal de 10 dBi. Elle est placée à 134 mm de l'ouverture du réseau ($F/D = 0,67$). Cette distance focale a été optimisée en utilisant le simulateur hybride développé en interne. Il est conçu à partir de données de simulations électromagnétiques (source focale et cellules élémentaires) et des expressions analytiques pour extraire les performances du dit réseau. Le réseau transmetteur démontre un gain mesuré de 33,8 dBi (correspondant à une efficacité d'ouverture de 51,2%) et une bande passante à -3 dB supérieure à 15,9%. Le rapport axial mesuré présente quelques variations sur toute la bande d'intérêt (27 à 32 GHz), mais il reste inférieur à 1 dB. Un très bon accord est observé entre les réponses de gain théoriques et expérimentales (Figure 2).

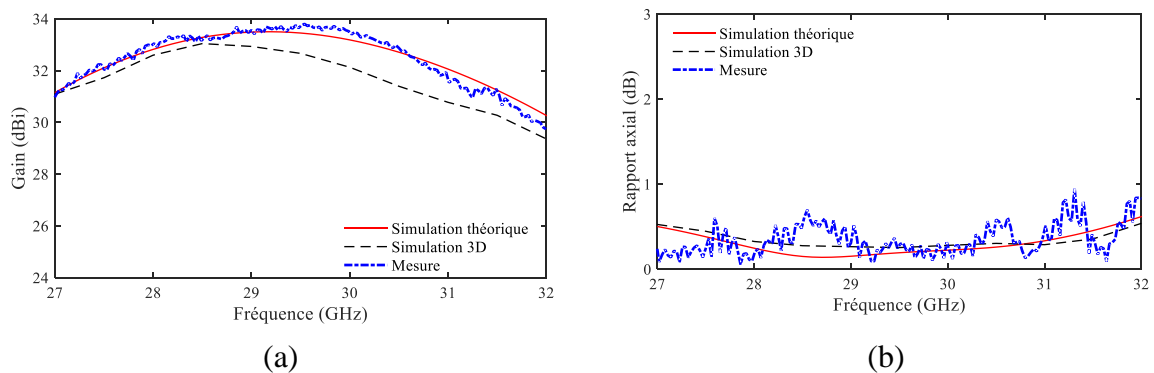


Figure 2 : Réseau transmetteur à faisceau collimaté : (a) gain et (b) rapport axial en fonction de la fréquence.

Par la suite, un second réseau transmetteur passif, de forme circulaire et constitué de 489 cellules élémentaires, est présenté. Sa distribution de phase a été optimisée à 29 GHz en utilisant un code d'algorithme génétique couplé à l'outil de simulation hybride développé en interne. Les faisceaux sont dépointés à $\pm 25^\circ$ avec un gain d'environ 18 dBi sur le plan horizontal et le plan vertical à la fréquence d'optimisation. Le réseau transmetteur est illuminé

par le cornet utilisé dans le réseau transmetteur à faisceau collimaté. Il est placé à 80 mm de l'ouverture du réseau (correspondant à $F/D = 0,64$). La bande passante en gain mesurée à -3 dB s'étend de 27,7 GHz à 32 GHz (ceci correspond à une bande passante fractionnelle de 14,8% à 29 GHz). Les diagrammes de rayonnement sur le plan vertical et le plan horizontal sont indiqués sur la Figure 3.

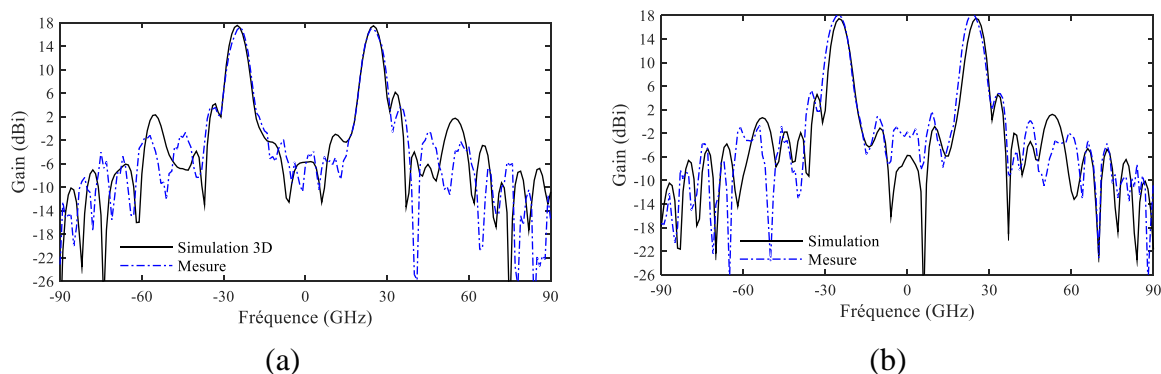


Figure 3 : Diagrammes de rayonnement (polarisation circulaire gauche) simulés et mesurés du réseau transmetteur à quatre faisceaux dans les (a) plan horizontal (29 GHz) et plan vertical (29 GHz).

La dernière partie de ce projet de thèse a concerné la conception d'un réseau transmetteur électroniquement reconfigurable dans la bande de fréquence 27-31 GHz. Dans ce contexte, une cellule élémentaire active à quatre états de phase (2 bits) en polarisation linéaire a été conçue et validée expérimentalement. Elle est composée de six couches métalliques imprimées sur trois substrats identiques. Les éléments rayonnants sont des antennes patch rectangulaires comprenant chacun deux diodes PIN pour contrôler la phase de transmission. La cellule élémentaire a démontré expérimentalement des pertes d'insertion minimales de 1,6 - 2,1 dB et une bande passante en transmission (à 3 dB) de 10-12,1% pour les quatre états de phase 0° , 90° , 180° et 270° .

Cette cellule a ensuite été utilisée pour la conception d'un réseau transmetteur électroniquement reconfigurable comprenant 14×14 cellules élémentaires et 784 diodes PIN. Un prototype a été réalisé et caractérisé ; il présente un gain maximum mesuré de 19,8 dBi, correspondant à une efficacité d'ouverture de 15,9%, et une bande passante à 3 dB de 4,7 GHz (26,2-30,9 GHz).

La capacité de dépointage du réseau transmetteur a été caractérisée en considérant la distribution de phase calculée à l'aide du simulateur hybride. Les diagrammes de rayonnement en co-polarisation pour les angles de dépointage compris entre -60° et $+60^\circ$ par pas de 10° dans les plans E et H sont présentés sur la Figure 4. Le gain maximal mesuré dans le plan E pour un dépointage à -60° et 60° est égal à 15,1 dBi et 13,1 dBi, respectivement, et à 14,4 dBi et 14,9 dBi dans le plan H. Pour un faisceau dépointé à -20° et 20° , nous avons mesuré un gain

maximum dans le plan E de 18,9 dBi et 18,7 dBi, respectivement, et de 19,1 dBi et 18,7 dBi dans le plan H, respectivement. Les résultats montrent que les diagrammes sont asymétriques sur les plans E et H en raison de la distribution des cellules élémentaires défectueuses. En effet, ces dernières sont plus importantes d'un côté que de l'autre.

En dépit de ces quelques éléments défailants (51 cellules élémentaires), ce prototype valide le principe de fonctionnement et la faisabilité de réseaux transmetteurs électroniquement reconfigurables en bande Ka, et à 2 bits de quantification de phase. Il constitue une des premières réalisations de ce type de réseau dans l'état de l'art actuel.

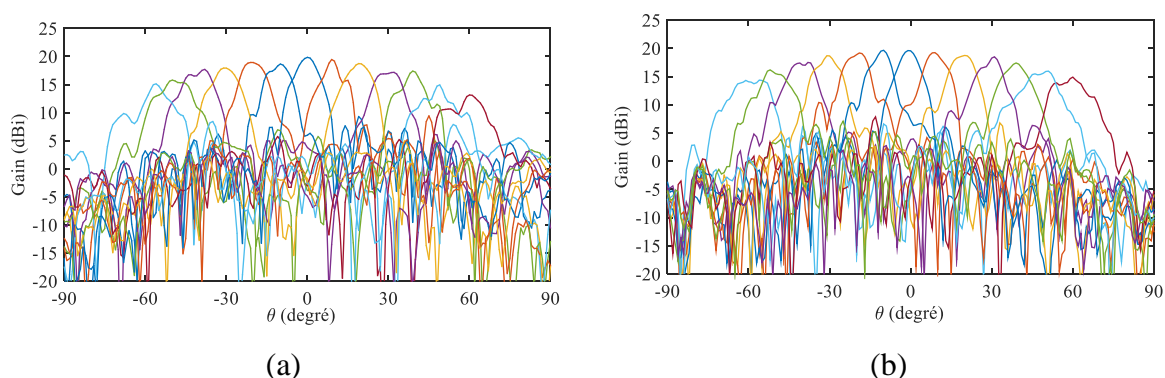


Figure 4 : Diagrammes de rayonnement mesurés du réseau transmetteur électroniquement reconfigurable dans les plans E (a) et H (b) à 29 GHz) en fonction de l'angle de dépointage de $\pm 60^\circ$.

Abstract

Nowadays, transmitarray antennas are of great interest for many civil and military applications in frequency bands between 10 and 110 GHz (5G mobile networks, point-to-point communication systems, radars, etc.).

This thesis aims to make major innovations in modeling and design of transmitarray antennas for Ka-band applications (28-40 GHz). It focuses on the development of numerical tools, and the design and demonstration of several prototypes with advanced functionalities, such as passive (broadband or multibeam) and active (at electronic reconfiguration) transmitarrays.

The first part of the work consists of a theoretical analysis of the transmitarray antenna. In a first step, the impact of the phase compensation method on the performance of the transmitarray is studied. The phase compensation law of the quasi-spherical wave incident on the array aperture is calculated using two methods called constant phase compensation and true-time delay (TTD) compensation. The numerical results show that TTD compensation allows an increase of the transmitarrays bandwidth and a reduction of the beam squint as compared to constant phase-shift compensation. In a second step, the operating principle of faceted transmitarrays is described in detail. The numerical simulation of a 3-facet transmitarray is validated through 3-D electromagnetic simulations. For a certain facet angle, the bandwidth and the beam scanning capability of the TA are improved at the expense of the gain.

The next step of the work concerns the design and prototyping of two passive transmitarray antennas, one with a collimated and a large bandwidth, and the other with four fixed beams. The two transmitarrays are based on a 3-bit unit-cell providing two functions, namely the phase compensation and the polarization conversion from linear to circular. The passive beam-collimated transmitarray exhibits a measured gain of 33.8 dBi (corresponding to an aperture efficiency of 51.2%) and a 3-dB gain-bandwidth larger than 15.9%. The quad-beam transmitarray phase distribution has been optimized by a genetic algorithm code coupled with an analytical tool. The array is designed to radiate four beams at $\pm 25^\circ$ in the horizontal and vertical planes at the optimization frequency.

The last part of the work aims to the design of a 27-31 GHz reconfigurable transmitarray antenna. Initially, an active unit-cell with four phase states (2 bit) in linear polarization was

ABSTRACT

designed and validated experimentally. It consists of six metal layers printed on three substrates. The radiating elements are rectangular patch antennas, each of them including two PIN diodes to control the transmission phase. The operating principle of the unit-cell has been experimentally validated with a minimum insertion loss of 1.6-2.1 dB and a 3-dB transmission bandwidth of 10-12.1% for the four phase states. 0° , 90° , 180° and 270° .

Then, this unit-cell was used for the design of a reconfigurable transmitarray antenna comprising 14×14 unit cells and 784 PIN diodes. A prototype was realized and characterized, it presents a measured maximum gain of 19.8 dBi, corresponding to an aperture efficiency of 15.9%, and a 3-dB bandwidth of 4.7 GHz (26.2% at 30.9 GHz). Despite some faulty elements, this prototype validates the operating principle and the feasibility of Ka-band transmitarray antennas with a 2-bit phase quantization. It is one of the first demonstration of such an antenna in the current state of the art.

ABSTRACT

General introduction

The telecommunications domain has greatly evolved in the last decades with the advent of a wide range of applications such as satellite communication (SatCom) systems, wireless fixed and mobile networks, and broadcast services. However, this abundance of emerging applications is not without consequence; it is accompanied with a global bandwidth scarcity at lower frequencies. Nowadays, the millimeter wave frequencies, spanning from 30 GHz to 300 GHz with free space wavelengths between 1 mm and 10 mm, are increasingly explored to overcome the limitation of spectrum resources. Millimeter waves are also attractive for their potential in miniaturizing systems and their immunity to interferences thanks to the shorter wavelength (the transmitted signal is highly attenuated). Beside these advantages, the millimeter-wave spectrum presents some inconvenients. First, the smaller size of components needs greater precision in manufacturing, so they are costly. Next, millimeter-wave frequency bands can hardly be used for long distance applications due to the significant atmospheric absorption. The Ka-band (27 – 40 GHz¹), which means Kurtz-Above, is the frequency band of interest for this thesis because of the numerous applications developed there. Among these applications, we can mention the 5th-Generation mobile wireless networks, SatCom systems, and the Internet of Space (IoS). This latter is a solution to yield high-speed data links throughout the world, including remote areas without access to a terrestrial network. This future network will complement the existent terrestrial networks and the SatCom systems to provide ubiquitous global connectivity.

Considered for a long time as a secondary issue on the overall system design, antennas play today an important role in the performances of many systems. Antennas with high directivity, large bandwidth for high data rate beyond several Gbit/s, and capability to focus the radiation beam are required for applications at millimeter-wave frequencies (satellites, point-to-point communications systems, radars, etc.). Two main families of antennas are used to achieve such properties. The first one is based on an optical approach, which optimizes the geometrical shape of the antenna to form the desired pattern, such as parabolic reflectors or lens

¹ IEEE Std 521-2002 Standard Letter Designations for Radar-Frequency Bands, 21 Jan. 2003.

antennas. The other is the antenna array approach, where discrete elements with a feed network are used to obtain a specific beam. Corporate-feed networks (e.g. waveguide-slot arrays, printed microstrip antennas arrays) and quasi-optical spatial feeds (e.g. reflectarray, transmitarray antennas) are the two main feeding topologies of antenna arrays. In the latter family, transmitarray antennas are among the most attractive for applications at millimeter waves. In fact, transmitarray antennas combine the favorable features of the optical and the antenna array theories. They do not suffer from high insertion loss of the beam-forming network compared to phased arrays. There is no feed blockage effect in contrast to the architecture of reflectarray antennas. Thanks to its low profile, transmitarray antennas are easily integrated onto various platforms (buildings, vehicles, aircrafts, etc.). A transmitarray antenna consists of one or several feeds and an array of antenna elements named unit-cells. Each unit-cell is composed of a first antenna working in receive mode, and connected through phase-shifters to a second antenna working in transmission mode. The phase-shifter is optimized in order to convert the incoming spherical wave into a planar one focused or collimated in the desired direction.

The objective of this thesis is to study, design and realize fixed-beam and electronically-reconfigurable transmitarray antennas at Ka-band. In addition to a large available bandwidth, Ka-band is also capable to operate in multipath environments compared to other higher frequencies. This thesis was carried out in CEA-Leti as a part of the French Research Agency (ANR) project labeled TransMil (Transmitarray antenna at Millimeter wave) in collaboration with the Institute of Electronics and Telecommunications of Rennes (IETR).

The manuscript investigates two main axes, namely fixed-beam and electronically-reconfigurable transmitarray antennas. The document is organized as follows.

In Chapter I, antenna applications and specifications at Ka-band are reviewed. Next, the operating principle of transmitarray antennas is briefly described. Finally, an overview of the literature on transmitarray antennas is presented according to the beam type, i.e. fixed or reconfigurable.

A theoretical analysis on the performances of transmitarrays according to their physical characteristics (size, shape etc.), and phase compensation is established in Chapter II. The two main techniques of phase compensation (compensation at single frequency and true time delay) are compared. The working principles of a faceted transmitarray structure and its advantages compared to a flat one are also established.

In Chapter III, a fixed beam transmitarray with a 3-bit phase resolution based on linearly, or circularly-polarized unit-cells is presented. The operation principle, electromagnetic simulation results and prototypes are demonstrated.

Chapter IV is dedicated to the design, optimization and prototyping of a 2-bit linearly-polarized electronically reconfigurable unit-cell.

In Chapter V, the concept of electronically reconfigurable transmitarray with a 2-bit phase resolution at 29 GHz is presented. Measurements are performed to demonstrate the proposed concept.

Finally, main conclusions, recommendations and open issues for future work are discussed in chapter VI.

Chapter I. Introduction

This introductory chapter is organized as follows. First, a general overview of mm-wave (millimeter-wave) applications is presented. We will focus on two main applications, 5th generation communication networks and SatCom systems, in which transmitarray antennas have attracted a lot of interest. Standardization established by institutions such as ITU (International Telecommunications Union), ETSI (European Telecommunications Standards Institute), ECC (Electronic Communications Committee), FCC (Federal Communications Commission), and NATO (North Atlantic Treaty Organization) for these applications are detailed. In the second section, the working principle of transmitarray antennas and also the recent state of the art covering fixed beam, switched beam and electronically reconfigurable transmitarray antennas are presented. The last section describes the theoretical model and technique of simulation in order to predict accurately all the parameters of the transmitarray antenna. Finally, conclusions and challenges for future transmitarray antennas are drawn.

1.1. Millimeter-wave applications and emerging technologies

According to the IEEE radar-band designation standard, mm-wave frequencies correspond to mm, V, W, and a part of Ka band [1] as presented in Table I-1. Previously reserved to military and scientific domains, the millimeter frequency spectrum has been more and more explored for numerous industrial and consumer applications in recent years [2].

Table I-1: IEEE radar-frequency letter band definition.

Band designation	Nominal frequency range (GHz)
Ka	27 - 40
V	40 – 75
W	75 – 110
mm	110 – 300

The main advantages of mm-wave frequency bands are the wide available bandwidth and better inherent security and privacy due to the strong propagation attenuation. Consequently, a huge number of civil and military applications are developed in these frequency bands, especially in Ka-band. Typically allocated for SatCom systems, Ka-band has

recently drawn increased attention for a lot of emerging applications, in the field of mobile communications, radars, and imaging systems.

- **Imaging systems**

As examples of imaging systems, we can mention the full body scanners used in some airports to detect hidden objects on passengers. These imaging systems typically work in the frequency band of 27 –33 GHz [3] or 70 –80 GHz [4].

- **Radars**

High-frequency automotive sensor technology, developed for adaptive cruise control, parking aid, blind angle control, or assistance systems (stop-and-go, braking, lane keeping, lane changing, firing of restraints and airbags), is another useful application developed at millimeter waves. Automotive sensors can be classified into three categories according to their detection range and directions. The main specifications of antennas for the different types of radars are defined Table I-2.

The first range of sensors, called Short Range Radar (SRR), creates a virtual safety belt around the vehicle. It looks in all directions around the vehicle at an approximate range of 0-30 m, with a wide Field Of View (FOV) (up to 160°). Its operating bandwidth is equal to 4 GHz to achieve high range resolution (≈ 5 cm). Typically, SRRs are based on 24 GHz technology [5]. However, the development of SRRs in the frequency band of 77– 81 GHz has been started due to emerging regulatory requirements, as well as the larger bandwidth availability, smaller sensor size and performance advantages [6].

We are interested now to the second range of sensors named Long Range Radar (LRR) sensors. They are characterized as having a range up to 200 meters with a narrow (10° to 20°) field of view (FOV). LRRs operate in the 76 –77 GHz band, and use a bandwidth of 0.5 to 1 GHz in order to achieve a range resolution of around 0.5 m. The 76 –77 GHz band has already been regulated in the 90's followed by standardization in Europe [7].

The last category of sensors is constituted by Medium Range Radar (MRR). It has been introduced to cover a range between SRR and LRR fields of detection. Traditionally, MRR operate at narrow band 24 GHz or Ultra-Wide Band (UWB) 79 GHz.

A presentation on the 5G and SatCom applications including details on specifications, standards, and typical antenna technologies and architectures is included in the next sections.

Table I-2: Antenna main specifications for automotive radars.

Performances	Long Range Radars (LRRs)	Short Range Radars (SRRs)
Gain	≥ 27.5 dBi	≥ 13.5 dBi
Azimuth scanning	$\pm 11^\circ$	$\pm 50^\circ$
Elevation scanning	$\pm 2.5^\circ$	$\pm 5^\circ$
Side lobe level	≤ -25 dB	≤ -25 dB

1.1.1. 5th generation communications networks

The field of wireless communications technology has evolved rapidly, since Guglielmo Marconi demonstrated successfully the ability to provide radio communications [8]. Mobile wireless networks technology has progressed from the first generation (1G) in 1980s, second generation (2G) in 1990s, third generation (3G) in 2000s, fourth generation (4G) in 2010s, and now fifth generation (5G) planned for 2020s. Contrariwise to all the previous generations, the 5G network technology will not only be an evolution of mobile networks. Considered as a new era in mobile communication technology, 5G networks will ensure user experience continuity even in critical environments (e.g. in trains on the move). Furthermore, it will be faster, highly reliable, and also a key enabler for a very large number of devices including smart objects in the Internet of Things.

The two main architectural options for 5G networks, named Distributed- and Centralized-Radio Access Networks (D-RAN and C-RAN), are presented in Figure I-1. In a fully distributed baseband deployment, backhaul links connect the Macro- and Small-cells to the Core Network. Instead, C-RAN is the best solution to enhance performance in traffic hotpots. In this architecture, fronthaul links ensure the data transfer from or to users and the Base Band Unit (BBU). The backhaul links ensure connection with the Core Network. Ultra-high data-rates are required for backhaul and fronthaul links.

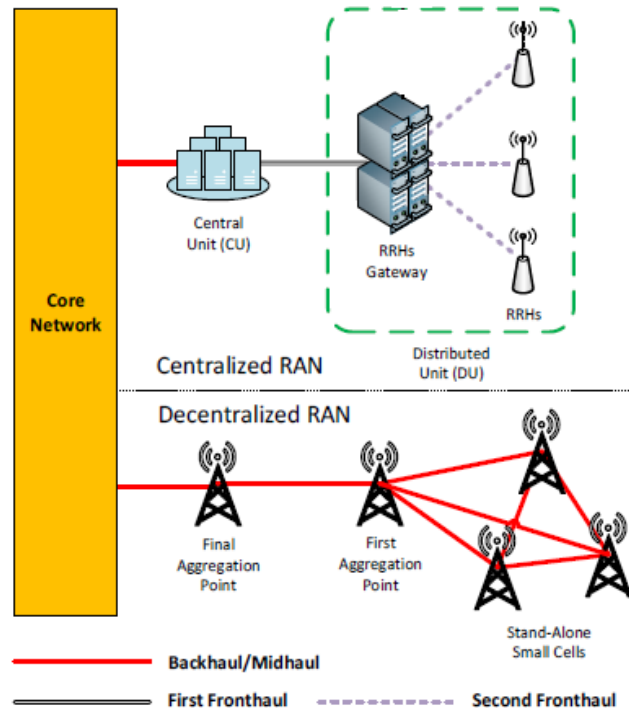


Figure I-1: D-RAN and C-RAN 5G network architectures with backhaul and fronthaul [9].

The large amount of under-utilized spectrum in millimeter wave frequency bands is an excellent candidate for the deployment of the future 5G network technology. Different frequency bands, especially the Ka-band (28 or 38 GHz), V-band (60 GHz) and the E-band (71– 76 GHz and 81– 86 GHz), have been explored for the 5G systems [10]. Recently, FCC is examining the possibility of licensing the frequency band 24 – 90 GHz for the use of cellular mobile network services [11]. There is still no consensus definition on the operating frequency band of 5G, even if Ka-band seems to be the band of choice. Indeed, there are enough free bands around 28 GHz. Moreover, it is possible to reuse 3GPP LTE (3rd Generation Partnership Project, Long Term Evolution) functionalities in this frequency band [12]. Apart from transmitarray antennas, other types of antenna arrays with fixed or reconfigurable beams such as reflectarrays and phased arrays have been presented in the literature as good candidates to be implemented for 5G systems (backhaul /fronthaul links, access points).

Phased array antennas

Several phased arrays have been presented in the open literature as good candidates for 5G applications. Some of them are described in the following.

In [13], a patch antenna at 3 GHz and an array antenna at 30 GHz of the same physical size have been designed and characterized for 5G systems. A full millimeter wave beamforming prototype has been also developed and fabricated, as shown in Figure I-2. Authors checked the

feasibility of millimeter wave bands near 28 GHz for the relatively large geographical coverage of cellular services.

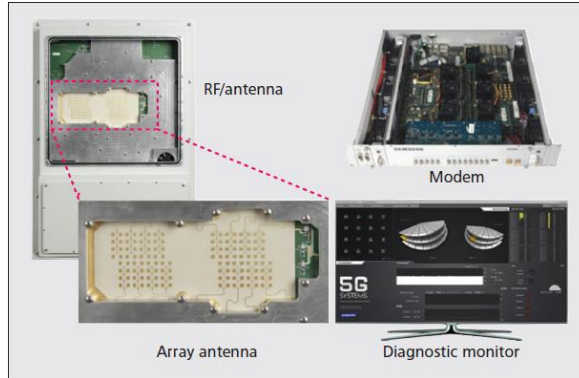


Figure I-2: Configuration of the mm-wave beamforming prototype [13].

Each transmit and receive antenna of the two channels is composed of 32 antenna elements with 8 horizontal and 4 vertical elements. The antenna array size is $60 \times 30 \text{ mm}^2$. The channels are connected to the RF unit, which contains phase shifters, mixers, and related RF circuitry. The phase shifters can be controlled in order to achieve the desired beam. The antennas performances are summarized in Table I.3.

Table I.3: Key system parameters of the mm-wave beamforming prototypes [13].

Key system parameters	Values
Carrier frequency	27.925 GHz
Subcarrier spacing	244.14 kHz
Array gain	18 dBi
Full Width at Half Maximum (FWHM)	10° (Horizontal)/ 20° (Vertical)
Beam scanning range	$\pm 30^\circ$ (Horizontal)
Effective isotropic radiated power (EIRP)	Max 49 dBm (Nominal 41 dBm)

A 32-element phased-array transceiver for 5G communication links is presented in [14]. A 28 – 32 GHz silicon core chip is implemented with 4 transmit (TX)/receive (RX) elements, and 6-bit phase control. Eight of these chips are placed on a printed circuit board (PCB) with integrated antennas and Wilkinson combiners. The array is measured on both transmit and receive mode in a 300 m wireless communication as illustrated in Figure I-3(a). It demonstrated a measured EIRP (effective isotropic radiated power) of 41 dBm at P1dB and a beam scanning capability of $\pm 20^\circ$ and $\pm 50^\circ$ in E-, and H-planes, with a power consumption of 4.2 W and 6.4 W in RX and TX modes, respectively (Figure I-3(b)).

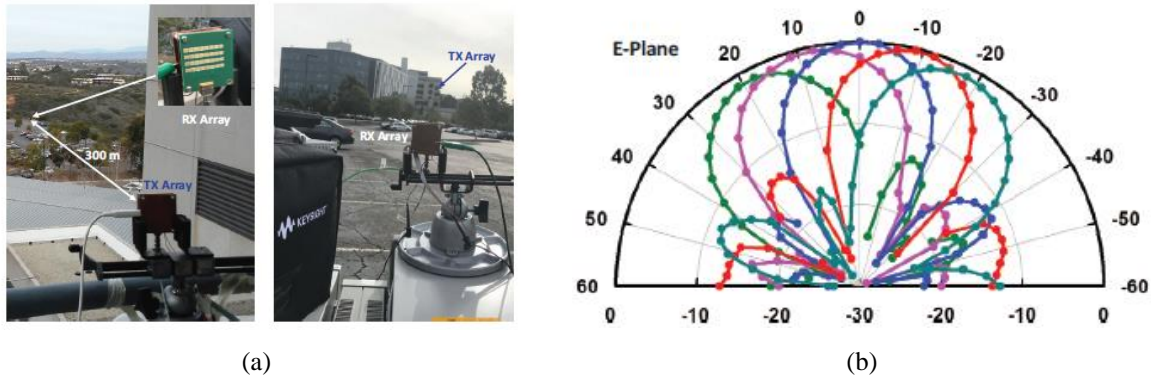


Figure I-3: 28 GHz phased array transceiver. (a) Measurement setup. (b) E plane radiation pattern at 29.5 GHz.

Reflectarray antennas

Recently, some interesting architectures that demonstrate good performances for 5G applications have been presented in the open literature.

A single layer polarization independent reflectarray antenna working at 28 GHz for future 5G cellular applications is presented in [15] (Figure I-4). The array, which size is $10\lambda \times 10\lambda$, is composed of 400 unit cells. Each unit-cell contains three circular rings optimized to achieve linear phases by changing their size. The designed reflectarray is fed by a 12 dBi gain pyramidal horn having aperture dimensions of $14 \times 12.4 \text{ mm}^2$ with WR-28 waveguide. The CST software simulation results of the antenna exhibit a gain of about 25 dBi, and an efficiency of 58% at 28 GHz with E- and H-plane half-power beam-widths of 43.8° and 48.2° , respectively.

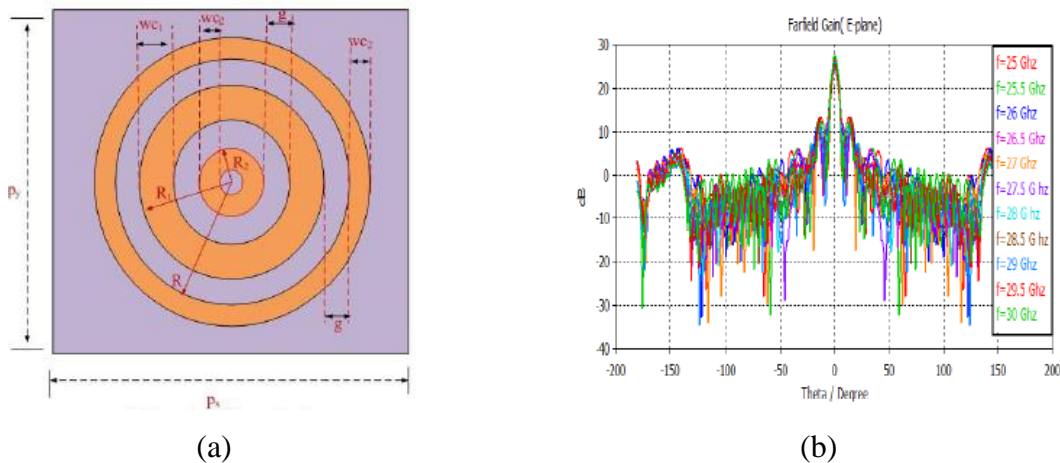


Figure I-4: Single layer polarization independent reflectarray antenna. (a) Top view of the unit-cell. (b) Radiation patterns in E-plane.

A 38 GHz folded reflectarray antenna for 5G point-to-point communication is presented in [16]. It is composed of an upper reflector with a polarizing grid, a lower reflector with printed patches and a feed horn. The distance between the two reflectors is equal to 37.8 mm which corresponds to a focal length of 75.6 mm. The array has demonstrated a gain of 30.9 dBi, an

efficiency of 53.7%, and low side-lobe level of about -23 dB. The 3-dB gain bandwidth is between 34 GHz and 42 GHz. The architecture and E-plane radiation pattern at 38 GHz are shown in Figure I-5.

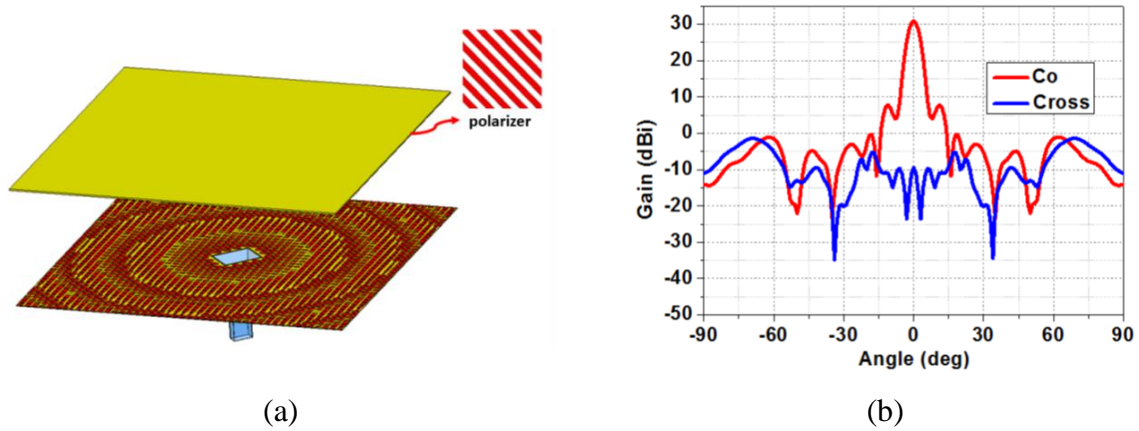


Figure I-5: (a) 3-D view and (b) radiation patterns in E-plane of the proposed folded reflectarray antenna at 38 GHz.

Another reflectarray that fulfills the masks defined by the ETSI institution for point-to-point communications is presented in [17]. This 260-mm compact square-shape dual-polarized offset reflectarray operating around 60 GHz is illuminated by two WR-15 open-ended rectangular waveguides (OE-RWGs) with orthogonal linear polarizations (x-, and y directions). It is based on a double-layer unit-cell with variable-size crossed dipoles. The normalized radiation patterns of the array at 60 GHz compared to the ETSI masks are illustrated in Figure I-6(a,b), a maximum gain of 33.1 dBi is obtained.

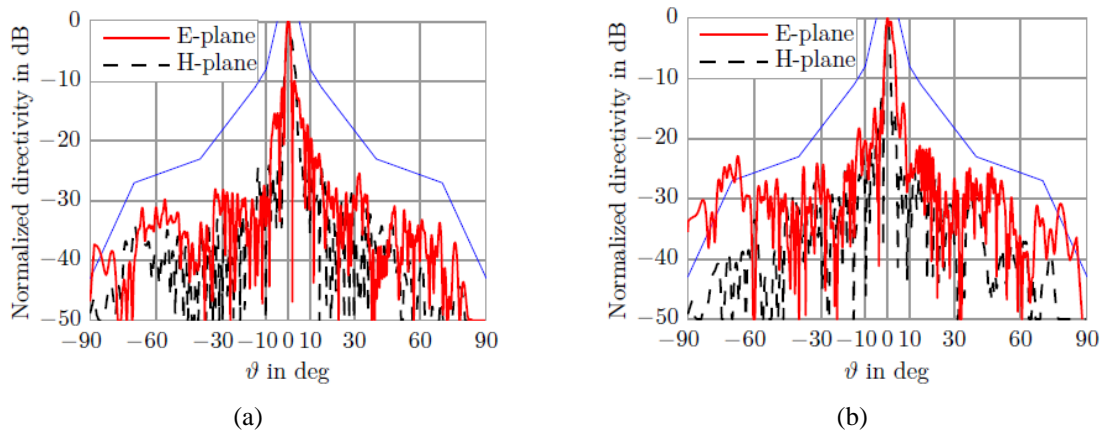


Figure I-6: Measured normalized radiation patterns in E-, and H-plane at 60 GHz with ETSI masks: (a) polarization in x-direction, (b) polarization in y-direction.

Specifications

The ETSI institution establishes in its document ETSI EN 302 217 [18] the operating rules of antennas for point-to-point communication systems. The radiation masks of the three classes of antennas (2, 3, and 4) that can be used for the frequency band 24- 34 GHz and 30-47 GHz are plotted in Figure I-7(a), and Figure I-7(b), respectively. Two alternative radiation

masks specifications of the class 3 (B, and C) for the frequency band 30-47 GHz are presented in Figure I-8 (a, b).

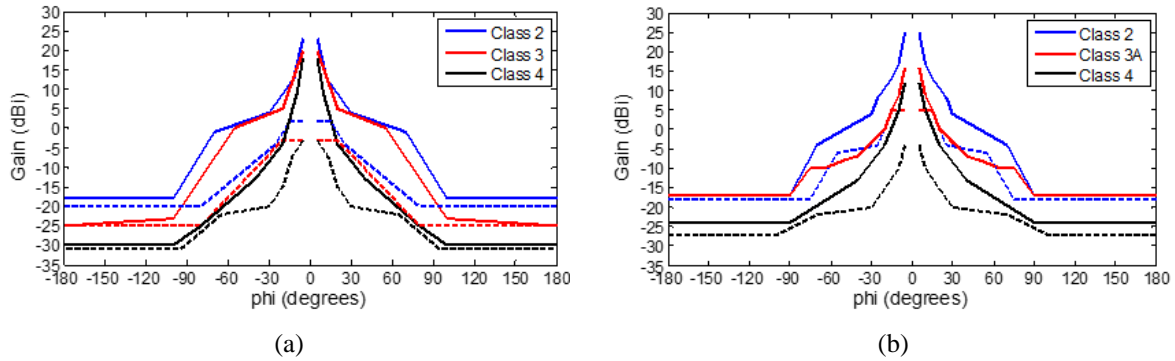


Figure I-7: Co-polar (solid line) and cross-polar (dotted line) components radiation masks of the ETSI 302 217 in the frequency band (a) 24 – 30 GHz, and (b) 30 – 47 GHz.

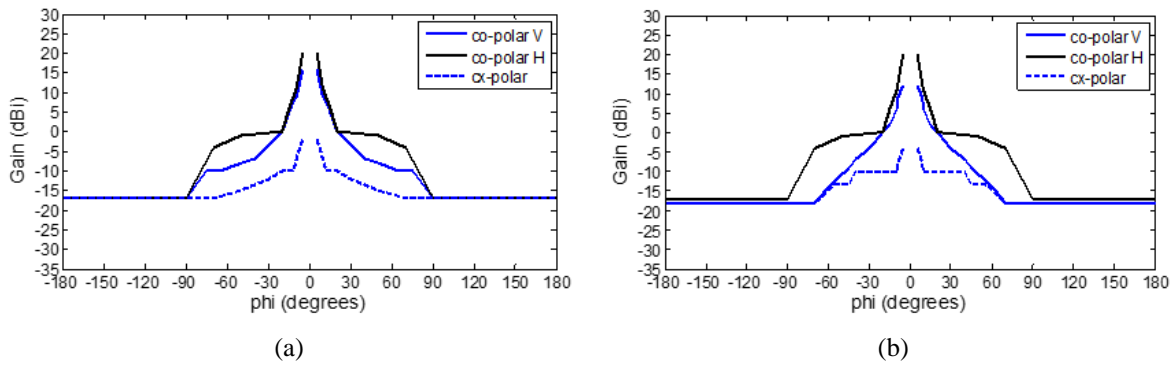


Figure I-8: Alternative radiation masks of the Class 3 antenna defined by of the ETSI 302 217 in the frequency band 30 – 47 GHz. (a) Class 3B and (b) class 3C.

1.1.2. SatCom systems

A satellite communication (SatCom) system is composed of three main parts, a space segment, an earth segment, and a user segment as depicted Figure I-9. The space segment is formed by at least one geostationary satellite which allows establishing bidirectional links between a set of gateways (GW) and the user terminals. The ground segment comprises a set of anchor GWs which are in charge of transmitting and receiving data, traffic management to or from user terminals, a Telemetry Tracking and Control station (TTC) to transmit and receive information to or from space, and a network control center. The user segment which is composed of a set of user terminals (Earth station terminals). Each terminal includes a reception, Down Link (DL) and a transmission Up Link (UL) channel.

Due to the increase of satellite uses, congestion has become a serious issue in the lower frequency bands. New technologies and services are being investigated at higher frequencies. In fact, the higher frequency bands typically give access to wider bandwidth, but are also more

susceptible to propagation attenuation and signal degradation due to the atmospheric absorption (rain, snow, etc.).

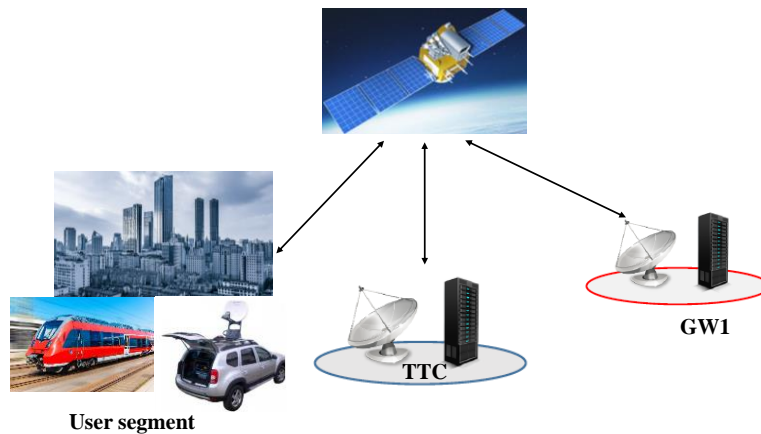


Figure I-9: The main building blocks of a satellite communication system.

SatCom systems provide services for government and civil applications over wide geographical areas and large numbers of users. Generally, the services can be classified as Mobile Satellite Services (MSS), Fixed Satellite Services (FSS), Broadcast Satellite Services (BSS), and military services. The different satellites are placed on a geostationary satellite orbit (GSO) or non-geostationary satellite orbit (non-GSO).

Several phased array and reflectarray antennas in circular or linear polarization have been demonstrated in the open literature for SatCom applications. Some of them are described as following.

Phased array antennas

An ultra-low profile phased array antenna (ThinKom's agile, ThinAir® Falcon-Ka2517), which ensures broadband in-flight connectivity using Ka-band High Throughput Satellites, or military WGS services (Wideband Global Satcom), is demonstrated in [19]. It provides high throughput (up to 400 Mbps Downlink and 100 Mbps Uplink) and with maximally efficient use of transponder bandwidth (1.5-3 bits/Hz). This antenna is useful for broadband in-flight connectivity using Ka-band High Throughput Satellites, or military services. The prototype and the main characteristics of the proposed array are shown in Figure I-10.

Dimensions: 127cm x 74cm x 8cm
Receive band: 17.8-21.2 GHz
Transmit band: 27.5-31 GHz
G/T: 15 to 18 dB/K (12.5 dB/K at 20° Elev)
EIRP: 48.5 to 51.5 dBW
Axial Ratio: < 2.0 dB typ.
Polarization: Switchable circular



Figure I-10: ThinKom’s agile, ThinAir® Falcon-Ka2517 antenna for broadband air flight connectivity [19].

Electronically reconfigurable arrays working in both Ku and Ka satellite bands are demonstrated in [20]. They are based on a diffractive metamaterials concept, named Metamaterial Surface Antenna Technology (MSAT). Beam scanning is achieved by using high-birefringence liquid crystals. This latter permits large range of beam scanning ($> 60^\circ$) with power consumption lower than 10 Watts and antenna thickness ~ 5.0 cm. The prototypes of the proposed antennas have demonstrated combined transmit and receive functions from a single aperture, dynamically controllable polarization, and ~ 30 dB of cross-polarization discrimination. A beam scanning capability of 360° is demonstrated in azimuth plane and the elevation scanning is higher than 60° (Figure I-11).

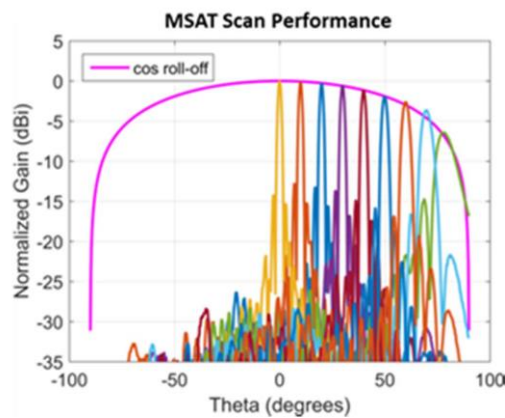


Figure I-11: 70cm Ku-band MSAT beam patterns vs. scan angle [20].

A Variable Inclination Continuous Transverse Stub (VICTS) array with 2 D mechanical beam scanning capability is presented by the company ThinKom [21]. This architecture requires 40% to 75% less area than a conventional phased array for the same G/T performance. The prototype and radiation pattern steered at 63° from the broadside are shown in Figure I-12.

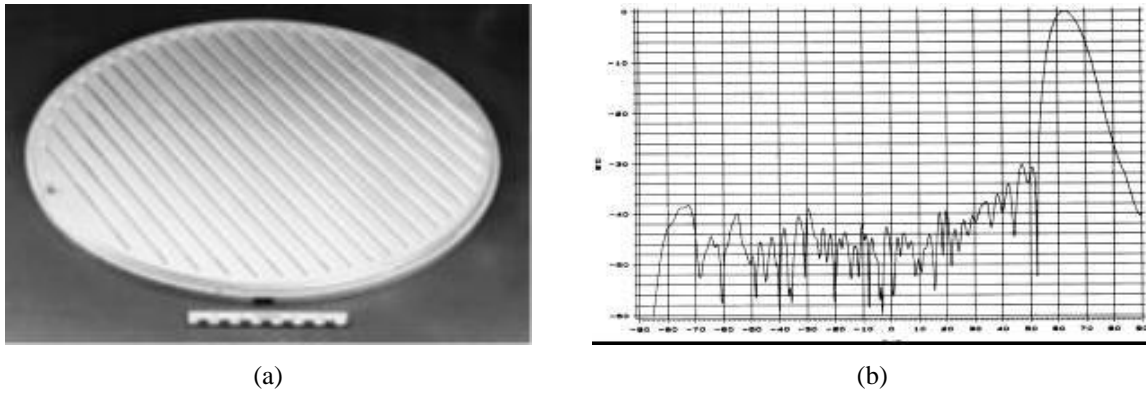


Figure I-12: (a) 51 cm diameter Ku-band Variable Inclination Continuous Transverse Stub (VICTS) array. (b) Measured elevation-plane pattern for the 51 cm VICTS array at 12.5 GHz (scanned to 63 degrees) [21].

In [22], an 8×8 phased array antenna with a combined mechanical and electrical beam steering is developed at Ka-band in the frame of the German-funded Project Kasanova. The transmitting (T_x) aperture is composed of circular horn antenna elements that are uniformly fed by two waveguide distribution networks for horizontal and vertical polarization. The receive (R_x) aperture is formed by a separate antenna, with the R_x horn element and the R_x waveguide networks being a scaled version (factor 1.5) of the T_x geometry. The mechanical positioning shall be achieved with an accuracy of approximately $\pm 1^\circ$ in azimuth and elevation, hence providing a coarse beam pointing towards the satellite. The fine positioning of the beam between -1° and 1° from boresight will be achieved electronically by means of four individual sub-arrays via true time delays. Good agreement is obtained between the simulated and measured radiation patterns in the $\phi=45^\circ$ azimuth cut as shown in Figure I-13.

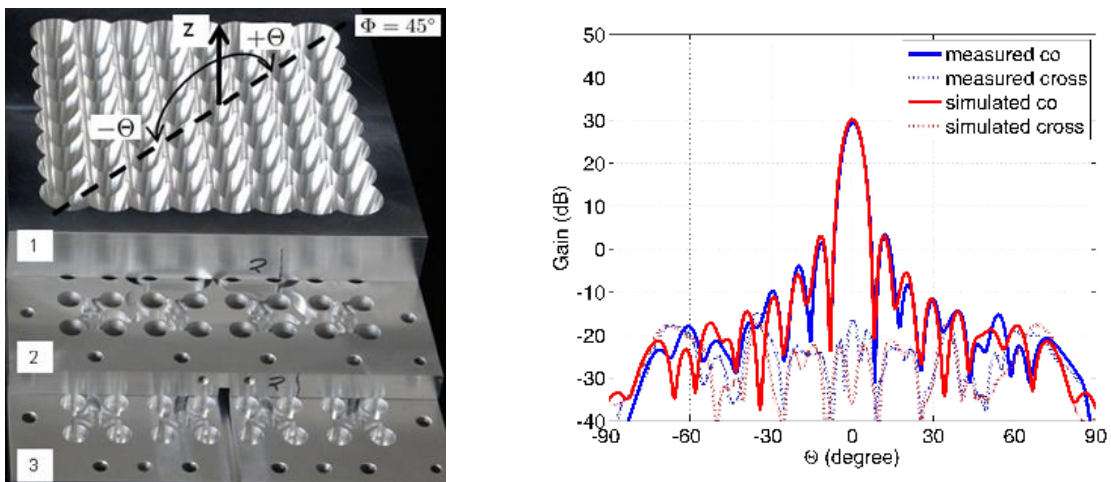


Figure I-13: Prototype of an 8×8 -element aperture (1) and two stacked waveguide networks for horizontal (2) and vertical polarization (3) for achieving arbitrary polarization control, and broadside radiation patterns.

Phased array antennas for SatCom on the move applications are already marketed as mentioned in [23], and [24].

In [23], the array is a dual-band (X/Ka) integrated Antenna/Terminal subsystem that provides high data rate satellite communications for the On-the-Move Tactical Warfighter. The prototype and the performances of the antenna are illustrated in Figure I-14.

High-efficiency antenna provides high throughput (up to 30 Mbps Downlink at 15 dB/K G/T and 12 Mbps Uplink at 48 dBW EIRP) with efficient use of transponder bandwidth (1.5-3 bits/Hz) is presented in [24]. The prototype and the performances of the proposed array are demonstrated in Figure I-15.

Dimensions: 76cm x 76cm x 33cm

Band X : Receive band (7.25-7.75 GHz)/ Transmit band (7.9-8.4 GHz)

Band K/ Ka: Receive band (19.2-21.2 GHz)/ Transmit band (29-31 GHz)

G/T (X): 4.5 dB/K at 20° Elev, **G/T (Ka):** 10.5 dB/K at 20° Elev

EIRP (X): 42 dBW (with integrated 60W BUC)

EIRP (Ka): 51 dBW (with integrated 50W BUC)

Axial Ratio: 2.0 dB typic

Polarization: LHCP or RHCP (manually switchable)



Figure I-14: X/Ka Commander Integrated Antenna/Terminal Subsystem.

Dimensions: 84cm x 20cm

Transmit band: 28.1-31 GHz

Receive band: 18.3-21.2 GHz

G/T: 15.5 dB/K

EIRP: 48 dBW (30 GHz, 12W BUC- up to 65 dBW w/6000W HPA)

Axial Ratio: < 2.0 dB typic

Polarization: Fixed or Switchable Circular (Orthogonal-Pol)



Figure I-15: K/Ka band array antenna for Office-in-the-Air Connectivity.

Reflectarray antennas

Several studies on reflectarray antennas have been recently presented in the open literature as mentioned in the following.

A shared aperture antenna for simultaneous operation at L- (1525 to 1661 MHz) and Ka-band (19.7 to 20.2 GHz and 29.5 to 30.0 GHz) is demonstrated in [25]. This array combines the advantages of high-speed data communication at Ka-band with stable data communication at L-band. It consists of 80×80 dual split-loop elements in a frequency selective surface (FSS) ground plane above an L-band 2×2 patch antenna array. The prototype provides a maximum directivity of 36.4 and 38 dBi at 20 and 29.8 GHz, respectively, with an aperture illumination efficiency in the two frequency bands up to 57% and 48%, respectively. A minimum directivity

of 11.8 dBi is demonstrated over the L-band. The simulated and measured directivity pattern in transverse plane of the proposed circularly polarized FSS-backed reflectarray antenna at 20 and 29.8 GHz are presented in Figure I-16.

A Ka-band reflectarray antenna integrated with solar cells as substrates has been designed, manufactured and characterized in [26]. The unit-cell is based on crossed dipoles which metal-covered area is much less compared with other elements such as microstrip patches. Good agreement is obtained between the measured and simulated frequency response of the proposed prototype as shown in Figure I-17. The array is fed by an 18.1 dBi linearly-polarized corrugated horn. It has demonstrated a measured gain of 26.3 dBi at 20 GHz and 1-dB gain bandwidth of 8.75%.

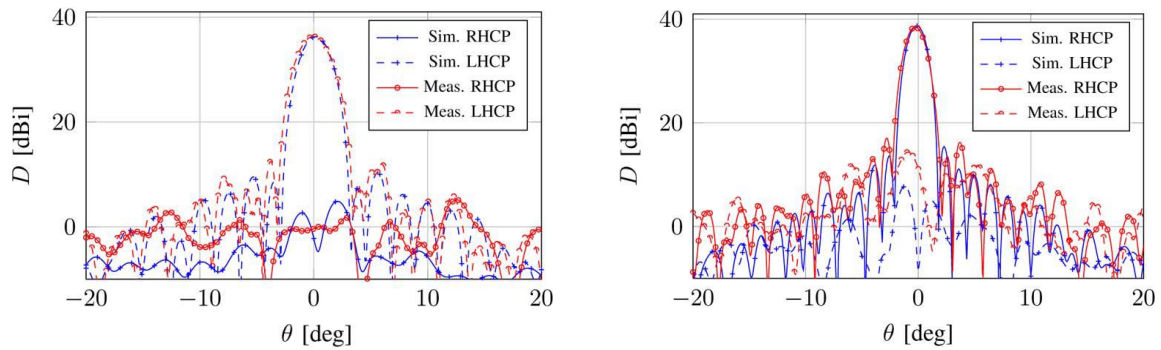


Figure I-16: Simulated and measured directivity patterns of the FSS-backed reflectarray antenna in transverse plane at 20 GHz (left) and 29.8 GHz (right).

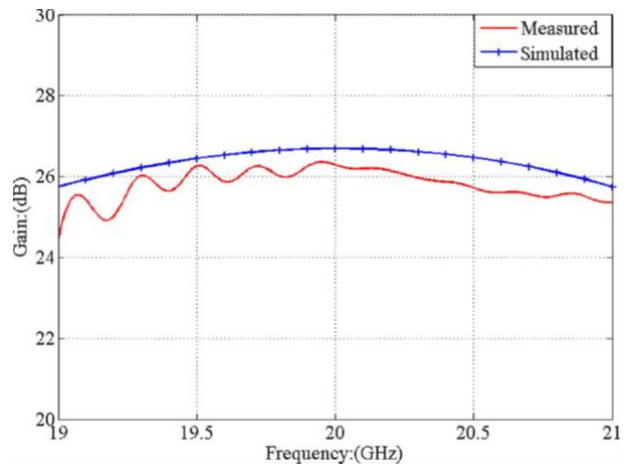
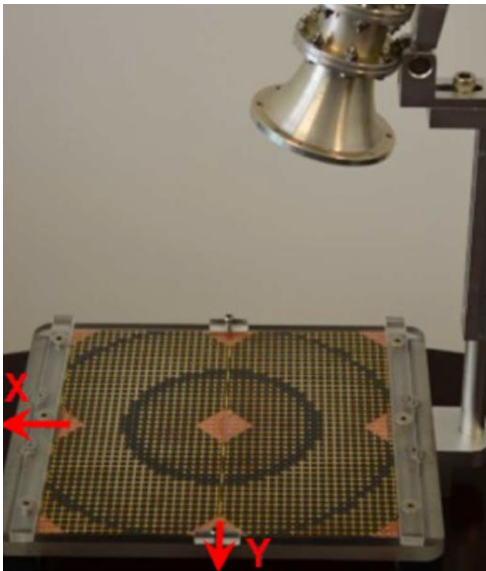


Figure I-17: Prototype of the proposed Ka-band reflectarray antenna integrated with solar cells (left) and measured gain within the operating frequency band (right).

Another reflectarray for Ka-band satellite communication applications is designed, optimized, fabricated and characterized in [27]. This folded reflectarray is based on 116 dual polarized square ring slot antennas with a multilayered PCB structure operating at 29.5- 30.8

GHz band for both transmitting and receiving with single linear polarization level. Beam scanning capability of the proposed passive reflectarray is possible thanks to the delay lines with varied lengths placed on each element of the array. The experimental results show that the presented reflectarray is capable of steering the beam up to $\pm 60^\circ$ in both E- and H-planes with low cross-polarization levels. Measured gains of 21.7 dBi and 18.4 dBi with low cross-polarization levels of about -21 dB are obtained for scan angles $\Theta = 0^\circ$ and 60° in the $\phi = 0^\circ$ cut plane, respectively. Figure I-18 shows the 3-D view of the folded reflectarray (on the left), and the radiation patterns in the $\phi = 0^\circ$ cut plane for a 60° scan angle.

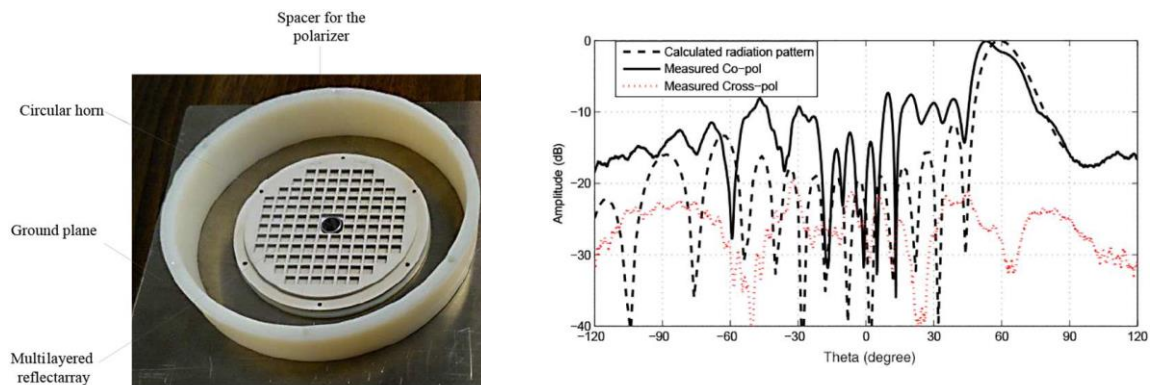


Figure I-18: 3-D view of the folded reflectarray antenna for SatCom applications at Ka-band (left), and radiation patterns (calculated and measured) at 60° in $\phi = 0^\circ$ cut plane (right).

Recently, a reflectarray antenna working independently in the transmit frequencies (from a satellite) in Ku-band (11–13 GHz) and Ka-band (19–20 GHz) has been demonstrated in [28]. The unit-cell of the array is composed of two orthogonal arrangements of eight parallel dipoles, five dipoles are placed in the lower layer and the other three are located in the higher layer. The proposed reflectarray is illuminated by two pyramidal feed horns in offset configuration, it exhibits a wide lower band (roughly 20% bandwidth for a gain variation smaller than 2 dB) and a narrow upper band (around 5% bandwidth for a gain variation smaller than 2 dB). The prototype and the gain as function of frequency in horizontal polarization are shown in Figure I-19.

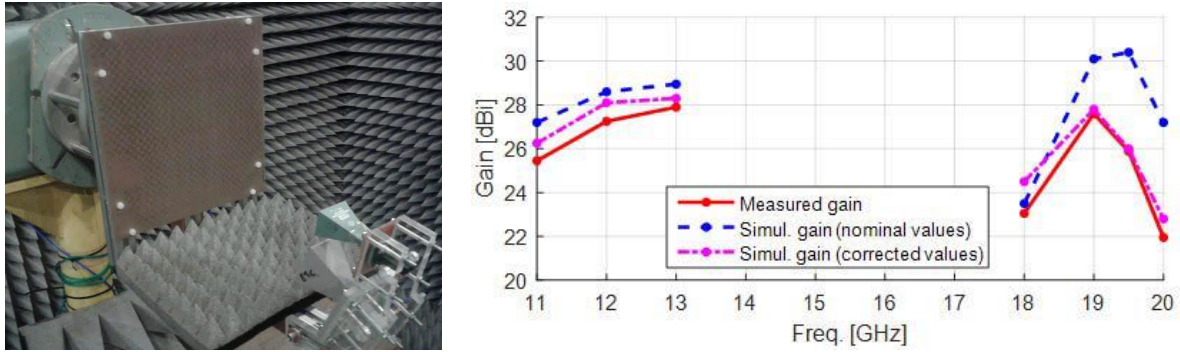


Figure I-19: Reflectarray prototype (left), and measured versus simulated gain in Ku/Ka bands for H-polarization (right).

Specifications for SatCom applications

Broadband is a key element of the developments in the electronic communication markets and also crucial to European competitiveness. The satellite market is a commercial one characterized by an intense competition between operators and technologies. In the European Union, electronic communications infrastructures and services are subject to the new regulatory framework, which is based on a technologically neutral approach. Broadband SatCom applications are typically implemented in the Ku/Ka-bands. The Ku-band is used for the downlink (DL, space to Earth) and the Ka-band is used for the uplink (UL, Earth to space). Broadband services using Ku/Ka-band satellites are suitable to rural and sub-urban areas where the availability of alternative services such as DSL or cable is not prevalent. In the ECC report 152 [29], the potential use of the Ku/Ka-bands for the implementation of broadband SatCom systems is analyzed. Improvements in Ku/Ka-bands technology include: a better individual coverage and high gain, the improvement of the spectrum efficiency thank to the implementation of the multi-spot frequency re-use, the possibility to have relatively small-size user antenna. Ku/Ka-bands broadband satellite services currently enable different applications such as internet, information and entertainment, broadband disaster management, national and international security domain.

a. Antenna on Earth station specifications

According to ITU regulations on SatCom, the world is divided into three regions [30]: (i) Europe, Africa, Middle East, Russia and Former USSR; (ii) United States of America; (iii) Asia, Oceania and Australia. The frequency bands allocated to civil applications is defined as: 17.3 – 20.2 GHz for space-to-Earth communications (DL), and 27.0 – 30.0 GHz for Earth-to-space communications (UL), in the Region 1 the frequency band is defined between 27.5 GHz and 30 GHz. Figure I-20 exhibits the spectrum allocation for satellite services in Ku/Ka-bands,

according to ITU regulation as a function of the Regions and including the different services (FSS, MSS, BSS, etc.).

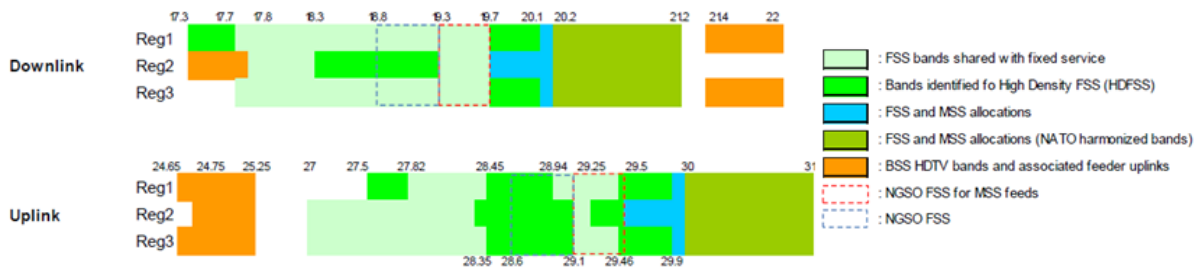
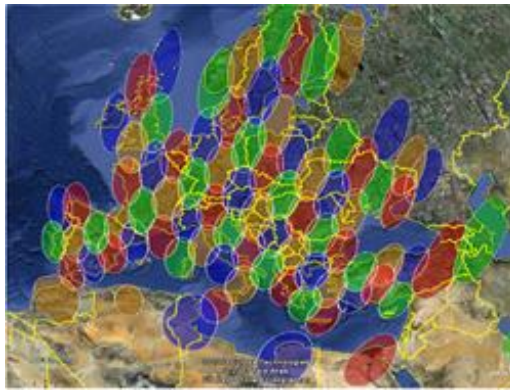


Figure I-20: Frequency band allocations for SatCom applications according to ITU.

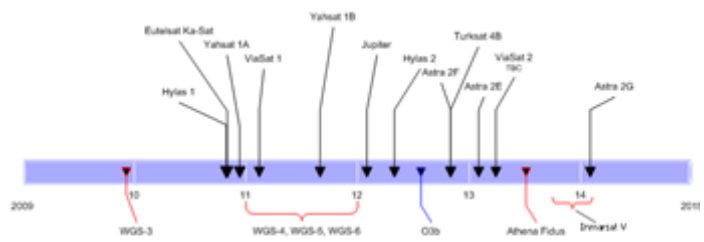
The frequency bands defined by NATO for military applications are 20.2 – 21.2 GHz for space-to-Earth communications (DL), and 30.0 – 31.0 GHz for Earth-to-space communications (UL).

The coverage of the Eutelsat Ka-Sat satellite launched in 2011 for ITU Region 1 is shown in Figure I-21(a). To each color corresponds one polarization (LH - left handedness or RH - right handedness) and one sub-channel [31]. End users are served by 82 spots on exclusive Ku/Ka-bands and in circular polarization, with a four-color frequency reuse scheme. Over 90 Gbit/s are provided by 237 MHz channels. Figure I-21(b) provides a summary of recent launchings of SatCom systems in Ku/Ka-bands [32].

Inmarsat Global Xpress (Figure I-21(c), Figure I-21(d)) is a new IP based Ka-band satellite network, with 3 Ka-band satellites (F1 launched on Dec. 8 2013, F2 launched on Feb. 1 2015, F3 delayed due to the launching failure on May 16 2015 at Kazakhstan) commissioned from Boeing, each offering two types of payloads, global (fixed beams) and HCP (steering beam). Inmarsat V (I5) provides (i) 89 fixed beams per satellite for global coverage in three satellite configurations (72 x 40 MHz Channels operating simultaneously for each satellite, 19.7 - 20.2 GHz DL, 29.5 - 30.0 GHz UL), and (ii) 6 steerable High Capacity spot beams per satellite for multi-regional, dynamic coverage (8 x 125 MHz channels for each satellite, 19.2 - 19.7 GHz Downlink, 29.0 - 29.5 GHz Uplink) [33].

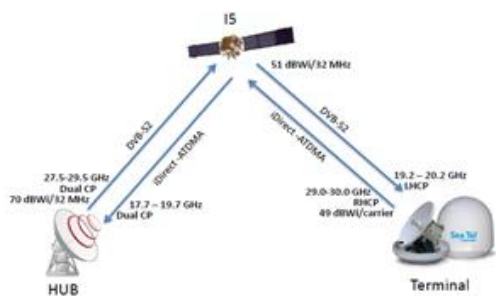


(a)



Band	Receive (GHz)	Transmit (GHz)
Military	20.2 - 21.2	30.0 - 31.0
Civilian	17.7 - 20.2	27.5 - 30.0
Inmarsat	19.2 - 20.2	29.0 - 30.0

(b)



(c)

	Maritime	Aeronautical	Land
EIRP (dBw)	49.0 – 52.5	44.0 – 46.0	49.0 (60cm) – 57.9 (1.8m)
G/T (dB/K)	15.0 – 18.3	11.1 - 12.4	15.0 (60 cm) – 25.2 (1.8m)
Tx freq range(GHz)	29.0 – 30.0	29.0 – 30.0	29.0 – 30.0
Tx max. inst. BW (MHz)	54.0	54.0	54.0
Tx polarisation	RHCP	RHCP	RHCP
Rx freq range(GHz)	19.2 – 20.2	19.2 – 20.2	19.2 – 20.2
Rx max inst. BW (MHz)	9.4 MHz	9.4 MHz	9.4 MHz
Rx polarisation	LHCP	LHCP	LHCP

(d)

Figure I-21: Ka-band SatCom coverage. (a) Ka-Sat coverage [31]. (b) Launch of satellites offering lower cost per bit Ku/Ka-bands capability [32]. (c) Satellite interface in Inmarsat Global Xpress [33], (d) Terminal characteristics for Inmarsat Global Xpress [33].

b. Specifications for Fixed Satellite Services (FSSs)

Communications between ground Earth stations at fixed locations is ensured by FSSs. They provide a large variety of services as data broadcasting, rural telephony, cellular backhaul, video services, etc. ETSI, ITU, and FCC are the institutions that establish the major recommendations and standards for FSSs in the case of Earth stations.

The recommendation ETSI EN (301 360 and 301 459) defines the specifications for user terminals transmitting towards geostationary satellite dedicated to FSSs in the frequency band 27.5 – 29.5 GHz [34]. In accordance with this recommendation, the maximum E.I.R.P (Equivalent or Effective Isotropic Radiated Power) in any 40 kHz band within the nominated bandwidth for each co-, cross-polarized components in any direction ϕ degrees from the antenna main beam axis shall not exceed some limits as illustrated in Figure I-22.

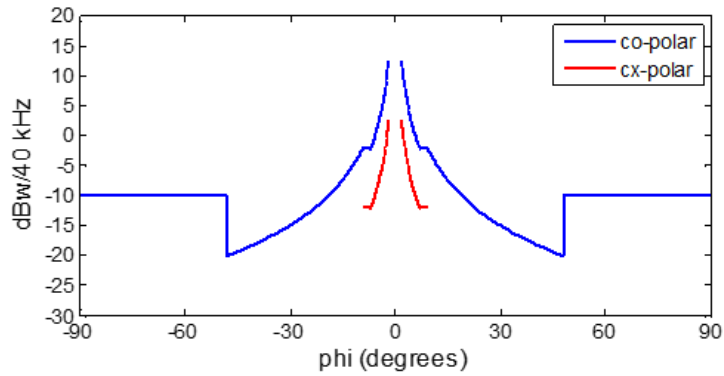


Figure I-22: Power mask of recommendations ETSI EN 301 360 and ETSI EN 301 459 in the case of one Earth Terminal.

Another recommendation, the ITU S.465-6, defines the radiation masks in the frequency range from 2 to 31 GHz in the case of Earth station antennas used in FSSs [35]. The radiation patterns should be adopted for angles between the direction considered and the axis of the main beam as depicted in Figure I-23.

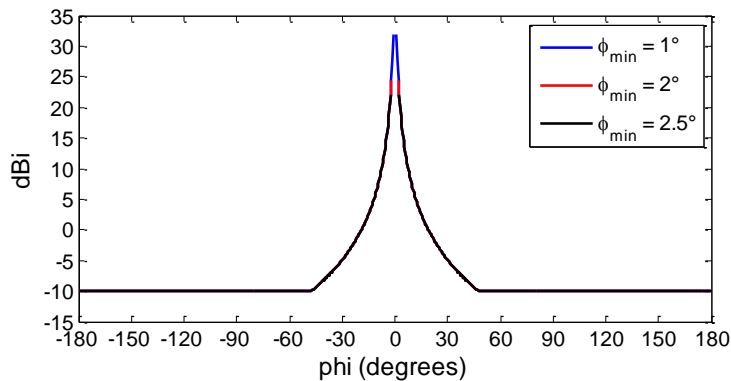


Figure I-23: Radiation mask of recommendation ITU S.465-6.

The FCC 25.138 [36] defines the limits for E.I.R.P spectral density of Earth station in and out of the arc $\pm 3^\circ$ of the GSO and gain radiation patterns as illustrated in Figure I-24.

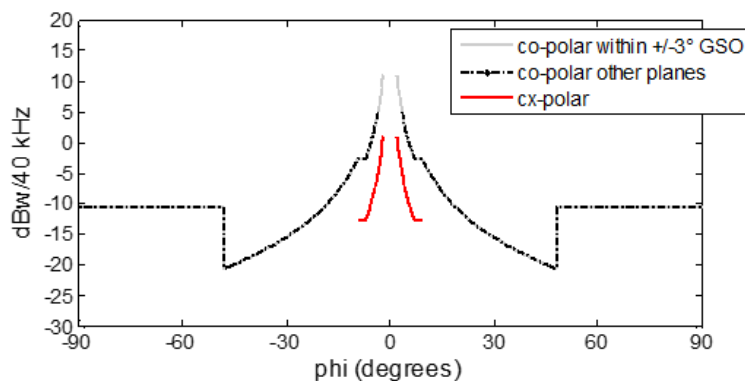


Figure I-24: Power mask of recommendation FCC 25.138. The masks are calculated considering one earth terminal (TDMA carriers with bandwidth > 40 kHz).

c. Mobile Satellite Services (MSSs) and Earth Stations on Mobile Platforms (ESOMPs)

Mobile Satellite Services (MSSs) refer to mobile-to-mobile or mobile-to-fixed voice and data communications to global users delivered via satellites. The Ku/Ka-bands are used for several satellite services by Earth Stations mounted On Mobile Platforms (ESOMPs) as telecommunications services to aircraft, ships, trains.

In Europe, antennas used for these services must fulfil recommendations established by ETSI EN 303 978 in the case of GSO satellites [37]. It defines the maximum E.I.R.P for ESOMPs transmitting towards satellites in geostationary orbit operating in Ka-band (Figure I-25).

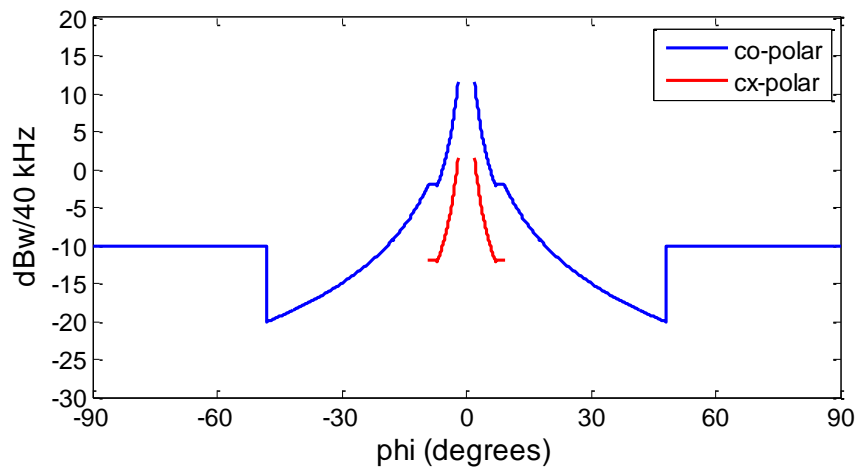


Figure I-25: Power mask of recommendation ETSI EN 303 978. The masks are calculated considering one Earth Terminal (TDMA carriers with bandwidth > 40 kHz).

1.2. Transmitarray antennas

For the last decades, transmitarray antennas (TAs) have been attractive for a large number of military and civil applications at millimeter waves such as SATCOM systems, point-to-point links, future high data-rate 5th generation (5G) mobile networks, wireless fronthaul/backhaul links, and radar systems. This antenna system is able to achieve high-gain, good efficiency, wideband, low-profile, and beam scanning capabilities at relatively low cost.

1.2.1. Transmitarray working principle

Similar to a dielectric lens, a transmitarray antenna (TA) is able to focus the radiated electromagnetic field in the desired direction. It combines both optical and antenna array principles. A TA is typically composed of several unit-cells illuminated by one or more spatial feeds, labelled focal sources (Figure I-26). Each unit-cell contains a first layer working in receive mode connected, through phase-shifters, to a second layer working in transmission mode. The phase-shifters are designed to convert the spherical phase front from the feed to a plane wave. In the case of electronically reconfigurable TA, active devices (RF switches,

amplifier modules, etc.) are integrated in the focal source level or in the unit-cell for path length compensation in order to steer the plane wave direction. Transmitarrays can be fabricated using standard Printed Circuit-Board (PCB) technologies, consequently they are lightweight and relatively low cost. Furthermore, they do not suffer from feed blockage effects in contrast to reflectarray antennas and could be easily integrated onto various platforms (buildings, vehicles, aircrafts, high speed trains, etc.).

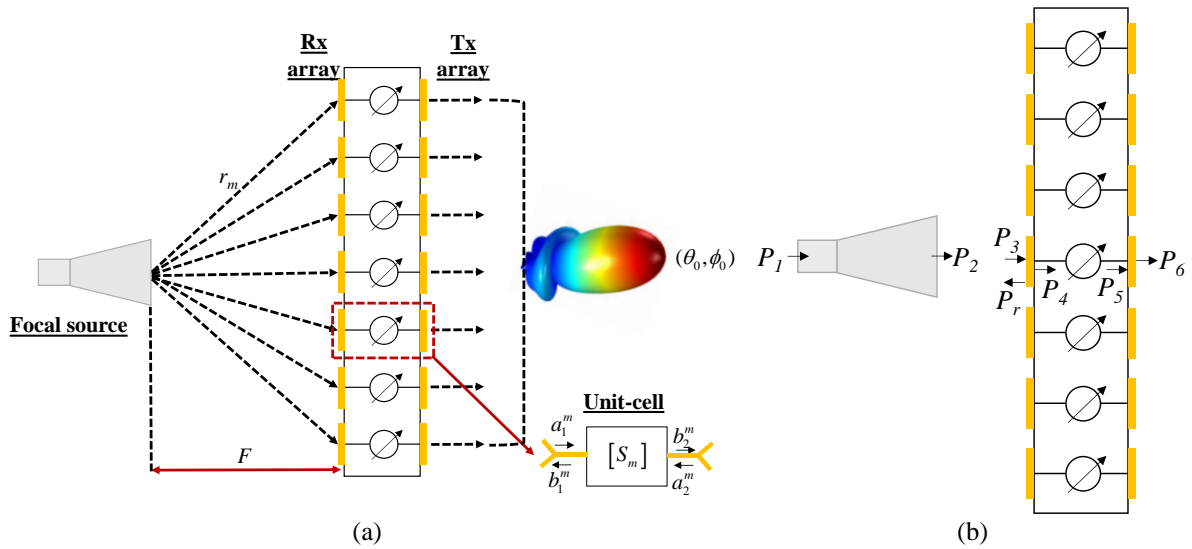


Figure I-26: (a) Schematic view of a transmitarray antenna. (b) Full power budget of a TA.

1.2.2. Analysis of a unit-cell

The characteristics of a unit-cell can be extracted using commercial electromagnetic simulation software. As depicted in Figure I-27, the simulation is performed considering periodic boundary conditions on the unit-cell lateral faces and Floquet port excitations on both sides of the elements. This simulation method emulates an infinite array of identical unit-cells and takes into account the mutual coupling effects [38].

The scattering parameters of a linearly-polarized unit-cell, namely reflection and transmission coefficients on both sides, can be directly obtained from the electromagnetic simulator by considering Transverse-Electric (TE) or Transverse-Magnetic (TM) modes. The choice of the TE or TM depends on the antenna architecture and its polarization. In contrast, for a circularly-polarized unit-cell, the antenna can operate in linear-polarization in Rx side and in circular-polarization in Tx side. In this case, the unit-cell implements both phase-shift and polarization transformation functions at the same time. The Left-, or Right-Handed Circular-Polarization (LHCP and RHCP) is calculated considering the correct combination of the two orthogonal modes TE and TM excited by the Floquet ports in the structure as provided in Appendix A.

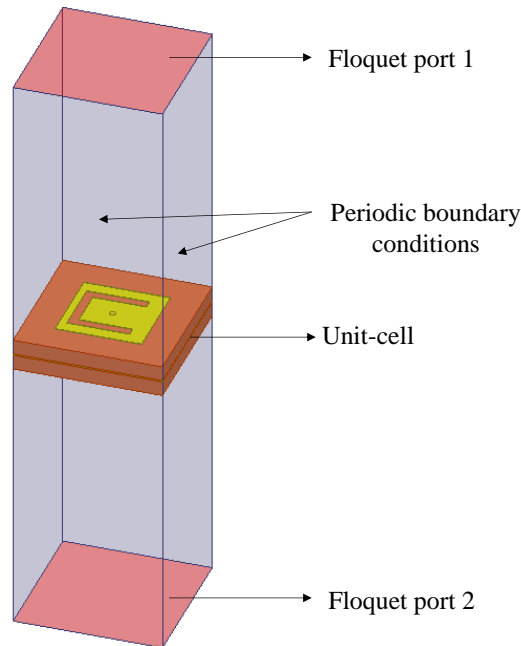


Figure I-27: Full-wave electromagnetic simulation setup of a unit-cell using periodic boundary conditions and Floquet port excitation.

1.2.3. Simulation techniques of a transmitarray antenna

The performances of a transmitarray antenna can be obtained using a full-wave electromagnetic simulation or a hybrid simulation method.

The hybrid simulation, combining electromagnetic simulation and analytical modeling, presents many advantages compared to the full-wave simulation. It allows the optimization of the phase distribution on the array aperture, the optimization of the array geometry (number of unit-cells, lattice, phase resolution, focal distance). In addition, it is an extremely fast simulation and does not require no computing resource consuming. The inconvenient of this simulation method is that it does not take into account some physical phenomena (diffraction, multiple reflection, etc.).

Full-wave simulation method

The full-wave simulation of a transmitarray antenna is performed with commercial electromagnetic simulators such as Ansys HFSS Software in our case. This simulation is done using the FE-BI (Finite Element-Boundary Integral) solver to reduce the computation time, but it still takes time. The FE-Bi solver utilizes Green's functions to calculate the fields in the free space. In this way, the required discretization of the computational domain is reduced. However, the computational time is still 3 to 4 hours per frequency point depending on the complexity of the structure, as in the case of the transmitarray antennas presented in this thesis

with an aperture of around 10λ or beyond. This technique is very useful to predict the performances of the transmitarray in a real environment.

Hybrid simulation technique

An *in-house* simulation tool was developed in CEA in order to reduce drastically (a few seconds) the computational time of the transmitarray antenna. It is based on a hybrid simulation technique, which includes full-wave simulations and analytical formulations. This simulator allows to predict accurately all parameters of the TA (directivity, gain, aperture efficiency, etc.) as demonstrated in previous works [39]-[41].

The transmitarray structure is divided in four parts, a focal source (*FS*), a receiving layer (*Rx*), an intermediate circuit, and a transmitting layer (*Tx*). The hybrid simulation utilizes measured or simulated data from a 3-D simulation software for each of part of the TA as input data. The focal source, the receiving and transmitting layers are characterized by their far field radiation patterns, electrical field phase, and gain. The intermediate circuit is characterized by its scattering matrix. Analytical formulations are developed in Matlab to establish the performances of the TA. The radiation vector of the transmitarray ($\vec{H}_{TA}(\theta, \phi)$) is calculated as the sum of the radiation pattern of each unit-cell.

$$\vec{H}_{TA}(\theta, \phi) = \sum_m b_{2tr}^m \vec{H}^{Tx,m}(\theta, \phi) \cdot e^{j\frac{2\pi}{\lambda} \sin(\theta) \cos(\phi) x_m} e^{j\frac{2\pi}{\lambda} \sin(\theta) \sin(\phi) y_m} \quad (\text{Eq I-1})$$

Where b_{2tr}^m is the wave transmitted by the unit-cell, and (x_m, y_m) indicates the position of the m -th unit-cell.

a) Full power budget of a transmitarray

The full power budget of a transmitarray is detailed in Figure I-26 (b). P_1 is in the input power feeding the focal source of the TA, it is fixed at 1 W. The total power radiated by the focal source is labelled P_2 . The incident power on the *Rx* layer and the power reflected by the TA are given by P_3 , and P_r , respectively. P_4 is the total power collected by the receiving layer. P_5 corresponds to the power transferred to the *T_x* layer. The total power radiated from the *T_x* layer is called P_6 .

The total efficiency of the array antenna is defined by:

$$\eta = \frac{P_6}{P_5} \cdot \frac{P_5}{P_4} \cdot \frac{P_4}{P_3} \cdot \frac{P_3}{P_2} \cdot \frac{P_2}{P_1} = \eta_{AL} \cdot \eta_{IL} \cdot \eta_{CA} \cdot \eta_{SO} \cdot \eta_{FS} \quad (\text{Eq I-2})$$

Where η_{AL} (P_6/P_5) is the efficiency of the transmitting antenna, η_{IL} (P_5/P_4) is the efficiency taking into account the insertion losses of the unit-cells, η_{CA} (P_4/P_3) is the efficiency

of the receiving array (it takes into account resistive, impedance, mismatch, and polarization mismatch losses), η_{so} (P_3/P_2) is the illumination efficiency taking into account the spill-over losses, and η_{FS} (P_2/P_1) is the efficiency of the focal source taking into account the resistive losses and mismatch losses.

b) Phase quantization effect on transmitarray performances

The transmitted electromagnetic wave can be focused in any desired direction or collimated by opportunely controlling the amplitude and/or phase of each-cell.

Ideally, a 360° phase-shift variation range is desirable to compensate the path length differences between the focal source and the unit-cells and to achieve a high aperture efficiency and low side-lobe levels. In practice, a limited number of phase-states (phase quantization) can be applied to reduce the complexity of the TA structure, particularly in the case of electronically reconfigurable architectures. Hence, a high phase resolution would require many active devices to control the transmission phase, which results in several limitations: (i) higher insertion loss, (ii) variation of the insertion loss as a function of the phase state, (iii) complexity of the design procedure, and (iv) integration issues inside a unit-cell whose size is typically in the order of half a wavelength.

The effect of phase quantization on a transmitarray performances (aperture efficiency, directivity, gain, and beam-steering capability) has been studied in [42], considering a transmitarray theoretical model (lossless and matched unit-cells) based on analytical formulas. The TA is composed of 20×20 unit-cells (square aperture $\lambda_0/2 \times \lambda_0/2$). It is illuminated by an ideal 10-dBi gain focal source (100% of efficiency) placed at F equals to $0.47D$, where D is the size of the array side. The cases of no phase compensation, 1-bit (0 and 180° states), 2-bit (0° to 270° by 90° step states), 3-bit (0° to 315° by 45° step states), and perfect compensation are studied.

The performances of the transmitarray are affected by the phase quantization. As depicted in Table I.4, phase quantization has an impact on the directivity due to phase quantization losses (L_{quant}). A 1-bit TA has significant phase quantization losses (3.5 dB). The latter decreases as the phase compensation increases (L_{quant} for a 2-bit TA equals 0.8dB). It should be noted that the quantization losses are in the case of the 3-bit network (0.2 dB) and very close to the perfect compensation. It is established that the side-lobe level is better when the number of phase states increases.

Table I.4: Impact of phase quantization on the TA performances.

Phase compensation	No phase compensation	1-bit	2-bit	3-bit	Perfect
Directivity (dBi)	11.6	26.6	29.3	29.9	30.1
Gain (dBi)	11.2	26.1	28.7	29.3	29.5
L_{quant}	18.5	3.5	0.8	0.2	0
SLL (dB)	20.9	20.2	24.4	25.0	25.0

1.2.4. State of the art on transmitarray antennas

The theory and numerical analysis of TAs have been introduced in 1968 [43], but transmitarray antennas have really attracted the attention of many antenna researchers in the late 1980s as alternatives to other high gain antennas such as reflectors, phased arrays, and reflectarrays. From this period to today, many passive [39], [44]-[47], and active transmitarrays [40], [48]-[50] have been demonstrated in large frequency bands. In the last years, literature reviews of transmitarray antennas have already been presented in many theses [51]-[53], so to avoid repetitions, only recent relevant works will be presented. Considering the structure of a TA, we can obtain three types of beam: (i) fixed beam, (ii) switched beam, and (iii) electronically-reconfigurable beams. In this section, a state of the art on transmitarrays envisaged for SatCom and future 5G networks systems will be established according to these three groups of TAs.

Fixed beam transmitarrays

A fixed beam transmitarray, also called passive TA, radiates in only one direction. In the past three years, several passive transmitarrays and unit-cells have been demonstrated in the open literature as mentioned hereafter. They are presented from the lowest to the highest frequency bands.

A circularly-polarized array, combining a reflectarray and a transmitarray together, with high gain bi-directional beams is presented in [54]. It is composed of 28×28 elements with 420 mm side length, spatially fed by a corrugated horn. Each element of the TA consists of a single-layer metal-only defected square ring slot element with a near-zero thickness. The proposed TA is ultra-thin ($0.0067\lambda_0$), lightweight, and low-cost without using dielectric substrates. The measured gains of the transmitted and reflected beams at 10 GHz are 25.5 dBi with 15% 1-dB gain bandwidth and 25.0 dBi with 14% 1-dB gain bandwidth, respectively. The radiation efficiencies correspond to 15%, and 14% for the transmitarray, and reflectarray, respectively. The prototype and the gains of the bi-directional high gain array are shown in Figure I-28(a), and Figure I-28(b), respectively.

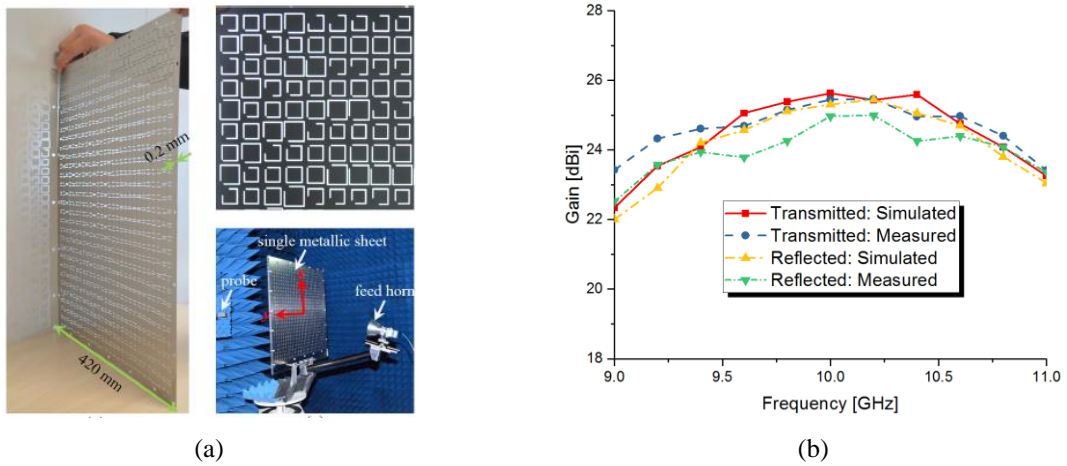


Figure I-28: (a) Prototype of the proposed bidirectional high gain array. (b) Simulated and measured transmitted (TA) and reflected (RA) gains of the Bi-HGA versus frequency [54].

A new structure of transmitarray antenna achieving high efficiency and wideband in X-band is presented [55]. The optimal focal distance corresponds to $F/D = 0.9$ and $D = 15\text{cm}$. The TA is composed of 185 cells with central elements having two layers and the number of layers increasing as we get closer to the edges such that the edge cells have five layers. The required phase range for the elements was reduced from 360° to 51.5° , consequently the bandwidth and efficiency increase. The fabricated TA is indicated in Figure I-29(a). They demonstrated a measured maximum gain of 22.3 dBi at 10.3 GHz with a 1-dB bandwidth of 23.4% and 65% efficiency. The measured and simulated realized gain and aperture efficiency of proposed transmitarray antenna are shown in Figure I-29(b).

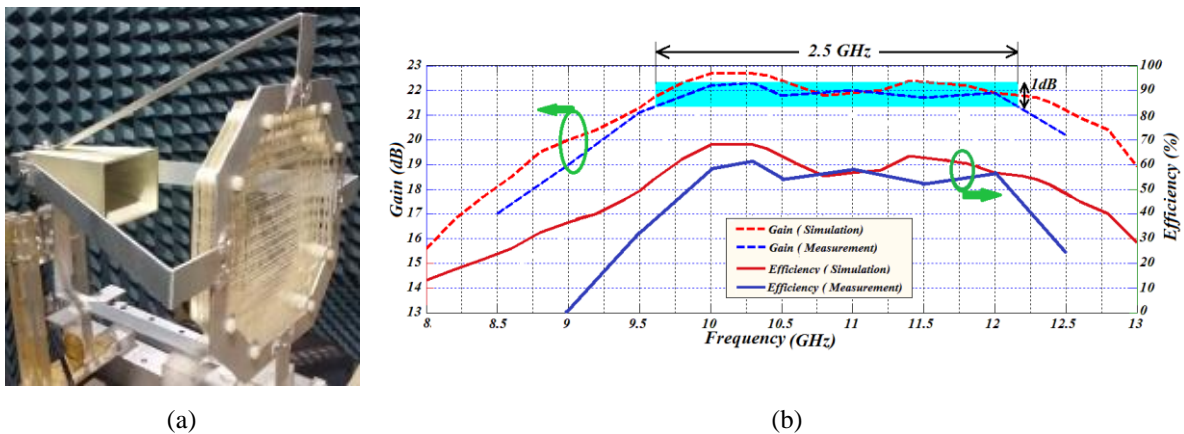


Figure I-29: High-efficiency wideband transmitarray antenna. (a) Fabricated prototype, (b) measured and simulated realized gain and aperture efficiency of the proposed transmitarray antenna.

A 14×14 element dual-band, dual polarized transmitarray antenna is presented in [56]. The TA can radiate in dual linear polarization and circular polarization depending on the feed used. The unit-cell is composed of three thin metallic layers with air gaps between the layers and do not use any dielectric substrates. Interleaved orthogonal slots, as well as crossed-dipole slot and uniplanar compact photonic bandgap slot elements are used to provide the lower and

upper frequency band resonators, respectively. The focal length-to-diameter ratio is equal to 0.8, which corresponds to a focal distance of 157 mm. The prototype of the proposed antenna demonstrates at 11 GHz a maximum measured gain of 23.74 dB with a 1-dB gain bandwidth of 6.8% and an aperture efficiency of 38%; at 12.5 GHz, a maximum gain of 24.45 dB is shown with 1-dB gain bandwidth of 5.4% and an aperture efficiency of 34.6%. The simulated and measured co- and cross-polar radiation patterns in E-plane for the lower and upper bands are shown in Figure I-30.

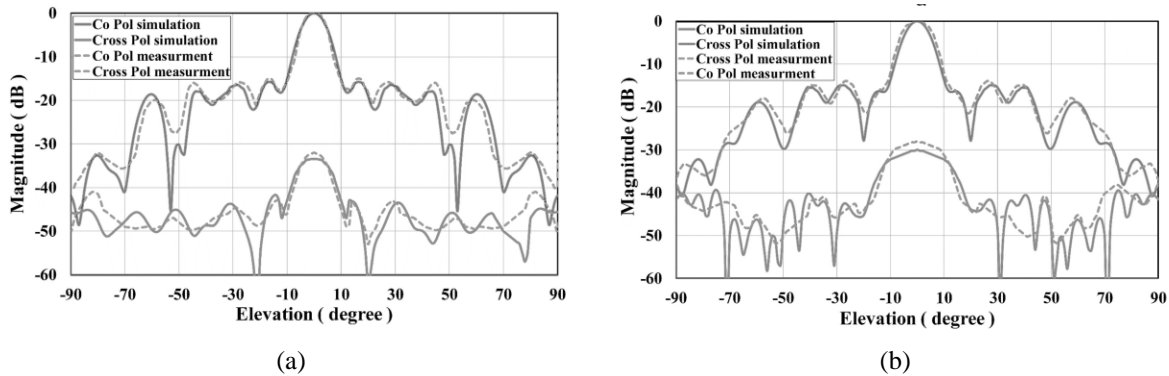


Figure I-30: Simulated and measured co- and cross-polar radiation patterns in E-plane (a) 11 GHz, and (b) 12.5 GHz.

A wideband linearly-polarized transmitarray with reduced profile working at 13.5 GHz is presented in [57]. The dimension of the TA is $90 \times 90 \times 8.1 \text{ mm}^3$, corresponding to a thickness of 0.36λ at 13.5 GHz. It is illuminated by a linearly polarized corrugated circular horn antenna placed at 90 mm, corresponding to a focal ratio F/D of 1. The unit-cell used in the TA is composed of a tri-layer frequency selective surface separated by a distance of quarter-wavelength at the frequency of interest to obtain the 360° phase shift range. The fabricated TA exhibits a 1-dB gain bandwidth of 16% at 13.5 GHz with an aperture efficiency of 60%. The 3-dB bandwidth covers the frequency band from 12 GHz to 14.5 GHz, which corresponds to a fractional bandwidth of 18.5%. The prototype and the gains (measured and simulated) as a function of frequency of the proposed transmitarray antenna are shown in Figure I-31(a), and Figure I-31(b), respectively.

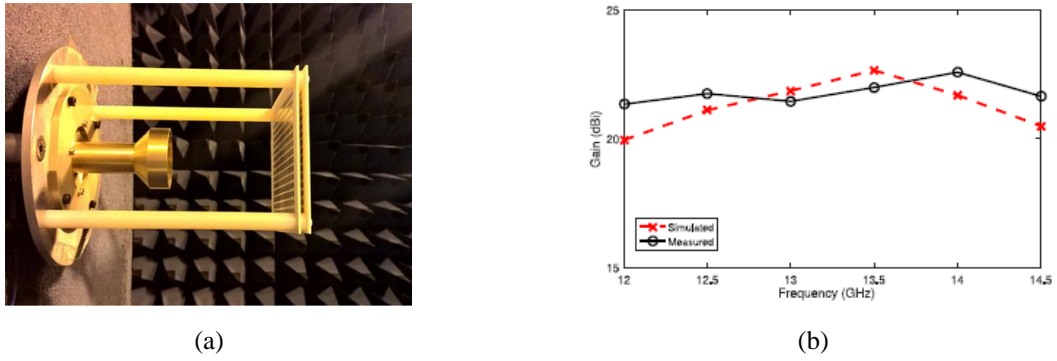


Figure I-31: (a) Fabricated wideband transmitarray under measurement. (b) Measured and simulated gains as a function of frequency [57].

A 20 GHz circular transmitarray prototype (Figure I-32(b)) based on double-layer unit-cells is illustrated in [58]. The circular aperture of the TA has a diameter (D) equal to 338 mm. The proposed linearly-polarized unit-cell is composed of two metallic microstrip patches with the shape of a modified Malta cross and exhibits an insertion loss of 1.75 dB with a phase shift range of 305° as shown in Figure I-32(a). The 2032-element transmitarray is illuminated by an 18 dBi gain corrugated horn placed at 420 mm above the TA aperture. It exhibits a 1-dB bandwidth of 5.9% (Figure I-32(c)), and an aperture efficiency of 40%. The simulated and experimental co-, and cross-polarization radiation patterns at broadside in E-plane are presented in Figure I-32(d). The maximum gain is 33 dBi. The first side lobe and cross-polarization levels are 22.5 dB and 28 dB lower than the main beam, respectively.

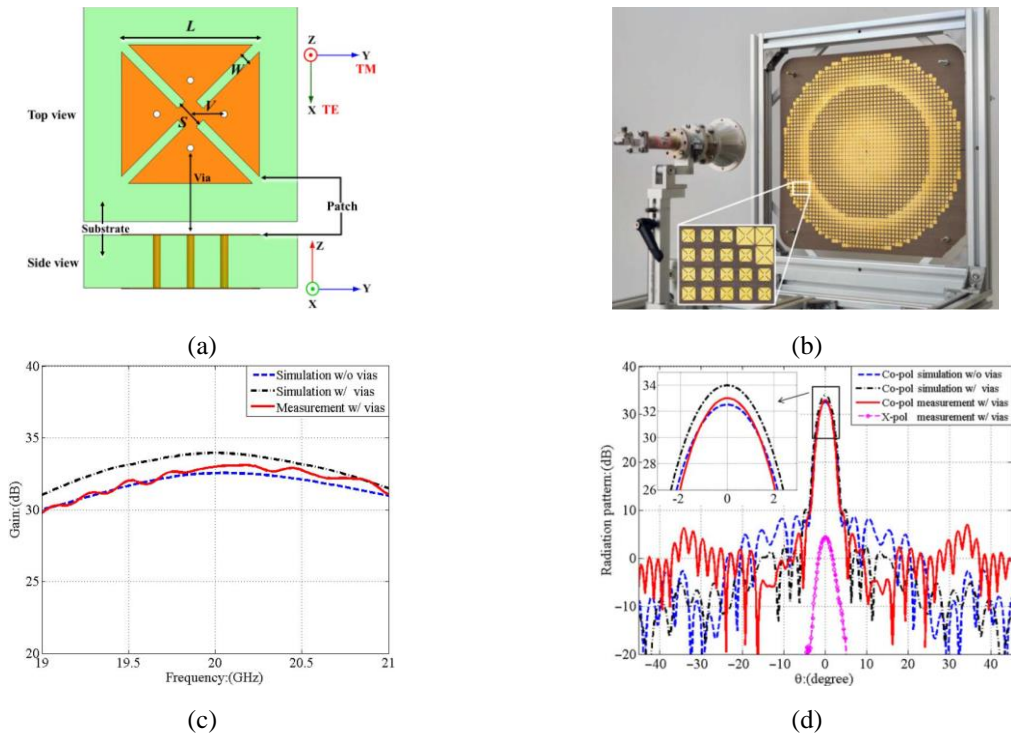


Figure I-32: 20 GHz double-layer linearly-polarized transmitarray antenna using Malta crosses with vias [58].

A fixed beam circularly-polarized transmitarray with sequential rotation at 30 GHz has been realized in [41]. The unit-cell consists of a linearly-polarized patch on the receive side, a circularly-polarized patch on the transmitting side, and a ground plane between the patches Figure I-33(a).

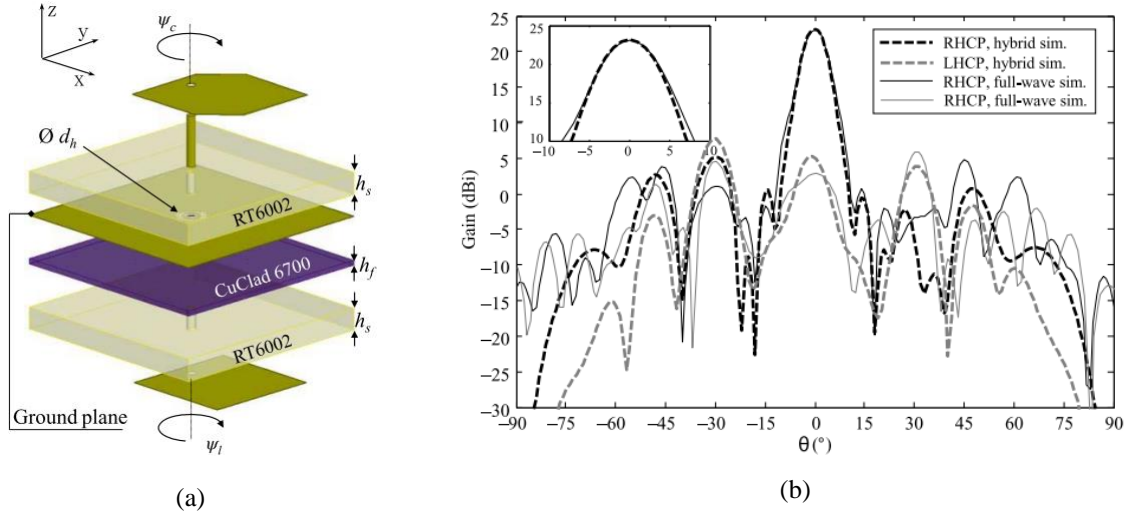


Figure I-33: Circularly-polarized transmitarray with sequential rotation at 30 GHz [41]. (a) 3-D exploded view of the unit-cell. (b) Simulated and measured radiation patterns in horizontal plane.

The patches are connected by a metallized via placed at their center and have an insertion loss of 0.2 dB. A $10\lambda_0 \times 10\lambda_0$ unit-cells transmitarray, illuminated by a focal source located at 52 mm from the TA, has been characterized. It presents a co-polarization gain of 22.8 dBi at broadside with a 3-dB gain bandwidth of 20%, and a 3-dB axial ratio bandwidth equal to 24%. Good agreement is obtained between the simulated and experimental results as shown in Figure I-33(b).

A compact transmitarray at 28 GHz, where the distance (h) between the source and the TA is reduced to 1/3 of the focal length (F) by using a folding principle, is demonstrated in [59]. The focal-length-to-diameter ratio (F/D) corresponds to 0.85 with D equals 98 mm and the total height of the structure is $h = 27.8$ mm. Its architecture is composed of a horn source, a polarization-rotating reflection surface, and linearly-polarized transmitting surface as shown in Figure I-34(a). The proposed unit-cell of the transmitting surface is composed of a pair of resonant elements based on two U-shaped slots and Uniplanar Compact Photonic Band Gap (UC-PBG). The x-polarized incident wave would be reflected by the unit-cell as a ground plane and transmitted in y-polarization with arbitrary phase-shift in the frequency band of interest. The polarization of the incident wave is transformed thanks to the broadband polarization-rotating reflection surface based on an artificial magnetic conductor (PRAMC). The measured maximum gain is 25.7 dBi at 27.8 GHz with an aperture efficiency of 46%. The 1-dB gain

bandwidth spans from 27.5 GHz to 28.9 GHz, this corresponds to a fractional bandwidth of 5% at 28 GHz, as shown in Figure I-34(b).

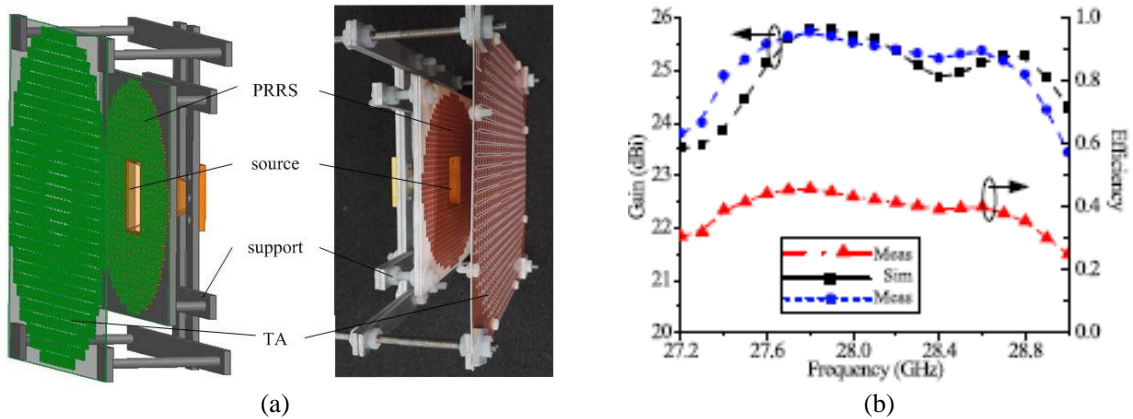


Figure I-34: Ultra low profile transmitarray using multifolded ray tracing principle [59]. (a) 3-D exploded view of the unit-cell. (b) Simulated and measured radiations patterns.

In [60], a unit-cell consisting of multiple layers with a center cross dipole with four strips on the boundary with a $\lambda_0/2$ periodicity is realized as shown in Figure I-35 (a). A continuous phase range of 360° and a transmission better than -1.6 dB at 30 GHz are obtained. This unit-cell can be used to design a circularly polarized transmitarray. In fact, the polarization of the transmitted wave depends on the relative polarization angle between the feed and the unit-cells. When the polarization of the feed is parallel to the diagonal of the unit-cell, this latter converts the linearly-polarized incident wave into a circularly polarized transmitted wave. Work is in progress to increase the axial ratio (Figure I-35 (b)) of the unit-cell.

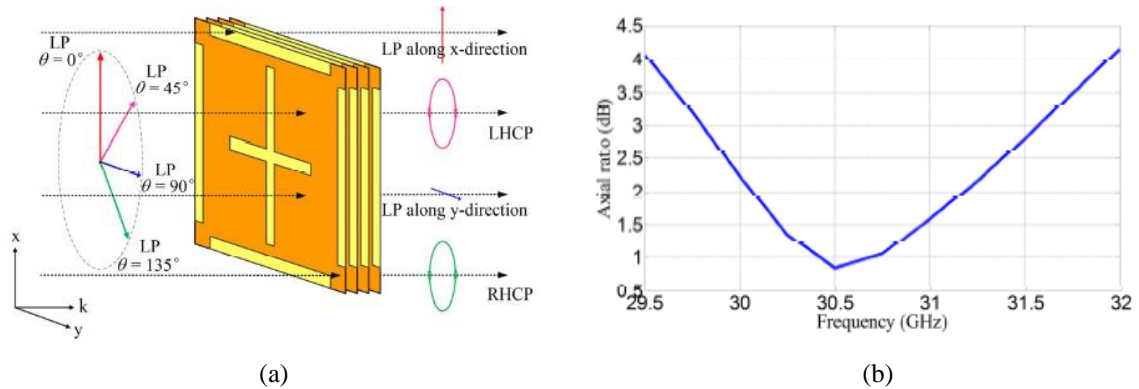


Figure I-35: Circularly-polarized transmitarray based on linearly-polarized unit-cell [60]. (a) Architecture of the unit-cell. (b) Axial ratio as a function of frequency.

The authors in [61] present a dual-band circularly-polarized transmitarray antenna for satellite-on-the-move systems working at downlink (19.7-20.2 GHz) and uplink (29.5-30 GHz). The unit-cell, as shown in Figure I-36(a), contains five-layer split-ring elements separated by four substrates. The proposed dual-band feed is placed at a distance of 63 mm from the array. The simulated radiation patterns of a 9×9 unit-cells transmitarray with an area of $72 \times 72 \text{ mm}^2$

show a directivity of 17 and 19 dBi and axial ratios of 1.9 and 3.2 dB at 20 and 30 GHz, respectively (Figure I-36(b)).

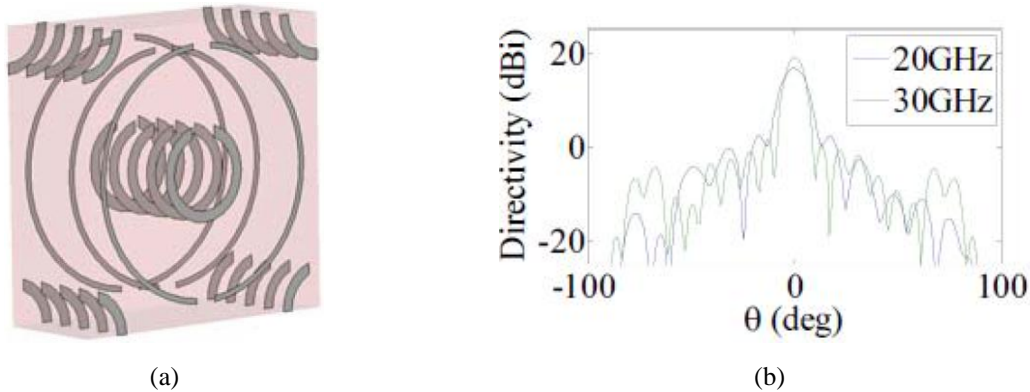
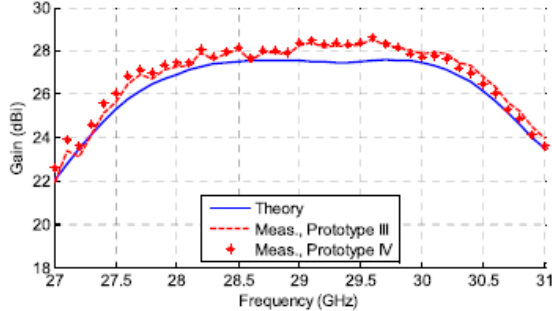


Figure I-36: Dual-band circularly-polarized transmitarray for SOTM systems [61]. (a) Perspective view of the unit-cell. (b) Broadside radiation pattern at 20 GHz and 30 GHz.

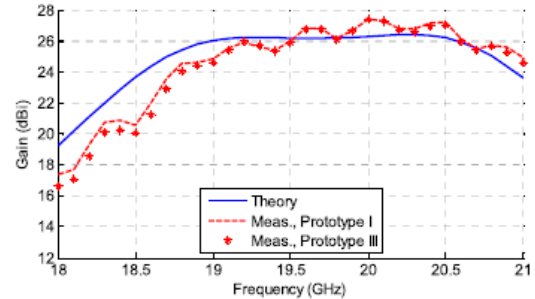
Dual-band transmitarray antennas working in dual linear polarization at Ka-band are demonstrated in [62]. The unit-cell is composed of identical narrow microstrip patches printed on the two outermost layers and connected by a metallized via hole, and it exhibits a 180° phase resolution in the frequency band of interest. Each realized TA comprises 900 elements (30×30 square lattice) for Up Link and 961 elements (31×31 square lattice) for Down Link. The TA is illuminated by two 10 dBi pyramidal feed horns placed at 110 mm. Good agreement is obtained between the theoretical and measured performances of the four fabricated prototypes described in Figure I-37 (a). The UL prototypes III and IV have demonstrated a gain of 28.3 and 28.4 dBi at 29.6 GHz, respectively, with a fractional bandwidth of 11.4% around 29 GHz (Figure I-37 (b)). The measured and theoretical fractional 3-dB gain bandwidths are equal to 10.7% and 11.3% around 19.5 GHz, respectively, for the DL prototypes I, and III (Figure I-37 (c)).

Prototype	Beam direction (φ, θ), scanning plane	
	Up-link	Down-link
Prototype I	($0^\circ, 0^\circ$), Broadside	($0^\circ, 0^\circ$), Broadside
Prototype II	($90^\circ, -30^\circ$), E-plane	($90^\circ, -30^\circ$), H-plane
Prototype III	($0^\circ, 20^\circ$), E-plane	($0^\circ, 0^\circ$), Broadside
Prototype IV	($0^\circ, 20^\circ$), E-plane	($90^\circ, 45^\circ$), H-plane

(a)



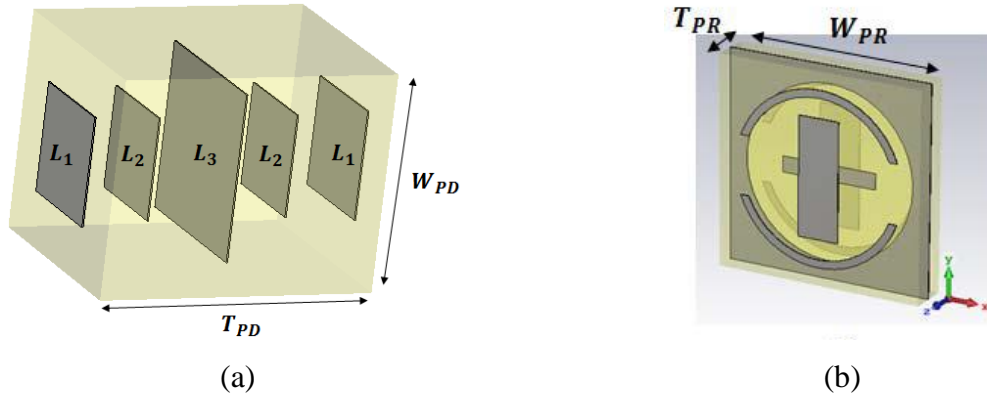
(b)



(c)

Figure I-37: Dual-band transmitarray at Ka-band with the capability of forming independent linearly-polarized beams [62]. (a) Beam directions of the proposed prototypes. Theoretical and measured gain as a function of frequency in (b) up link and (c) down link bands.

The authors in [63] have compared the working principle of the phase delay (PD) and phase rotation (PR) unit-cells and analyze their impacts on a circularly polarized TA performances. The proposed PD cell is composed of five subwavelength square capacitive patches with different side length as shown in Figure I-38 (a). The phase shift of the transmission coefficient can be changed by varying the lengths of the unit-cell. The PR cell consists of three metal layers separated by 0.508 mm thick Duroid 5880 dielectric slabs, as shown in Figure I-38(b). Cell rotation by ϕ° about the z-axis introduces a $2\phi^\circ$ phase shift in the transmission coefficient. The PD-based and PR-based TAs are designed for single band wide-angle beam steering operating at the satellite Ka-band. The measured performances of the two prototypes are summarized in Figure I-38(c). The PR TA present better axial ratio because of its filtering effect. However, PD cells are easier to design and insensitive to feed polarization.



		PD-TA	PR-TA
Feed 3dB AR bandwidth (GHz)		0.4 (29.85–30.25)	
Area dimensions (mm)		190 × 140	
Thickness (mm)		3.35	1.05
Weight (g)		214	66
Central beam	Gain (dBi)	29.1	29.5
	Axial-ratio (dB)	2.7	0.9
	3dB Gain bandwidth (GHz)	2.5 (29-31.5)	1.9 (29-30.9)
	3dB AR bandwidth (GHz)	0.6 (30–30.6)	>4.0 (>(28-32))
	3dB Gain and AR bandwidth (GHz)	0.6	1.9
Scan loss (dB)		2.8	3.0
Back lobe for most titled beam (dB)		-17.6	-18.8

(c)

Figure I-38: (a) Phase delay (PD) unit-cell. (b) Phase rotation (PR) unit-cell. Performances of both TA types [63].

A 60 GHz linearly-polarized transmitarray (Figure I-39(a)) for backhauling applications is presented in [64]. Four types of unit-cells based on via-hole technique have been designed in order to obtain the eight phase states required for a 3-bit phase resolution. The TA contains 1264 unit-cells arranged in a planar circular-shape array with a radome layer. The simulated gain as a function of frequency agrees well with experimental data as shown in Figure I-39(b). The TA presents a 1-dB fractional gain bandwidth of 15.4% (57-66.5 GHz) as depicted in Figure I-39 (c). The authors also proved that the co-, and cross polarization radiations pattern of the transmitarray nearly fulfill the masks defined by ETSI as depicted in Figure I-39(c), and Figure I-39 (d), respectively.

A wideband transmitarray antenna for D-band applications based on the low-temperature co-fired ceramic (LTCC) technology is presented in [65]. The unit-cell used in the proposed array is composed of a pair of wideband magneto-electric dipole as the receive/transmit elements, together with a substrate integrated waveguide (SIW) aperture-coupling transmission structure for independent phase adjustability. It demonstrated a 360-

degree phase coverage. The fabricated prototype has a square radiation aperture of 4 cm × 4 cm, and contains 40×32 unit-cells. It presents a measured peak gain of 33.45 dBi at 150 GHz with an aperture efficiency of 44%, and a 3-dB gain bandwidth of 24.3% (124-158 GHz) as shown in Figure I-40.

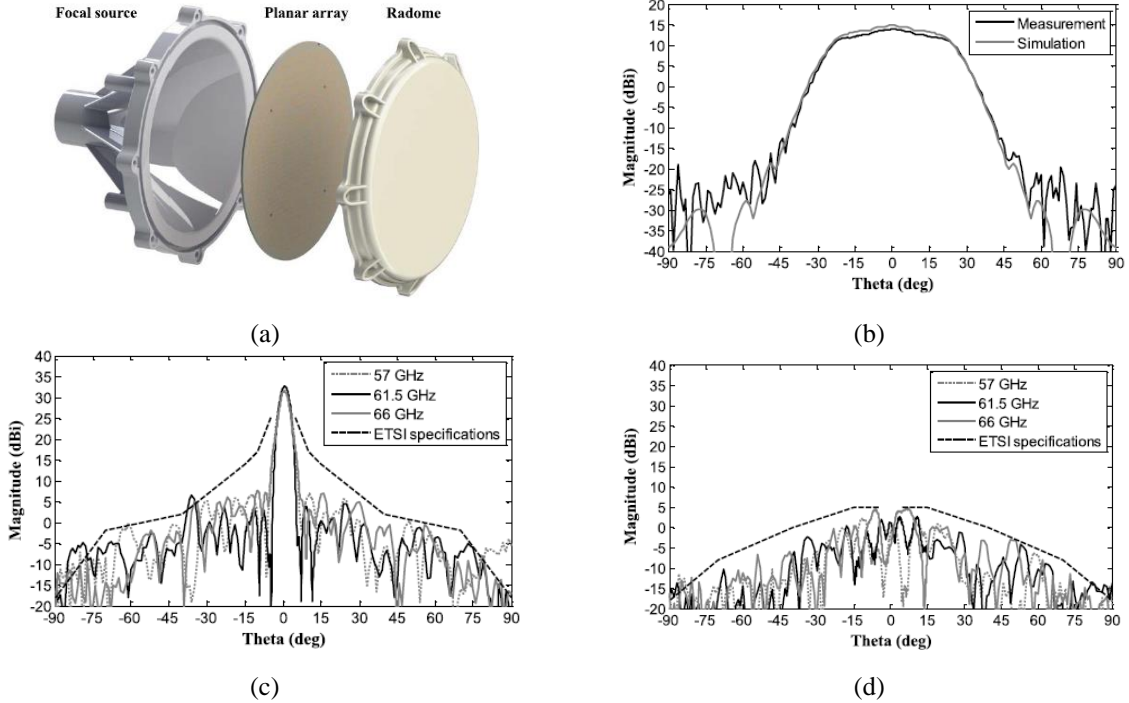


Figure I-39: 60 GHz linearly-polarized transmitarray for backhauling [64]. (a) Prototype of the TA. (b) Measured and simulated gain as a function of frequency. (c) Co-, and cross-polarization radiation patterns of the TA for different frequencies (57 GHz, 61.5 GHz, and 66 GHz) compared to ETSI masks.

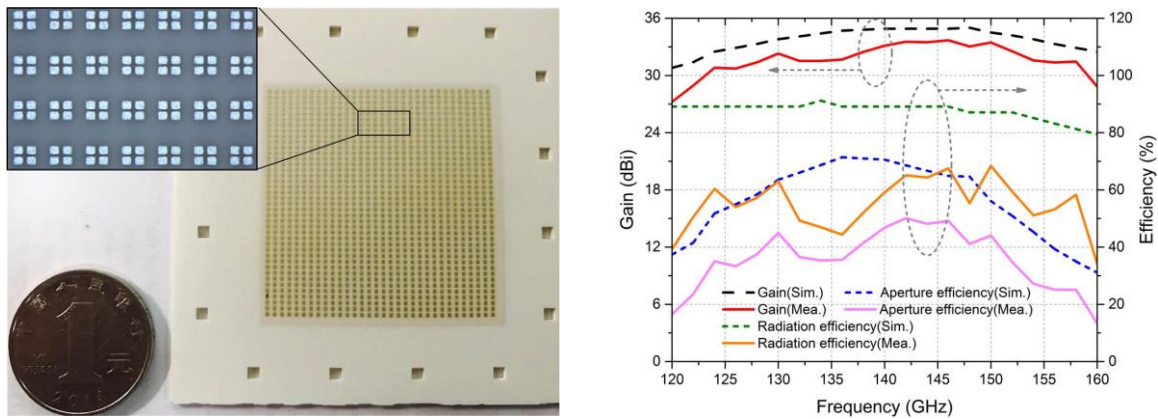


Figure I-40: Fabricated 140 GHz high gain LTCC-integrated transmitarray (left); simulated and measured gain and corresponding efficiency within the frequency band of interest (right) [65].

A 250-GHz transmitarray antenna illuminated by a WR-03 opened waveguide has been investigated and fabricated using standard PCB technology [66]. The unit-cell is composed of a V-shaped pattern and metallic grating separated by a 0.127-mm Rogers 5880 substrate. It demonstrated a 360° phase coverage with a transmission coefficient lower than -3.52 dB at 250

GHz. The manufactured transmitarray with this unit-cell has presented a measured gain of 28.8 dBi with an aperture efficiency of 32% at 250 GHz as illustrated in Figure I-41. The measured and simulated radiation patterns both in E and H planes feature side-lobe levels lower than -18 dB.

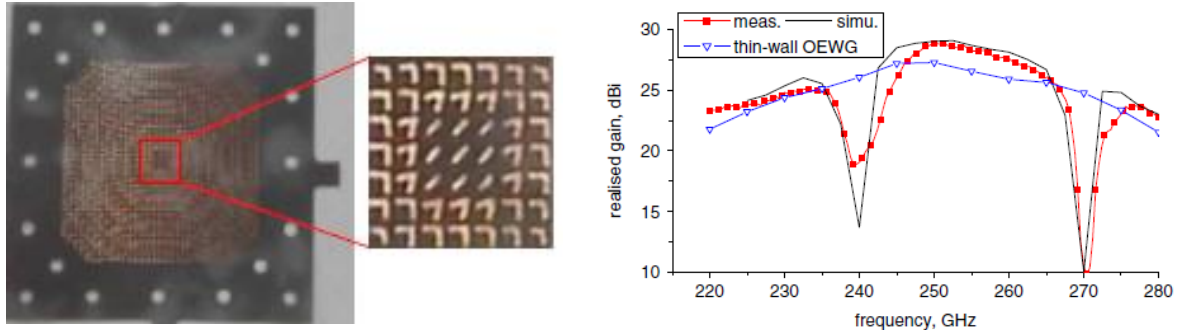


Figure I-41: Prototype and frequency response (gain as a function of frequency) of the two-layer transmitarray [66].

Switched beam transmitarrays

Switched beam transmitarrays are able to produce a finite number of fixed beam patterns or to switch from one fixed beam to another. Some recent switched beam transmitarrays developed in Ka-band to mm-band are presented hereafter.

Authors in [67] present the general technique to design arbitrarily large dual-band transmit arrays. The procedure is demonstrated for two offset transmit array implementations operating in circular polarization at 20 GHz (R_x) and 30 GHz (T_x). This array is useful for Ka-band satellite-on-the-move terminals with mechanical beam-steering capability. The unit-cell (Figure I-42(a)) is based on juxtaposed square patches with strip loops centered with the patches. The periodic metallic patches behave as a low-pass filter, whereas a grid of loops works as a high-pass filter. The combination of the two elements (loop plus patch) works as a bandpass filter. In addition, it is possible to define independently the lower and upper frequencies of the passband, by changing the element dimensions. The fabricated TA is illuminated by two standard-gain horns. It exhibits a measured gain of 24 dBi at 20 GHz and 27 dBi at 30 GHz. The beam-steering capability is demonstrated by shifting the feed between -30 mm and 30 mm with 15-mm steps relative to the central position as presented in Figure I-42(b,c).

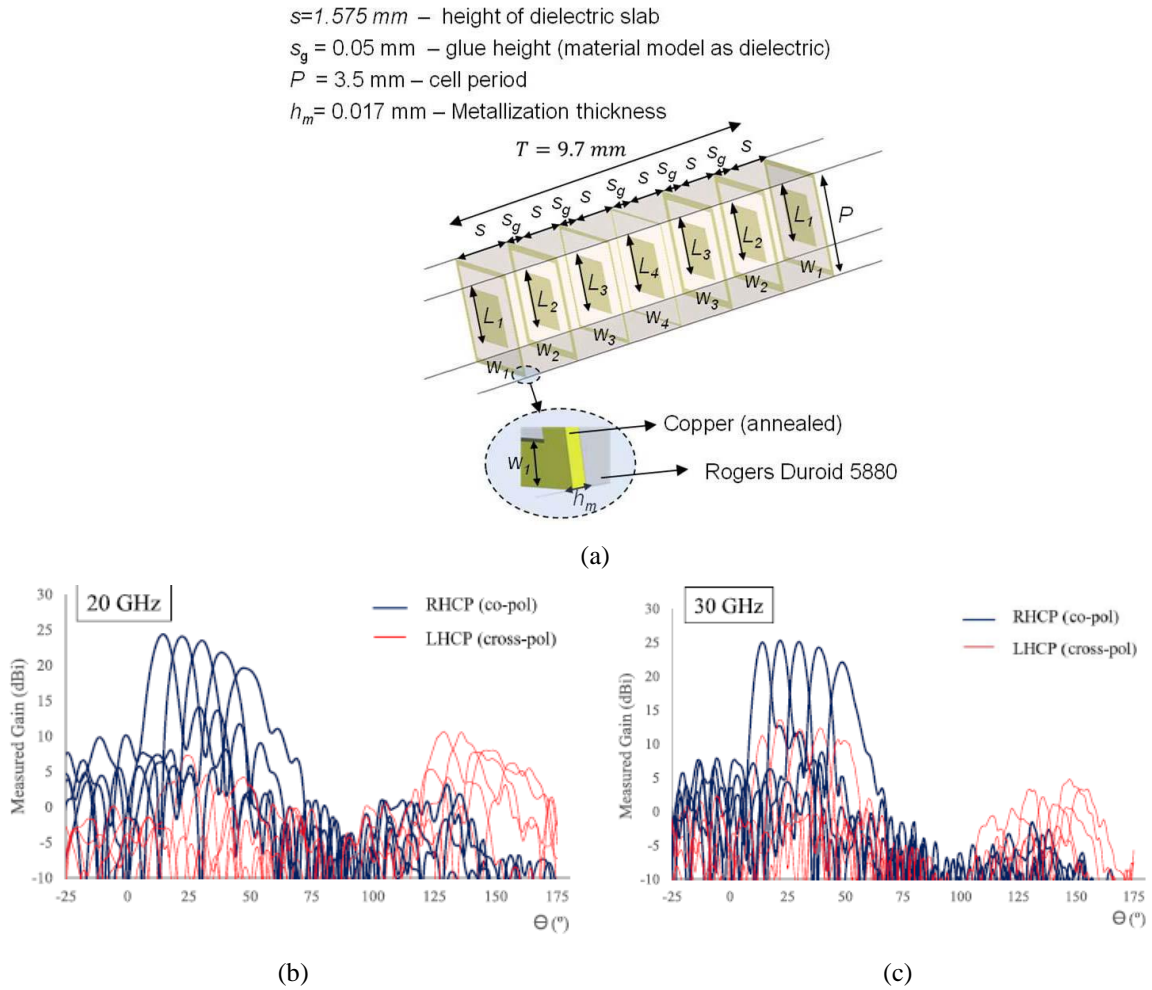


Figure I-42: High-gain dual band-beam steering transmitarray at Ka-band. (a) Unit-cell configuration. Measured radiation patterns at (b) 20 GHz and (c) 30 GHz [67].

A transmitarray antenna composed of a planar double-layered metamaterial (MTM)-based surface lens and seven feeding elements based on patch antennas working at 28 GHz is presented in [68]. The measured gain of the realized array corresponds to 24.2 dBi at 27.5 GHz with an aperture efficiency of 24.5%, and 3-dB gain-bandwidth of 26.6-30 GHz. The prototype can achieve a scanning coverage of $\pm 27^\circ$ with a gain tolerance of 3.7 dB as shown in Figure I-43.

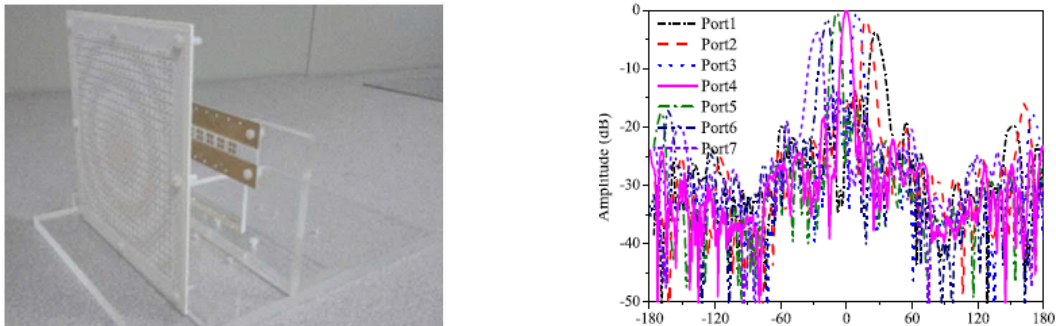


Figure I-43: Prototype of the proposed lens with seven-element feeding antenna (left), and measured scanned beam at 28 GHz (right) [68].

A switched beam linearly polarized transmitarray operating in V band for millimeter waves applications such as wireless backhaul is presented in [69]. Different unit-cells are used in the TA in order to have nearly 3-bits of phase quantization. The transmitarray is illuminated by a switched focal array of five patch antennas with 2.6 mm center-to-center spacing, consequently five beams pointing at 0° , $\pm 2.4^\circ$, and $\pm 4.8^\circ$ are obtained as shown in Figure I-44. The realized gain is equal to 23.5 dBi at 61.6 GHz with a 3-dB bandwidth of 10.3%.

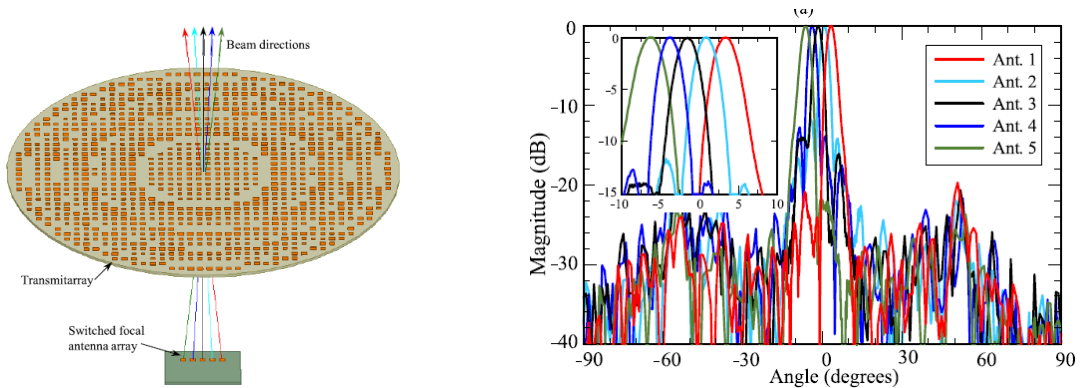


Figure I-44: Switched-beam transmitarray at V-band [69]. (a) Principle. (b) Experimental radiation patterns in H-plane at 61 GHz.

A dual layer transmitarray working at 77 GHz for automotive radars is presented in [70]. The linearly polarized unit-cell consists of two coplanar patches printed on opposite sides of the PCB with a 1-bit phase resolution (two phase states of 0° and 180°). Four beams with a specific coverage of $\pm 15^\circ$ can be obtained using four SIW slot antennas as primary feeds. The TA prototype exhibits a gain greater than 18.5 dBi at 76.5 GHz, a good agreement is obtained between the numerical and measured results as shown in Figure I-45.

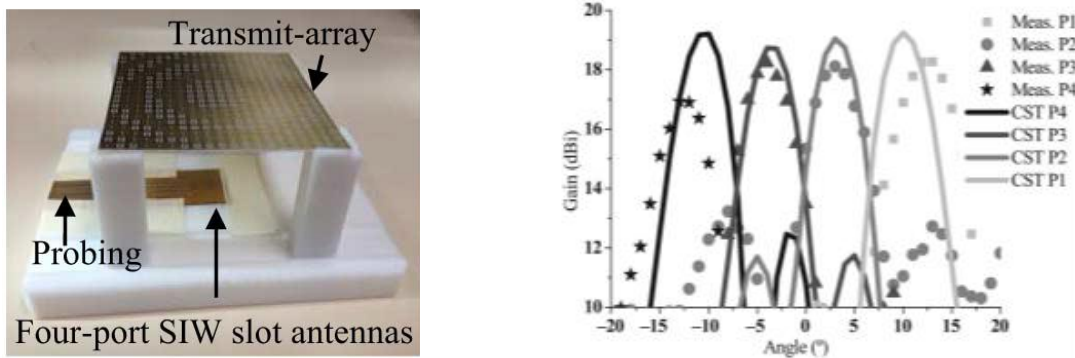


Figure I-45: Coplanar transmitarray with four SIW slot primary feeds at 76.5GHz [70].

Electronically reconfigurable transmitarrays

Electronically reconfigurable transmitarrays are obtained using switchable or tunable devices such as microelectromechanical systems (MEMS), p-i-n diodes, varactors, or micro-

fluidic systems. There are few electronically reconfigurable transmitarray prototypes in the open literature, especially at higher frequencies for SatCom systems or 5G networks.

In this part, an overview of the main reconfigurable unit-cells and transmitarrays demonstrated to date from C-band to mm-band is presented. For each frequency band, transmitarray antennas are firstly described, followed by examples of reconfigurable unit-cells in which there is no full TA demonstration.

In C-band [71], a fully reconfigurable 6×6-element transmitarray in linear polarization was experimentally demonstrated (Figure I-46(a,b)). The array unit-cell consists of two balanced bridged-T phase shifters and two differential proximity coupled patch antennas. The incident waves are firstly coupled into two microstrip lines with balanced signal using the proximity-coupled differential feed. The bottom microstrip lines are aperture-coupled to the microstrip line on the other side of the ground plane in order to transfer the signal from the input side to the output side. The signals pass through two cascaded balanced bridged-T phase shifters, and are then proximity-coupled to the output patch antenna, which radiates the outgoing waves. Thanks to the varactors integrated on the unit-cell, this latter produces more than 400° of phase range by changing the biasing voltage and an insertion loss varying from 1.7 dB to 5.2 dB. The maximum broadside directivity and gain are 19.9 dBi and 15 dBi, respectively. A beam scanning capability of ±50° is demonstrated in both E-, and H-planes at 5 GHz (Figure I-46 (c,d)). The main advantage of this architecture is the lack of via to connect the transmitting and receiving layers, but coupling methods that are used affect the radiation performance of the TA (poor cross-polarization level is observed).

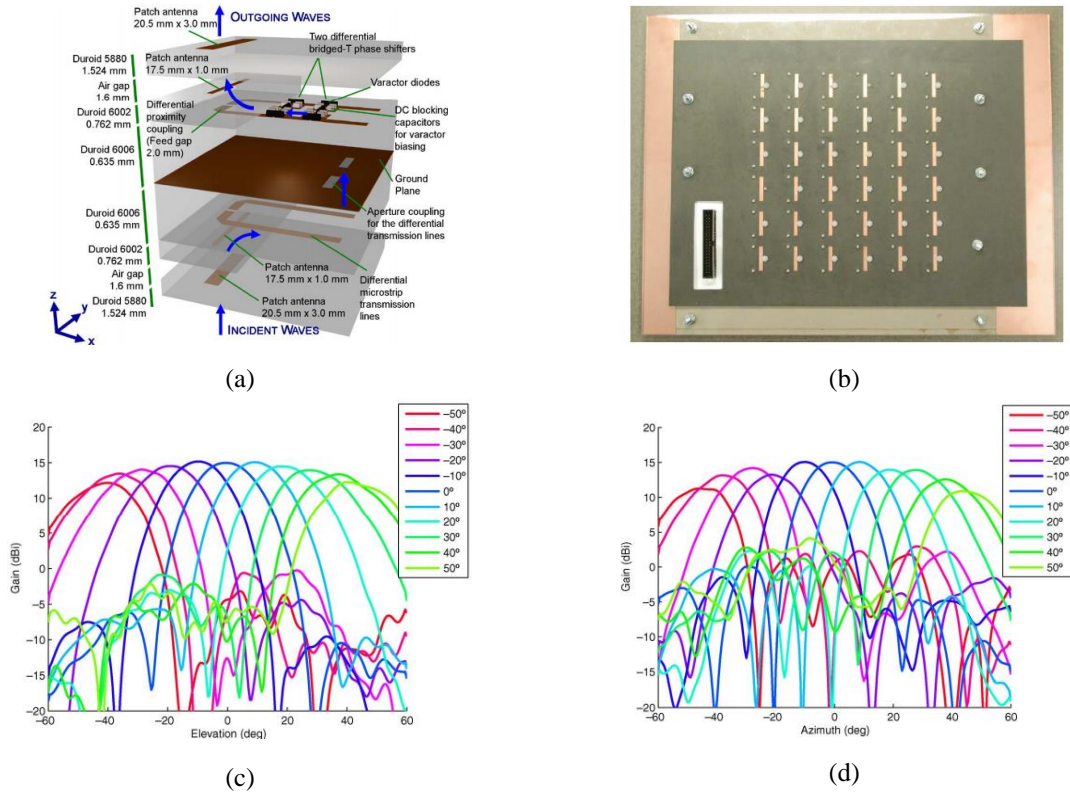


Figure I-46: 36-element reconfigurable transmitarray based on varactors at 5 GHz [71]. (a) Unit cell design. (b) Prototype of the TA. Measured radiation patterns (c) E-plane, (d) H-plane.

An 8×8 unit-cell reconfigurable transmitarray ($215 \times 215 \text{ mm}^2$) (Figure I-47(a)) with beam steering and polarization conversion capabilities at 5.4 GHz is presented in [72]. The distance from the transmitting horn to the transmitarray aperture is about 1.5 m. The unit-cell is composed of a two-layer stacked patches in receiving mode, a 360° reflective phase-shifter, and a polarization tunable patch structure loaded by PIN diodes and working in transmission mode. Illuminated by a 19.7 dBi gain horn, the realized TA has demonstrated a beam scanning capability of $\pm 60^\circ$ in both E-, and H-planes in two orthogonal linearly polarized modes with a broadside gain of 17 dBi. The left-, and right-handed circular polarization conversion is also possible over an 8.5% fractional bandwidth, with cross-polarization ratio higher than 15 dB. The radiation patterns at 5.4 GHz in E-plane are presented in Figure I-47(b). The principal drawbacks of the proposed architecture is its higher insertion loss and the working frequency limitation due to the increased resistive loss of the varactors diodes at higher frequency.

A circularly-polarized reconfigurable transmitarray antenna with 1-bit of phase quantization is presented in [73]. The TA is composed of 6×6 low-loss (insertion loss lower than 2 dB) unit cells based on two layer stacked patches integrated with a quadrature bridged reflection-type phase shifter as receiving cell, while a CP patch with 1-bit phase resolution is utilized as the transmission cell, as illustrated Figure I-48(a). The fabricated prototype has

presented a broadside gain of 14.8 dBi at 4.8 GHz with an axial ratio (AR) of 0.65 dB, and a beam-scanning capability of $\pm 45^\circ$ in the principal and diagonal planes. The far field radiation patterns of the TA in the diagonal planes are shown in Figure I-48(b). A limited CP bandwidth of about 100 MHz is observed due to the narrow working band of the CP Tx cell.

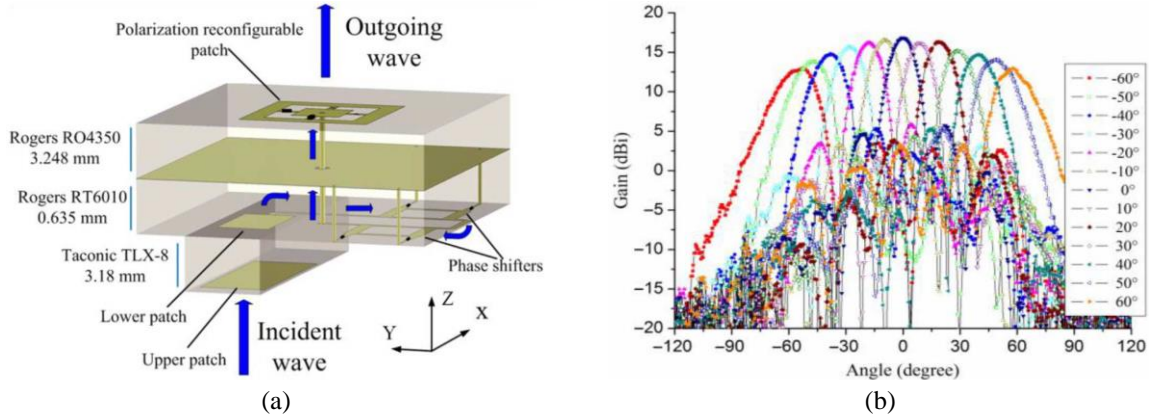


Figure I-47: Reconfigurable transmitarray with beam-steering and polarization conversion capabilities [72]. (a) Architecture of the proposed unit-cell. (b) Far-field radiation patterns in E-plane at 5.4 GHz.

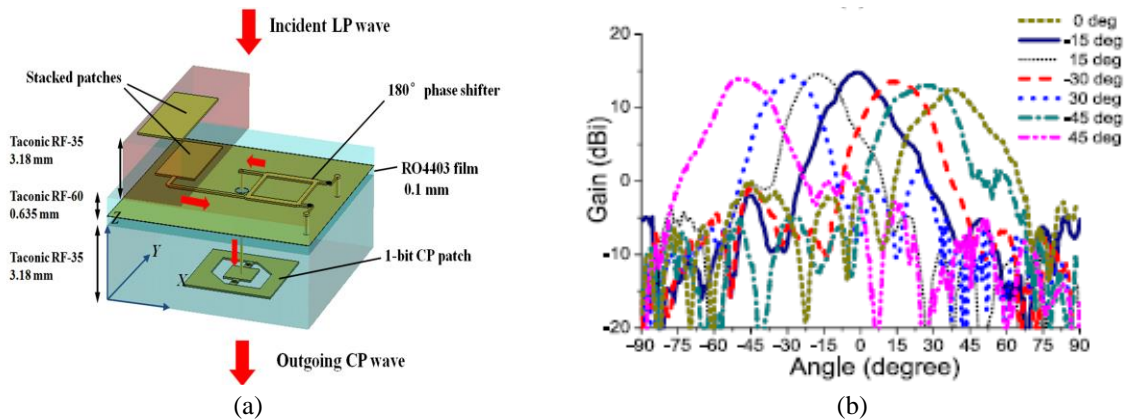


Figure I-48: Circularly-polarized reconfigurable transmitarray antenna [73]: (a) architecture of the unit-cell, (b) far-field radiation pattern in the diagonal plane at 4.8 GHz.

A compact 6×6 element array at 4.8 GHz based on the reconfigurable transmitarray described in [71] including a leaky-wave feed is presented in [74], as shown in Figure I-49(a). A coupling layer is designed to control the power transferred from the waveguide to each unit-cell of the transmitarray loaded by varactor diodes to tune the transmission phase. In addition to the low profile (the thickness is reduced by a factor of roughly 10 to $0.75\lambda_0$), this integrated-feed array also offers improvement on aperture amplitude distribution control, as well as the spillover control. The experimental measurements demonstrated a full-space pencil beam steering capability of $\pm 45^\circ$ in the principal and diagonal planes with good agreement with simulations (Figure I-49(b)). The gain equals 15.6 dBi with a directivity of 20.5 dBi, and a 2-

dB bandwidth of 9% at 4.8 GHz with an aperture efficiency of 34%. Despite its low profile, the TA has a significant insertion loss of about 3.4 dB.

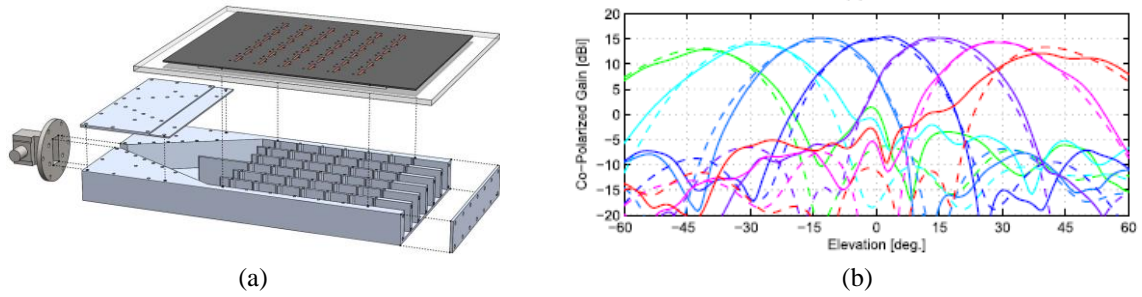


Figure I-49: Electronically-reconfigurable transmitarray with integrated leaky-wave feed [74]. (a) Exploded model of the proposed TA. (b) Measured and simulated co-polarized realized gain at 4.8 GHz in the diagonal plane.

Still in C-band, a 5×5 -unit-cell electronically-reconfigurable Frequency Selective Surface (FSS)-inspired transmitarray is presented in [75]. The unit-cell is composed of five stacked layers of a square-slot FSS unit-cell loaded with SMD varactor diodes and by an additional sixth layer dedicated to the feed. The TA can achieve a 2-D beam scanning capability with ranges up to Az (Azimut) = 28° and El (Elevation) = 26° with 1° of angular resolution at 5.2 GHz as shown in Figure I-50. It is difficult to realize this structure at higher frequencies because the insertion loss will be significant.

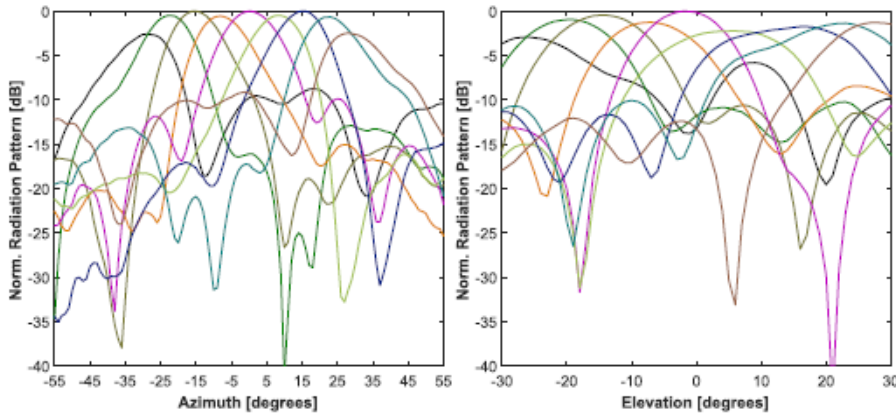


Figure I-50: Measured radiation patterns at 5.2 GHz for different steering angles in azimuth (left) and elevation (right) planes [75].

To overcome the losses of varactors, an amplifying tunable linearly-polarized unit-cell (Figure I-51(a)) working in C-band is proposed in [76]. It consists of stacked patches, an amplifier, and a phase shifter. The latter is realized by two cascaded quadrature-bridge reflection-type phase shifters with varactor diodes. The unit-cell has an average measured gain of 7.7 dBi with a 3-dB bandwidth of 10.6% (Figure I-51(b)). It achieves over 400° of phase shift in the frequency band of 4.95 GHz to 5.5 GHz (Figure I-51(c)). Even if the elementary cell presents good performances, it is still too complex for structures in Ka-band and beyond.

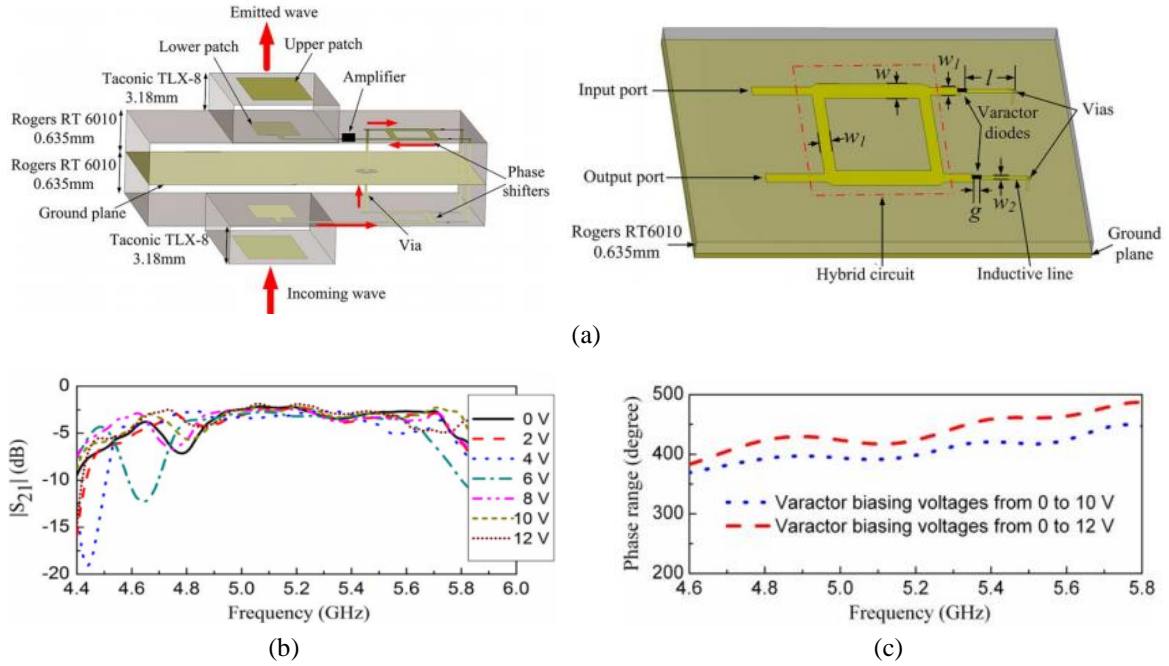


Figure I-51: (a) Schematic model of the amplifying unit-cell with electronically reflection-type phase shifter. Measured frequency responses: (b) transmission coefficient, (c) phase tuning range [76].

In X-band, a 400-element linearly polarized electronically-reconfigurable transmitarray (Figure I-52(a)) has been demonstrated in [77]. The TA is based on a simple wideband 1-bit phase quantization architecture of unit-cell. The unit-cell is composed of a rectangular patch antenna loaded by a U-slot on the receiver side and a patch antenna with the same size loaded by an O-slot on the transmitter side. These patches were connected to each other by a metal via hole at the center of the element. The 1-bit phase quantization was realized by integrating two pin diodes on the transmitter side patch antenna.

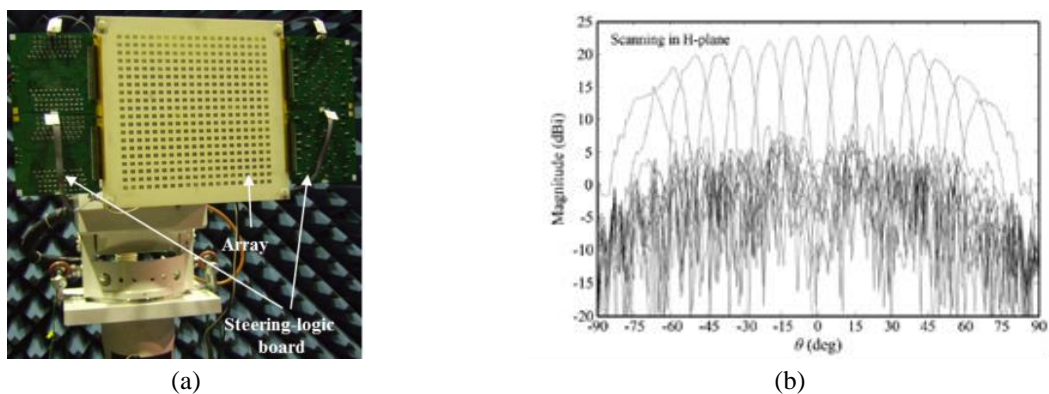


Figure I-52: Electronically reconfigurable transmitarray in X-band [77]. (a) Schematic view of the TA. (b) H-plane beam scanning capability.

The TA is illuminated by a 10-dBi gain horn placed at 214 mm from the aperture of the TA. It exhibits a directivity, gain, spill-over loss and power efficiency of 25.6 dBi, 22.8 dBi, 1.34 dB, and 52.9% respectively, with a fractional 3-dB bandwidth of 15.8% at 9.8 GHz. The

beam steering angle reaches $\pm 70^\circ$ in H plane and $\pm 40^\circ$ in E planes as shown in Figure I-52(b). This X-band TA presents good radiation performances and reconfigurable unit-cells at higher frequencies can be based on the same architecture.

Another X-band reconfigurable transmitarray (8×8 unit-cells) with 1-bit of phase resolution working in circular polarization (CP) is proposed in [78]. The unit-cell of the TA is composed of two metallic layers connected by a metallized via-hole (Figure I-53(a)). The transmission layer contains also two diodes to achieve phase tuning. The experimental measurement demonstrated a circularly-polarized wave around 10.2 GHz with an insertion loss less than 1.4 dB, as shown in Figure I-53(b). A dynamic polarization switching of the emitted wave between left- and right-handed circular polarization was numerically demonstrated.

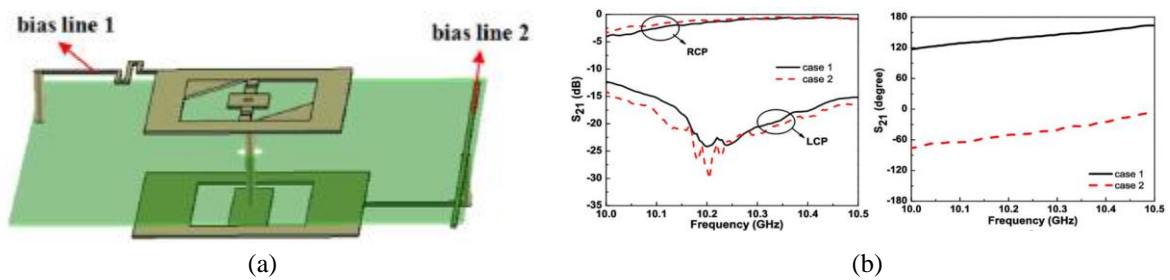


Figure I-53: Electronically reconfigurable circularly-polarized transmitarray in X-band [78]. (a) Schematic view of the unit-cell. (b) Measured transmission characteristics of the fabricated transmitarray.

Recently, numerous reconfigurable unit-cells in X-band for transmitarray antennas have been proposed in the open literature. Some of them are described in the following.

A dual-linearly polarized unit-cell with 1-bit of phase resolution in X-band is presented in [79]. It consists of two-layer microstrip patches working in receive (Rx) and transmit (Tx) modes, connected by a metallized via hole. The operation of the unit-cell is the following. The x-polarized incident wave is received by the Rx antenna, and its transmission phase would be shifted by 0° or 180° thanks to the two p-i-n diodes mounted on the O-slot in x-direction. The Tx antenna can tune the polarization state and transmit the guided wave signal to the free space in x or y polarization. A 1-bit phase tuning is achieved at two orthogonal linear polarization modes as depicted in Figure I-54 with insertion loss of about 1.1 dB at 10.5 GHz.

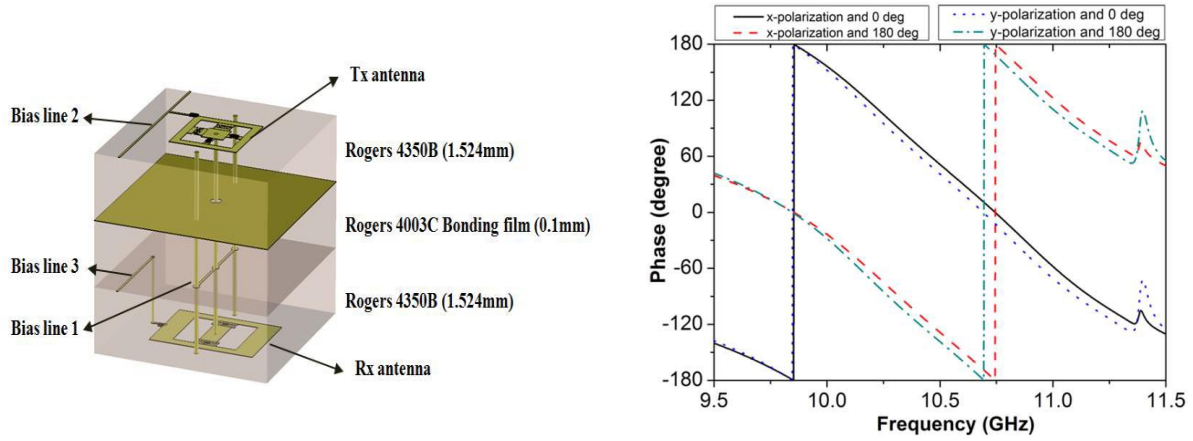


Figure I-54: Dual linearly polarized unit-cell with 1-bit phase resolution in X-band [79].

A reconfigurable circularly polarized transmitarray unit-cell based on microfluidics approach is proposed in [80]. The unit-cell, optimized in X-band, consists of two nested split ring slots formed by a liquid metal injected into the channels. The beam is oriented in a specific direction by implementing a rotational phase shift through the displacement of the liquid metal in the channels. The unit-cell exhibits a continuous 360° phase shift, and a good agreement is obtained between the simulation and measurement results within the frequency range of 8-10 GHz as presented in Figure I-55. Unit-cells based on microfluidics technology are still in a fundamental step and not enough robust to be used in a fully reconfigurable transmitarray.

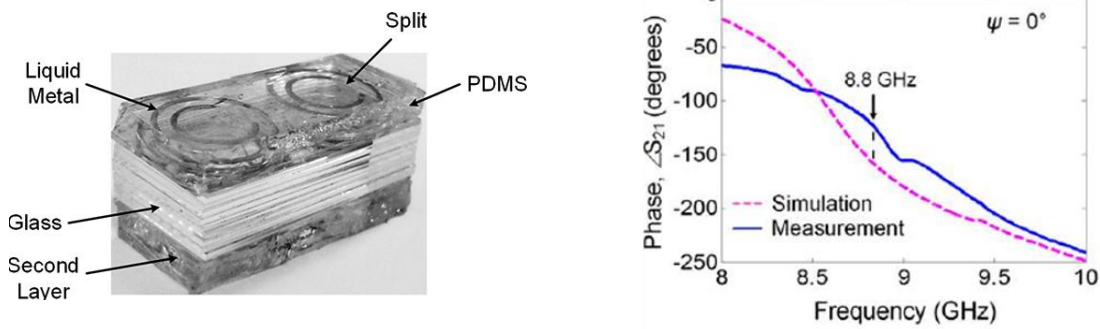


Figure I-55: Circularly-polarized reconfigurable transmitarray unit cell based on microfluidics at X band [80].

The performance of a Ku-band 1-bit reconfigurable transmitarray composed of low loss (1.6 dB) 16×16 unit-cells with aperture size of $128 \text{ mm} \times 128 \text{ mm}^2$ is numerically studied in [81]. The unit-cell consists of two orthogonal H-shaped slots coupled through a stripline, as depicted in Figure I-56 (left). Two PIN diodes are integrated on the transmission line in order to achieve a 180° phase difference. The TA is illuminated by a linearly-polarized corrugated horn with a gain of 14.4 dBi positioned at 111 mm above the aperture center. It shows a full-wave simulated gain of 18.8 dBi and an aperture efficiency of 23% at 12 GHz. The simulated

3-dB gain bandwidth is 21.9% (11.4–14.2 GHz). The normalized radiation patterns in the two principal planes are plotted in Figure I-56 (right).

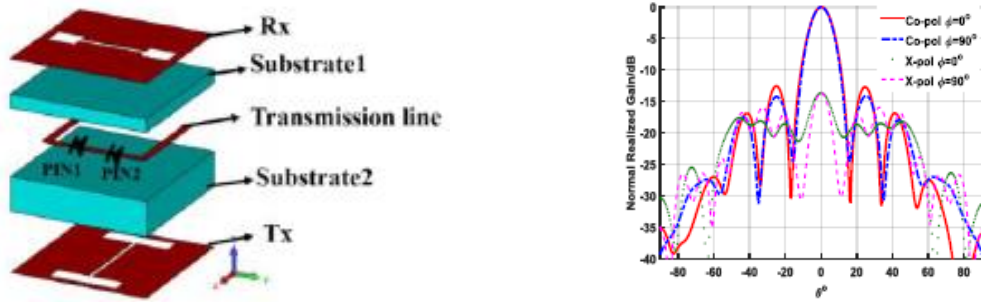


Figure I-56: A Ku-band 1-bit reconfigurable transmitarray: architecture of the proposed unit-cell (left), and radiation patterns (right) [81].

A K-band linearly polarized electronically reconfigurable transmitarray is presented in [82]. It is composed of a linear arrangement of five unit-cells consisting of multiple RF-laminate layers with varactor-loaded patches as tunable elements and a slot as coupling aperture. Each unit-cell achieves a continuous phase tuning of 360° . The TA experimentally demonstrated a beam scanning capability of $\pm 30^\circ$ at 24 GHz, as shown in Figure I-57. The unit-cell based on varactors has a significant insertion loss as illustrated by the authors in a previous work [83].

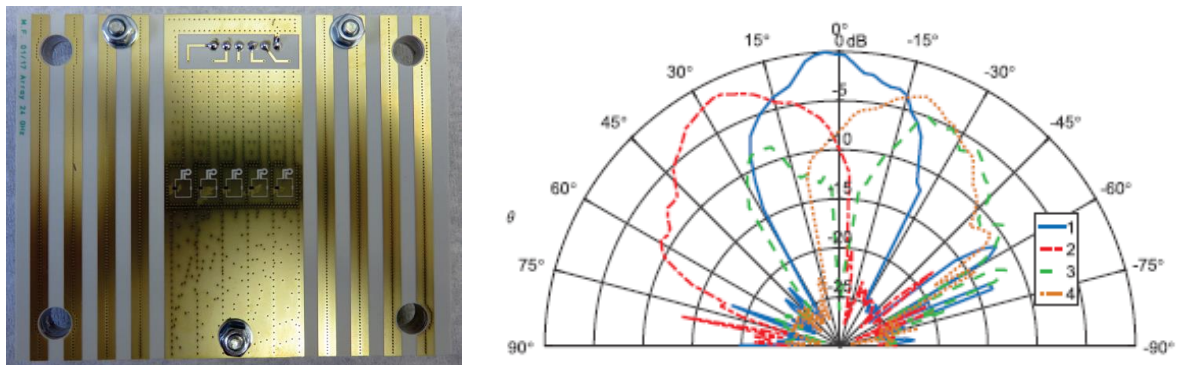


Figure I-57: K-band linearly-polarized reconfigurable transmitarray: fabricated prototype (left), and radiations patterns (right) [82].

A 2-bit 484-element reconfigurable transmitarray working in Ka-band has been demonstrated in [84]. The unit-cell consists of three layers with RF MEMS switches. The top and bottom metal layers contain the slot antennas that function as the first and last resonators of the antenna-filter-antenna (AFA). The middle layer accommodates the stripline resonators. The TA is illuminated by a 15 dBi gain horn antenna with a focal length of 4.5cm. It steers the beam at an angle of $\pm 40^\circ$ in H and E planes as shown Figure I-58. In H plane, the scan range was limited by the radiation performance of the slot. In E plane, a beam scanning up to $\pm 50^\circ$ was possible but at the expense of a significant loss. The maximum scan loss is about 5.4 dB and the SLL (Side Lobe Level) is equal to 3.5 dB.

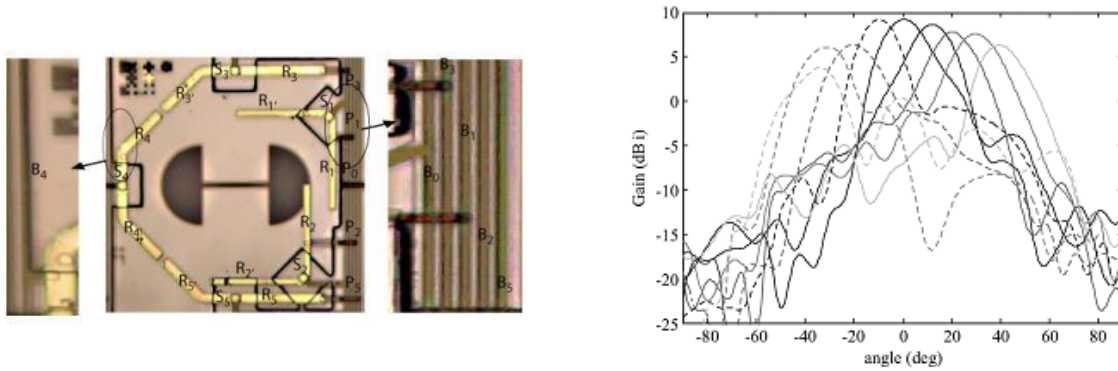


Figure I-58: 2-bit electronically reconfigurable transmitarray based on RF-MEMS switched unit-cells [84].

Recently, an electronically reconfigurable transmitarray working in Ka-band is demonstrated in [85]. The linearly-polarized unit-cell is based on patch antennas with 1-bit of phase quantization using p-i-n diodes. A 20×20 -element transmitarray (Figure I-59(a)) is demonstrated using this unit-cell. Left- or right-handed circular polarization is obtained by a pseudo-random sequential rotation ($0^\circ/90^\circ/180^\circ/270^\circ$). The prototype is illuminated by a horn antenna as a focal source with a focal ratio $F/D = 0.6$ (D is the size of the array). As depicted in Figure I-59(b), the TA has a broadside gain of 20.8 dBi, a relative 3-dB bandwidth of 14.6% at 29 GHz with a radiation efficiency of 58%. A 2-D beam scanning capability of $\pm 60^\circ$ is experimentally demonstrated. The TA prototype can be also fed with a 2×2 planar focal array of SIW (Substrate Integrated Waveguide) slot-subarray, thereby reducing the focal ratio from 0.6 to 0.36.

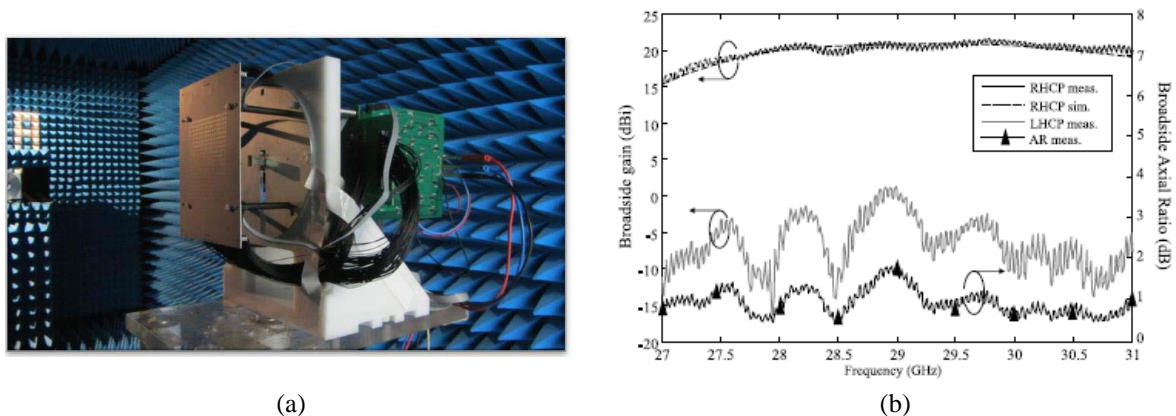


Figure I-59: (a) Prototype of a Ka-band 400-element circularly polarized transmitarray, (b) simulated and measured frequency response (broadside) [85].

A dual-band TA architecture for K/Ka-band SatCom applications has been presented in [86]. As shown in Figure I-60(a), the TA is composed of a feed antenna which, in the case of transmitting mode operation (Ka-band), distributes the RF signal to the dual-band antenna elements guided by the multi-functional SiGe BiCMOS ICs (Integrated Circuits). The stack of the TA unit-cell is composed of three functional parts: a lower multilayer PCB with the

orthogonal-mode dual-band patch antenna, the chip (SiGe BiCMOS IC) and the upper board (Figure I-60(a)). The manufactured submodule is composed by four transmit antennas (operating at 30 GHz) and two receiver channels (operating at 20 GHz). They ensure the uplink and downlink for SATCOM systems. The measured and simulated radiation patterns on both planes (E, H) for transmit and receive antennas are presented in Figure I-60(b). In both frequency bands K/Ka, a good agreement between the experimental results and the simulated far field patterns is obtained.

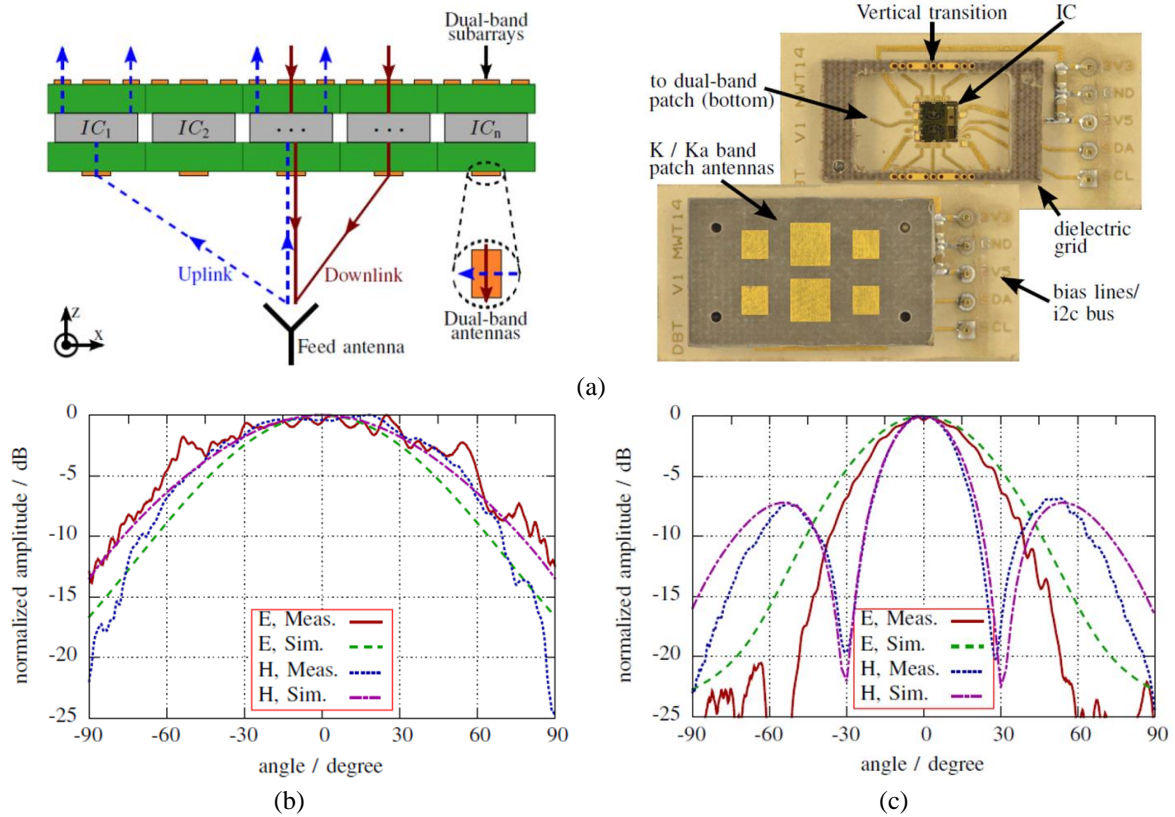


Figure I-60: (a) Active dual-band TA and realized module. Measured and simulated radiation patterns: (b) Receive antenna at 20 GHz, (c) Transmit antenna at 30 GHz [86].

1.3. Conclusion

In this chapter, we have shown that high frequency band is useful for numerous applications (radars, imaging systems, 5th generation networks, SatCom systems, etc.). We have focused our investigations on the future 5th generation (5G) mobile communication networks and SatCom systems in Ka-band, which is the frequency band of interest in this thesis.

In addition to transmitarrays, we have illustrated through some prototype examples in the open literature that others kind of antenna arrays, especially phased array and reflectarray antennas, are also good candidates for 5G and SatCom systems. The radiation pattern masks for these applications provided by the international standardization institutions are presented.

The working principle of the transmitarray, the simulation technique of both unit-cells and TA, and its power budget are reviewed.

The state of the art on passive and electronically reconfigurable transmitarray antennas from C- to mm-bands have been presented. Several topologies of passive transmitarray antennas with large bandwidth, dual or multiband and dual-polarization properties have been described. Some solutions to reduce the focal distance of transmitarrays have been investigated, and promising results have been demonstrated. Many active unit-cells and transmitarray antennas, based on p-i-n diodes, varactors, microfluidics, and MEMS technologies, for beam-steering and beamforming have been presented in the open literature. Huge progress has already been done in passive and active TAs, although efforts still need to be made. Some of these challenges are the design of low loss TA structure with high aperture efficiency and low-profile.

The performances of the relevant passive, switched beam and electronically reconfigurable transmitarrays presented in the literature are summarized in Table I.5, Table I.6, and Table I.7, respectively.

Table I.5: Performances of existing fixed beam transmitarrays.

Reference	[54]	[55]	[56]	[57]	[58]	[41]	[59]	[61]	[62]	[64]	[65]
Layers	1	5	3	3	2	3	3	5	3	3	7
Technology	Metal only	Metal only	Metal only	PCB	PCB	PCB	PCB	PCB	PCB	PCB	LITC
Freq. (GHz)	10	10.3	11/12.5	13.5	20	30	28	20/30	19.5/29.6	60	140
Polar.	CP	LP	dual CP/LP	LP	LP	CP	LP	dual CP	dual LP	LP	LP
F/D	-	0.9	0.8	1	1.2	0.52	0.28	0.87	~0.6	0.7	~1.9
Phase range	360°	51.5°	300°	360°	305°	1-bit	360°	360°	180°	3-bit	360°
Gain (dBi)	25.5	22.3	23.7/24.4	~22.0	33.0	22.8	25.7	-	27.4/28.4	32.5	33.4
Ap. eff. (%)	15.0	65.0	38.0/34.6	60.0	40.0	15.1	46.0	-	21.2/20.1	42.7	50.1
1-dB BW (%)	15	23.4	6.8/5.4	16	5.9	-	5	-	10.7/8.3	15.4	10.7
3-dB BW (%)	-	-	-	18.5	-	20.0	46.0	-	11.4/11.3	19.5	24.4

CHAPTER I. INTRODUCTION

Table I.6: Performances of existing switched beam transmitarrays.

Reference	[67]	[68]	[69]	[70]
Layers	7	2	3	2
Technology	PCB	PCB	PCB	PCB
Freq. (GHz)	20.0/30.0	27.5	60.0	76.5
Polar.	Dual band CP	LP	LP	LP
F/D	0.9	0.5	-	~0.5
Phase range	360°	240°	3-bit	1-bit
Gain (dBi)	24 /27 dBi	24.2	23.5	18.5
Ap. eff. (%)	-	24.5	-	-
1-dB BW (%)	-	-	-	-
3-dB BW (%)	-	12.6	10.3	-
Beam scanning capability	Elev. = 50°	± 27°	± 4.8°	± 15°

Table I.7: Performances of existing electronically beam transmitarrays.

Reference	[71]	[72]	[73]	[74]	[75]	[77]	[84]	[85]
Layers	7	4	4	7	5	4	3	4
Technology	PCB	PCB	PCB	PCB	PCB	PCB	PCB	PCB
Phase shifters	Varactors	PIN diodes	PIN diodes	Varactor diodes	Varactor diodes	PIN diodes	MEMS	PIN diodes
Freq. (GHz)	5.0	5.4	4.8	4.8	5.2	9.8	34.8	29.0
Polar.	LP	LP	CP	LP	LP	LP	LP	CP
F/D	-	~7.0	~13.7	~0.3	-	0.7	-	0.6
Phase range	400°	360°	1-bit	400	360°	1-bit	2-bit	1-bit
Gain (dBi)	15	17	14.8	15.6	19.9	22.7	9.2	20.8
Ap. eff. (%)	-	28.5	27.6	34.0	-	15.8	6.2	9.5
1-dB BW (%)	-	-	-	-	-	-	-	-
3-dB BW (%)	-	8.5	2	9% (2-dB BW)	~1.9	15.8	-	14.6
Beam scanning capability	±50° E-, and H-planes	±60° E-, and H-planes	±45° xoz-, and yoz-planes	±45° E-, and H-planes	Az.=28° E1.=26°	±40°/±60° E-, and H-planes	±40° E-, and H-planes	±60° E-, and H-planes

In view of existing transmitarrays in the literature, the aim of this thesis is to design, optimize and show the proof of concept through prototyping of:

- high gain fixed beam transmitarrays in linear and circular polarization with 3-bit of phase quantization;
- 2-bit electronically reconfigurable transmitarray based on PCB technology and PIN diodes to control the phase of the transmitted wave.

Chapter II. Theoretical analysis of transmitarray antennas

Two main theoretical analysis of transmitarray antennas, true time delay (TTD) phase compensation method and faceted array, are addressed in this chapter, which is organized as follows. The section 2.1 is dedicated to the analysis of the impact of the true time delay compensation method on the performances of the transmitarray in terms of bandwidth and beam scanning capability. The principle of faceted array and its advantages on the beam-steering performances of the transmitarray are presented in section 2.2.

2.1. Impact of the phase compensation method on transmitarray performances

As previously mentioned, the transmitted electromagnetic wave can be focused or collimated by opportunely controlling the transmission phase of each unit-cell. Phase-shifters optimized at a single frequency or delay lines can be used for this purpose. When a constant phase-shift compensation is applied to steer the beam in a desired direction, it is observed, as well known, that the beam is squinted as a function of frequency [87]. This phenomenon is more pronounced for wide scan angles. As for classical phased arrays [88], [89], the beam squint could be removed or reduced by using time delay based methods rather than phase shifters. This type of phase compensation is called True Time Delay (TTD) method. Furthermore, in the case of spatial feeding arrays (reflectarray antennas [90] and TAs), due to the feeding technique, the phase compensation method also impacts the array bandwidth. Indeed, for this kind of antennas, a phase compensation is also required to compensate the path length differences between the focal source and the unit-cells. Recently, several passive TAs based on TTD compensation have been presented in the open literature [91], [92], but electronically reconfigurable TAs have not yet been demonstrated experimentally due to the complexity of TTD implementation.

In this section, a numerical analysis of the impact of the phase compensation method on the radiation performance of TAs is presented. For the first time, the impact of the constant phase-shift and TTD phase compensation on the TA scanning capability and bandwidth are investigated and carefully compared. A generic analytical model has been used in the proposed analysis to investigate the performance of transmitarray antennas. The considered transmitarray

is based on ideal configurations with lossless and matched unit-cells. It is illuminated by an ideal focal source ($\cos^n\theta$, $n=4$) with a gain of 10 dBi and 100% of efficiency. The optimal distance (F) between the focal source and the array (Figure I-26) has been opportunely optimized to maximize the antenna peak gain at the center frequency.

Two phase compensation methods, constant phase-shift, and True Time Delay (TTD), are implemented in the *in-house* simulation tool. The impact of the phase compensation method is studied in terms of directivity, gain, aperture efficiency, and beam scanning capability.

The required phase compensation for each unit-cell takes into account the path length between the focal source and the specific unit-cell, the phase responses of the unit-cell and focal source, and the required phase gradient to steer the main beam in a desired direction (θ_0 , ϕ_0). Its general expression is given by:

$$ph(S_{21}^m) = k(r_m - \sin \theta_0 \cos \varphi_0 x_m - \sin \theta_0 \sin \varphi_0 y_m) - \phi_m^{inc}(\theta_{FS}, \varphi_{FS}) - \phi_{FS}(\theta_m, \varphi_m) \quad (\text{Eq II-1})$$

where k is the wave number in vacuum, r_m is the distance between the focal source and the unit-cell m , (x_m, y_m) are the coordinates of the unit-cell m . $\phi_m^{inc}(\theta_{FS}, \varphi_{FS})$ is the radiation pattern in phase of the m -th unit-cell in the incident direction (θ_{FS} , φ_{FS}) of the focal source, and $\phi_{FS}(\theta_m, \varphi_m)$ is the phase radiated by the focal source in the direction (θ_m , φ_m) of the m -th unit-cell.

For the constant phase-shift compensation method, the required phase compensation expressed in (Eq II-1) becomes as follows:

$$ph(S_{21}^m, \lambda_0) = \frac{2\pi}{\lambda_0}(r_m - \sin \theta_0 \cos \varphi_0 x_m - \sin \theta_0 \sin \varphi_0 y_m) - \phi_m^{inc}(\theta_{FS}, \varphi_{FS}) - \phi_{FS}(\theta_m, \varphi_m) \quad (\text{Eq II-2})$$

Where λ_0 is the wavelength at the design frequency f_0 .

It is easy to see that this phase compensation is valid only over a narrow frequency band and that a phase error proportional to the difference in path length becomes significant when the frequency varies significantly compared to f_0 . In the particular case of TAs, this phase error impacts the bandwidth of the antenna and its steering capability (beam-squint).

TTD compensation can be introduced as a unique solution to avoid both bandwidth [90] and beam-squint limitations. In this case, the phase compensation depends on the frequency and the wave number as shown in the following equation:

$$\begin{aligned}
 ph(S_{21}^m, \lambda) = & \frac{2\pi}{\lambda} (r_m - \sin \theta_0 \cos \varphi_0 x_m - \sin \theta_0 \sin \varphi_0 y_m) \\
 & - \phi_m^{inc}(\theta_{FS}, \varphi_{FS}) - \phi_{FS}(\theta_m, \varphi_m)
 \end{aligned} \tag{Eq II-3}$$

2.1.1. Impact on the bandwidth

20×20-, 30×30-, and 40×40-unit-cell ideal TAs (unit-cell size $0.5\lambda_0 \times 0.5\lambda_0$) have been designed to study the impact of the phase compensation method on the TA bandwidth. In all cases, the TA is illuminated by a 10-dBi ideal focal source with 100% efficiency.

The numerical results are provided for the frequency range f_{min} - f_{max} . These frequencies are chosen in order to cover the full SatCom Ka-band ($f_{min} = 27$ GHz, $f_0 = 29$ GHz, and $f_{max} = 32$ GHz).

A continuous phase-shift in the range 0° - 360° has been considered for each unit-cell when constant phase-shift method is applied, whereas a linear phase-delay with more than one cycle of 360° is used in the case of TTD.

In the case of a constant phase-shift compensation, when an ideal unit-cell is used, the TA bandwidth is limited because the correction of the path lengths between the focal source and the unit-cells is computed at a single frequency. This bandwidth reduction becomes even more pronounced for large array dimensions.

The TTD compensation method can be used opportunely to improve the bandwidth as shown in Figure II-1. In this figure, the maximum gain of the three considered square arrays (20×20, 30×30 and 40×40 unit-cells) is plotted as a function of frequency for both compensation methods. The optimal focal ratio (F/D , where D is the length of the array side) for the 20×20, 30×30, and 40×40 TAs is equal to 0.5, 0.51, and 0.51, respectively.

Figure II-1 clearly demonstrates the TA bandwidth enlargement for large TAs. Indeed, when constant phase-shift compensation is applied, the theoretical 1-dB relative bandwidths are equal to 13.4% and 10% for 30×30 and 40×40 TAs, respectively, whereas it covers the whole frequency band between f_{min} and f_{max} when TTD compensation is applied.

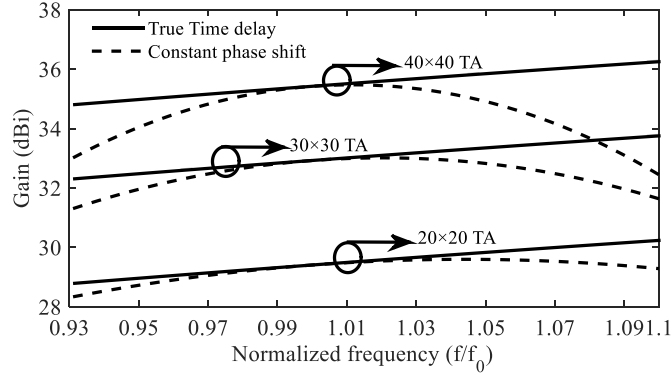


Figure II-1: TA peak gain at broadside for three different TAs and for both phase compensation techniques as a function of the normalized frequency f/f_0 .

2.1.2. Impact on the radiation pattern in the broadside direction

The phase compensation of the 40×40 TA is plotted in Figure II-2 for the TTD phase compensation and for three different frequency points (f_{min} , f_0 , and f_{max}). As expected, the phase distribution changes as a function of frequency. For the constant phase-shift compensation, the phase distribution is the same for all frequencies between f_{min} and f_{max} and is the same as the one calculated with the TTD method at f_0 .

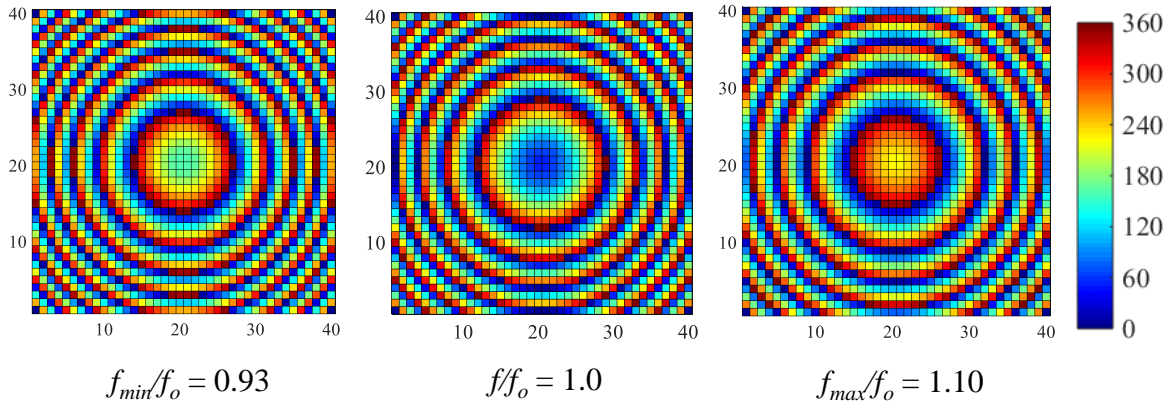


Figure II-2: Phase distribution of the 40×40 TA when TTD phase compensation technique is used for the normalized frequencies f/f_0 .

The broadside radiation patterns calculated in E-plane for constant phase-shift and true time delay compensation methods are plotted in Figure II-3, Figure II-4, respectively, at f_{min} , f_0 and f_{max} . The peak gain increases with frequency when TTD phase compensation is implemented (it equals 34.8, 35.4 and 36.3 dBi at f_{min} , f_0 , and f_{max} , respectively), whereas it reaches its maximum value at f_0 (35.4 dBi) and becomes lower at f_{min} (33.0 dBi) and f_{max} (32.2 dBi). The main results are summarized in Table II-1. Note that the difference between gain and directivity only originates from spill-over loss since the primary feed and the unit-cells are ideal.

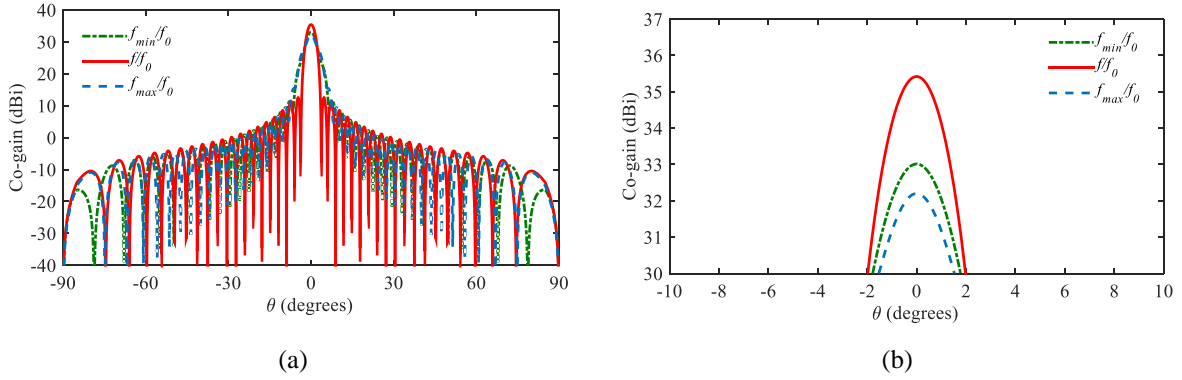


Figure II-3: (a) Radiation patterns (E-plane) of the 40×40 TA for three different frequencies using constant phase-shift compensation, (b) A zoom on the main beam for elevation angle θ_0 ranging from -10° to 10° .

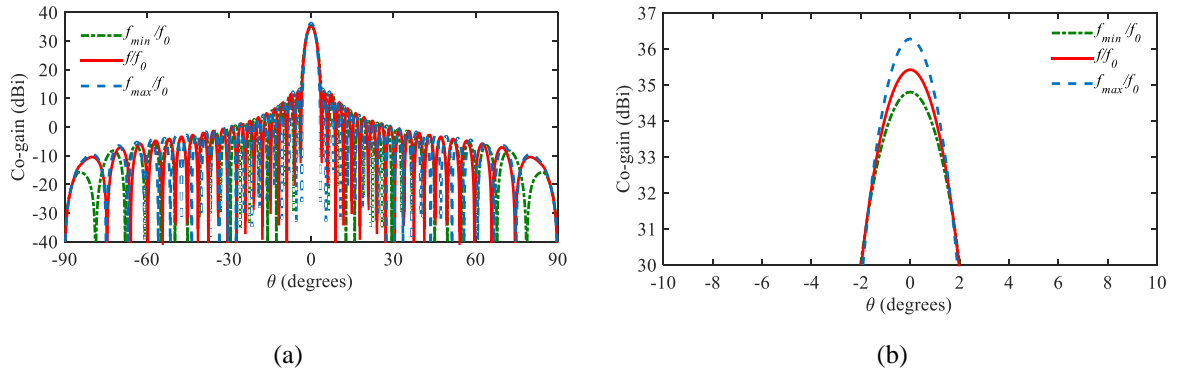


Figure II-4: (a) Radiation patterns (E-plane) of the 40×40 TA for three different frequencies using true-time delay compensation, (b) A zoom on the beam for elevation angle θ_0 ranging from -10° to 10° .

Table II-1: Impact of phase quantization on the TA performances.

Phase compensation	Freq.	Dir. (dBi)	Gain (dBi)	SLL (dB)
Constant phase shift (@ f_0)	f_{min}	33.7	33.0	-21.7
	f_0	36.2	35.4	-22.8
	f_{max}	32.9	32.2	-22.6
True Time Delay (TTD)	f_{min}	35.5	34.8	-22.9
	f_0	36.2	35.4	-22.9
	f_{max}	37.0	36.3	-22.9

2.1.3. Impact on the beam scanning capability

We investigate here the scanning capability as a function of the elevation angle θ_0 (fixed cut-plane). For brevity, only the results obtained for two scanning angles, 30° and 60° , are reported for the 40×40 TA in E-plane in Figure II-5, and Figure II-6, respectively.

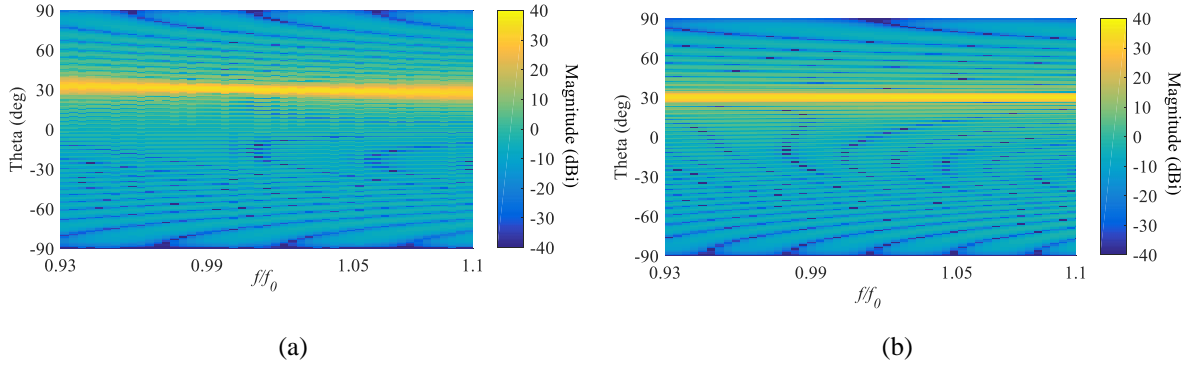


Figure II-5: Radiation patterns of the 40×40 TA steered at 30° in E-plane. (a) Constant phase-shift compensation. (b) TTD compensation.

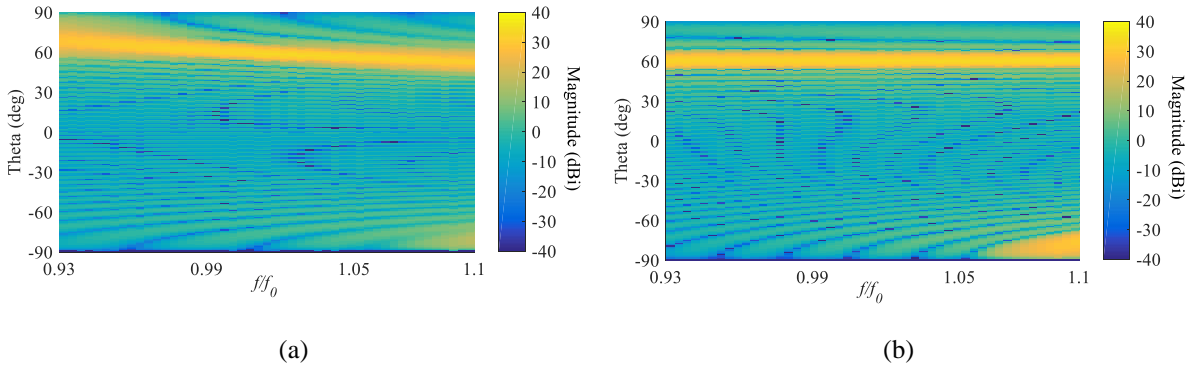


Figure II-6: (a) Radiation patterns of the 40×40 TA steered at 60° in E-plane. (a) Constant phase-shift compensation. (b) TTD compensation.

As expected, the effective scan angle decreases with frequency for constant phase-shift compensation: it varies between 27° (at f_{max}) and 32° (at f_{min}), and between 52° (at f_{max}) and 67° (at f_{min}) when the desired scan angle is 30° and 60°, respectively. Comparison with the results obtained with TTD phase compensation clearly confirms that there is no beam squint in the TTD case.

The main results are summarized in Table II-2 and Table II-3 for scan angles 30° and 60°, respectively. In these tables, $\Delta Gain$ is the difference between the gain obtained at the effective scan angle and the gain at the desired scan angle. It varies between 3.9 dB (at f_{min}) and 4.8 dB (at f_{max}) when the beam is steered at 30° and between 8.0 dB (at f_{min}) and 12.0 dB (at f_{max}) for a scan angle of 60°.

Table II-2: Performance of the TA when the beam points at 30°.

Phase compensation	TA Perf.	f_{min}	f_0	f_{max}
Constant phase shift (f_0)	Dir. (dBi)	32.9	35.5	32.4
	Gain (dBi)	32.1	34.8	31.7
	ϵ_{AP} (%)	38.6	61.8	24.8
	θ (°)	32.0	30.0	27.0
	Δ Gain (dB)	3.9	0	4.8
True Time Delay (TTD)	Dir. (dBi)	34.9	35.5	36.4
	Gain (dBi)	34.2	34.8	35.7
	ϵ_{AP} (%)	61.8	61.8	61.8
	θ (°)	30.0	30.0	30.0
	Δ Gain ((dB)	0	0	0

Table II-3: Performance of the TA when the beam points at 60°.

Phase compensation	TA Perf.	f_{min}	f_0	f_{max}
Single frequency (f_0)	Dir. (dBi)	29.4	33.1	30.8
	Gain (dBi)	28.7	32.4	30.0
	ϵ_{AP} (%)	17.5	35.7	17.0
	θ (°)	67.0	60.0	52.0
	Δ Gain (dB)	8.0	0	12.0
True Time Delay (TTD)	Dir. (dBi)	32.5	33.1	34.0
	Gain (dBi)	31.8	32.4	33.3
	ϵ_{AP} (%)	35.7	35.7	35.7
	θ (°)	60.0	60.0	60.0
	Δ Gain (dB)	0	0	0

The radiation patterns (in E-plane) of the 40×40 TA when pointing at 60° are plotted at f_{min} , f_0 and f_{max} in Figure II-7. The extreme stability of the radiated beam is confirmed when applying TTD phase compensation.

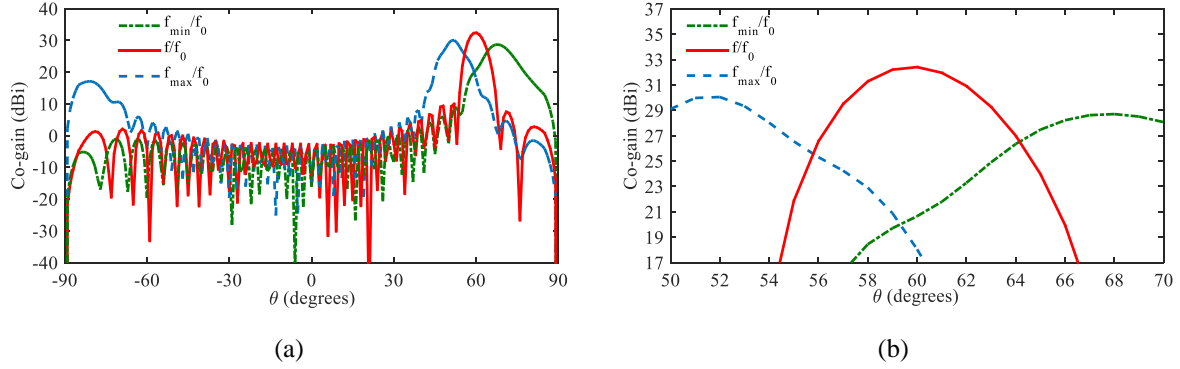


Figure II-7: (a) Radiation patterns (E-plane) of the 40×40 TA for three different frequencies using constant phase-shift compensation when the beam is steered at 60° , (b) zoom on the beam for elevation angle θ_0 ranging from 50° to 70° .

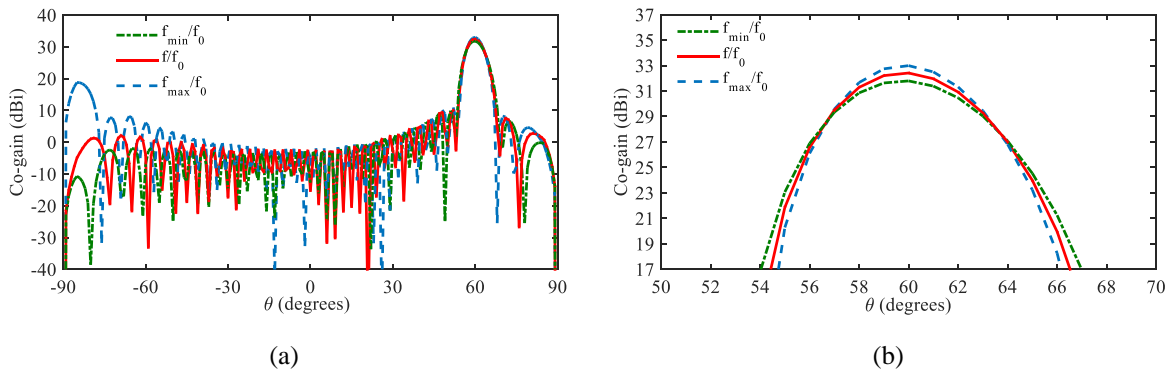


Figure II-8: (a) Radiation patterns (E-plane) of the 40×40 TA for three different frequencies using TTD compensation when the beam is steered at 60° , (b) zoom on the beam for elevation angle θ_0 ranging from 50° to 70° .

The analysis done in this part has shown that the constant phase-shift method is valid only over a narrow frequency band and produces a phase error proportional to the difference in path length. This error becomes significant when the frequency varies significantly compared to the center frequency f_0 . In the particular case of TAs, this phase error impacts the bandwidth of the antenna and its steering capability (beam-squint). Hence, TTD compensation can be introduced as unique solution to avoid both bandwidth [86] and beam-squint limitations. In this case, the phase compensation does not depend on the frequency.

2.2. Faceted transmitarray

A transmitarray (TA) is typically composed of a planar, faceted or conformal array realized in PCB (Printed Circuit Board) technology and illuminated by a focal source or a focal array.

From the array theory, it is well known that the element radiation patterns and the array geometry have an impact on the scanning capability and performance. As in the case of phased arrays and reflectarrays, the scan range of a TA could be increased using a conformal or faceted

radiating aperture. Furthermore, a faceted architecture can enhance the aerodynamics when the antenna is mounted on the fuselage of an aircraft or reduce the visual impact of the antenna. Previous works on reflectarrays concluded that the use of a convex conformal architecture could increase the antenna bandwidth [93], [94].

An n-faceted array is an array composed of n planar sub-arrays (panels). Each sub-array is oriented in a specific direction and it is necessary to take into account the orientation and coordinates of each unit-cell to derive the array radiation patterns.

The objective of the study addressed in this section is to investigate the performance of faceted TA and validate the proposed CAD tool through full-wave EM simulations.

2.2.1. Design methodology of a faceted transmitarray

The design methodology of a faceted transmitarray (geometrical arrangement, radiation patterns) is described in detail in this section.

Geometry

To convert a flat array into a faceted one, the latter must firstly be divided into n -sub-arrays or panels. Then, each panel is tilted at an angle α in order to obtain the desired shape. For this purpose, three types of rotation [95], [96] can be applied according to x, y and z directions labelled (R_Z , R_Y , R_X), as shown in Figure II-9.

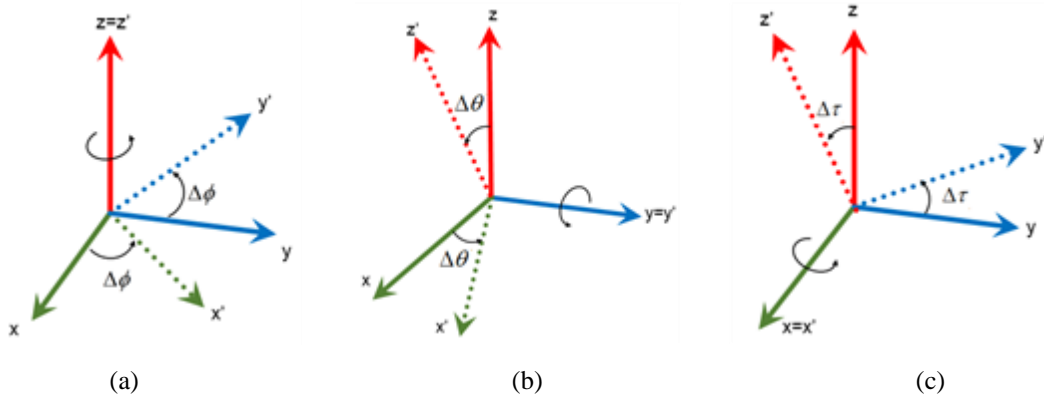


Figure II-9: Three elementary rotations. (a) Around z-axis. (b) Around y-axis. (c) Around x-axis.

The considered unit-cell at initial position $P(x_p, y_p, z_p)$ will be in position $M(x_m, y_m, z_m)$ after rotation. The latter after the transformation defined by the following equation:

$$M = R_z \cdot R_y \cdot R_x \cdot P . \quad (\text{Eq II-4})$$

Where (R_Z , R_Y , R_X) are the matrices corresponding to three elementary rotations. These latter are expressed:

$$\begin{aligned}
 R_z &= \begin{pmatrix} \cos(\Delta\phi) & -\sin(\Delta\phi) & 0 \\ \sin(\Delta\phi) & \cos(\Delta\phi) & 0 \\ 0 & 0 & 1 \end{pmatrix}, \\
 R_y &= \begin{pmatrix} \cos(\Delta\theta) & 0 & \sin(\Delta\theta) \\ 0 & 1 & 0 \\ -\sin(\Delta\theta) & 0 & \cos(\Delta\theta) \end{pmatrix}, \\
 R_x &= \begin{pmatrix} 1 & 0 & 0 \\ 0 & \cos(\Delta\tau) & -\sin(\Delta\tau) \\ 0 & \sin(\Delta\tau) & \cos(\Delta\tau) \end{pmatrix}.
 \end{aligned} \tag{Eq II-5}$$

In our case, only a rotation around y-axis is considered (see Figure II-9(b)). A translation must be done before applying the R_y matrix transformation. Indeed, the center of rotation is not the same for all cells.

The examples of 2- and 3-faceted TA generated from a flat array are shown in Figure II-10. The panels are tilted to the same angle α .

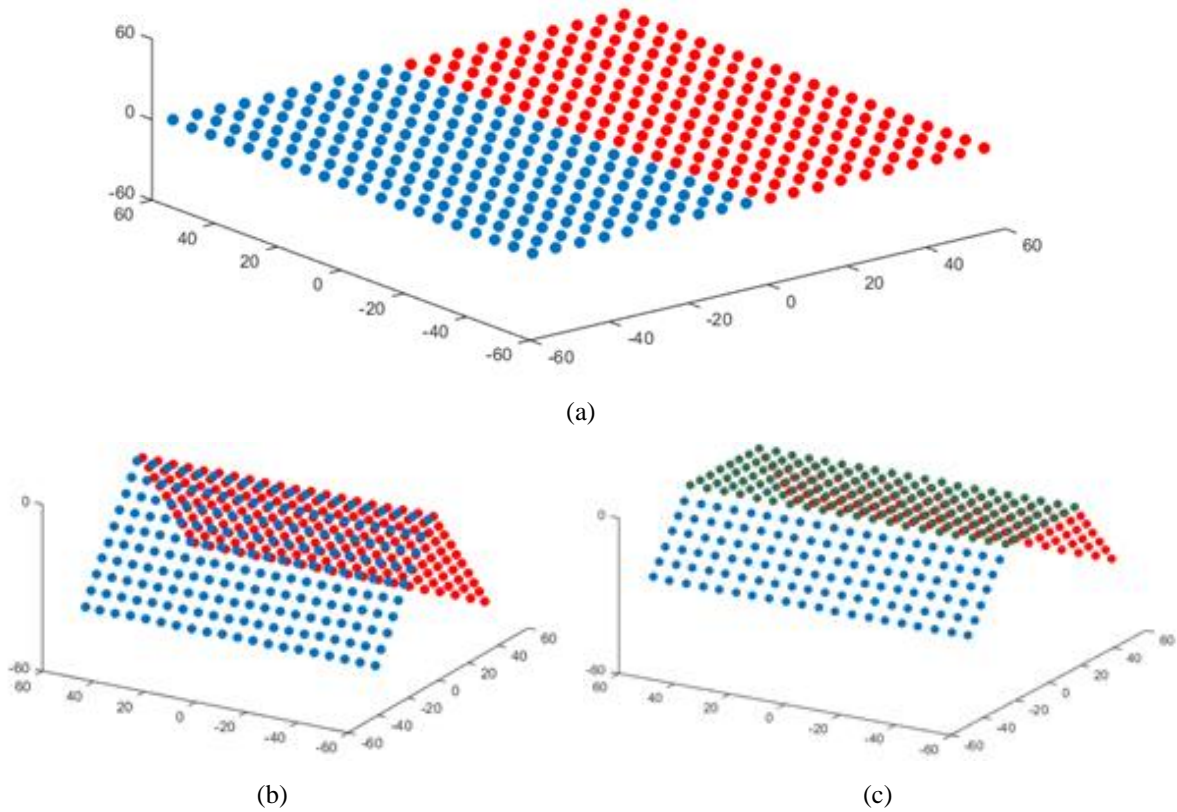


Figure II-10: Different shapes of transmitarray. (a) Flat shape. (b) 2-facets. (c) 3-facets.

Phase compensation principle

Let us consider a 3-facet TA illuminated by a feed horn, as illustrated in Figure II-11. This figure shows also actual constant-phase unit cells (presented in detail in chapter 3) used in full-wave simulations performed in the following sections to validate the theoretical model presented here.

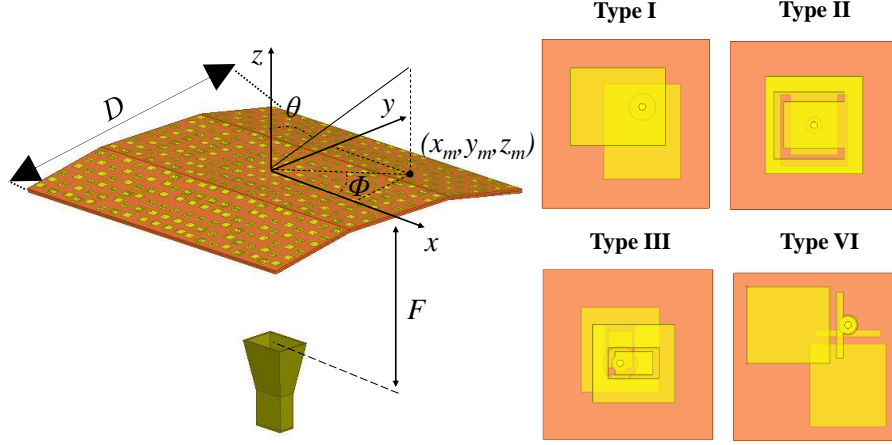


Figure II-11: Schematic view of a 3-facet TA (left) and unit-cells used for full-wave simulations (right).

As it is well known, the relative phase of the electromagnetic wave radiated by the unit-cell m is expressed as:

$$\varphi_m^r(x_m, y_m, z_m) = \varphi_{FS}(\theta_m, \phi_m) - k_0 r_m + \varphi_m^{inc}(\theta_{FS}, \phi_{FS}) + ph(S_{21}^m) \quad (\text{Eq II-6})$$

Where $\varphi_{FS}(\theta_m, \phi_m)$ is the phase radiated by the focal source towards the direction (θ_m, ϕ_m) of unit-cell m , k_0 is the wave number in vacuum at the center frequency f_0 , $r_m = \sqrt{(F + z_m)^2 + x_m^2 + y_m^2}$ is the distance between the phase centers of the focal source and the unit-cell m , F is the focal distance, (x_m, y_m, z_m) are the coordinates of unit-cell m , $\varphi_m^{inc}(\theta_{FS}, \phi_{FS})$ is the phase of the radiation pattern of unit-cell m in the incident direction (θ_{FS}, ϕ_{FS}) from the focal source, and $ph(S_{21}^m)$ is the phase shift introduced by unit-cell m .

On the other hand, the main beam can be steered in direction (θ_0, ϕ_0) using a simple linear phase distribution across the array aperture, as given by:

$$\varphi_m(x_m, y_m, z_m) = -k_0(\sin(\theta_0)\cos(\phi_0)x_m + \sin(\theta_0)\sin(\phi_0)y_m + \cos(\theta_0)z_m) \quad (\text{Eq II-7})$$

By combining (Eq II-6) and (Eq II-7), the required phase shift for each unit-cell can be derived as:

$$\begin{aligned} ph(S_{21}^m) = & k_0(r_m - \sin(\theta_0)\cos(\phi_0)x_m \\ & - \sin(\theta_0)\sin(\phi_0)y_m - \cos(\theta_0)z_m) \\ & - \varphi_m^{inc}(\theta_{FS}, \phi_{FS}) - \varphi_{FS}(\theta_m, \phi_m) \end{aligned} \quad (\text{Eq II-8})$$

(Eq II-8) is used to define the phase distribution over the TA aperture and scan the radiated beam in 2D over a large angular window.

2.2.2. Simulation of a 400-element 3-facet transmitarray

The considered TA is composed of 400 elements arranged on a three-panel 20×20 lattice: the central panel and lateral panels contain 8×20 and 6×20 elements, respectively. Both lateral panels are inclined by an angle α with respect to the central panel. All numerical results have been obtained assuming constant-phase ideal unit-cells and focal source ($\cos^n \theta$, $n=4$) with 100% efficiency. The optimal focal ratio F/D is equal to 0.5, so the focal source is placed at $F = 51$ mm from the aperture of the 3-faceted TA, D is the length of the array side as indicated in Figure II-11.

Full-wave EM simulations have been performed to validate the Matlab implementation to of the faceted TA model. Comparison between the radiation patterns of the 3-faceted TA ($\alpha = 10^\circ$) obtained with the numerical tool (Matlab) and full-wave simulations are presented in Figure III-12, and show excellent agreement.

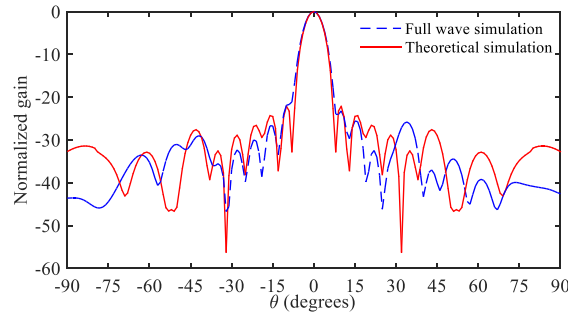


Figure II-12: Normalized gain versus frequency of the 3-facet TA; comparison of the theoretical model with a full-wave simulation.

The impact of the panels angles on the bandwidth of a 400 elements 3-facet TA is analyzed considering three values of α : 10° , 30° and 70° . The gain-frequency response of the three configurations is plotted in Figure II-13.

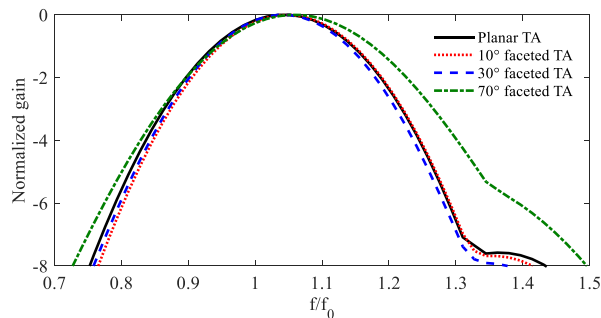


Figure II-13: : Normalized gain versus frequency of the planar and 3-facet TAs.

For a strongly faceted array ($\alpha = 70^\circ$ here), the bandwidth of the TA is improved and this bandwidth enlargement is probably explained by lower path length differences between the central and lateral cells in the case of a faceted array as compared to a planar one. But a gain

reduction is observed compared to the planar configuration. The areas of the planar and faceted arrays are expressed by the following equations (Eq II-9),(Eq II-10), respectively.

$$Area_{planar\ array} = 100\lambda^2 \quad (\text{Eq II-9})$$

$$Area_{faceted\ array} = 40\lambda^2 + 2 * 30\lambda^2 \cos(\alpha) \quad (\text{Eq II-10})$$

Where α and λ correspond to the tilted angle of the faceted array and the wavelength, respectively.

The ratio of the two areas is equal to:

$$Area_{faceted\ array} = 0.4\lambda^2 + 0.6\cos(\alpha) \quad (\text{Eq II-11})$$

For $\alpha = 70^\circ$, this ratio corresponds to 0.6 or -2.2 dB. This value is much closed to the loss obtained (-1.7 dB) between the planar and 70-faceted arrays in the Table II-4.

Table II-4: Maximum gain of the 3-facet TA as function of the desired scan angle.

Desired scan angle (°)	Planar	Gain dBi (actual scan angle)		
		3 facets $\alpha = 10^\circ$	3 facets $\alpha = 30^\circ$	3 facets $\alpha = 70^\circ$
0	29.1 (0°)	29.2 (0°)	29.1 (0°)	27.4 (0°)
10	29.0 (10°)	29.0 (10°)	28.9 (10°)	27.2 (10°)
20	28.8 (20°)	28.8 (20°)	28.7 (20°)	26.4 (19°)
30	28.5 (30°)	28.5 (30°)	28.3 (30°)	26.1 (30°)
40	27.9 (40°)	28.0 (40°)	27.7 (40°)	25.9 (40°)
50	27.1 (49°)	27.2 (50°)	26.8 (50°)	25.5 (50°)
60	26.1 (59°)	26.1 (59°)	25.2 (58°)	25.0 (60°)
70	24.7 (68°)	24.6 (68°)	23.9 (69°)	24.1 (70°)
80	22.9 (73°)	22.7 (74°)	22.0 (77°)	22.7 (78°)

2.2.3. Numerical simulation of 3-facet transmitarrays of different sizes

Three configurations of TAs (Figure II-14) have been considered in order to analyze the impact of the geometry on the beam scanning capability of a 3-faceted transmitarray. In all cases, the size of the central panel is fixed to 20×20 elements. The lateral panels for the three configurations, named *config. 1*, *config. 2*, *config. 3*, are composed of 5×20, 10×20, and 20×20 elements, respectively.

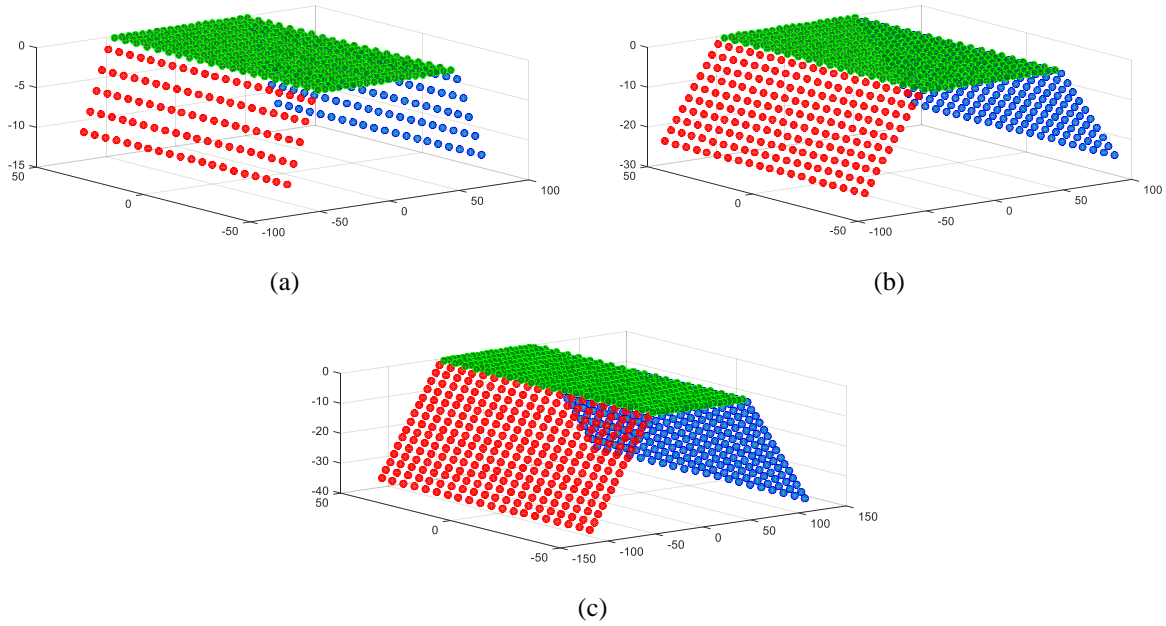


Figure II-14: Schematic view of the 3-facet TAs for the three configurations : (a) *config. 1* (30×20), (b) *config. 2* (40×20), and (c) *config. 3* (50×20).

The optimal focal distances of the 3-faceted transmitarray in *config. 1*, *config. 2*, *config. 3* correspond to $F = 62$ mm, 73 mm, and 84 mm, respectively, as shown in Figure II-15. The focal ratios (F/D) for the *config.1*, *config. 2*, *config. 3* are equal to 0.41, 0.36, and 0.28, respectively.

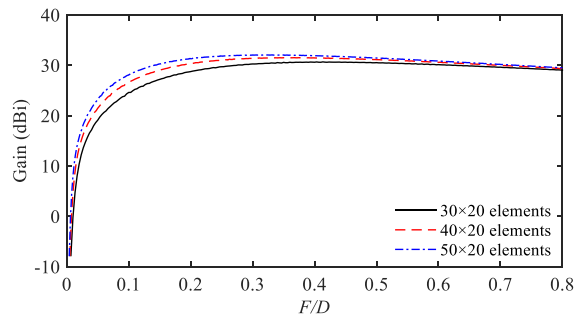


Figure II-15: Gain versus focal ratio for the three configurations of the 3-facet TAs.

The maximum gain and scanning capability of the 3-facet TA in the *config. 1*, *config. 2* and *config. 3* are summarized in Table II-5, Table II-6, and Table II-7, respectively.

The beam scanning capability of the 3-facet transmitarray increases when the number of unit-cells in the lateral panels increases. For the 3-facet TA tilted at $\alpha = 30^\circ$, the beams scanning reach 79° , 83° , and 85° for the TAs in the *config.1*, *config.2*, and *config.3*, respectively. The maximum beam scanning angle is observed for the panel angle $\alpha = 70^\circ$ in all configurations of the 3-facet TAs and is equal to 82° , 86° , and 88° for the TAs in the *config.1*, *config.2*, and *config.3*, respectively.

The radiations patterns when the beam is scanned at $\theta_0 = 80^\circ$ are plotted in Figure II-16, Figure II-17, Figure II-18, and Figure II-19 for the three configurations of 3-facet TAs considering a tilted angle $\alpha = 0^\circ, 10^\circ, 30^\circ$, and 70° , respectively.

As shown in figures, the beam scanning capability and the gain of the 3-facet TAs increase when the number of unit-cells and the tilted angle of the lateral panels increase.

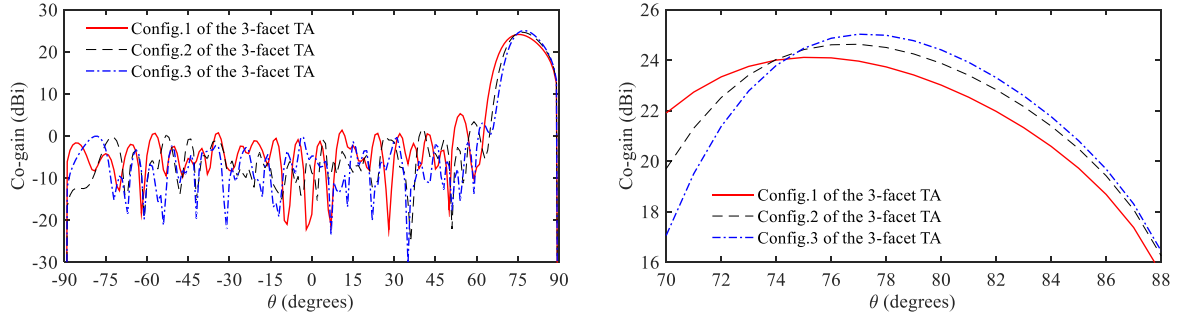


Figure II-16: (a) Radiation patterns of the three configurations of the 3-facet TA when the lateral panels are tilted at $\alpha = 0^\circ$ (i.e. case of a planar array), (b) zoom on the beam for elevation angle θ_0 ranging from 70° to 88° .

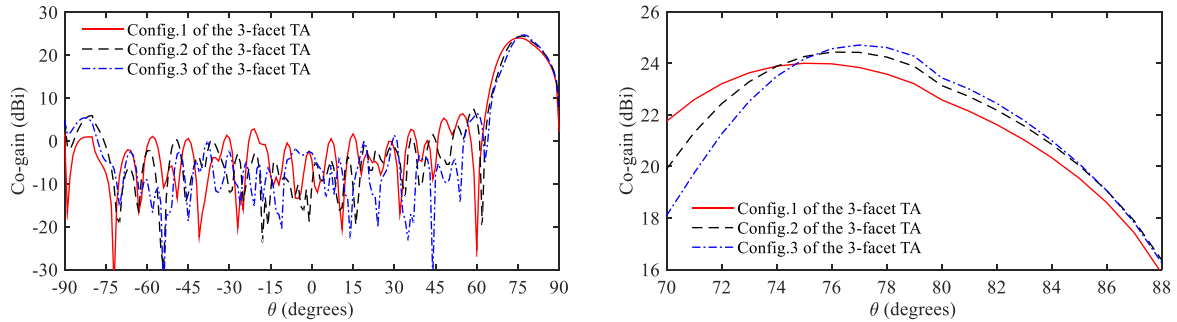


Figure II-17: (a) Radiation patterns of the three configurations of the 3-facet TA when the lateral panels are tilted at $\alpha = 10^\circ$, (b) zoom on the beam for elevation angle θ_0 ranging from 70° to 88° .

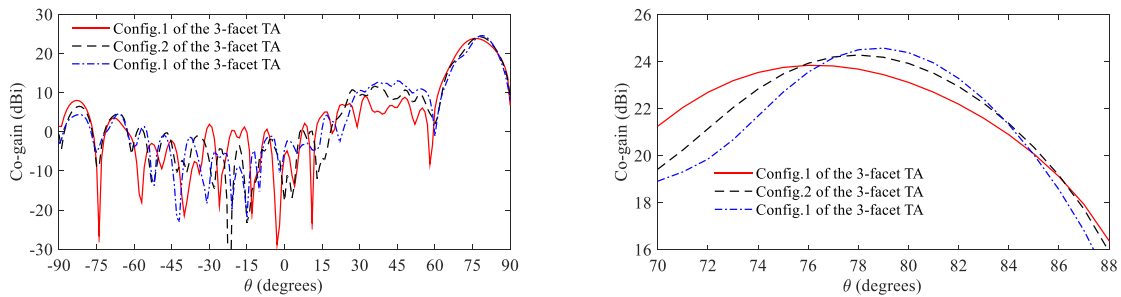


Figure II-18: (a) Radiation patterns of the three configurations of the 3-facet TA when the lateral panels are tilted at $\alpha = 30^\circ$, (b) zoom on the beam for elevation angle θ_0 ranging from 70° to 88° .

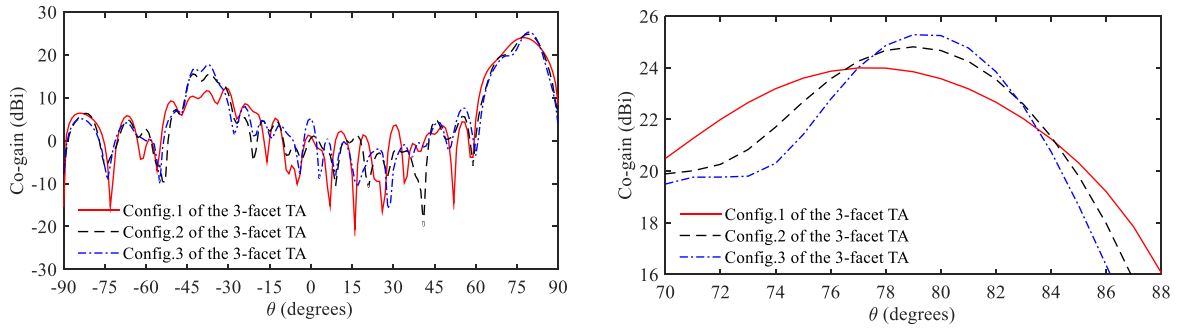


Figure II-19: (a) Radiation patterns of the three configurations of the 3-facet TA when the lateral panels are tilted at $\alpha = 70^\circ$, (b) zoom on the beam for elevation angle θ_0 ranging from 70° to 88° .

The phase distributions for the three configurations (config.1, config.2, config.3) of the 3-facet TA when the beam is steered at $\theta_0 = 80^\circ$ and the lateral panels are tilted at $\alpha = 70^\circ$ are shown in Figure II-20, Figure II-21, and Figure II-22, respectively. It is interesting to note a clear discontinuity between the phase distributions on the left panel and the other two panels. Hence, the left panel is oriented at the opposite of the main beam direction and does not contribute to the main beam. In this case, the phase shift calculation for this panel is irrelevant as performed according to the expressions derived in the current model and this panel may be responsible for the high side lobe observed around -40° in Figure II-19. Further work would probably be necessary to optimize the phase distribution of the panel opposite to the steering direction to minimize the side-lobe levels.

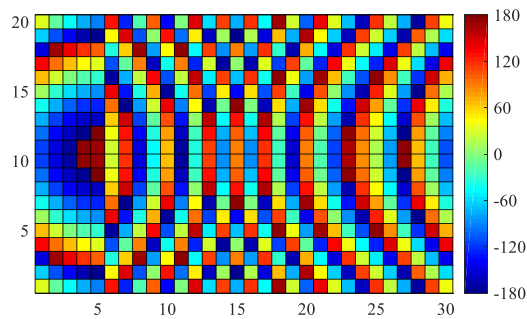


Figure II-20: Phase distribution of the 3-facet TA with $\alpha = 70^\circ$ in the config. 1 (5×20 , 20×20 , 5×20 panels). The beam is steered at $\theta_0 = 80^\circ$.

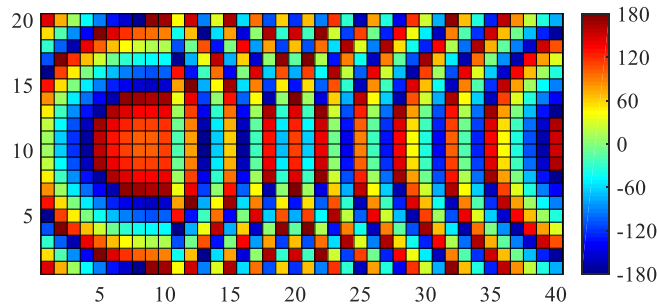


Figure II-21: Phase distribution of the 3-facet TA with $\alpha = 70^\circ$ in the config. 2 (10×20 , 20×20 , 10×20 panels). The beam is steered at $\theta_0 = 80^\circ$.

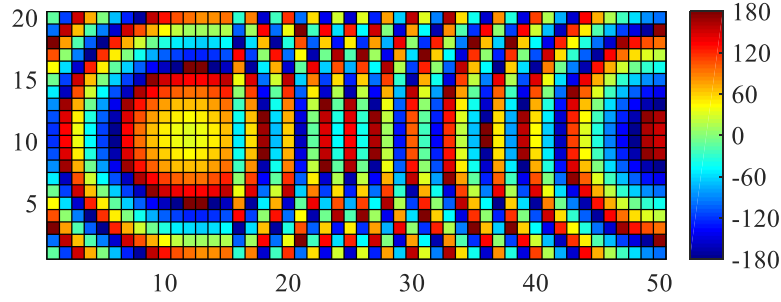


Figure II-22: Phase distribution of the 3-facet TA with $\alpha = 70^\circ$ in the config. 3 (15×20, 20×20, 15×20 panels). The beam is steered at $\theta_0 = 80^\circ$.

Table II-5: Maximum gain of the 3-facet TA as a function of the desired scan angle: config. 1 (30×20 elements).

Desired scan angle (°)	Gain dBi (actual scan angle)			
	Planar	3 facets $\alpha = 10^\circ$	3 facets $\alpha = 30^\circ$	3 facets $\alpha = 70^\circ$
0	30.7 (0°)	30.7 (0°)	30.7 (0°)	30.1 (0°)
10	30.5 (10°)	30.6 (10°)	30.6 (10°)	30.0 (10°)
20	30.3 (20°)	30.4 (20°)	30.4 (20°)	29.5 (20°)
30	30.0 (30°)	30.0 (30°)	30.0 (30°)	29.2 (30°)
40	29.5 (40°)	29.5 (40°)	29.5 (40°)	28.8 (40°)
50	28.7 (50°)	28.7 (50°)	28.6 (50°)	28.2 (50°)
60	27.6 (60°)	27.6 (60°)	27.3 (60°)	27.3 (60°)
70	26.1 (69°)	26.1 (69°)	25.8 (69°)	26.0 (69°)
80	24.1 (75°)	24.0 (75°)	23.8 (76°)	24.0 (77°)
90	22.8 (78°)	22.5 (78°)	21.9 (79°)	21.4 (82°)

Table II-6: Maximum gain of the 3-facet TA as a function of the desired scan angle: config. 2 (40×40 elements).

Desired scan angle (°)	Gain dBi (actual scan angle)			
	Planar	3 facets $\alpha = 10^\circ$	3 facets $\alpha = 30^\circ$	3 facets $\alpha = 70^\circ$
0	31.5 (0°)	31.5 (0°)	31.5 (0°)	30.6 (0°)
10	31.4 (10°)	31.5 (10°)	31.4 (10°)	30.4 (10°)
20	31.2 (20°)	31.3 (20°)	31.2 (20°)	29.7 (20°)
30	30.8 (30°)	30.9 (30°)	30.8 (30°)	29.6 (30°)
40	30.3 (40°)	30.4 (40°)	30.2 (40°)	29.3 (40°)
50	29.6 (50°)	29.6 (50°)	29.3 (50°)	28.7 (50°)
60	28.4 (60°)	28.5 (60°)	27.8 (60°)	27.9 (60°)
70	26.9 (69°)	26.9 (69°)	26.3 (70°)	26.7 (70°)
80	24.6 (77°)	24.4 (77°)	24.3 (78°)	24.8 (80°)
90	23.2 (79°)	22.5 (79°)	21.4 (83°)	20.9 (86°)

Table II-7: Maximum gain of the 3-facet TA as a function of the desired scan angle: config 3 (50×20 elements).

Desired scan angle (°)	Gain dBi (actual scan angle)			
	Planar	3 facets $\alpha = 10^\circ$	3 facets $\alpha = 30^\circ$	3 facets $\alpha = 70^\circ$
0	32.0 (0°)	32.0 (0°)	31.9 (0°)	30.7 (0°)
10	31.9 (10°)	32.0 (10°)	31.8 (10°)	30.6 (10°)
20	31.7 (20°)	31.8 (20°)	31.6 (20°)	29.8 (20°)
30	31.4 (30°)	31.4 (30°)	31.2 (30°)	29.6 (30°)
40	30.9 (40°)	30.9 (40°)	30.6 (40°)	29.4 (40°)
50	30.1 (50°)	30.1 (50°)	29.7 (50°)	28.9 (50°)
60	29.0 (60°)	29.0 (60°)	28.0 (60°)	28.2 (60°)
70	27.4 (69°)	27.3 (69°)	26.6 (70°)	27.1 (70°)
80	25.0 (77°)	24.7 (77°)	24.6 (79°)	25.3 (80°)
90	23.4 (80°)	21.9 (79°)	21.2 (85°)	21.2 (88°)

2.3. Conclusion

The main theoretical analysis on true-time delay phase compensation and faceted transmitarray principles, are addressed in this chapter.

In the section 1, a detailed analysis of phase compensation impacts on TA performance has been presented for an array operating over a 17% frequency band, e.g. corresponding to 27-32 GHz. The principle of TTD and single frequency phase compensation has been described. In particular, we have quantified precisely the performance improvement induced by TTD phase compensation in terms of peak gain, gain bandwidth, and side lobe levels for large size transmitarrays. TTD compensation has been introduced as a solution to avoid both bandwidth and beam-squint limitations. In this case, the phase compensation does not depend on the frequency.

The objective of the section 2 is to present and validate the working principle of a faceted transmitarray. The principle of faceted transmitarrays has been described in detail and implemented in Matlab. The numerical implementation of 3-facet transmitarrays was validated through 3-D electromagnetic simulations. Good agreement has been obtained between the theoretical and simulated results. We showed that for a certain angle of the faceting, the bandwidth and the scanning performance are improved at the cost of a gain reduction.

For different 3-facet transmitarray sizes with a fixed number of unit-cells in the center panel, the beam scanning capability increases when the number of unit-cells in the lateral panels increases. The maximum scanning angles correspond to 82°, 86°, and 88° for the 30×20, 40×20, and 50×20 elements 3-facet TAs, respectively. Radiation patterns show that further work would

be needed on the optimization of the phase distribution to minimize the side-lobe levels and in particular the appearance of a spurious lobe in the case of large scan angles attributed to the radiation of the panel opposite to the desired scanning direction.

Chapter III. Design and optimization of passive unit-cells and fixed-beam transmitarray antennas

Various broadband linearly- and circularly-polarized unit-cells working in Ka-band and also fixed beam transmitarrays that can be used in civil (27 GHz- 30 GHz) or military (30 GHz- 31 GHz) applications are presented in this chapter. The section 3.1 is dedicated to the design, optimization and sensitivity analysis of linearly-polarized unit-cells based on patch antennas. The design and simulation of a fixed beam transmitarray based on these linearly-polarized unit-cells are presented in section 3.2. The performances of circularly-polarized unit-cells and transmitarrays are presented in sections 3.3, and 3.4, respectively. In the last section (section 3.5), single- and quad-beams transmitarrays are demonstrated.

3.1. Linearly-polarized unit-cells

Linearly polarized antennas are useful in numerous communication systems such as wireless backhaul applications in future 5G mobile networks, and satellite communications (SatCom) services in harsh weather conditions (e.g rain, wind) [97], [98].

The aim of this section is to design various broadband unit-cells that could be used in civil or military applications for Earth-to-space communication (UL). All the unit-cells presented in this chapter are based on microstrip patch antennas, which typically consist of a thin metallic conductor bonded to a thin grounded dielectric substrate. Microstrip antennas are generally low profile, relatively small in volume, lightweight, and have low production costs (Printed Circuit Board technologies).

3.1.1. Passive unit-cell based on a simple microstrip patch antenna

The simplest and widely used microstrip patch antenna configuration is the planar one, precisely the rectangular shape. This kind of patch antenna has a number of useful properties, but its fundamental limitation is its narrowband impedance matching. The typical bandwidth of a standard patch antenna is lower than 10% (reflection coefficient lower than -10 dB) when thin substrates are used (e.g. thickness $< 0.07 \lambda_0$ in the case of a dielectric constant around 2.3). The performances of a flat patch antenna are mainly defined by its length L_p , width W_p , and the feed

position. The values of these parameters can be easily predicted using analytical formulations (i.e. cavity model, etc.) according to the expected performances.

Architecture

The proposed passive unit-cell based on simple rectangular patch antennas is presented in Figure III-1(a). The structure is realized in standard PCB technology and is composed of three metal layers. The radiating elements are two identical rectangular patch antennas working in transmit (T_x) and receive (R_x) modes placed on the top and bottom layers of the dielectric structure, respectively. They are connected by a metallized via hole whose diameter is $200\ \mu\text{m}$. The patch antennas are printed on two identical substrates (Rogers RT/Duroid 6002, $\epsilon_r = 2.94$, $\tan\delta = 0.0012$, thickness = $0.508\ \text{mm}$) separated by an $18\text{-}\mu\text{m}$ thick copper ground plane and are bonded by a CuClad 6700 film ($\epsilon_r = 2.35$, $\tan\delta = 0.0025$, thickness = $40\ \mu\text{m}$). The dimensions of the unit-cell and patch are $5\times 5\ \text{mm}^2$ ($\lambda_0/2\times\lambda_0/2$ at $30\ \text{GHz}$) and $2.5\times 2.65\ \text{mm}^2$, respectively.

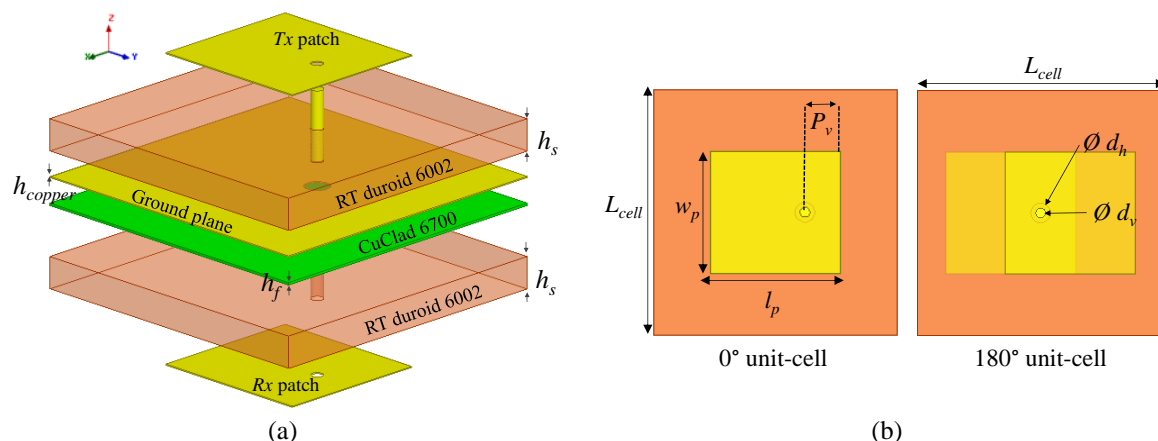


Figure III-1: Proposed simple patch unit-cell with 1-bit phase resolution. (a) 3-D exploded view. (b) Top view.

All geometrical and electrical parameters of this unit-cell are summarized in Table III-1. Two types of unit-cell (namely 0° and 180° unit-cells) are obtained by a 180° physical rotation (1-bit) of the upper patch with respect to the via connection as presented in Figure III-1(b).

Table III-1: Main features of the 1-bit simple patch unit-cell.

Parameters	Values
Unit-cell dimensions	$L_{cell} = 5\ \text{mm}$
Patch sizes	$l_p = 2.65\ \text{mm}$, $w_p = 2.5\ \text{mm}$, $h_{copper} = 0.018\ \text{mm}$
Substrates	Rogers RT/Duroid 6002 ($\epsilon_r = 2.94$, $\tan\delta = 0.0012$, $h_s = 0.508\ \text{mm}$)
Bonding film	CuClad 6700 ($\epsilon_r = 2.35$, $\tan\delta = 0.0025$, $h_f = 40\ \mu\text{m}$)
Via connection	$d_v = 0.2\ \text{mm}$
Ground plane opening	$d_h = 0.4\ \text{mm}$
Via position	$P_v = 0.725\ \text{mm}$

Frequency response

The unit-cell has been simulated using the commercial software Ansys HFSS with periodic boundary conditions and Floquet port excitations under normal incidence. The simulated magnitude of the scattering parameters (S_{11} , S_{21}), the transmission phase of each state, and also the differential phase-shift between both states of the unit-cell are presented in Figure III-2((a), (b),(c), (d)), respectively. Very similar results are obtained for the two states of the unit-cell with a 10-dB return loss bandwidth of 2.8 GHz (28.6- 31.4 GHz). The unit-cells exhibit a low insertion loss ($S_{21} = -0.16$ dB at 30 GHz) and a relative 1-dB transmission bandwidth of 11% at 30 GHz). A 180° phase shift is obtained between the two states of the unit-cell with a maximum error of about 4° .

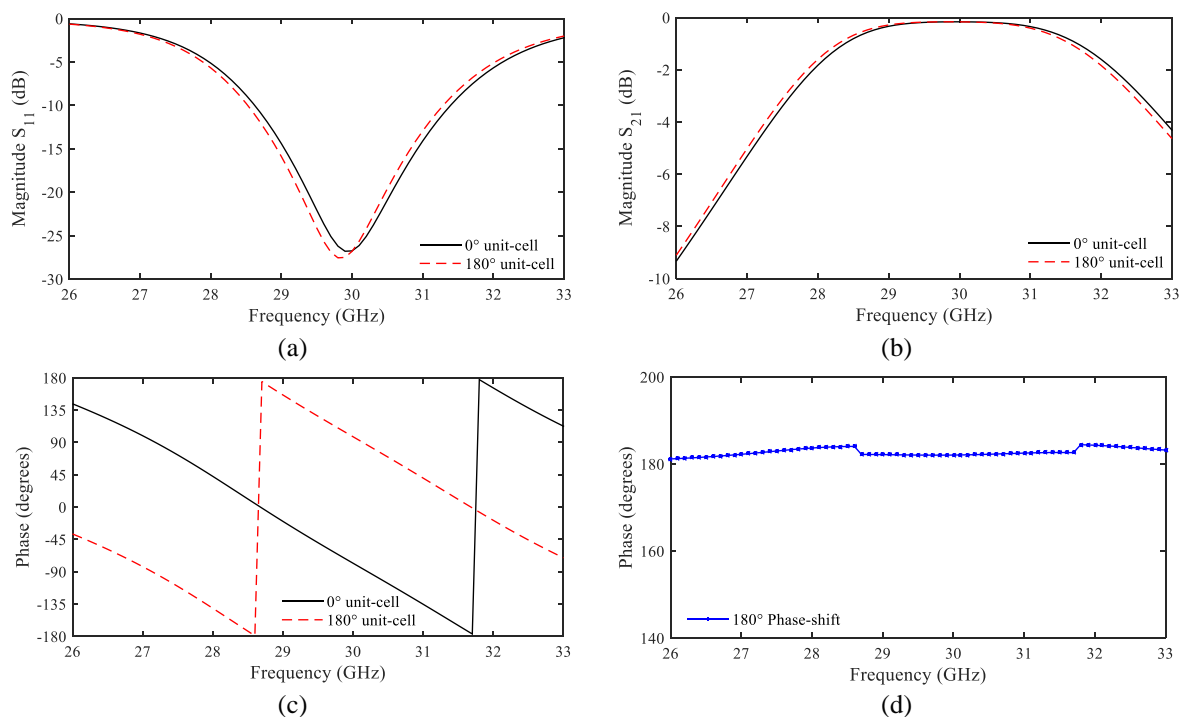


Figure III-2: Simulated results of the simple patch unit-cell. (a) and (b) Magnitude of the reflection S_{11} and transmission S_{21} coefficients. (c) Transmission phase. (d) Differential phase-shift.

Parametric analysis of the scattering parameters

An exhaustive parametric study of the unit-cell based on simple patches has been performed. This analysis is done in order to understand the impact of the main geometrical parameters on the unit-cell behavior in view of the design of more complex unit-cell architectures. This sensitivity analysis is also necessary to analyze the feasibility of the proposed unit-cell using standard PCB technology. Here, the effects of several parameters (the size of the radiated element, the feed position, and the radius of the hole in the ground plane) on the unit-cell performances are analyzed.

Patch dimensions (length and width)

The impact of the patch width (w_p) has been analyzed by changing the nominal value to take account the typical fabrication error ($\pm 30 \mu\text{m}$). As illustrated in Figure III-3(a), a frequency shift of the unit-cell reflection coefficient (S_{11}) by about 100 MHz (0.3%) is observed. The 3-dB transmission bandwidth is similar for the three values of the patch width (2.47, 2.5 and 2.53 mm) and is equal to 5 GHz, this corresponds to a relative transmission bandwidth of 16.7% at 30 GHz (Figure III-3(b)).

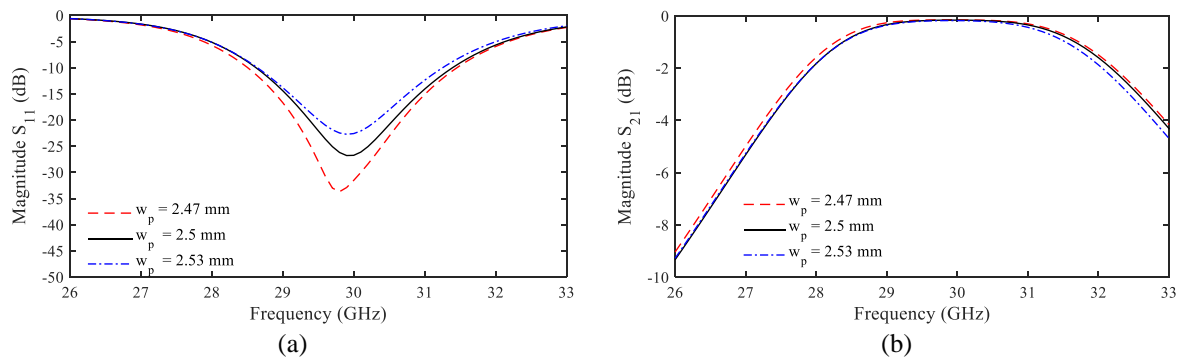


Figure III-3: Impact of typical fabrication errors for the patch width on the S-parameters. (a) Reflection, (b) transmission coefficients.

Figure III-4 shows that a variation of $\pm 30 \mu\text{m}$ of the length (l_p) of both T_x and R_x patches shifts the reflection coefficient by about $\pm 450 \text{ MHz}$ (1.5% at 30 GHz). The -10 dB reflection coefficient bandwidth of the unit-cell is equal to 3, 2.9 and 2.7 GHz for patch length equal to 2.68, 2.65 and 2.62 mm, respectively. The maximum shift on the 3-dB transmission bandwidth is equal to 400 MHz (1.3%).

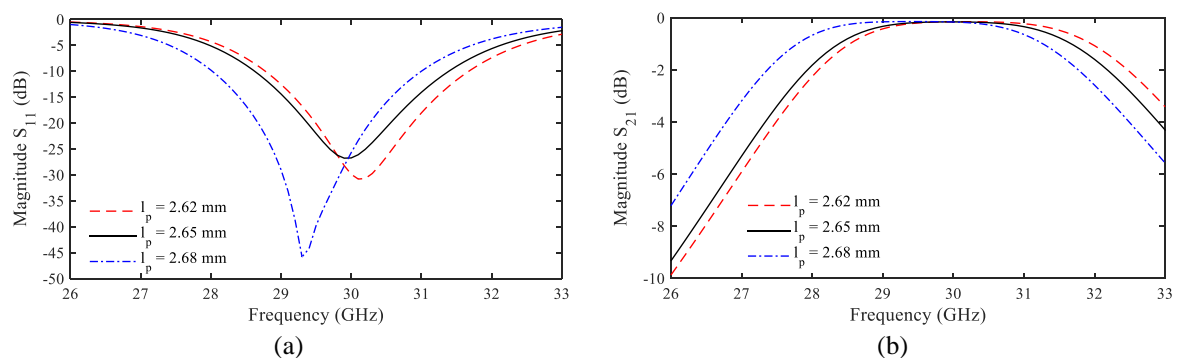


Figure III-4: Impact of typical fabrication errors for the patch length on the S-parameters. (a) Reflection, and (b) transmission coefficients.

Effect of the feed position

The variation of the unit-cell scattering-parameters considering three different feed-point locations on the patch ($P_v = 0.625, 0.725$ and 0.825 mm) are illustrated in Figure III-5. The feed point is selected as a point where the reflection coefficient is the lowest at the

resonance frequency [99]. For the feed located at 0.825 mm, a poor impedance matching (> 10 dB) is observed. The largest bandwidth observed in the case of the feed point at 0.625 mm is due to the double resonance behavior (29 GHz and 31.5 GHz). The relative 3-dB transmission bandwidth is 11%, 16.7% and more than 19% at 30 GHz for the feed point at 0.825, 0.725 and 0.625 mm, respectively.

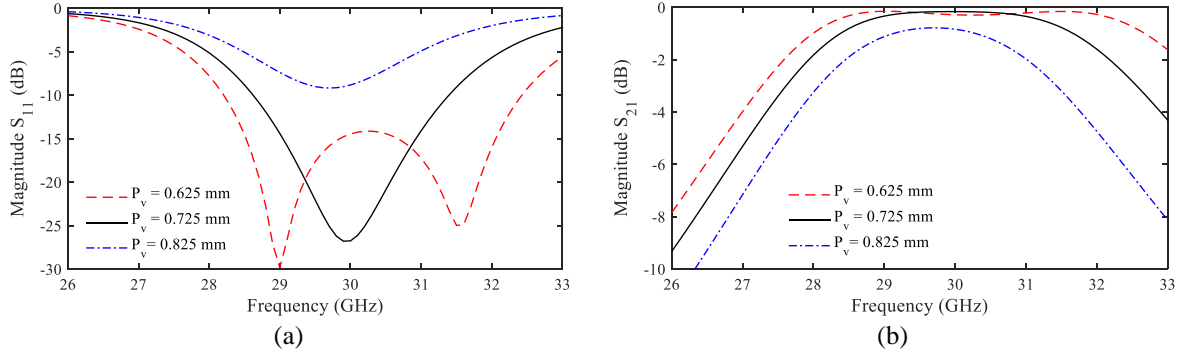


Figure III-5: Impact of the feed location on the S-parameters. (a) Reflection, and (b) transmission coefficients.

Effect of the hole diameter in the ground plane

Figure III-6 exhibits the scattering parameters for three values of the hole diameter ($d_h = 0.2, 0.3$ and 0.4 mm) in the ground plane. The reflection coefficient at the resonance frequency decreases with the hole diameter. The 10-dB return loss bandwidth corresponds to 2.8 GHz, 2.6 GHz and 2.4 GHz for a diameter of the hole equal to 0.4, 0.6 and 0.8 mm, respectively. The 3-dB transmission bandwidth is similar for the three diameter values and spans from 27.8 GHz to 32.5 GHz (this corresponds to a relative bandwidth of 15.7% at 30 GHz).

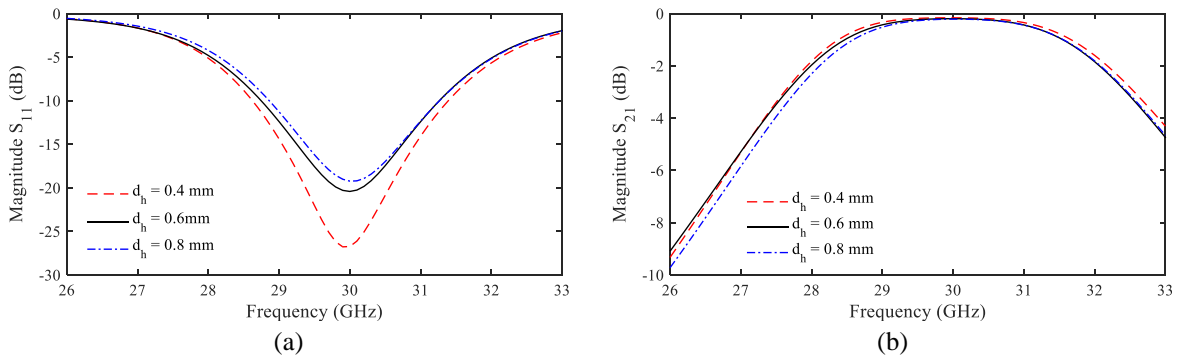


Figure III-6: Impact of the ground-plane hole diameter on the S-parameters. (a) Reflection, and (b) transmission coefficients.

3.1.2. Broadband passive unit-cells with 1-bit of phase resolution

Wideband passive unit-cells in Ka-band for UL communications with at least 13% of relative bandwidth will be presented in this section. They are based on patch antennas which are attractive solutions thanks to their small size, low weight and relatively low fabrication cost.

On the other hand, the drawback of this antenna topology is its narrow bandwidth. So, many researchers have engaged for the last 20 years to propose solutions in order to overcome this limitation. Some of these innovations consist in having several resonant structures into one antenna by adding more patches. Bandwidth enhancement can be also achieved by a specific feed configuration of the patch and impedance matching networks [100]. Increasing the substrate thickness for a larger distance between the patch and the ground plane or decreasing the dielectric constant of the substrate are other techniques to obtain a large bandwidth [101].

The broadband unit-cells with 1-bit of phase resolution presented in the following are obtained by optimization of the patch antenna dimensions and using various shapes of cutting slots in the antenna. However, the substrate and bonding film materials and thicknesses, as well as the size of all unit-cells, are the same as the ones used for the simple patch unit-cell presented in section 3.1.1. As shown for the simple patch, the 180° unit-cell (obtained by a 180° physical rotation of the T_x patch around the via) presents very similar results to the ones of the 0° unit-cell in all topologies.

Unit-cell based on simple patch antenna

Thanks to the parametric analysis performed in section 3.1.1, the dimensions, the feeding position, and the hole diameter in the ground plane of the simple patch unit-cell have been easily modified to obtain a broadband unit-cell. The top view and all main parameters of the unit-cell are shown in Figure III-7(a) and Figure III-7(b), respectively.

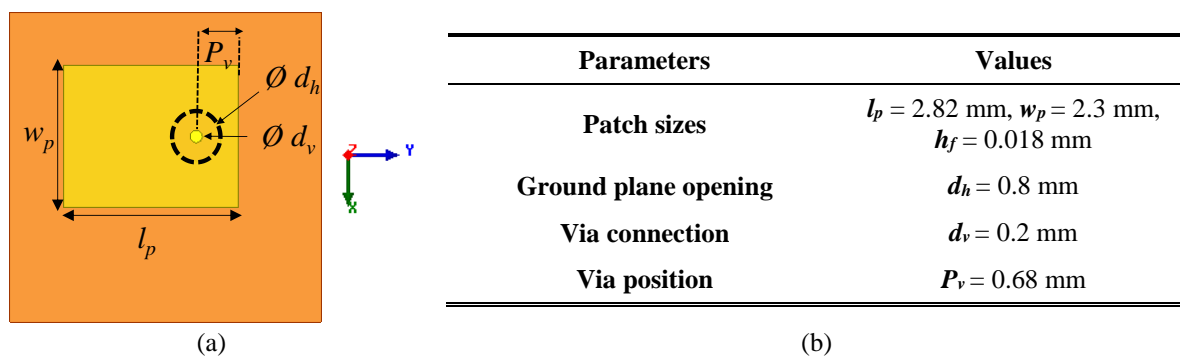


Figure III-7: Broadband unit-cell based on simple patches. (a) Top view. (b) Parameters values.

Figure III-8 indicates that the 10-dB return loss bandwidth is from 27.2 GHz to 31.2 GHz, which corresponds to a relative bandwidth of 13.8% at 29 GHz. The insertion loss at 29 GHz corresponds to 0.3 dB and the relative 1-dB transmission bandwidth is equal 15.2% at 29 GHz. This bandwidth is larger than the one exhibited in the initial patch described in section 3.1.1, that is 11.4% at 29 GHz

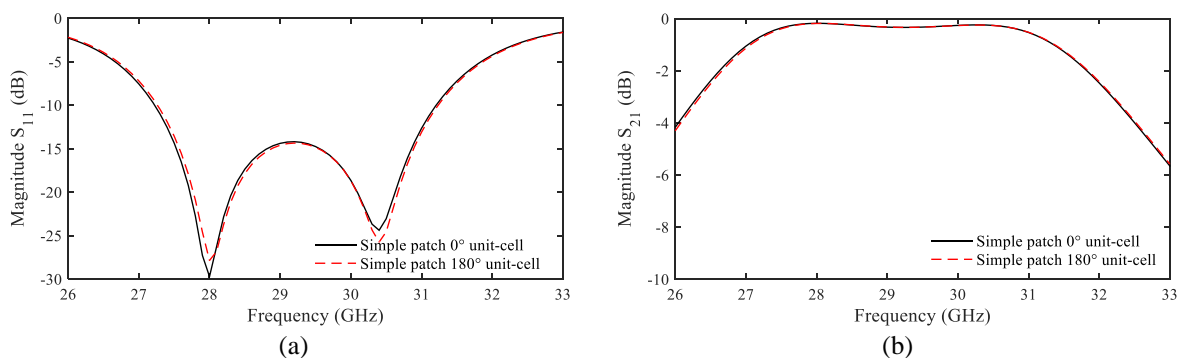


Figure III-8: Simulated S-parameters of the broadband unit-cell based on simple patch antennas. Magnitude of the (a) reflection S_{11} and (b) transmission S_{21} coefficients.

Unit-cell based on U-shaped slot loaded patch antennas

In addition to modifying the dimensions, the Tx and Rx patch antennas are also loaded by a U-shape slot to obtain another broadband unit-cell structure named U-shaped slot unit-cell as shown in Figure III-9(a). The main design parameters are summarized in Figure III-9(b). The 10-dB return loss bandwidth spans from 27.8 GHz to 31.6 GHz, and the insertion loss at 29 GHz is equal to 0.3 dB with a relative transmission 1-dB bandwidth of 14.1% at 29 GHz as illustrated in Figure III-10 (a) and Figure III-10(b).

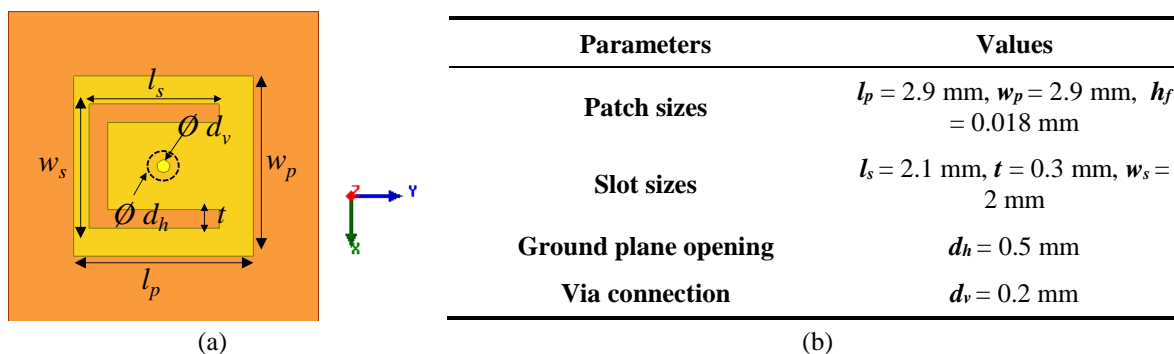


Figure III-9: (a) Top view and (b) main features of the proposed U-shaped slot unit-cell.

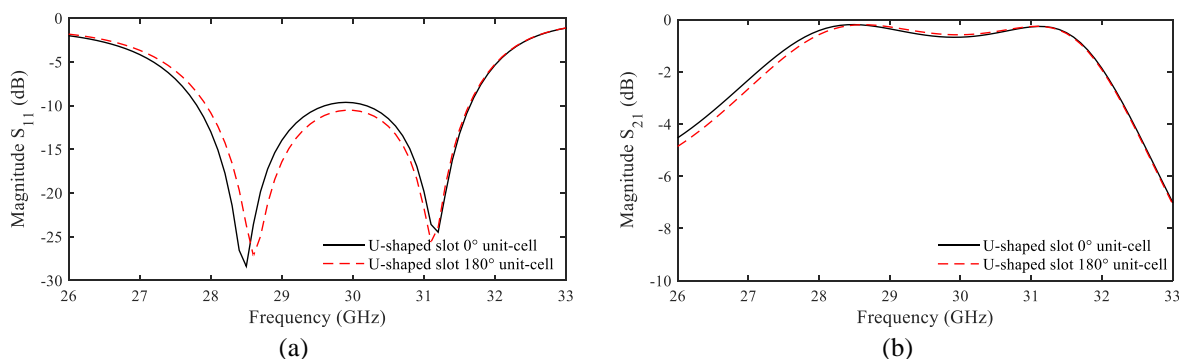


Figure III-10: Simulated S-parameters of the U-shaped slot unit-cell. Magnitude of the (a) reflection S_{11} and (b) transmission S_{21} coefficients.

Unit-cell based on O-shaped slot loaded patch antennas

The O-slot unit-cell consists of two rectangular patches loaded by an O-shaped slot and connected by a centered metallized via. The unit-cell top view and its dimensions are indicated in Figure III-11(a) and Figure III-11(b), respectively. The 3-D simulated results have demonstrated that the unit-cell has an insertion loss of 0.9 dB at 29 GHz, and a relative 1-dB transmission bandwidth of 7% at 29 GHz as shown in Figure III-12.

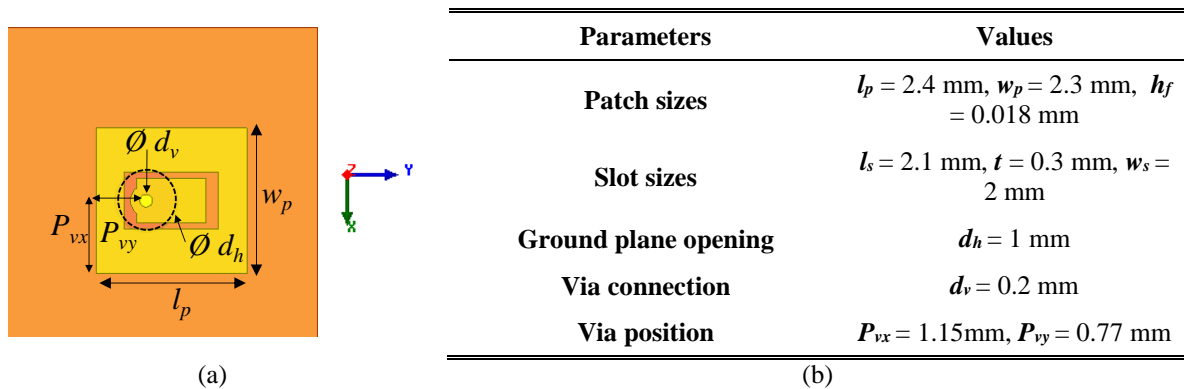


Figure III-11: (a) Top view and (b) main features of the proposed O-shaped slot unit-cell.

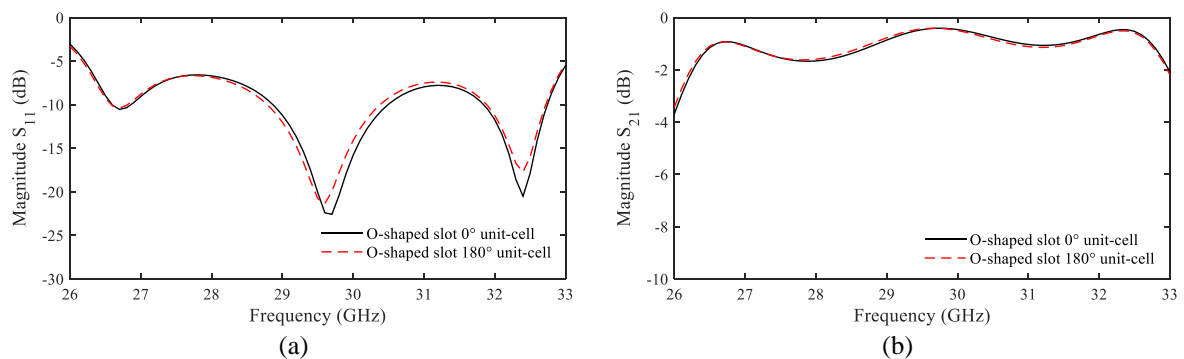


Figure III-12: Simulated S-parameters of the O-shaped slot unit-cell. Magnitude of the (a) reflection S_{11} and (b) transmission S_{21} coefficients.

Unit-cell based on capacitively-coupled patch antennas

The last broadband unit-cell is inspired from the technique of bandwidth enhancement by capacitive feed coupling. In this case, a small feed patch is placed very close to the transmission radiating patch antenna. In this way, a better impedance matching and desired frequency bandwidth is obtained. The top view of the unit-cell and its main features are shown in Figure III-13. This topology of patch antenna exhibits a 10-dB return loss bandwidth between 27 GHz and 30.9 GHz, with an insertion loss equal to 0.6 dB at 29 GHz and a relative 1-dB transmission bandwidth of 15.2% as indicated in Figure III-14.

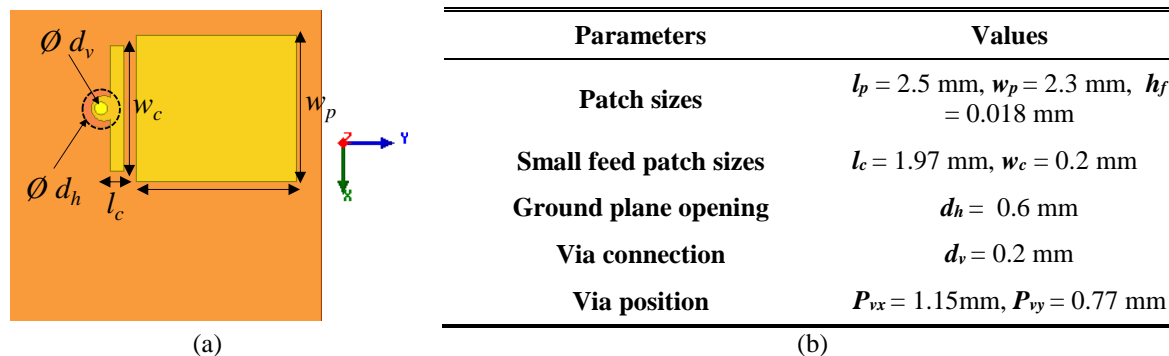


Figure III-13: a) Top view and (b) main features of the proposed capacitively-coupled unit-cell

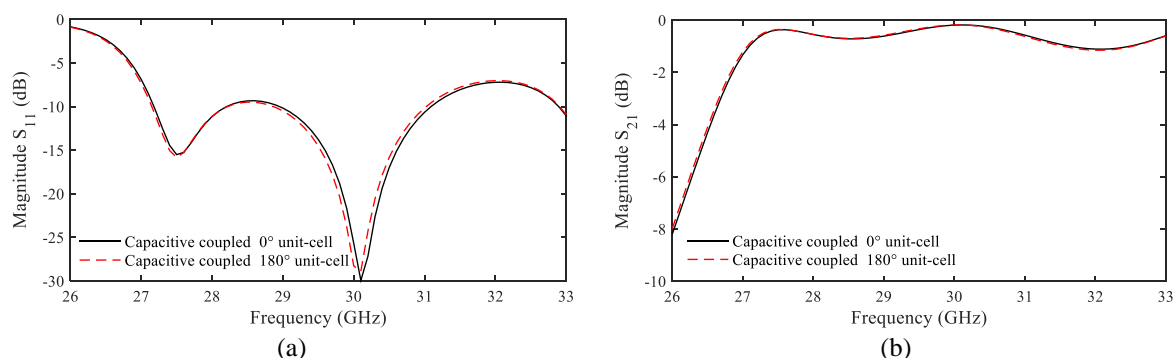


Figure III-14: Simulated S-parameters of the capacitively-coupled unit-cell. Magnitude of the (a) reflection S_{11} and (b) transmission S_{21} coefficients.

3.1.3. Broadband passive unit-cells with 3-bit of phase resolution

As it is well known, the phase-shift range and resolution affect the transmitarray performances. In theory, a 360° phase-shift range is desirable to achieve a high aperture efficiency and low side-lobe levels. The magnitude of the side-lobe levels decreases when the number of phase states increases. In practice, a limited number of phase states could be used to achieve a relatively simple and cheap unit-cell architecture, and to obtain a relatively broadband behavior.

In this section, 3-bit phase quantization using the four types of 1-bit broadband unit-cells presented before (section 3.1.2) will be demonstrated. This provides eight possible phase states starting from 0° to 315° with 45° steps. The four broadband unit-cells, simple patch, U-shaped slot, O-shaped slot, and capacitively-coupled unit-cells presented previously, are used as the 0° , 45° , 90° and 135° phase states. By turning the transmission patch (T_x) of each unit-cell by 180° with respect to the via connection, the 180° , 225° , 270° and 315° unit-cells are obtained. Each unit-cell and its corresponding 180° counterpart are summarized in Figure III-15.

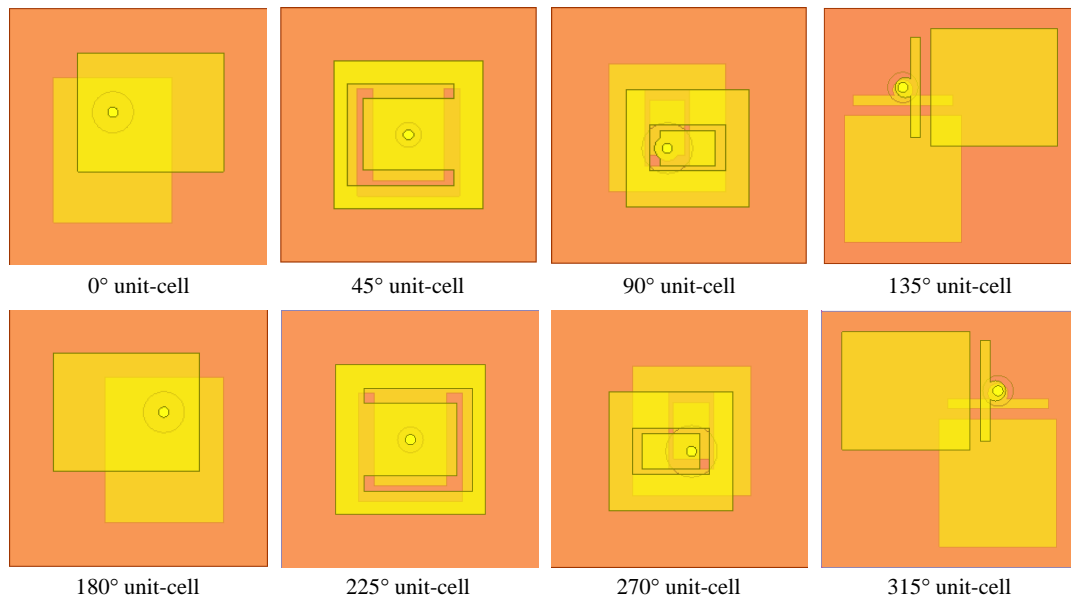


Figure III-15: Scheme of the eight unit-cells with 3 bits of phase quantization (top view).

The simulated magnitude of the reflection and transmission coefficients (S_{11} and S_{21}) of all unit-cells performed with the commercial Ansys HFSS software with periodic boundary conditions and Floquet port excitation under normal incidence are shown in Figure III-16(a), and Figure III-16(b), respectively.

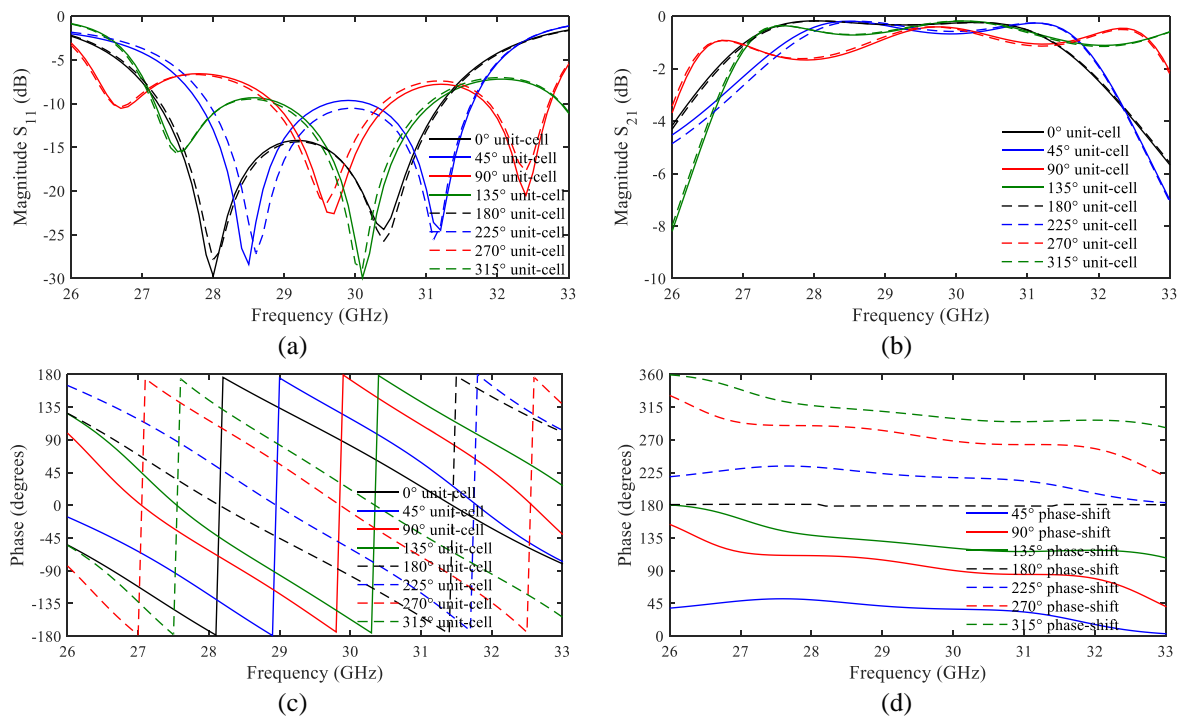


Figure III-16: S-parameters of the 0° , 45° , 90° , 135° , 180° , 225° , 270° and 315° unit-cells. Magnitude of the (a) reflection S_{11} , and (b) transmission S_{21} coefficients. (c) Transmission phase. (d) Phase-shift between the 0° unit-cell and the other states.

The relative 1-dB transmission bandwidth of the unit-cell based on simple patch (0° and 180° unit-cells), O-shaped slot patch (45° and 225° unit-cells), U-shaped slot patch (90° and 270° unit-cells), and capacitively-coupled patch (135 and 315° unit-cells) corresponds to 15.2%, 14.1%, 7% and 15.2% at 29 GHz, respectively, with an insertion loss lower than 0.86 dB. Their transmission phases and the differential phase-shift between the 0° unit-cell and the others are illustrated in Figure III-16(c), and Figure III-16(d), respectively. This differential phase-shift at 29 GHz between the 0° and the others unit-cells is equal to 41°, 104°, 130°, 179°, 224°, 282°, and 309° for the 0°, 45°, 90°, 180°, 225°, 270°, and 315° unit-cells, respectively.

3.2. Fixed-beam linearly-polarized transmitarray with 3 bits of phase resolution

A 400-element transmitarray has been designed using the 3-bit unit-cells proposed in section 3.1.3. These unit-cells present a good impedance matching, low insertion loss, and quasi-linear phase response in the band of interest (27 GHz -31 GHz) for SatCom Uplink applications. The TA has been optimized at 29 GHz using the *ad-hoc* simulation tool validated in the CEA previous works [39]-[41]. This code uses a hybrid technique of simulation which includes full-wave simulations and analytical formulations. The array is illuminated by a standard horn with a 10-dBi gain. The optimal focal distance ($F = 75$ mm, which corresponds to a focal ratio of $F/D = 0.75$) and phase distribution have been calculated in order to maximize the aperture efficiency. The frequency response of the transmitarray (gain at broadside as a function of frequency) performed with the *ad-hoc* simulation tool (named theoretical simulation), and compared to that obtained using Ansys HFSS (named full-wave simulation) are shown in Figure III-17. The theoretical and full-wave radiation patterns (co-, and cross polarizations) in E-, and H-planes at 29 GHz are shown in Figure III-18 and Figure III-19, respectively. The broadside gain at the frequency of optimization (29 GHz) is 27.4 dBi with an aperture efficiency of 47%. The 1-dB gain bandwidth is between 28.5 GHz and 31.8 GHz, which corresponds to a relative bandwidth of 11.4% at 29 GHz. The performance of the proposed TA is summarized in Table III-2. A good agreement is obtained between the theoretical and simulated results.

Table III-2: Performance of the proposed linearly-polarized transmitarray at 29 GHz.

Directivity (dBi)	Gain (dBi)	Side lobe level (SLL) (dB)	Aperture efficiency (%)	1-dB gain bandwidth (%)
29.7	27.4	21.4	47	11.4

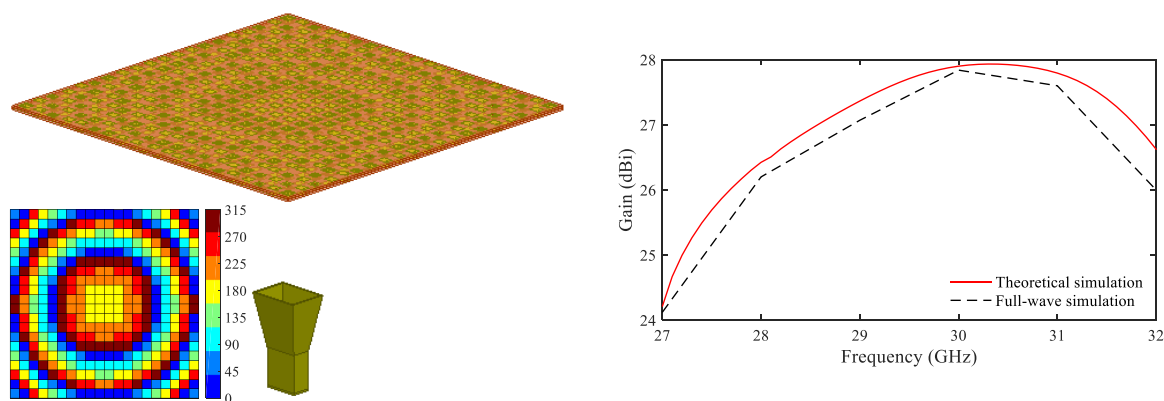


Figure III-17: 20×20-element transmitarray with 3 bits of phase quantization. (a) Schematic view and phase distribution. (b) Gain as a function of frequency.

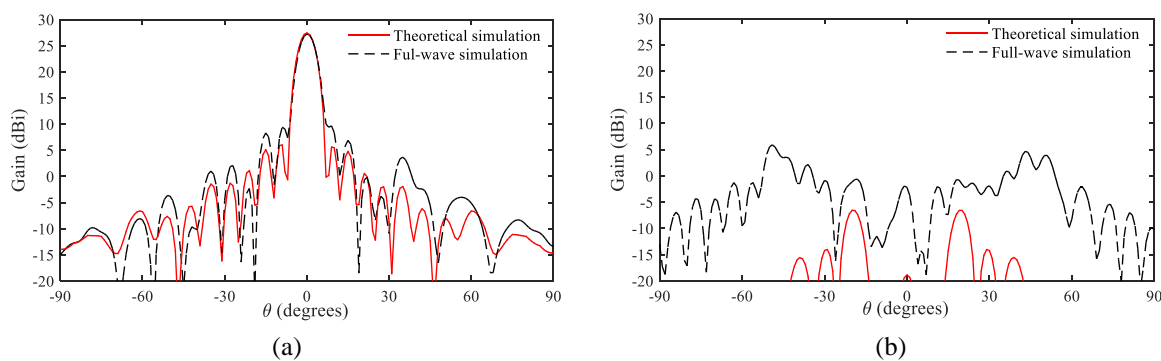


Figure III-18: Theoretical and full-wave simulated radiation patterns at 29 GHz in E-plane: (a) co-, (b) cross-polarizations.

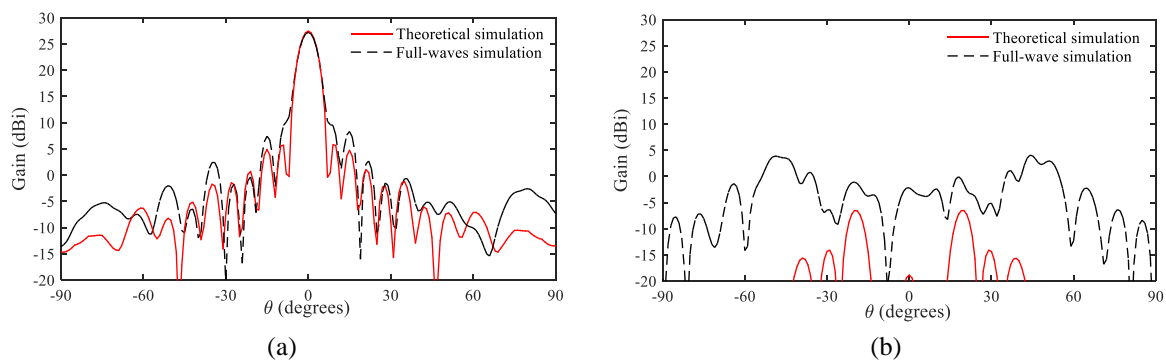


Figure III-19: Theoretical and full-wave simulated radiation patterns at 29 GHz in H-plane: (a) Co-, (b) Cross-polarizations.

3.3. Circularly-polarized unit-cells

The aim of this section is to demonstrate the performances of 3-bit circularly-polarized unit-cells for a fixed-beam transmitarray in Ka-band. Previously, we have presented wideband linearly-polarized unit-cells that are useful for SatCom systems and also for 5G backhaul links. However, circularly-polarized antennas are preferred for many millimeter-wave applications

such as indoor communication systems, outdoor broadcast fixed links, and outdoor mobile platforms [102]. Linearly-polarized antennas need a strict polarization alignment between the transmitter and the receiver whereas communications with arbitrary polarization orientation for the transmitter and receiver are possible with circularly-polarized antennas [103]. Furthermore, circularly-polarized antennas have the ability to ensure robust communication in urban environment where polarization losses due to buildings walls or ground surface are reduced.

3.3.1. Unit-cell architecture

The unit-cell consists of three metal layers printed on two identical substrates (Rogers RT duroid 6002) bonded with an Arlon CuClad 6700 film. A square patch ($l_c \times l_c \text{ mm}^2$) with a pair of opposite truncated corners is printed on the transmitting layer and a linearly-polarized rectangular patch ($w_l \times l_l \text{ mm}^2$) is printed on the receiving layer. The two patches loaded by a U-slot are connected by a metallized via hole (diameter d_v) located at their center. This structure is chosen to avoid the S-parameters variations when the patch is rotated to obtain the desired phase shift and achieve a larger bandwidth. The transmitting layer of the proposed unit-cell ensures the phase shift and the polarization transformation at the same time.

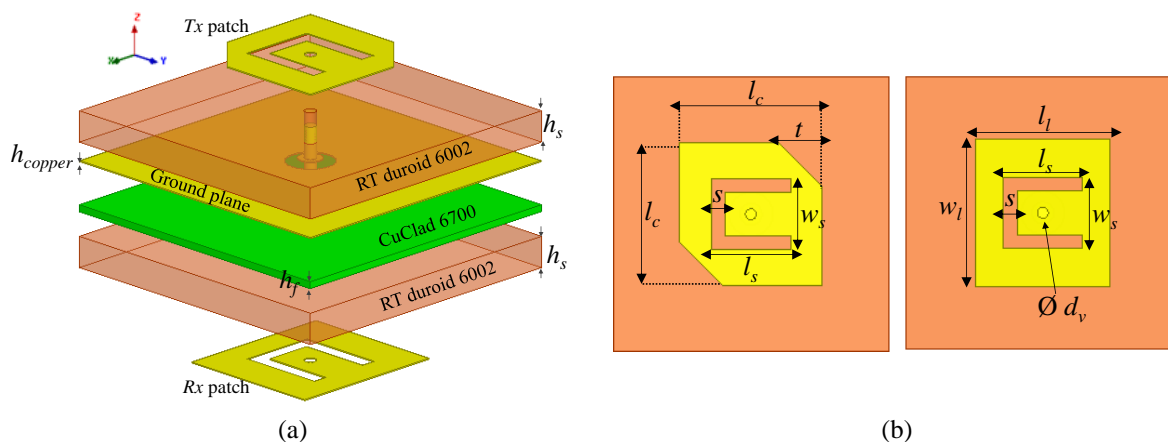


Figure III-20: Proposed 3-bit circularly-polarized unit-cell. (a) 3-D exploded view. (b) Transmitting and receiving layers.

The unit-cell size is $5 \times 5 \text{ mm}^2$ ($\lambda_0/2 \times \lambda_0/2$ at 30 GHz where λ_0 is the wavelength in free space at this frequency). The architecture of the unit-cell is shown in Figure III-20, and its dimensions are provided in Table III-3.

Table III-3: Geometrical dimensions of the proposed unit-cell.

Parameters	Values
Transmitting patch sizes	$l_c = 2.6$ mm, $t = 0.8$ mm, $s = 0.25$ mm, $l_s = 1.45$ mm, $w_s = 1.3$ mm
Receiving patch sizes	$l_l = 2.45$ mm, $w_l = 2.7$ mm, $h_{copper} = 0.018$ mm
Substrates	Rogers RT/Duroid 6002 ($\epsilon_r = 2.94$, $\tan\delta = 0.0012$, $h_s = 0.508$ mm)
Bonding film	CuClad 6700 ($\epsilon_r = 2.35$, $\tan\delta = 0.0025$, $h_f = 114$ μ m)
Via connection	$d_v = 0.2$ mm
Ground plane opening	$d_h = 0.8$ mm

The eight phase states required for the 3-bit unit-cells (0° , 45° , 90° , 135° , 180° , 225° , 270° , and 315°) have been obtained by rotating the transmitting layer with 45° steps.

3.3.2. Full-wave simulation of the proposed 3-bit unit-cell

The proposed unit-cell has been simulated using the commercial software Ansys HFSS with periodic boundary conditions and Floquet port excitations. The scattering parameters (left- or right-handed circular polarization, LHCP or RHCP) are calculated by combining the two orthogonal modes (TE (Transverse- Electric) and TM (Transverse-Magnetic)) excited by the Floquet ports in the structure.

The magnitude of the reflection coefficients referred to receiving (Floquet port 1) and transmitting layers, named S_{11} , and S_{22} , are plotted in Figure III-22(a) and Figure III-22(b), respectively. The return loss remains lower than -10 dB between 27 and 32 GHz for both receiving (S_{11}) and transmitting (S_{22}) sides, which corresponds to a 17.2% fractional bandwidth around 29 GHz. The transmission coefficient corresponding to the Left-Handed Circular Polarization (LHCP) at transmitting layer is depicted in Figure III-22(c). The 3-dB transmission bandwidth is greater or equal to 15.9% around 29 GHz for all unit-cell states.

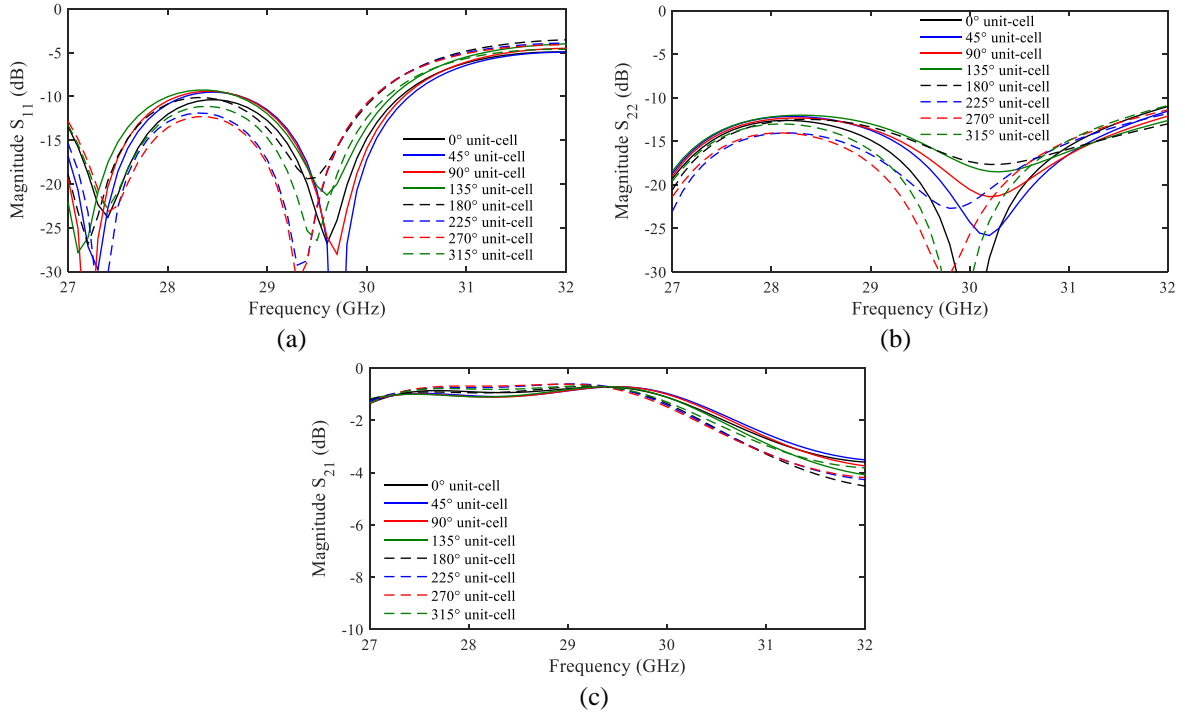


Figure III-21: S-parameters of 3-bit circularly-polarized unit-cells. Magnitude of the (a) reflection coefficients referred to the (a) receiving (S_{11}) and (b) transmitting (S_{22}) layers. (c) Transmission coefficient S_{21} .

The transmission phase of all unit-cells and the phase-shift between the 0° unit-cell and the other states are presented in Figure III-22(a) and Figure III-22(b), respectively. The differential phase-shift at 29 GHz between the 0° and the other unit-cells corresponds to 47° , 89° , 134° , 183° , 220° , 265° , and 312° for the 0° , 45° , 90° , 180° , 225° , 270° , and 315° unit-cells, respectively.

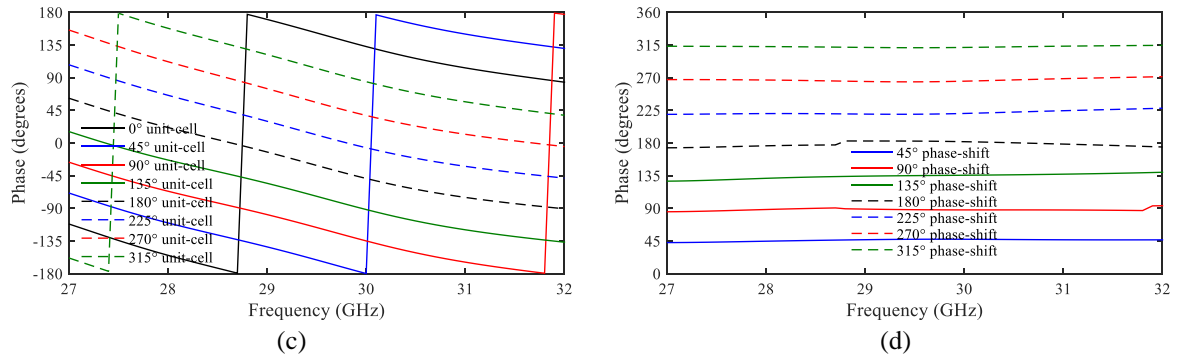


Figure III-22: (a) Transmission phase and (b) phase-shift between the 0° unit-cell and the other states.

3.4. Fixed-beam circularly-polarized transmitarrays with 3 bits of phase resolution

This section is organized as follows. Firstly, a 400-element circularly-polarized transmitarray optimized using the *ad-hoc* simulation tool and validated by full-wave simulation is presented. Next, the impact of phase quantization on the performance of a 40×40 -element

array is demonstrated and compared to the mask defined by the European Telecommunication Standardization Institution (ETSI). Finally, a quad-beam transmitarray with 3-bit of phase quantization is presented. All the transmitarrays presented in this section are based on the CP unit-cell proposed in the previous section 3.3.

3.4.1. Simulation of the 400-element transmitarray

The performances of a 400-element transmitarray, illuminated by a standard horn with a nominal gain of 10 dBi, is presented. The TA has been optimized using the ad-hoc simulation tool as in the case of the linearly-polarized transmitarray (section 3.2). The optimal focal distance ($F = 67$ mm) and the phase distribution have been calculated at 29 GHz in order to maximize the aperture efficiency of the TA. This corresponds to a focal ratio (F/D) equal to 0.67 where D is the dimension of the array (100 mm). The theoretical results of the TA are compared to those obtained using Ansys HFSS. The latter is done using the FE-BI solver to reduce the computation time. The gain and axial ratio (AR) responses calculated as a function of frequency considering a broadside beam are plotted in Figure III-23(a) and Figure III-23(b), respectively. The 1-dB gain bandwidth is equal to 14.8% at 29 GHz and the AR is lower than 1 dB in the frequency band 27-32 GHz. The numerical results obtained using the *ad-hoc* simulation tool are in a good agreement with the EM simulation. A maximum difference around 1 dB is obtained at 31 GHz.

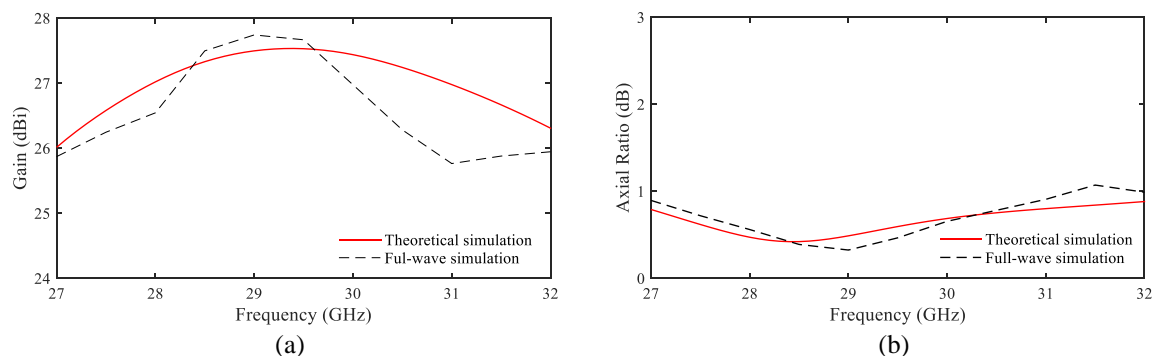


Figure III-23: Theoretical and simulated frequency responses of the 20×20-element circularly-polarized transmitarray: (a) broadside gain, and (b) axial ratio.

Figure III-24 and Figure III-25 show broadside radiation patterns (LHCP and RHCP) calculated and simulated in 0° and 90° planes at 29 GHz, respectively.

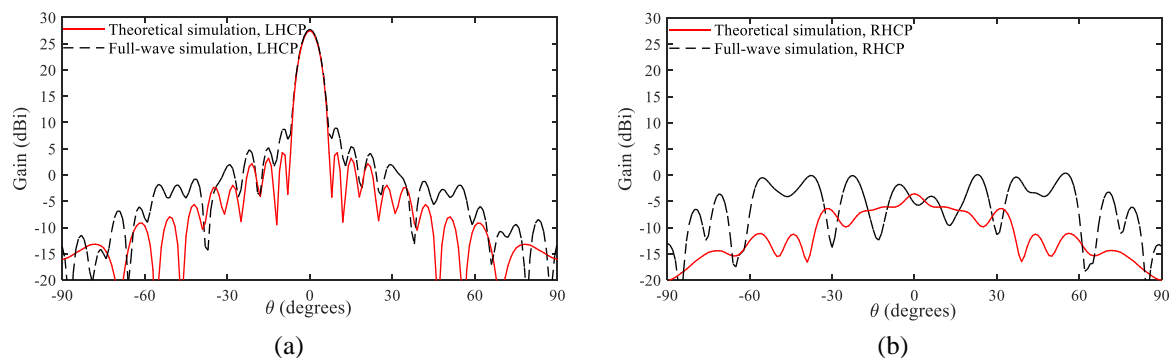


Figure III-24: 20×20-element circularly-polarized transmitarray: LHCP and RHCP radiation patterns in the 0° plane.

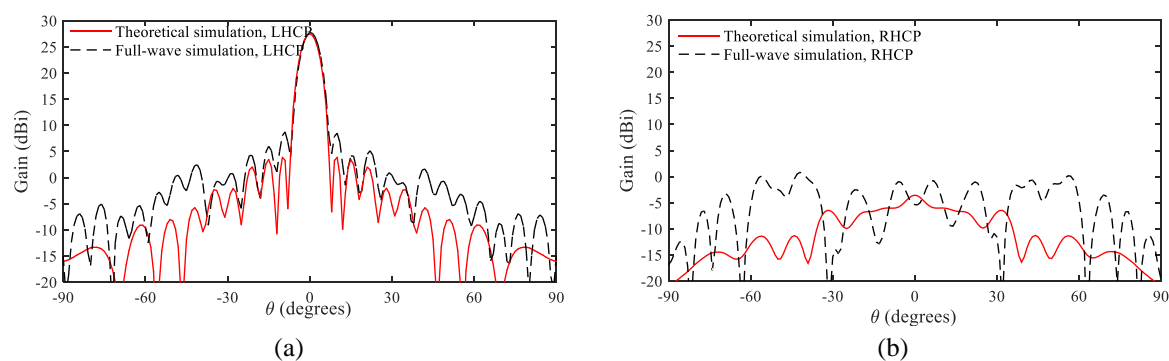


Figure III-25: 20×20-element circularly-polarized transmitarray: LHCP and RHCP radiation patterns in the 90° plane.

A good agreement is obtained between Ansys HFSS and the in-house simulation tool as in the case of the linearly-polarized TA. The maximum simulated LHCP gain is equal to 27.5 dBi, the RHCP gain is lower than 1 dBi, and the aperture efficiency is 47.8%. The error between the theoretical and simulated maximum LHCP gain is less than 0.3 dB.

3.4.2. Impact of phase quantization on the circularly-polarized transmitarray

In this section, the impact of phase quantization on TA performances is simulated. As it is well known, a perfect phase-shift resolution is desirable to achieve a high aperture efficiency and low side-lobe levels (SLLs). However, for reasons of relative simple architecture and prototyping cost of the transmitarray, a limited number of phase quantization states is implemented. A 40×40-element TA based on the 3-bit circularly-polarized unit-cell presented in section 3.3 has been used for a broadside radiation to analyze the impact of 1-, 2-, 3-bit of phase quantization with the ad-hoc simulation tool. The focal distance F is fixed to $0.67 \times D$ ($D = 200$ mm is the size of the array side). The phase distributions and frequency responses (gain and axial ratio) of the 1-, 2-, 3-bit TA are presented in Figure III-26 and Figure III-27,

respectively. All the results performed with the *ad-hoc* simulation tool are synthesized in Table III-4. From this table, it is possible to observe that the phase quantization has an impact on the directivity and also the SLL of the TA. As expected, the aperture efficiency increases when the phase quantization level is higher. For the considered array, the aperture efficiency using 1-, 2-, 3-bit phase quantization is equal to 22.1%, 40.2%, and 47.5%, respectively.

Table III-4: Effect of phase quantization on the 1600-element circularly-polarized transmitarray.

Phase compensation	1-bit	2-bit	3-bit
Dir. (LHCP) (dBi)	32.0	34.6	35.3
Gain (LHCP) (dBi)	30.2	32.8	33.5
Aperture efficiency (%)	22.1	40.2	47.5
Side-lobe level (dB)	21.8	23.5	24.0

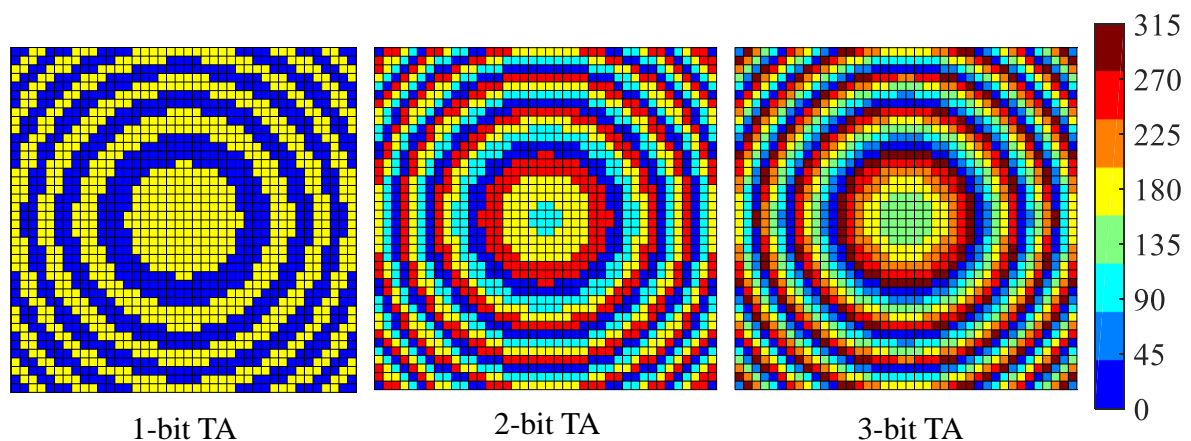


Figure III-26: Phase distribution of the 1-, 2-, and 3-bit transmitarray for a broadside beam.

The radiation patterns (co- and cross-polarization components) computed in the 0° plane of the 3-bit TA with 1-, 2-, and 3-bit of phase quantization are compared to the radiation masks defined by ETSI for point-to-point applications in the frequency range 24-47 GHz [18] (see Figure III-28(a) and Figure III-28(b)). It was concluded that the 1-bit TA exhibits a high cross-polarization level that reaches 18.4 dB and obviously bad axial ratio (much higher than 3 dB). The 2- or 3-bit phase quantization are good with respect to the ETSI recommendations in terms of radiation masks.

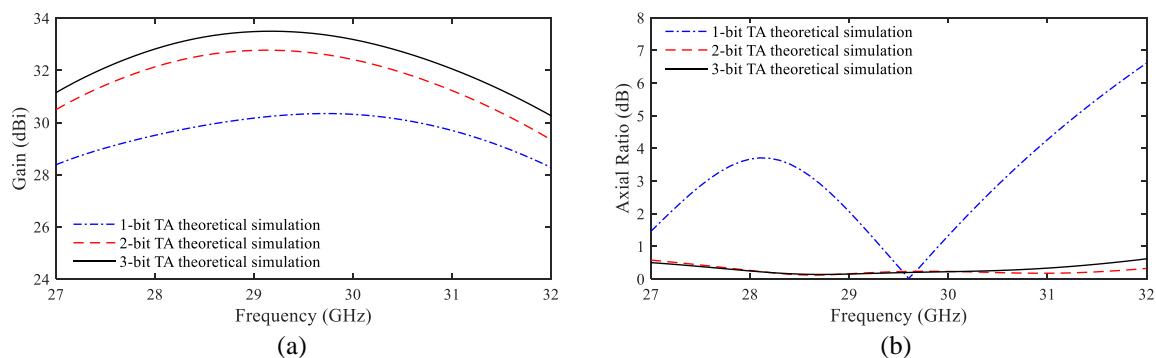


Figure III-27: (a) Theoretical broadside gain, (b) and axial ratio as a function of frequency for the 3 transmitarrays.

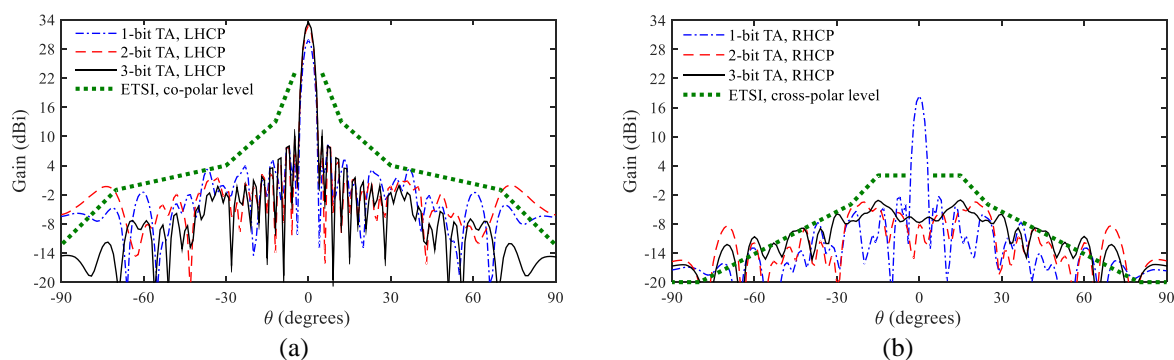


Figure III-28: Comparison between the (a) co-, and (b) cross polarization radiation patterns of the 1-, 2-, 3-bit transmitarray and the ETSI masks.

According to the theoretical results, the 3-bit circularly-polarized transmitarray is demonstrated to be a good candidate for point-to-point applications at Ka-band. A full-wave simulation using HFSS is performed in order to confirm this conclusion. As shown in Figure III-29 and Figure III-30, a good agreement is demonstrated between the theoretical and full-wave results with a difference of 0.5 dB only between the two maximum LHCP gains.

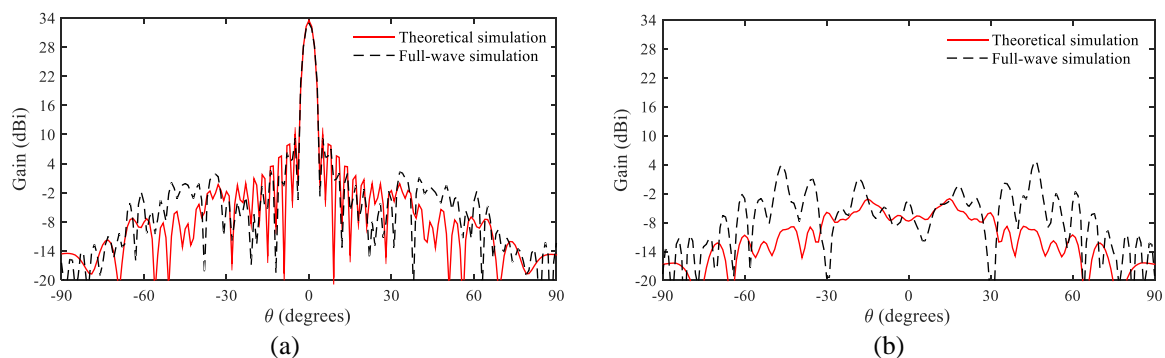


Figure III-29: Theoretical and simulated radiation patterns in the 0° plane at 29 GHz: (a) LHCP, (b) RHCP.

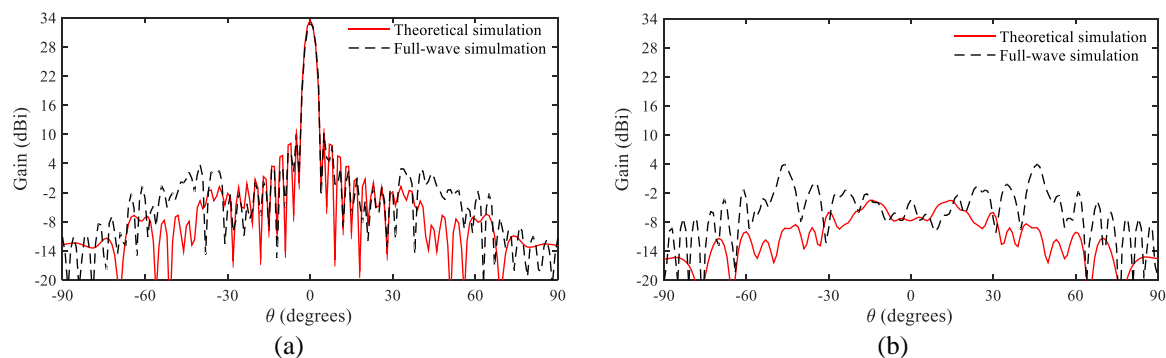


Figure III-30: Theoretical and simulated radiation patterns in the 90° plane at 29 GHz: (a) LHCP, (b) RHCP.

3.4.3. Fixed quad-beam transmitarray with 3 bits of phase quantization

Multi-beam antennas have drawn attention of researchers, as in [104]-[107], because they are useful in applications such as automotive radars and mm-wave 5G backhauling systems. They are also employed in satellite systems for broadcast services over a geographical region of interest.

In this section, a 489-element circular quad-beam transmitarray (with a diameter D of 125 mm) based on the 3-bit circularly-polarized unit-cell described in section 3.3 is optimized at 29 GHz using the genetic algorithm code coupled to CEA *ad-hoc* simulation tool developed by K. Pham from IETR as a part of Transmil project. More details about this code can be found in [108]. The array is designed to radiate four beams at $\theta = \pm 25^\circ$ in the horizontal and vertical planes at the frequency of optimization. The transmitarray is illuminated by a 10-dBi gain linearly-polarized horn placed at $F = 80$ mm. The theoretical code is validated by full-wave simulations performed with the software Ansys HFSS. The 3-D scheme for full-wave simulation and the phase distribution of the TA are presented in Figure III-31.

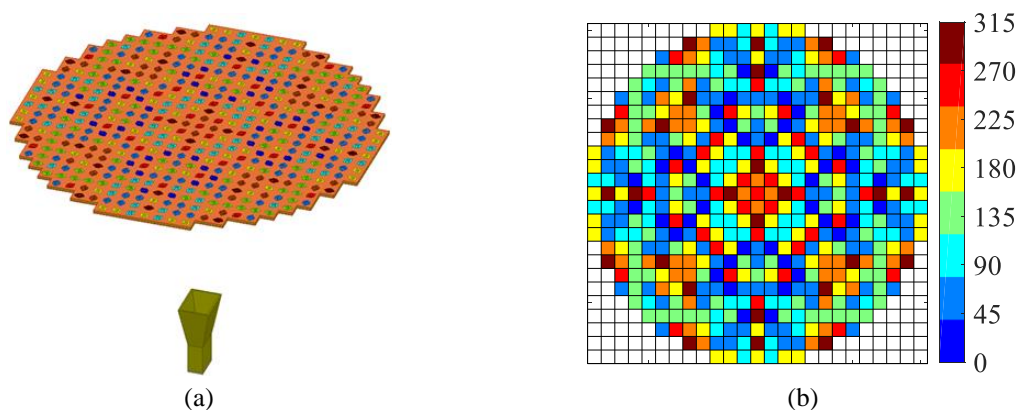


Figure III-31: Circularly-polarized quad-beam transmitarray: (a) 3-D scheme, (b) 3-bit phase distribution optimized at 29 GHz.

The RHCP and LHCP radiation patterns of the proposed TA in the vertical and horizontal planes are presented in Figure III-32. They confirm once again the good agreement between the theoretical and simulated performances of the TA with a difference of 0.7 dB only between the two maximum gain values. A simulated maximum gain of 17.5 dBi is obtained at $\theta_0 = \pm 25^\circ$. The side-lobe and cross-polarization levels in the vertical plane are equal to 13.3 dB and 20.6 dB, respectively. Similar results are obtained in the other plane.

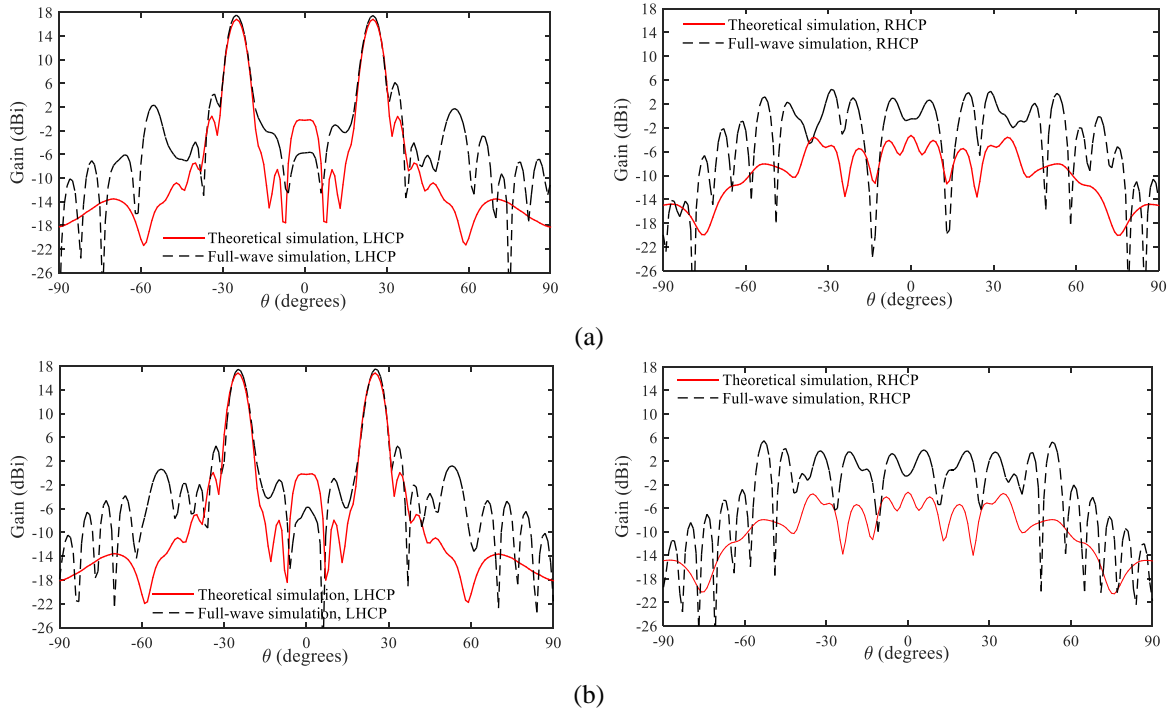


Figure III-32: Theoretical and simulated LHCP and RHCP radiation patterns of the proposed quad-beam transmitarray in (a) vertical and (b) horizontal planes.

3.5. Prototyping and characterization of fixed-beam transmitarrays

Very satisfactory theoretical and simulated results have been demonstrated for the linearly- and circularly-polarized transmitarrays with 3 bits of phase quantization. For further validation, we decided to prototype the 1600-element single- and quad-beam circularly-polarized transmitarrays described in sections 3.4.2 and 3.4.3. The measured results of the two transmitarrays are presented in this section and compared to those obtained by simulations. All the measurements have been performed in the anechoic chamber of CEA-Leti.

3.5.1. Measurements of the 1600-element single-beam transmitarray

The far-field radiation patterns of the 1600-element single-beam transmitarray have been measured in vertical, horizontal, and diagonal planes. The measurement setups of the TA in the vertical and diagonal planes are depicted in Figure III-33(a) and Figure III-33(b).

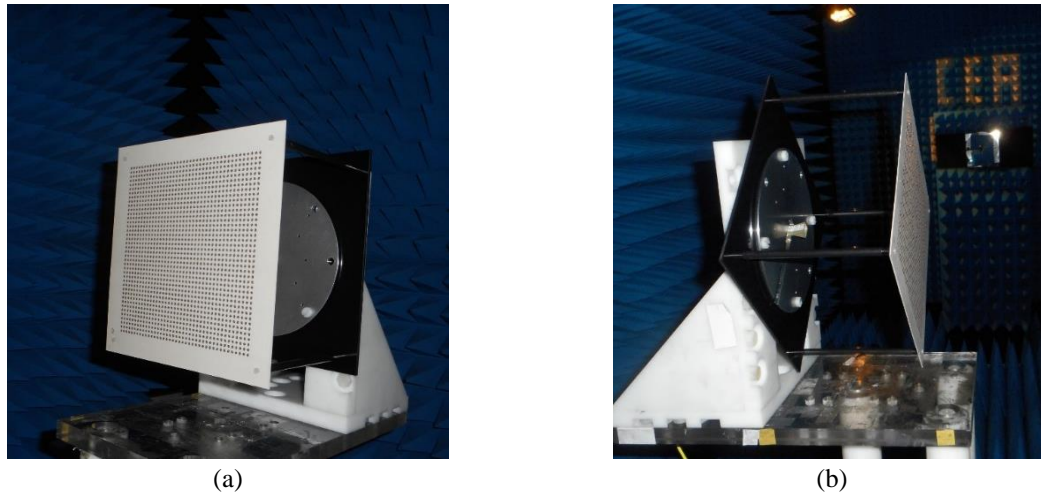


Figure III-33: Far-field measurement setup of the 1600-element single-beam circularly-polarized TA in (a) vertical and (b) diagonal planes.

The theoretical, full-wave simulated, and measured gain and axial ratio of the transmitarray from 27 GHz to 32 GHz are illustrated in Figure III-34(a) and Figure III-34(b), respectively. The 3-dB measured gain bandwidth extends from 27.0 GHz to 31.6 GHz (4.6 GHz), this corresponds to a fractional bandwidth of 15.9% at 29 GHz. A good agreement is observed between theoretical and experimental gain responses. However, the simulated gain is slightly lower than the measured one probably due to the limited computing resources, which limit convergence accuracy in the full-wave simulations. The measured axial ratio exhibits some variations across the whole band of interest (27-32 GHz) and some discrepancies with the simulated values but these differences are in the range of ± 0.5 dB and in accordance with measurement accuracy at Ka-band.

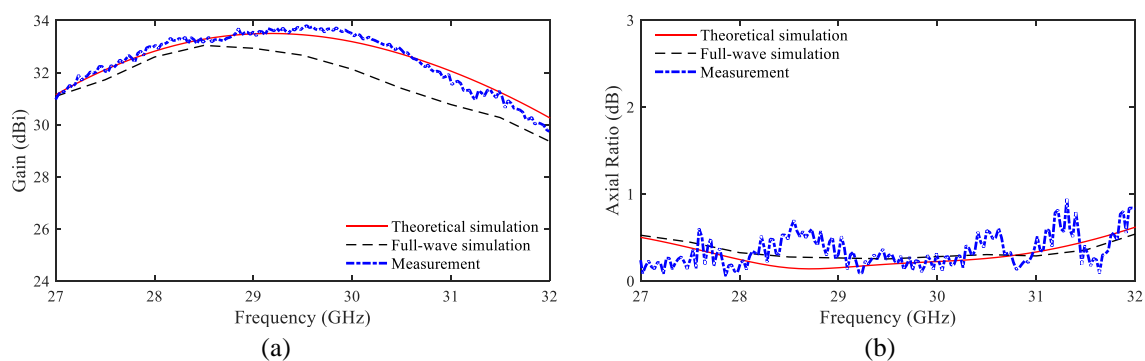


Figure III-34: Theoretical and simulated frequency responses of the 1600-element single-beam circularly-polarized transmitarray: (a) broadside gain and (b) axial ratio.

The measured and full-wave simulated radiation patterns at the frequency of optimization of 29 GHz for the horizontal and vertical planes are plotted in Figure III-35(a) and Figure III-35(b), respectively. The measured LHCP maximum gain is equal to 33.8 dBi with a side-lobe level of 22.6 dB below the peak gain. There is a difference of 0.7 dB between the

measured and simulated maximum LHCP gain. Despite the slightly higher measured RHCP level (-1.22 dBi) compared to the expected one (-3 dBi), the transmitarray demonstrates an acceptable cross-polarization level of 35.1 dB. This value is close enough to the ETSI requirements for point-to-point wireless link applications, especially in the axis [18]. The main characteristics of the transmitarray in terms of gain, bandwidth, cross-polarization level, and side-lobe level are reported in Table III-5.

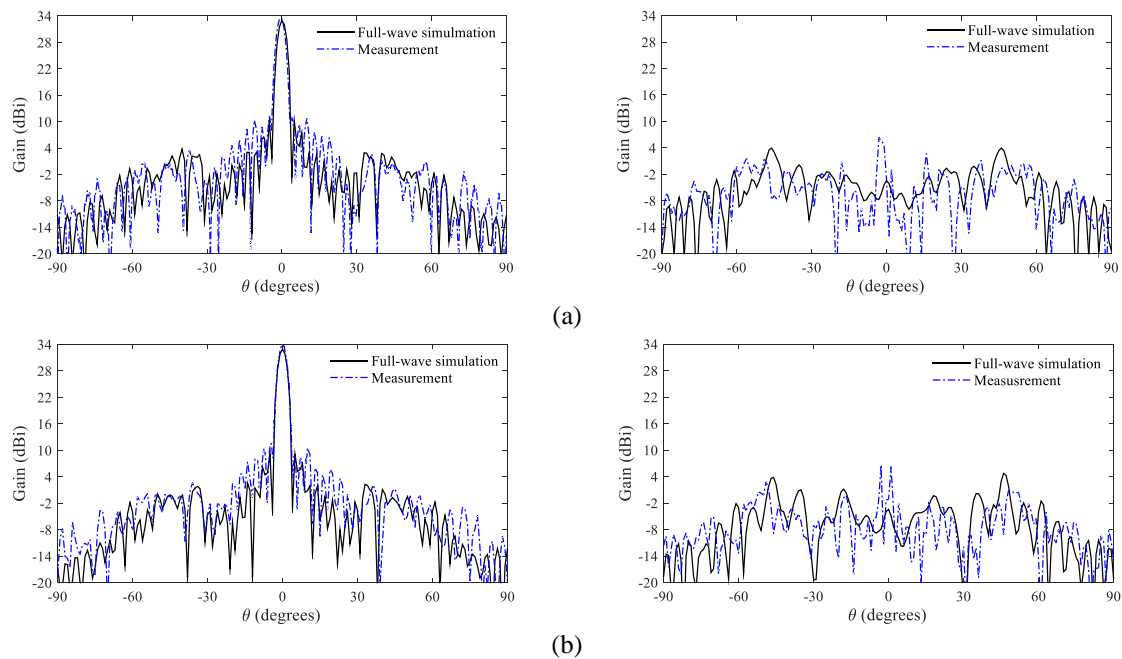


Figure III-35: Simulated and measured radiation patterns of the 1600-element single-beam circularly-polarized transmitarray antenna: (a) vertical and (b) horizontal planes.

Table III-5: Measured performances of the proposed 1600-element fixed-beam transmitarray

Parameters	Gain	3-dB bandwidth	Side lobe level	Cross-pol level
Values	33.8 dBi	>15.9%	22.6 dB	35.1 dB

The measured gain (LHCP and RHCP) as a function of the frequency and elevation angle in the vertical plane are shown in Figure III-36. These graphs show that the radiation patterns remain nearly constant over the full frequency band.

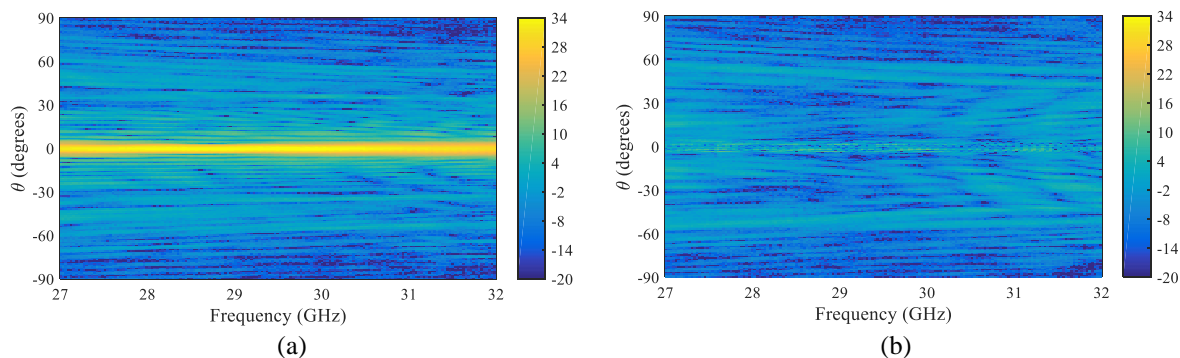


Figure III-36: Measured gain as a function of the frequency and elevation angle in the vertical plane: (a) LHCP, (b) RHCP.

The radiation patterns (LHCP and RHCP) measured at 27 GHz, 29 GHz, and 32 GHz in the horizontal, vertical, and diagonal planes are represented in Figure III-37, Figure III-38, Figure III-39, respectively. Very similar experimental results are demonstrated in the three cut-planes for each frequency. The maximum gain is equal to 31.9 dBi and 30.5 dBi with cross-polarization levels of 30.0 dB and 24.9 dB at 27 GHz and 32 GHz, respectively.

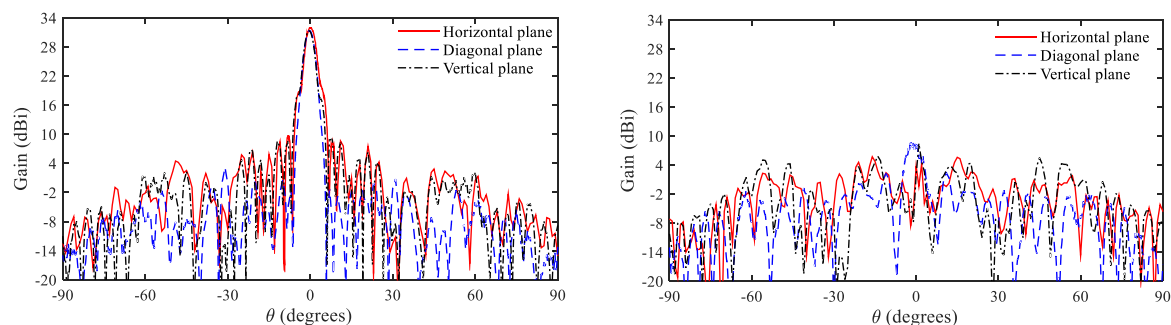


Figure III-37: Measured radiation patterns (LHCP and RHCP) in the vertical, diagonal and horizontal planes at 27 GHz.

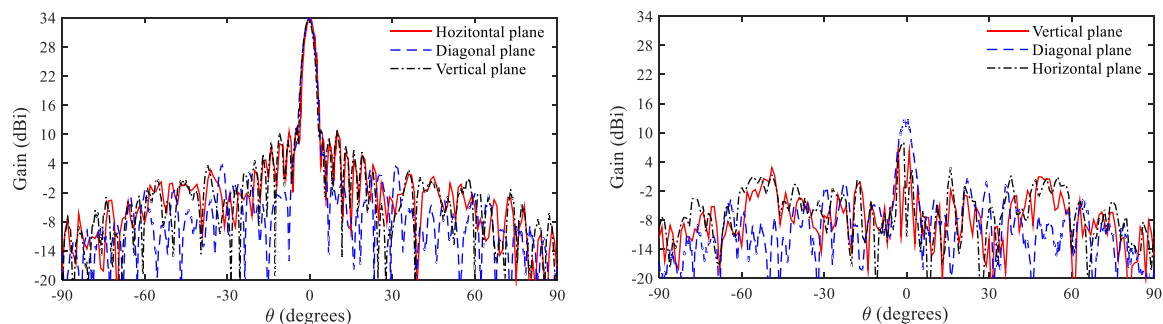


Figure III-38: Measured radiation patterns (LHCP and RHCP) in the vertical, diagonal and horizontal planes at 29 GHz.

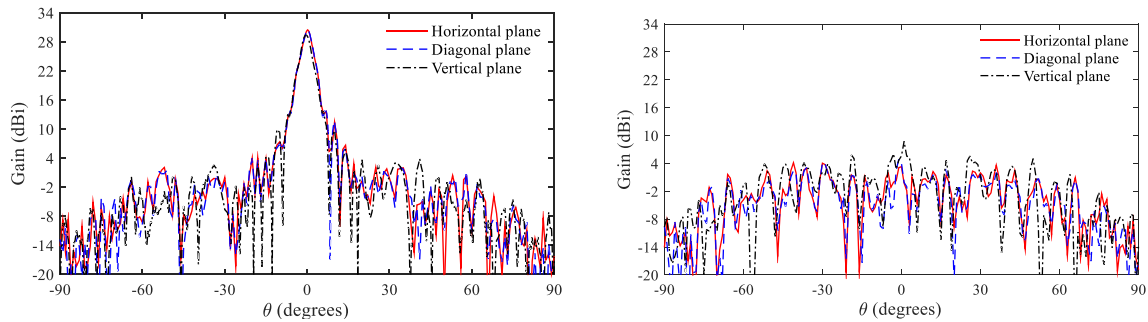


Figure III-39: Measured radiation patterns (LHCP and RHCP) in the vertical, diagonal and horizontal planes at 32 GHz.

3.5.2. Measurement of the quad-beam transmitarray

The quad-beam transmitarray prototype is tested in the anechoic chamber in horizontal and vertical planes as shown in the image of the setup (Figure III-40).

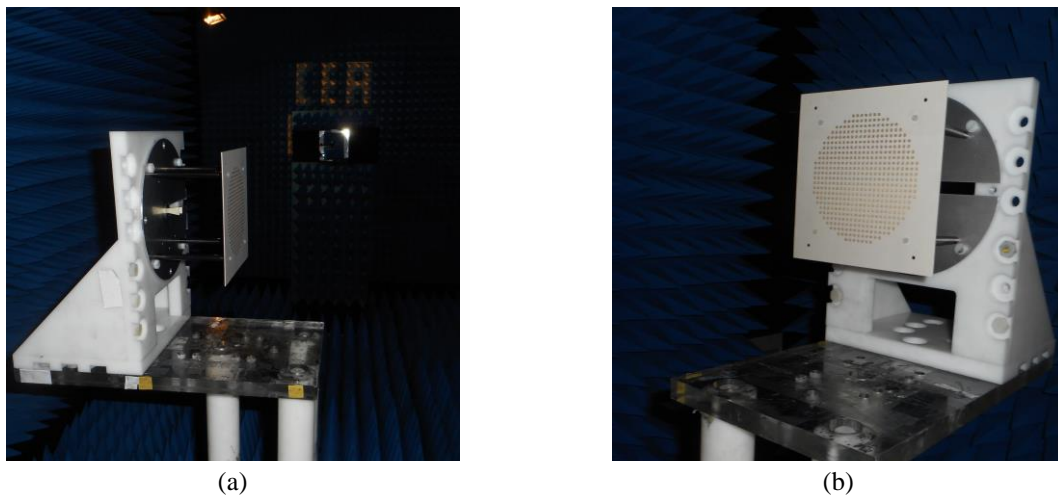


Figure III-40: Far-field measurement setup of the 489-element quad-beam transmitarray: (a) vertical, and horizontal planes.

The theoretical and full-wave simulated gain of one of the four beams (very similar results have been obtained for the other three beams) are compared to the measured gain of the four beams, as depicted in Figure III-41. The 3-dB measured gain bandwidth extends from 27.7 GHz to 32 GHz (this corresponds to a fractional bandwidth of 14.8% at 29 GHz). The fluctuation observed on the simulated and experimental frequency responses are probably due to the multiple reflections between the flat array and the horn used as focal source.

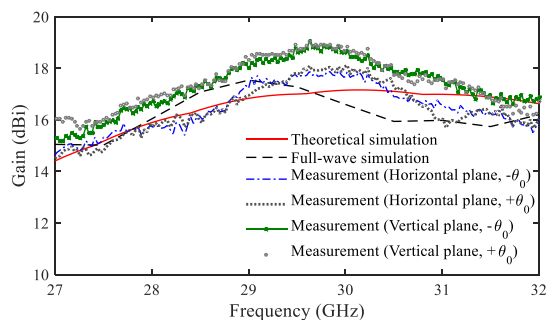


Figure III-41: Theoretical, simulated, and measured frequency responses of the quad-beam transmitarray.

Comparisons between the simulated and measured radiation patterns (LHCP and RHCP) at the frequency of optimization (29 GHz) in both vertical, and horizontal planes are shown in Figure III-42 and Figure III-43, respectively. The four beams are pointed at $\pm 25^\circ$ for both horizontal and vertical planes. Good agreement is shown between the measured and simulated LHCP results with a maximum gain equal to 18 dBi and a side-lobe level of 12.9 dB. The measured RHCP level is also in good agreement with the expected one. A cross-polarization level of about 19 dB is demonstrated.

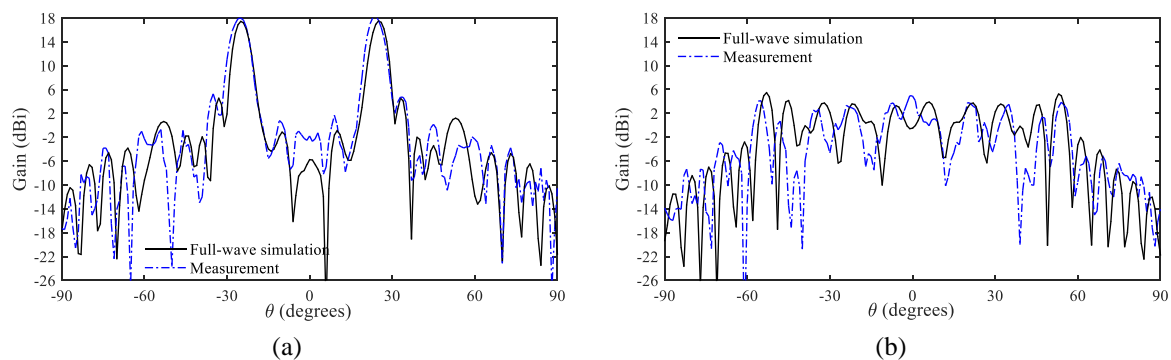


Figure III-42: Simulated and measured radiation patterns in the vertical plane at 29 GHz: (a) LHCP, (b) RHCP.

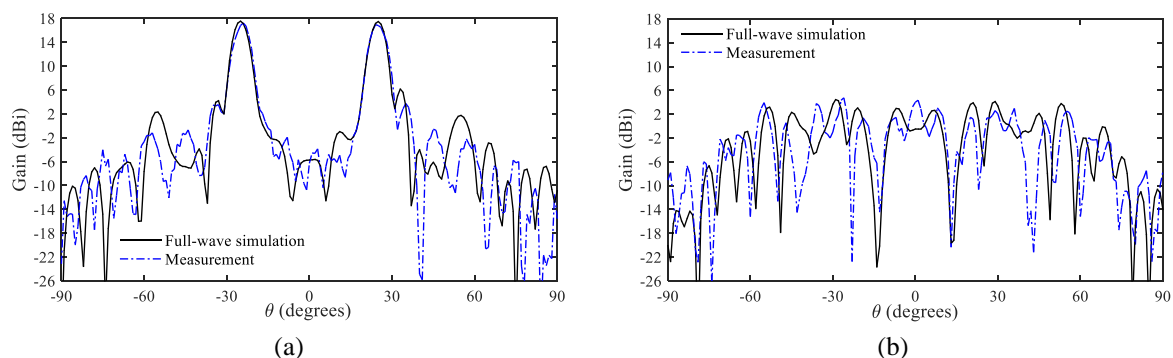


Figure III-43: Simulated and measured radiation patterns in the horizontal plane at 29 GHz: (a) LHCP, (b) RHCP

The measured gain as a function of the frequency and elevation angle in both vertical and horizontal planes are presented in Figure III-44 and Figure III-45. A beam squint of $\pm 3^\circ$

compared to the desired direction is observed in the frequency band of interest for all the four beams.

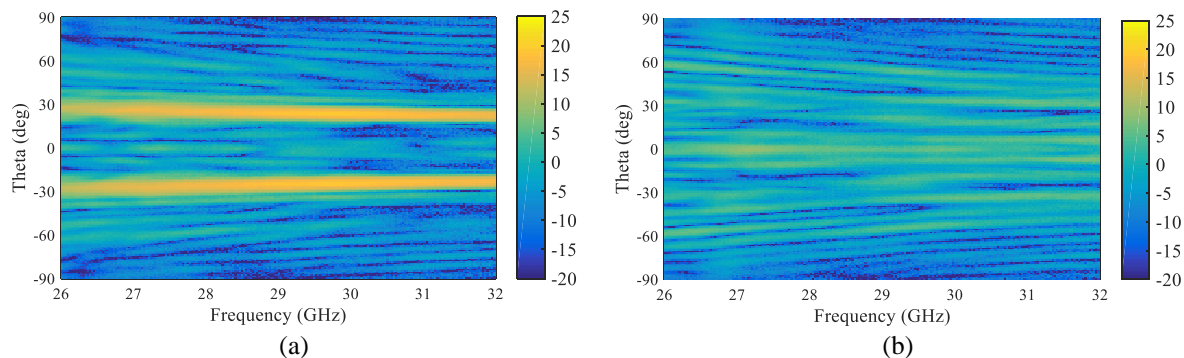


Figure III-44: Measured gain as a function of the frequency and elevation angle in the vertical plane.

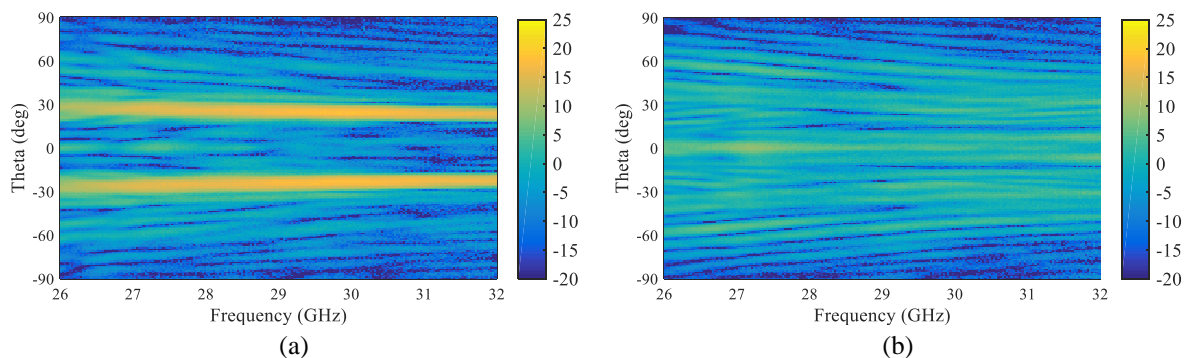


Figure III-45: Measured gain as a function of the frequency and elevation angle in the horizontal plane.

3.6. Conclusion

In this chapter, the performance of linearly- and circularly-polarized TAs working in Ka-band with a phase compensation up to 3 bits has been presented.

Firstly, the behavior and simulated results of the four broadband unit-cells, which the 3-bit linearly-polarized TA is based on, are presented. The simple ($0^\circ/180^\circ$), O-shaped slot ($45^\circ/225^\circ$), U-shaped slot ($90^\circ/270^\circ$), and capacitively-coupled ($135^\circ/315^\circ$) patches unit-cells exhibit an insertion loss lower than 0.86 dB at 29 GHz with a 1-dB transmission bandwidth of 15.2%, 14.1%, 7% and 15.2% at 29 GHz, respectively. Next, a TA composed of 20×20 elements has been designed and optimized using the in-house simulation tool and validated through EM full-wave simulations. Both simulations were found to be in excellent agreement. The proposed TA exhibits a broadside gain of 27.4 dBi with an aperture efficiency of 47%, and a 1-dB relative gain bandwidth of 11.4% at 29 GHz (28.5-31.8 GHz).

The next step of this chapter addressed the design of Ka-band transmitarrays working in circularly polarization with a phase compensation up to 3 bits. The TAs are based on a CP

unit-cell which has demonstrated reflection coefficients lower than -10 dB between 27 and 32 GHz. This corresponds to a 17.2% fractional bandwidth around 29 GHz. The 3-dB transmission bandwidth is greater or equal to 15.9% at 29 GHz for all unit-cell states. The results obtained using the in-house simulation tool in the case of a 20×20 TA have been confirmed through EM full-wave simulations. This TA presents a gain of 27.5 dBi at 29 GHz and a 1-dB bandwidth of 14.8%. The impact of phase quantization has been analyzed in the case of a 40×40 TA. It was shown that the radiation patterns of a 1600-element TA with 2- or 3-bit phase quantization is able to meet the ETSI recommendations defined in the case of point-to-point applications.

In view of the good theoretical results obtained with TAs based on CP unit-cells, the last parts of this chapter were dedicated to the design and prototyping of the transmitarrays with 3 bits of phase quantization. The first prototype comprises 1600 unit-cells and exhibits a single pencil beam, whereas the second one produces a quad-beam radiation pattern. A measured gain of 33.8 dBi, an aperture efficiency of 51.2%, and a 3-dB gain bandwidth >15.9% have been obtained in the case of the single-beam transmitarray. The quad-beam transmitarray demonstrated four beams at $\theta_0 = \pm 25^\circ$ with a gain around 18 dBi. A good agreement is obtained between theoretical calculations, full-wave simulations, and measured results for both prototypes.

Chapter IV. Design and optimization of active unit-cells for electronically reconfigurable transmitarrays

Reconfigurable antennas are needed in many applications requiring beam scanning and/or beam shaping, such as radar systems, satellite communications, and mm-wave 5G for mobile backhaul links or mobile access points. Previously, reconfigurable antennas were designed using mechanically-rotating systems. This beam reconfiguration technique is still employed because it is cheap, weather resistant and easy to implement. However, this technique can cause instabilities due to mechanical vibrations, a higher latency, and is bulky in the case of a large-aperture transmitarray. Since the 1980s, thanks to the miniaturization and progress of electronics components, electronically-reconfigurable antennas have been implemented by including these components in the transmit/receive modules. In the open literature, beam-steering transmitarray antennas from C-band to mm-wave frequencies are designed using electronically-reconfigurable unit-cells which integrate switchable or tunable devices such as PIN diodes, microelectromechanical systems (MEMS), micro-fluidic systems or varactors to control locally the transmission phase of the considered TA. Despite these numerous researches, efforts are still ongoing to improve the phase resolution, the cost, the weight and reliability of active unit-cells for electronically-reconfigurable transmitarrays. Several linearly- or circularly-polarized electronically-reconfigurable unit-cells and transmitarray antennas with 1-bit of phase quantization have been already demonstrated in our frequency band of interest (27-32 GHz). However, to our best knowledge, a single example of 2-bit electronically-reconfigurable transmitarray at Ka band has been previously presented in the open literature [49] and it demonstrated a rather limited experimental efficiency due the high insertion loss and/or lack of reliability of MEMS devices.

The objective of this chapter is to propose linearly- and circularly-polarized electronically-reconfigurable unit-cells with 2 bits of phase resolution working in Ka band. Firstly, the design and simulated results of the linearly-polarized unit-cell are presented. Next, the impact of biasing lines on the scattering parameters of the proposed unit-cell is studied. Then, the optimized linearly-polarized unit-cell is fabricated and characterized in a waveguide

simulator. The final part of this chapter addresses the design and optimization of a circularly-polarized unit-cell with 2 bits of phase resolution.

4.1. Design and optimization of an active linearly-polarized unit-cell with 2 bits of phase resolution

Nowadays, increasing the phase resolution with low insertion loss and complexity are the main challenges in the design of reconfigurable unit-cells for transmitarray antennas. Considering these two design criteria, a 2-bit electronically reconfigurable linearly-polarized unit-cell is proposed in this section.

The architecture of the unit-cell was proposed by Lucas Di Palma, and it was the subject of a patent [109]. Its architecture was previously based on six metal layers printed on three Rogers RT/Duroid 6002 substrates ($\epsilon_r = 2.94$, $\tan\delta = 0.0012$) and bonded with two Arlon CuClad 6700 films. It is realized in standard PCB technology. After all optimizations of the unit-cell and the TA based on this structure, we figured out that the manufacturer was unable to fabricate the circuit because the pressure to assemble the RT Duroid substrates, which are soft, using the Arlon CuClad 6700 bonding film caused short circuits. So, he suggested us to replace the bonding film CuClad 6700 by the RO4450F ($\epsilon_r = 3.52$, $\tan\delta = 0.004$). The thickness of the bonding film, previously equal to 114 μm , was now changed to 100 μm . As expected, the characteristics (relative permittivity (ϵ_r), dissipation factor ($\tan\delta$)) and thickness of the material affect the performance of the antenna. Consequently, the unit-cell was re-optimized again considering the new bonding film. For brevity, only simulations performed with the new bonding film (RO4450F) with a thickness of 100 μm are presented.

4.1.1. Architecture

The 3D-exploded view of the proposed linearly-polarized unit-cell with 2 bits of phase quantization is shown in Figure IV-1(a). It is composed of six metal layers printed on three Rogers RT/Duroid 6002 substrates and bonded with two RO4450F films. The unit-cell size is $5.1 \times 5.1 \times 1.3 \text{ mm}^3$ ($\lambda_0/2 \times \lambda_0/2 \times \lambda_0/8$ at 29 GHz, where λ_0 is the wavelength in free space at this frequency). The upper and bottom metal layers are labelled M1 and M6, respectively. These radiating elements consist of center-fed O-slot rectangular patch antennas working in transmit (Tx) and receive (Rx) modes, respectively. These two patch antennas (Figure IV-1(b),(g)) are connected by a 200- μm diameter metalized via hole located at their center and are separated by a ground plane. Two PIN diodes MA4GFCP907 [110] are flip-chipped on each patch antenna to tune the transmission phase; they are controlled by two bias lines printed on the opposite side

of each patch substrate (Figure IV-1 (c),(f)). The bias networks include microstrip radial stubs (M2) and capacitors (M5) to isolate the RF signals in transmit and receive sides, respectively. The DC connection to ground (M4) (Figure IV-1(e)) is realized with a short circuit stub (M3) (Figure IV-1(d)). All dimensions of the unit cell are provided in Table IV-1.

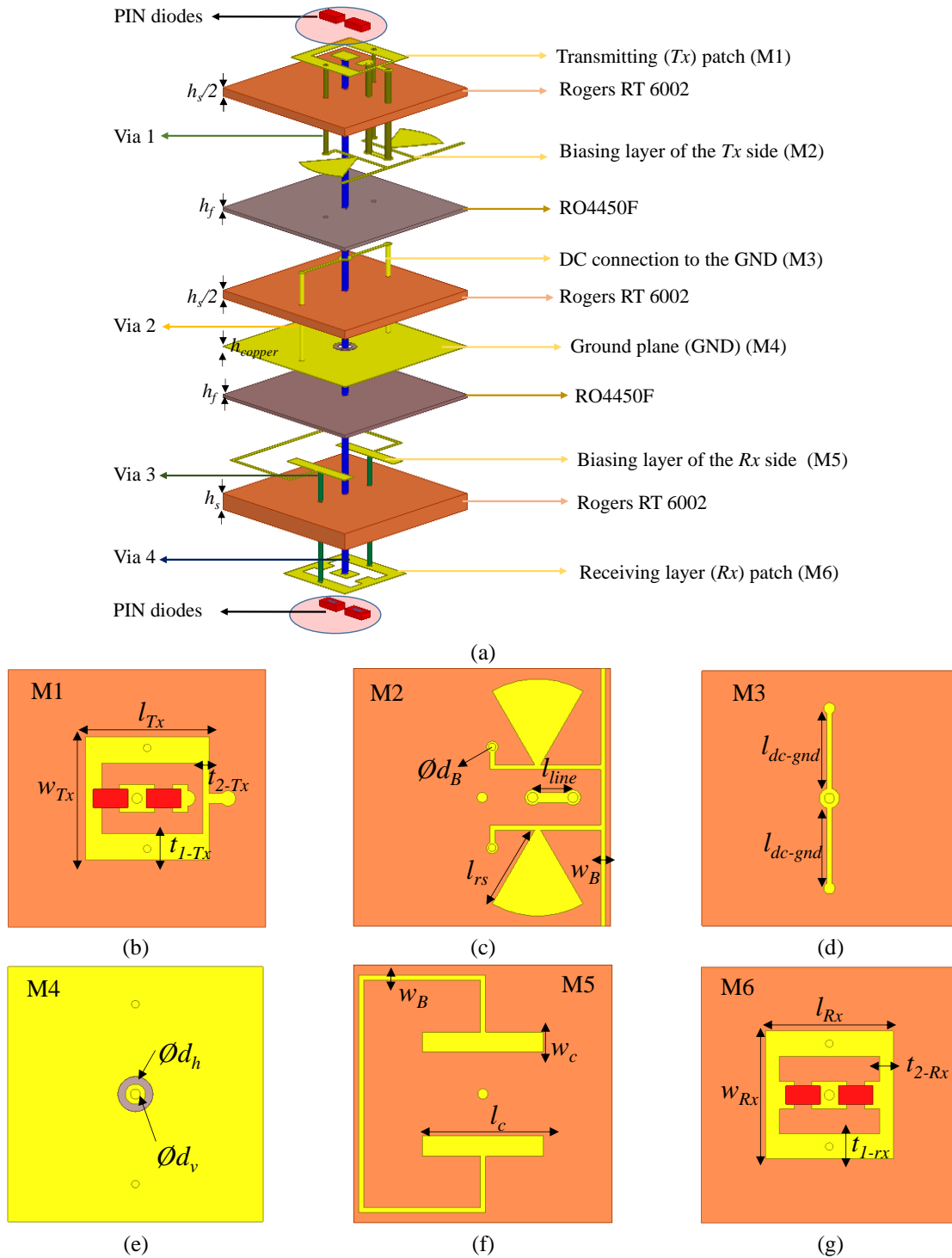


Figure IV-1: Proposed 2-bit linearly-polarized unit-cell: (a) Schematic view, (b) transmitting layer, (c) biasing layer of the transmission side, (d) DC connection to the ground layer, (e) ground plane, (f) biasing layer of the receive side, and (g) receiving layer.

The scattering parameters (S-parameters) of the diodes on a coplanar transmission line were determined up to 35 GHz in [53] with two-port measurements and short-open-load-thru (SOLT) calibration to extract their equivalent lumped-element models. The *ON*-, and *OFF*-states of the PIN diode are modeled by a lumped series L-R circuit ($R_{ON} = 4.2 \Omega$, $L_{ON} = 0.05$ nH) and a shunt R-C circuit ($R_{OFF} = 300 \text{ K}\Omega$, $C_{OFF} = 42$ fF) as shown in Figure IV-2. The substrate of the diode is modelled as Gallium-Arsenide material ($\epsilon_r = 12.9$) and its dimensions are: $0.686 \times 0.368 \times 0.19 \text{ mm}^3$.

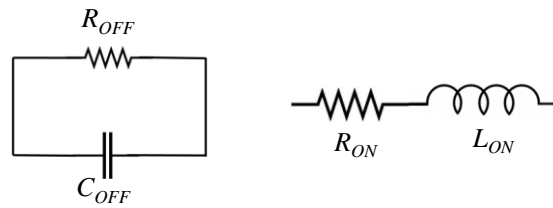


Figure IV-2: Equivalent lumped-element models of the PIN diode (MA4GF907) in the *ON*, and *OFF* states.

The two PIN diodes on each radiating element are always biased in opposite states: one PIN diode is switched ON while the other one is in OFF-state. Switching between these two states leads to opposite surface currents on the transmitting metal layer, named *Tx-01*, and *Tx-10* as shown in Figure IV-3(a), and Figure IV-3(b), respectively.

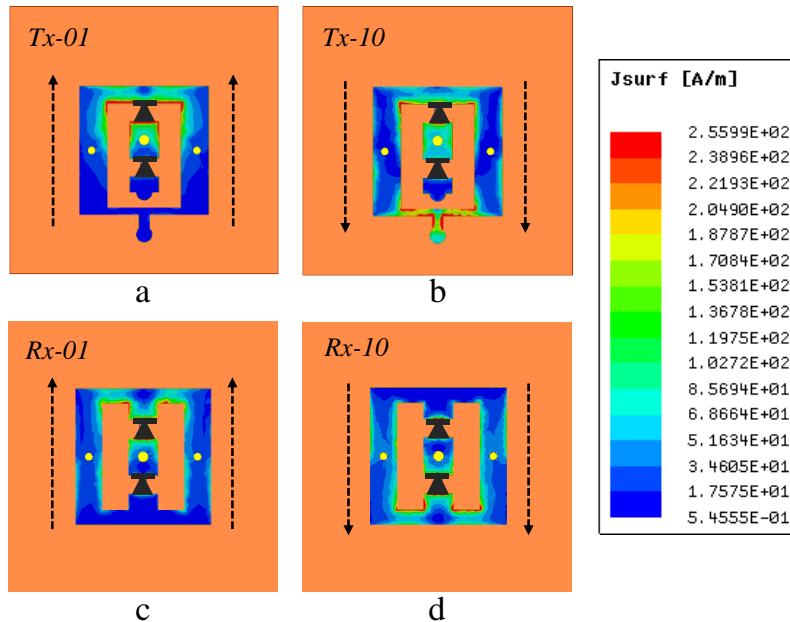


Figure IV-3: Surface current distribution: (a) and (b) on Tx layer, (c) and (d) on Rx layer.

Thus a 90° phase-shift is obtained on the *Tx* patch antenna thanks to the delay line printed on the opposite side of its substrate. Two distributions of surface-current are also observed on the reception metal layer labelled *Rx-01*, and *Rx-10* as illustrated in Figure IV-3(c),

CHAPTER IV. DESIGN AND OPTIMIZATION OF ACTIVE UNIT-CELLS FOR
ELECTRONICALLY RECONFIGURABLE TRANSMITARRAYS

Figure IV-3(d), respectively. A 180° phase-shift is achieved on the Rx patch antenna. The phase configurations are summarized in Table IV-2.

Table IV-1: Dimensions of the proposed 2-bit unit-cell (Figure IV-1(a)).

Parameter	Value (mm)	Parameter	Value (mm)	Parameter	Value (mm)
l_{Tx}	2.45	l_{dc-gnd}	1.5	t_{1-Rx}	0.275
w_{Tx}	2.45	w_c	0.4	t_{2-Rx}	0.5
t_{1-Tx}	0.525	l_c	2.4	h_s	0.508
t_{2-Tx}	0.125	\varnothing_{dh}	0.7	h_f	0.1
\varnothing_{dB}	0.15	\varnothing_{dv}	0.2	h_{copper}	0.018
l_{rs}	1.68	l_{Rx}	2.55	l_{line}	0.58
w_B	0.1	w_{Rx}	2.55		

Table IV-2: Different combinations of the reception and transmission layers corresponding to the four phase states.

Phase-shift state	Tx phase state	Rx phase state
0°	$Tx-01$	$Rx-10$
90°	$Tx-10$	$Rx-10$
180°	$Tx-01$	$Rx-01$
270°	$Tx-10$	$Rx-01$

4.1.2. Simulation results

The proposed 2-bit unit-cell, described in section 4.1.1, has been simulated for the four phase states using the commercial software Ansys-HFSS with periodic boundary conditions on the unit-cell lateral faces and Floquet port excitations on both sides of the element. As already mentioned, this method exploits the symmetry of the unit-cell to reproduce an infinite array of identical unit-cells in the same states, so it takes into account the mutual coupling effects. The full-wave simulations have been performed under normal incidence and linear polarization.

The magnitude of the reflection on the receiving side (S_{11}), and transmission coefficients (S_{21}) are plotted in Figure IV-4(a), and Figure IV-4(b), respectively. The 10-dB return loss bandwidth is equal to 7.9%, 9.6%, 10.3%, and 4.5% at 29 GHz for the 0° , 90° , 180° , and 270° states, respectively. The 0° , 90° , 180° , and 270° states exhibit a minimum insertion loss equal to 1.0, 0.8, 1.0, and 0.8 dB, and a relative 3-dB transmission bandwidth of 9.6%, 16.5%, 12.1%, and 15.5% at 29 GHz, respectively. The transmission phase and the differential phase-shift between the 0° state and the others are illustrated in Figure IV-4(c) and Figure IV-4(d), respectively. The phase difference between two consecutive phase states is around 90° with a maximum error of 34° in the frequency band of interest (26–31 GHz). The phase differences at

29 GHz between the 0° unit-cell and the other states (90° , 180° , and 270° unit-cells) correspond to 122° , 198° , and 291° , respectively. All the simulated results of the proposed active unit-cell are summarized in Table IV-3.

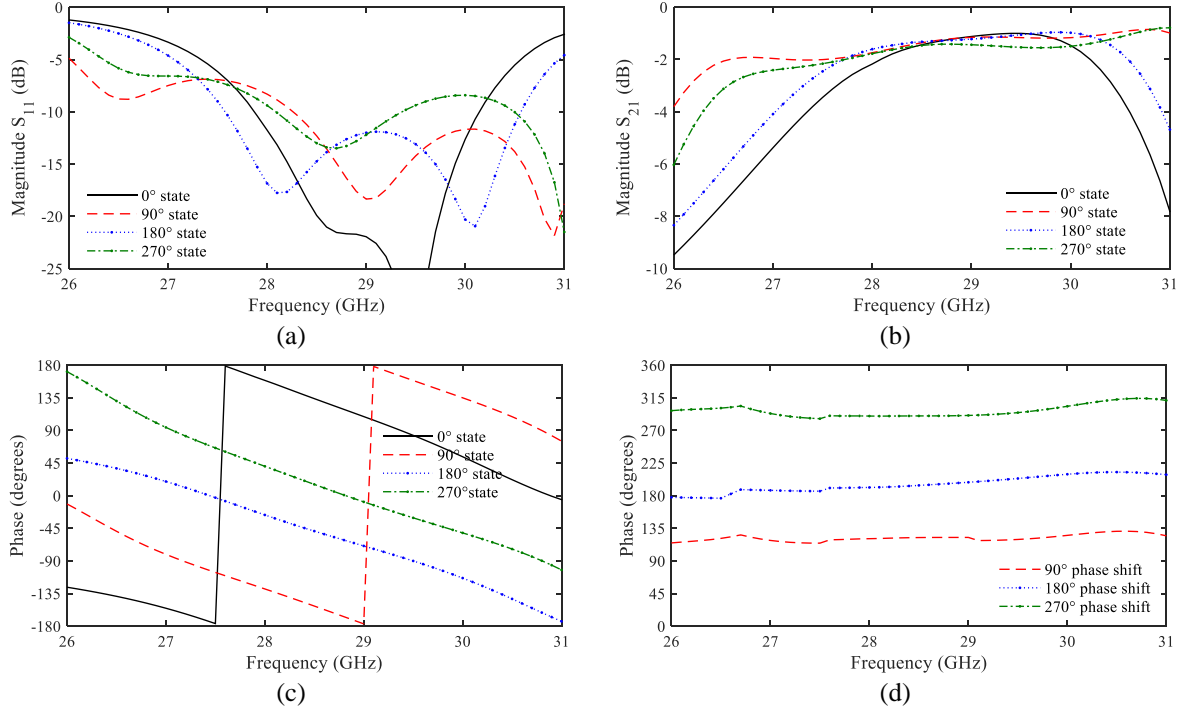


Figure IV-4: Frequency responses of the proposed 2-bit linearly-polarized unit-cell. Magnitude of the (a) reflection and (b) transmission coefficients. (c) Transmission phase. (d) Phase-shift between the 0° state and the other states.

Table IV-3: Simulated performances of the 2-bit linearly-polarized unit-cell.

	0°	90°	180°	270°
S_{11}				
10-dB bandwidth	27.9 - 30.2 GHz	28.2- 31.0 GHz	27.6 - 30.6 GHz	28.1 - 29.4 GHz
Minimum insertion loss	1.0 dB	0.8 dB	1 dB	0.8 dB
S_{21}				
3-dB bandwidth	27.6 - 30.4 GHz	26.2 - 31.0 GHz	27.3 - 30.8 GHz	26.5 - 31.0 GHz

4.1.3. Impact of bias lines

The proposed 2-bit unit-cell will be used as a building block of a 196-element transmitarray. Thus, the impact of inserting multiples bias lines on the S-parameters has been studied. The proposed 2-bit unit-cell with two bias lines to control the four p-i-n diodes is modified by inserting fourteen lines. That corresponds to the worst case (unit-cell with the largest number of bias lines) when a 14×14 -element transmitarray is considered.

The arrangement of the fourteen bias lines was chosen taking into account space constraints. The bias lines of the transmit patch diodes are distributed between the M1 layer (5 lines) (Figure IV-5(a)) and the M2 layer (2 lines) (Figure IV-5(b)). Regarding the diodes on the receive side, two bias lines have been printed on the same side as the patch antenna working in receive mode (M6) (Figure IV-5(c)) and five lines are printed on the inner metal layer (M5) (Figure IV-5(d)).

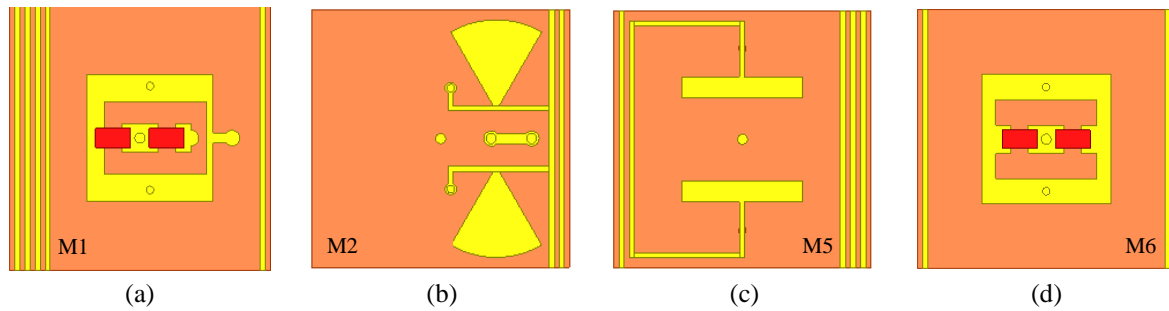


Figure IV-5: Bias lines arrangement of the 2-bit unit-cell: (a) transmitting T_x , (b) T_x biasing network, (c), receiving R_x , and (d) R_x biasing network layers.

The modified unit-cell is simulated for the four states with periodic conditions and Floquet mode excitation under normal incidence. The scattering parameters (magnitude of the reflection and the transmission coefficients) of the unit-cell with two and fourteen bias lines are compared for the four states. As shown in Figure IV-6, the effect of bias lines is negligible on the performances of the unit-cell as the frequency responses are very similar. So, this unit-cell is suitable for the design of a 2-bit electronically reconfigurable transmitarray.

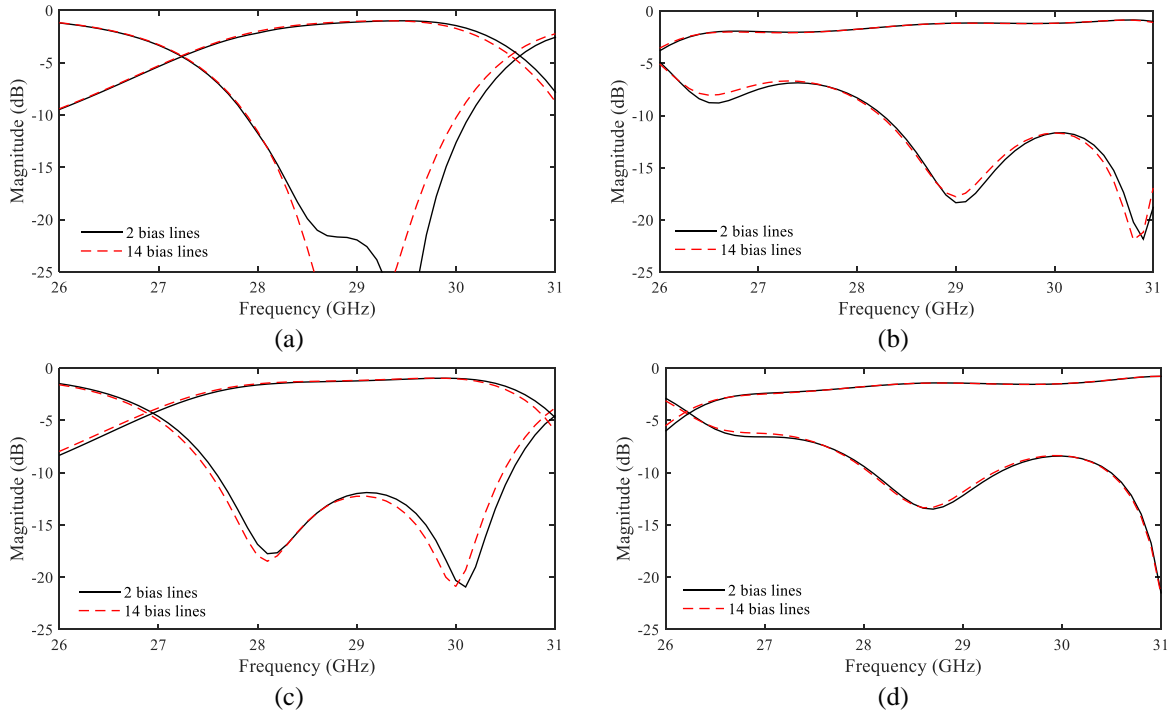


Figure IV-6: Impact of bias lines on the performances of the proposed 2-bit linearly-polarized unit-cell: (a) 0°, (b) 90°, (c) 180°, and (d) 270° states.

4.1.4. Waveguide setup

Since the characterization of the unit-cell will be performed in a waveguide, its performances are also studied by considering this setup. The unit-cell is encapsulated in a waveguide simulator based on two standard WR-28 waveguides ($7.11 \times 3.56 \text{ mm}^2$) [111] as shown in Figure IV-7. It includes two coax-to-waveguide (WR-28) adaptors and two WR-28 straight waveguide sections. Two tapered transitions, with a length of 1.2 mm, are placed between the rectangular section of the waveguide and the square section of the unit-cell.

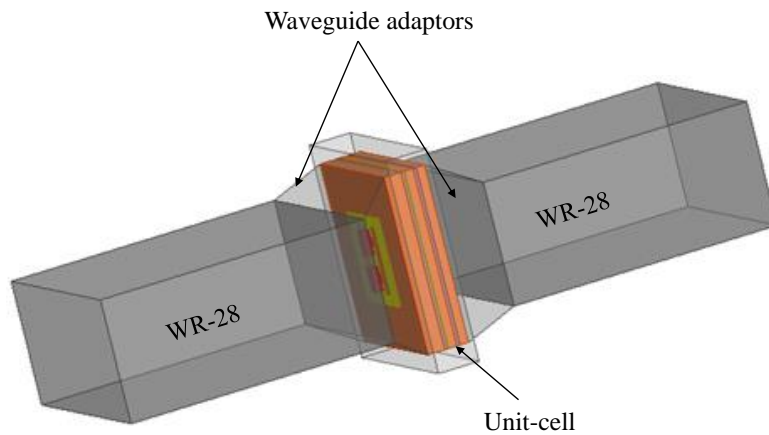


Figure IV-7: Scheme of the waveguide setup to test the unit-cell.

Generally, the dominant mode of any waveguide corresponds to that with the lowest cut-off frequency. In the case of rectangular waveguides, the dominant propagation mode is the

TE₁₀ mode (Transverse Electric mode). The propagation in the waveguide can be modelled as a plane wave with an incidence angle in the E plane defined as [112]:

$$\sin(\theta) = \frac{\lambda_0}{\lambda_c} . \quad (\text{Eq IV-1})$$

Where λ_0 is the free-space wavelength and λ_c is the cut-off guided wavelength. We must notice that the waveguide will transmit energy only at frequencies above the cut-off frequency which is defined in general as:

$$f_{cmn} = \frac{c_0}{2} \sqrt{\left(\frac{m}{a}\right)^2 + \left(\frac{n}{b}\right)^2} . \quad (\text{Eq IV-2})$$

Where (m,n) are integers that define the number of half wavelengths that will fit in the (a,b) dimensions of the waveguide.

For the fundamental mode (TE₁₀) in the rectangular waveguide, λ_c is given by:

$$\lambda_c = 2a . \quad (\text{Eq IV-3})$$

Where a is the width of the waveguide section (a is equal to 7.112 mm for a WR28 waveguide). At 26 GHz, 29 GHz, and 31 GHz, the incidence angles θ of the waves are equal to 54.2°, 44.6°, and 42.9°, respectively (eq. IV.1). For comparison, a Floquet simulation of the unit-cell is also performed under oblique incidence ($\theta = 45^\circ$) in E-plane. The scattering parameters of the proposed 2-bit unit-cell calculated considering the waveguide simulator and Floquet setup under oblique incidence are plotted in Figure IV-8. Very similar results are obtained in both simulation setups (waveguide simulator and Floquet port excitation). The transmission phase and the phase-shift between the 0° unit-cell and the other states when the simulation is performed in waveguide are shown in Figure IV-9(a) and Figure IV-9(b), respectively. The transmission phase difference between the four states is around 90° with a maximum error of 40° in the frequency band 26-31 GHz.

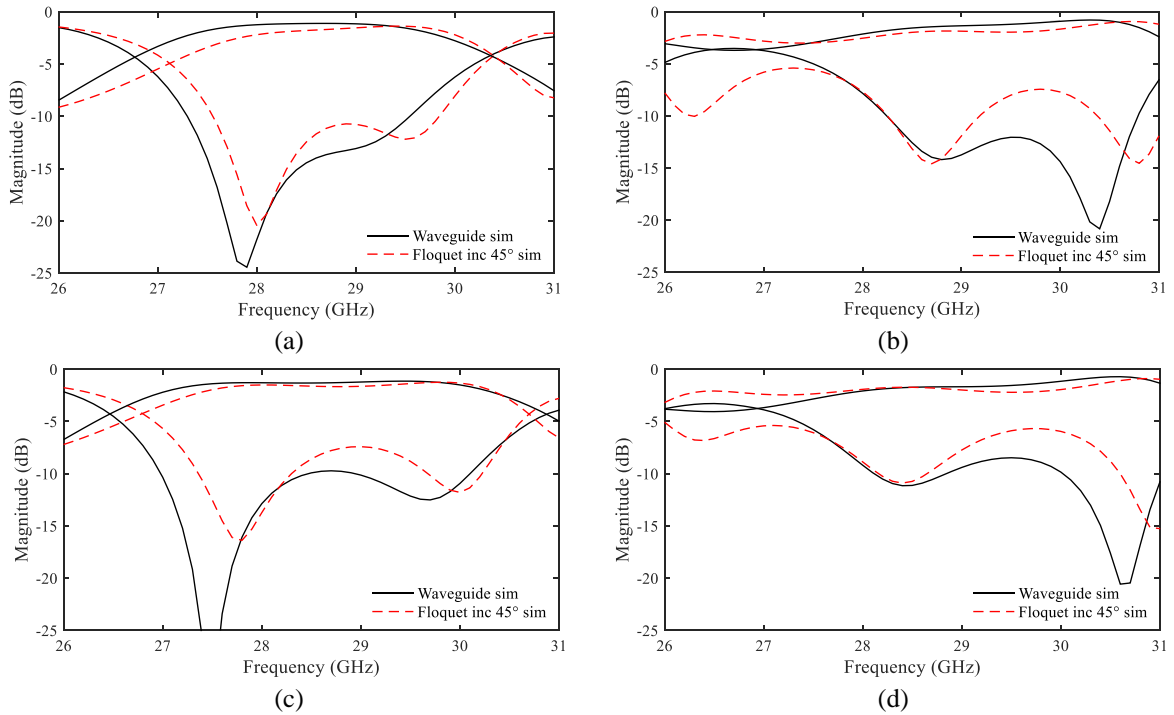


Figure IV-8: Scattering-parameters of the 2-bit linearly-polarized unit-cell performed with a waveguide simulator and Floquet ports under oblique incidence : (a) 0° , (b) 90° , (c) 180° , and (d) 270° states.

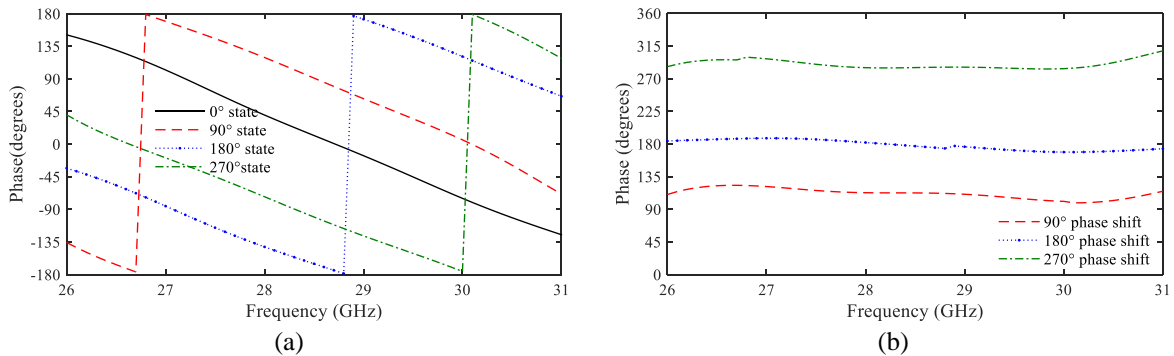


Figure IV-9: (a) Transmission phase and (b) phase-shift between the 0° state and the other states performed in waveguide simulator.

4.2. Experimental results

The proposed 2-bit linearly-polarized electronically reconfigurable unit-cell was fabricated on Rogers Duroid 6002 with RO4450F as bonding films in order to validate the numerical results. Two rows of metallic via holes are surrounding the unit-cell in order to warranty the continuity of the waveguide in the measurement setup. The prototype contains also two bias lines (1 mm wide), passing through the rings of vias, and pads for the ground connections to effect a reverse bias on the diodes placed on the top and bottom of the unit-cell.

Three variant of unit-cells were realized, the unit-cell with 2, 6 and 14 bias lines as shown in Figure IV-10, which corresponds of the best, middle and worst configurations of the unit-cell, respectively.

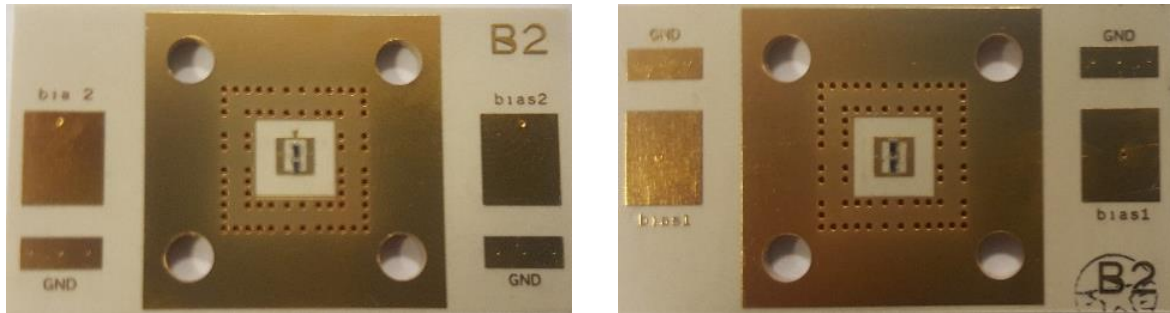


Figure IV-10: Prototype of the proposed 2-bit linearly-polarized unit-cells: transmitting, and receiving layers on left and right, respectively.

The test setup consists of the unit-cell encapsulated in the waveguide WR-28 connected to a two-port network analyzer. This latter is calibrated using the TRL (Through-Reflect-Line) two-port calibration technique with the reference planes fixed at the end of the waveguide, so the two adaptors are not taken into account in the calibration. A current generator is used to control the PIN diodes, and the forward bias current is fixed at 10 mA. The fabricated unit-cells with bias wires and mounted in the waveguide are depicted in Figure IV-11.

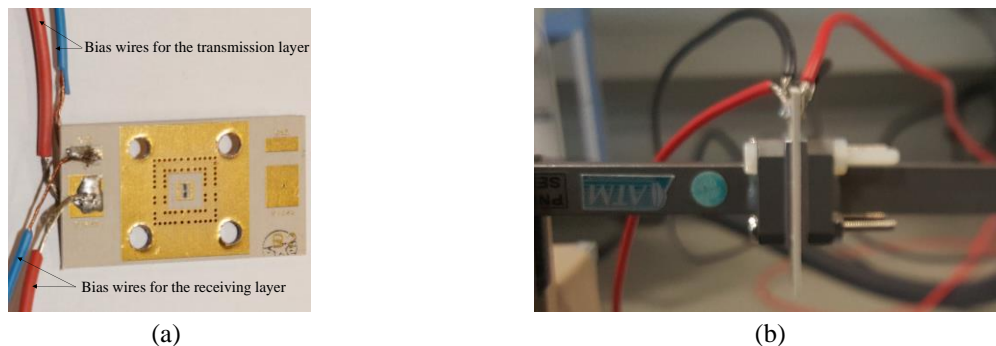


Figure IV-11: Fabricated unit-cells with (a) bias wires and (b) placed in the waveguide.

4.2.1. Fabricated unit-cell with two bias lines

The measured magnitude of the reflection and transmission coefficient of the fabricated unit-cell with 2 bias lines for the four states (0° , 90° , 180° , and 270°) are compared to the outcome of the numerical simulations (waveguide simulation and Floquet simulation with a 45° angle of incidence), as depicted in Figure IV-12, Figure IV-13, Figure IV-14, and Figure IV-15, respectively.

CHAPTER IV. DESIGN AND OPTIMIZATION OF ACTIVE UNIT-CELLS FOR ELECTRONICALLY RECONFIGURABLE TRANSMITARRAYS

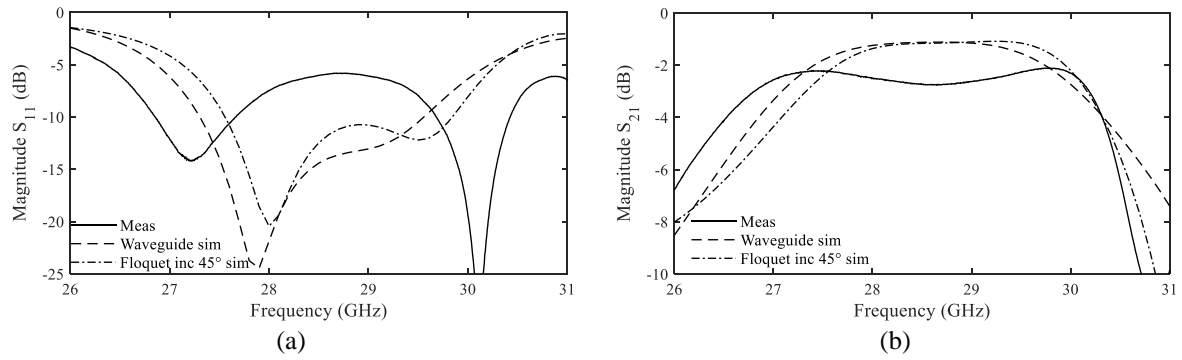


Figure IV-12: Measured (in WR-28 waveguide) and simulated scattering parameters magnitudes in the 0° state: (a) reflection (S_{11}) and (b) transmission (S_{21}) coefficients.

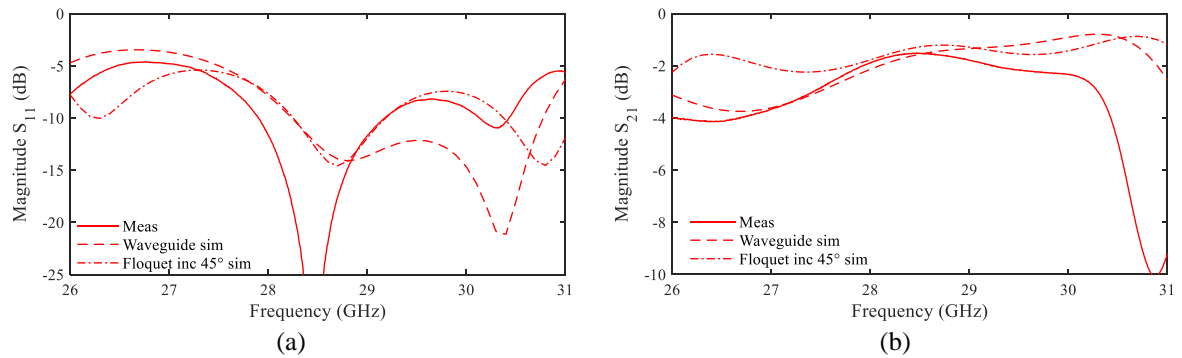


Figure IV-13: Measured (in WR-28 waveguide) and simulated scattering parameters magnitudes in the 90° state: (a) reflection (S_{11}) and (b) transmission (S_{21}) coefficients.

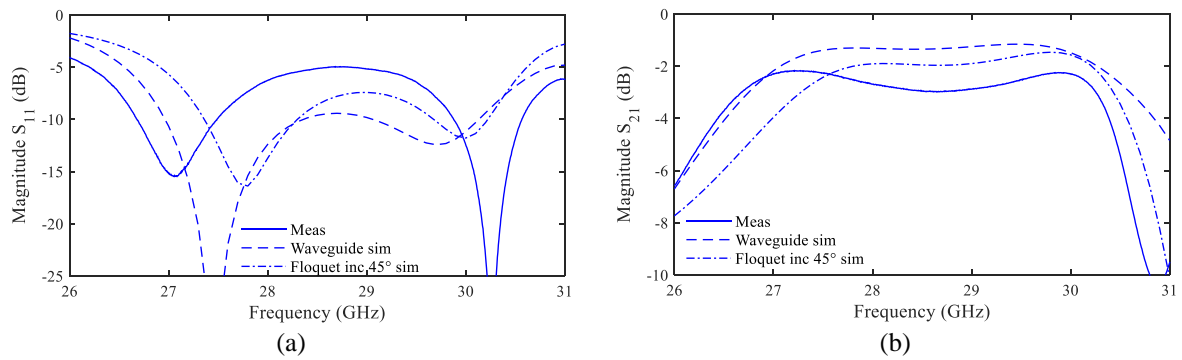


Figure IV-14: Measured (in WR-28 waveguide) and simulated scattering parameters magnitudes in the 180° state: (a) reflection (S_{11}) and (b) transmission (S_{21}) coefficients.

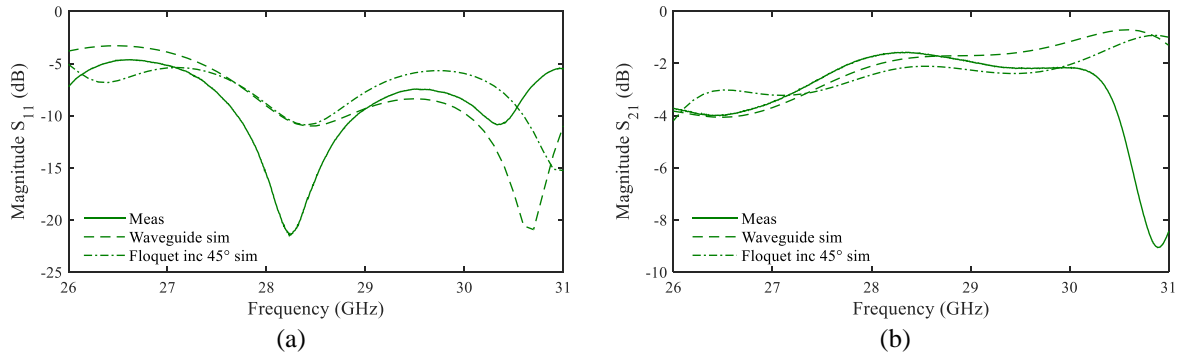


Figure IV-15: Measured (in WR-28 waveguide) and simulated scattering parameters magnitudes in the 270° state: (a) reflection (S_{11}) and (b) transmission (S_{21}) coefficients.

There are differences between the measured and simulated scattering parameters magnitudes (reflection and transmission coefficients) for the four states of the unit-cell, which are probably due to fabrication errors and a positioning error of the holes used for measurement in waveguide. Retro-simulations will be addressed in section 4.2.3 to identify the possible failures in the fabrication process. Impedance mismatch and frequency shift are observed on the measured results of the fabricated unit-cell. The measured scattering parameters demonstrate a minimum insertion loss of 2.1 dB, 1.5 dB, 2.3 dB, and 1.6 dB for the 0° , 90° , 180° , and 270° states, respectively. The measured relative 3-dB transmission bandwidth corresponds to 11.7%, 10.0%, 12.1%, and 10.3% at 29 GHz for the 0° , 90° , 180° , and 270° states, respectively. A comparison of the experimental and simulated results performed in the WR-28 waveguide of the four states of the unit-cell is summarized in Table IV-4. Despite experimental insertion losses higher than expected in simulations, their levels remain interesting compared to the state of the art and in the perspective of an actual application. Likewise, the experimental reflection coefficients remain acceptable below -6 dB over most of the frequency band.

The measured transmission phase and the phase difference between the 0° and the other states of the unit-cell are presented in Figure IV-16(a,b), respectively. The phase shifts between the 0° state and the other states (90° , 180° , and 270°) are equal to 124° , 178° , and 315° , respectively.

CHAPTER IV. DESIGN AND OPTIMIZATION OF ACTIVE UNIT-CELLS FOR ELECTRONICALLY RECONFIGURABLE TRANSMITARRAYS

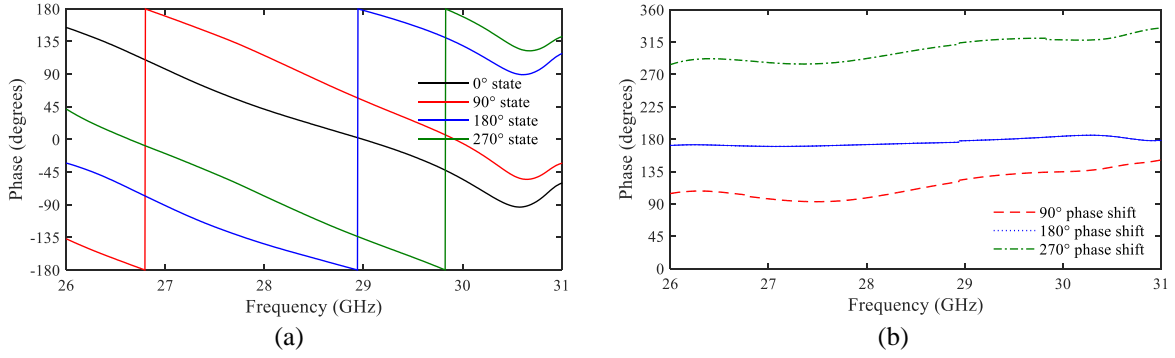


Figure IV-16: (a) Measured transmission phase of the four states of the proposed 2-bit unit-cell and (b) phase-shift between the 0° state and the other states.

Table IV-4: Measured and simulated performances in the waveguide of the 2-bit linearly-polarized unit-cell.

	S_{11} 10-dB bandwidth (GHz)		Minimum insertion loss (dB)		S_{21} 3-dB bandwidth (GHz)	
	Sim.	Meas.	Sim.	Meas.	Sim.	Meas.
0° state	27.1-29.6	26.8-27.6 29.6-30.4	1.0	2.1	27.0-30.1	26.8-30.2
90° state	28.3-30.7	27.9-29.2 30.1-30.4	0.8	1.5	27.4-31.0	27.4-30.3
180° state	27.0-30.1	26.6-27.5 29.9-30.6	1.0	2.3	26.8-30.5	26.7-30.2
270° state	28.2-28.8 30.1-31.0	27.7-28.9 30.2-30.4	0.8	1.6	27.5-31.3	27.3-30.3

4.2.2. Fabricated unit-cell with more than two bias lines

The proposed active unit-cell with 2 bits of phase quantization is planned to be used as a building block of the transmitarray. The TA is composed of 14×14 unit-cells, so the maximum number of bias lines in a unit-cell is equal to fourteen. The unit-cell with six and fourteen bias lines are characterized in waveguide as the one with two bias lines. As depicted in Figure IV-17, Figure IV-18, Figure IV-19, and Figure IV-20, the effect of bias lines on the performance of the four states of the active unit-cell is insignificant.

CHAPTER IV. DESIGN AND OPTIMIZATION OF ACTIVE UNIT-CELLS FOR ELECTRONICALLY RECONFIGURABLE TRANSMITARRAYS

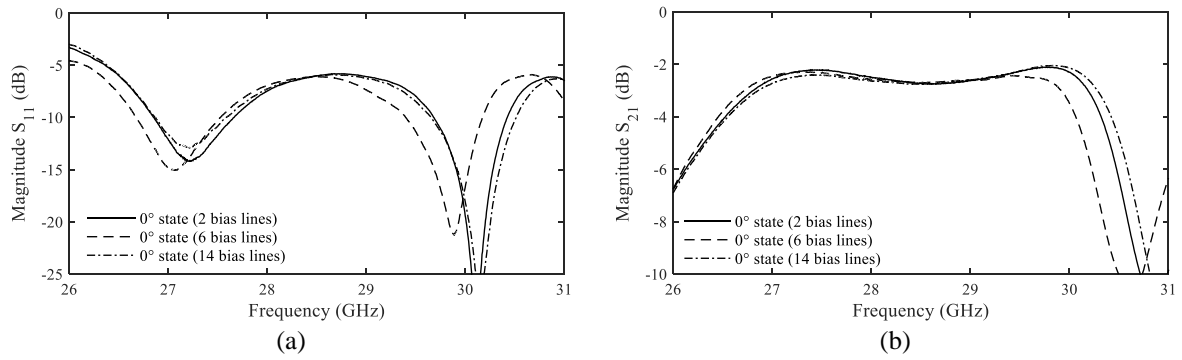


Figure IV-17: Impact of bias lines on the measured scattering parameters magnitudes in the waveguide in the 0° state: (a) reflection (S_{11}) and (b) transmission (S_{21}) coefficients.

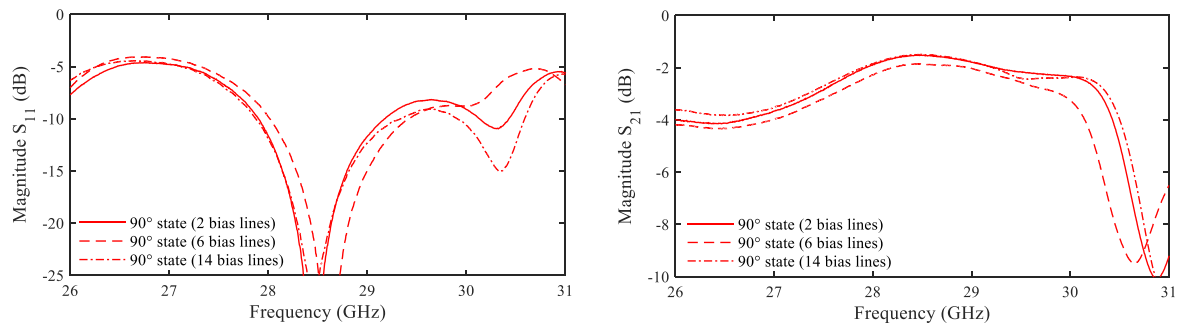


Figure IV-18: Impact of bias lines on the measured scattering parameters magnitudes in the waveguide in the 90° state: (a) reflection (S_{11}) and (b) transmission (S_{21}) coefficients.

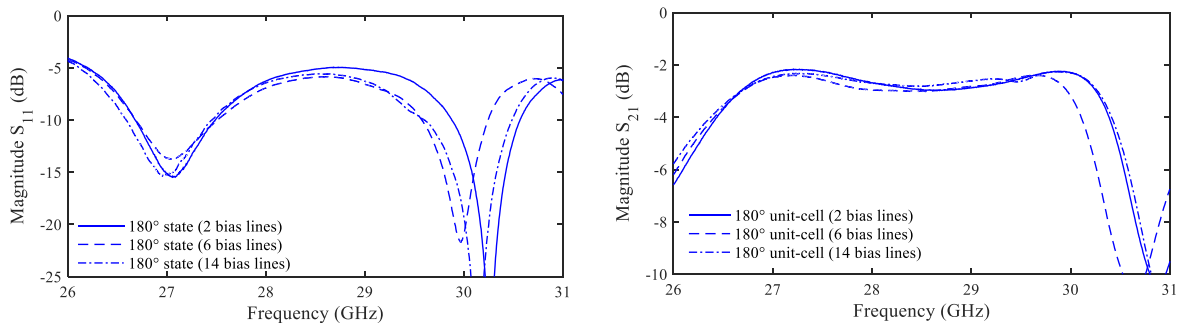


Figure IV-19: Impact of bias lines on the measured scattering parameters magnitudes in the waveguide in the 180° state: (a) reflection (S_{11}) and (b) transmission (S_{21}) coefficients.

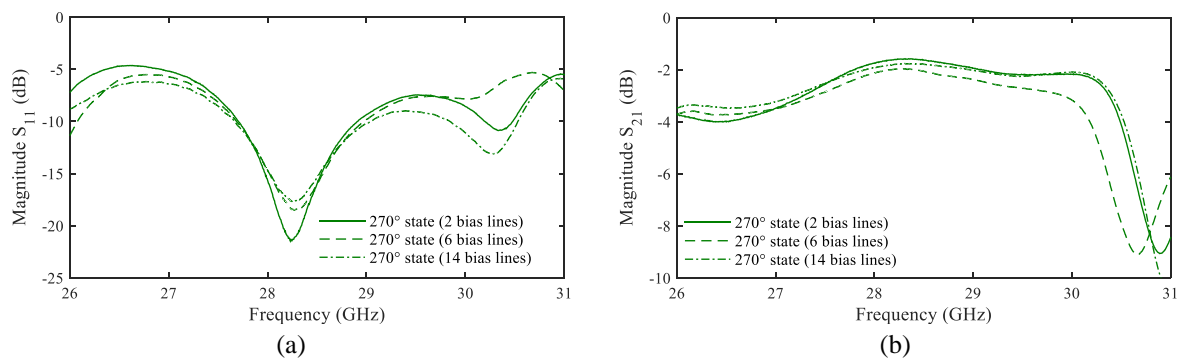


Figure IV-20: Impact of bias lines on the measured scattering parameters magnitudes in the waveguide in the 270° state: (a) reflection (S_{11}) and (b) transmission (S_{21}) coefficients.

4.2.3. Sensitivity analysis of the 2-bit linearly-polarized unit-cell

In order to investigate the difference between the measured and numerical results, waveguide simulations (Figure IV-7) have been performed in this section. As it is well known, manufacturing uncertainties limit the accuracy of fabricated PCBs. We have identified the main parameters which can be the cause of an impedance mismatch in the case of our active linearly-polarized unit cell. These parameters are: the diameter of the center via that connects the receiving and transmission layers, the thickness of bonding films, the dimensions of R_x and T_x patches, and the misalignment engendered when assembling of the layers.

In addition, an error was made in the layout of the unit-cells regarding the position of the holes for mechanical attachment to the waveguide (the holes are rotated by 90° with respect to the correct positions), so a part of the unit-cell is outside the waveguide (Figure IV-21).

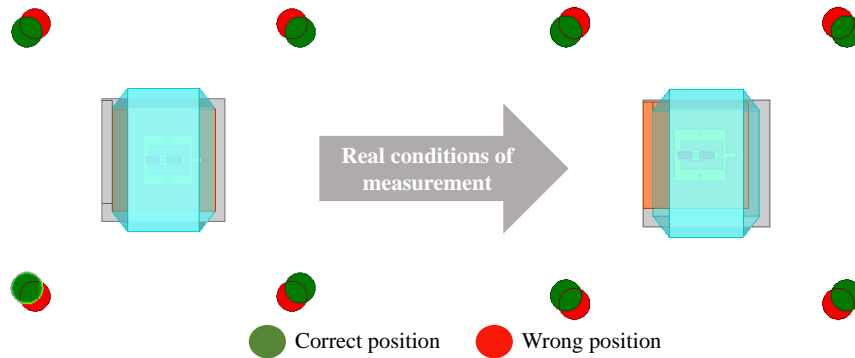


Figure IV-21: Holes positioning error for the measurement of the active unit-cell in the waveguide.

The scattering parameters of the four states of the active unit-cell considering the error on the position of the holes have been performed in the waveguide and compared to measured results for the four states, as depicted in Figure IV-22(a,b,c,d). The simulated insertion losses are equal to 1.1 dB, 1.1 dB, 1.7 dB, 1.9 dB, whereas the measured values correspond to 2.6 dB, 1.8 dB, 2.9 dB, and 1.9 dB at 29 GHz for the 0° , 90° , 180° , and 270° states, respectively. We concluded that a part of the mismatch of the unit-cell is due to this positioning error, but this is not the only mistake in the unit-cell.

CHAPTER IV. DESIGN AND OPTIMIZATION OF ACTIVE UNIT-CELLS FOR ELECTRONICALLY RECONFIGURABLE TRANSMITARRAYS

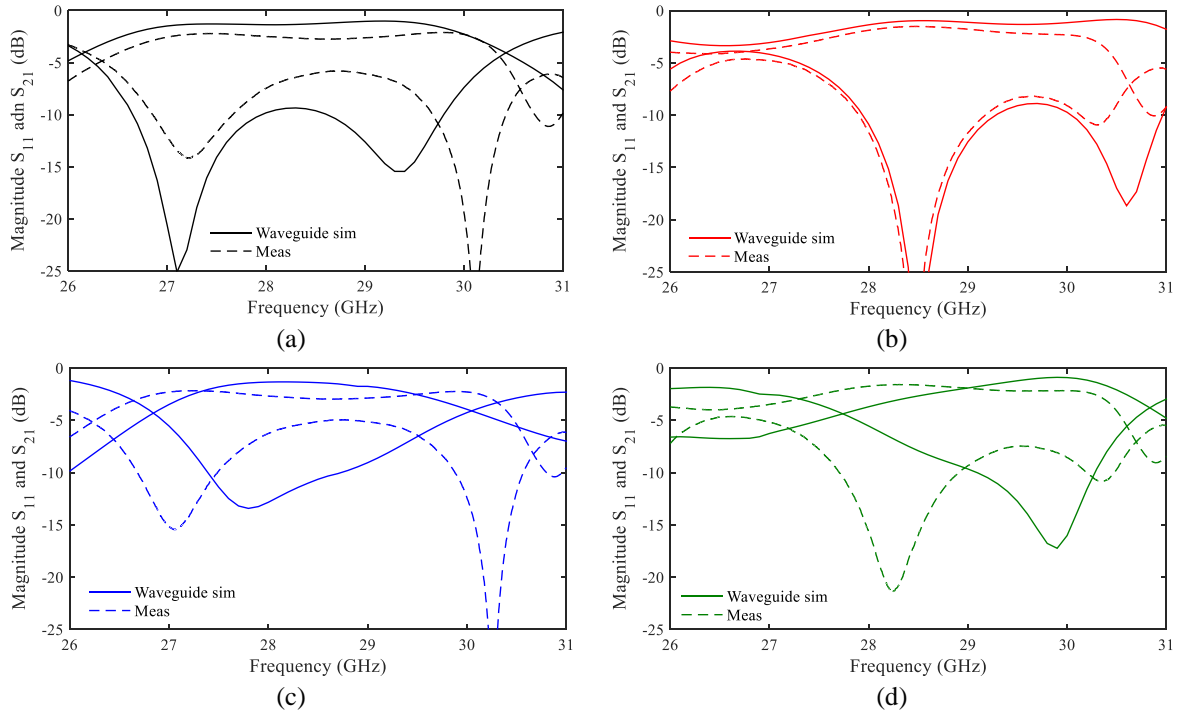


Figure IV-22: Measured and simulated scattering parameters magnitudes in the waveguide (taking into account holes positioning errors) in the (a) 0°, (b) 90°, (c) 180°, and (d) 270° states.

In addition to the holes positioning error, the manufacturing errors have been inspected as following. For reason of brevity, only the simulations results of the 0° and 90° states are presented.

The nominal lengths of the T_x and R_x patches (L_{Tx} , L_{Rx}) are varied by $\pm 30 \mu\text{m}$, which is generally the maximum error of fabrication for PCB technology. The magnitudes of the scattering parameters considering these variations are compared to the measured results as shown in Figure IV-23 and Figure IV-24. The considered error on both nominal T_x and R_x lengths has not changed the 3-dB transmission bandwidth of all states of the unit-cell.

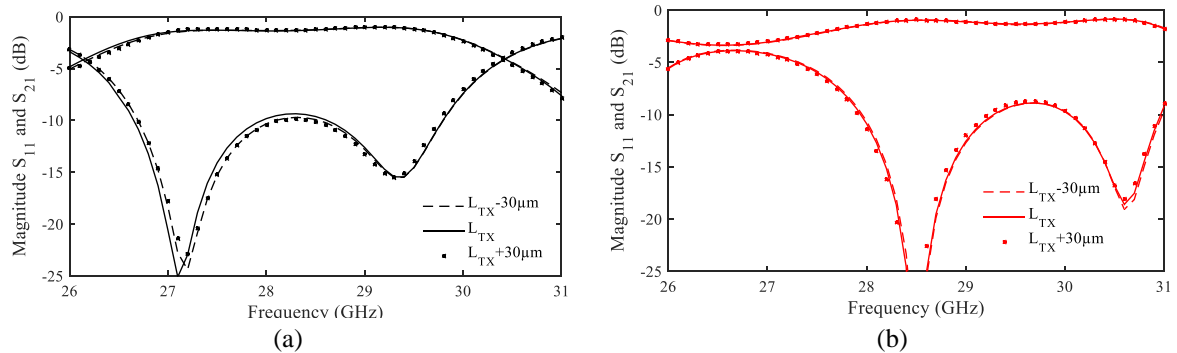


Figure IV-23: Impact of typical fabrication errors for the transmission patch length on the S-parameters: (a) 0° and (b) 90° states.

CHAPTER IV. DESIGN AND OPTIMIZATION OF ACTIVE UNIT-CELLS FOR ELECTRONICALLY RECONFIGURABLE TRANSMITARRAYS

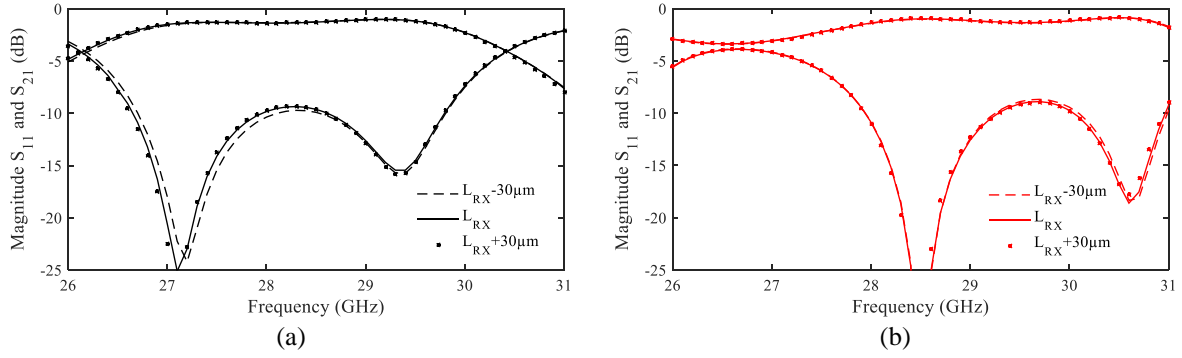


Figure IV-24: Impact of typical fabrication errors for the receiving patch length on the S-parameters: (a) 0° and (b) 90° states.

The final thickness of the bonding film may decrease during the assembly of the different layers of the unit-cell. Simulated results of the unit-cell (0° and 90° phase states) have been obtained by varying the nominal thickness of the transmission and receiving bonding films, as shown in Figure IV-25 and Figure IV-26, respectively. The bonding film thickness does not impact significantly the scattering parameters of the unit-cell.

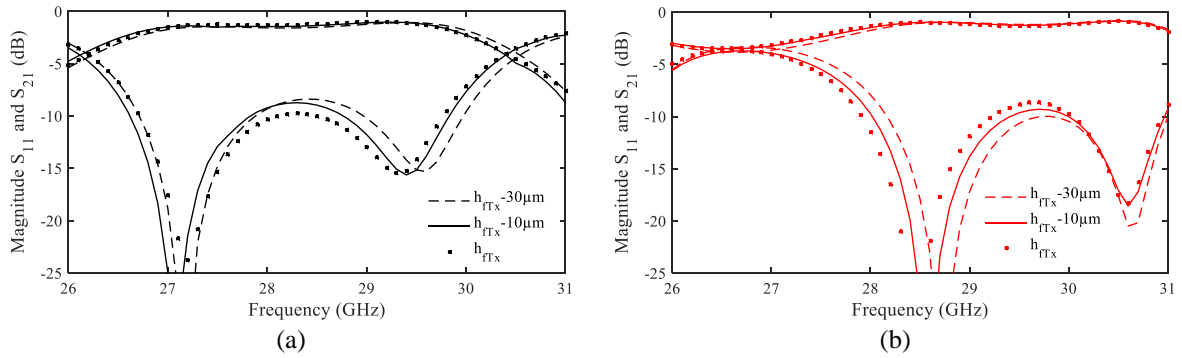


Figure IV-25: Impact of typical fabrication errors for the transmission bonding film thickness on the S-parameters: (a) 0° and (b) 90° states.

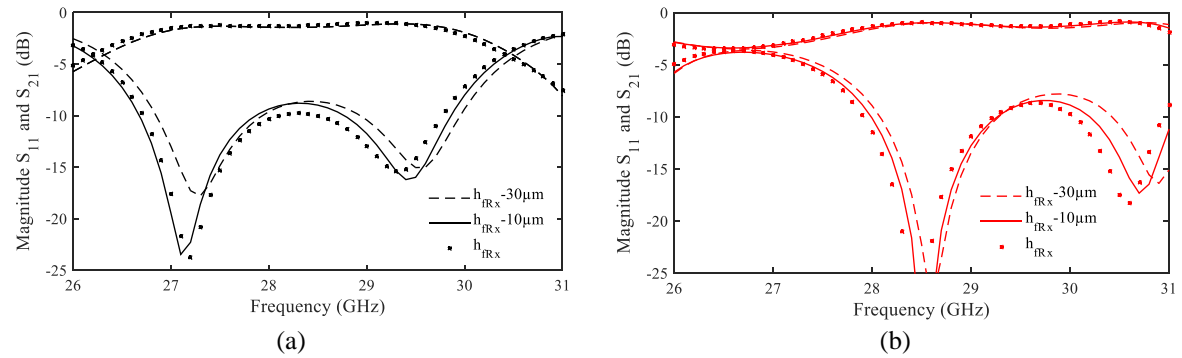


Figure IV-26: Impact of typical fabrication errors for the receiving bonding film thickness on the S-parameters: (a) 0° and (b) 90° states.

The nominal diameter of the center metallized via \varnothing_{dv} is varied by $\pm 30 \mu\text{m}$ to take into account possible manufacturing errors for the 0° and 90° unit-cells, as shown in Figure IV-27. A frequency shift of $\pm 200 \text{ MHz}$ and $\pm 300 \text{ MHz}$ is produced for the 0° and 90° states,

respectively. The insertion losses are almost the same as for the nominal diameter of the center via.

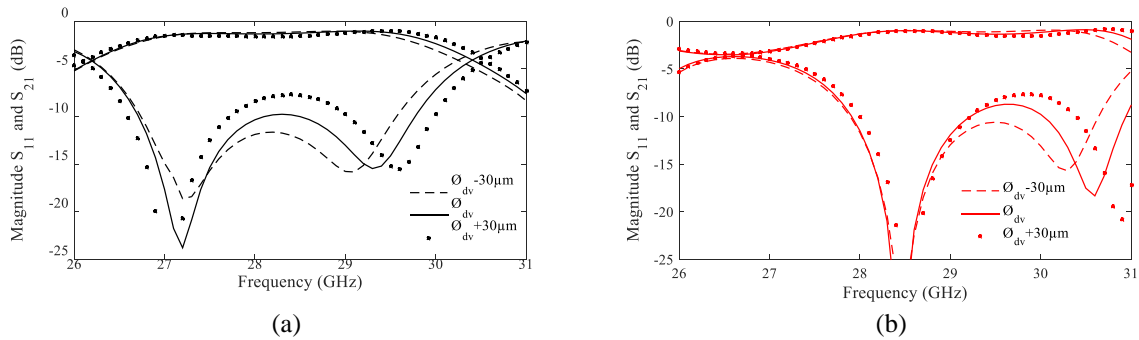


Figure IV-27: Impact of typical fabrication errors for the diameter of the metallized via on the S-parameters: (a) 0° and (b) 90° states.

The analysis of possible manufacturing errors and also holes positioning errors did not fully explain the difference between the measured and simulated results. The elementary cell has six layers, so it is difficult to list all the possible errors. Despite the significant insertion losses measured, the working principle of the active unit-cell with 2 bits of phase quantization has been validated.

4.3. Design and optimization of an active circularly-polarized unit-cell with 2 bits of phase resolution

In this section, the design and numerical simulations of a 2-bit circularly-polarized unit-cell, inspired from the linearly polarized unit-cell (section 4.1), are presented in detail.

4.3.1. Architecture of the proposed unit-cell

The structure of the proposed circularly-polarized unit-cell, inspired from the linearly-polarized one, includes six metal layers printed on three Rogers RT/Duroid 6002 substrates ($\epsilon_r = 2.94$, $\tan\delta = 0.0012$) and two Arlon CuClad 6700 films ($\epsilon_r = 2.35$, $\tan\delta = 0.0025$). We maintained this initial stack because we did not have enough time to re-optimize the circularly-polarized unit cell to fulfil the manufacturer requirements. Figure IV-28 shows the 3-D exploded view of the proposed circularly-polarized unit-cell at Ka-band with all dimensions summarized in Table IV-5.

The radiating elements working in receive and transmission mode are printed on both outermost metallic layers. A circularly-polarized O-shaped slot patch antenna with two truncated corners is used on the transmitting layer (M1, Figure IV-28(b)), while the receiving layer (M6, Figure IV-28 (f)) is composed of an O-shaped slot rectangular patch antenna. The two patch antennas are connected by a 200- μm diameter centered via-hole and separated by a

CHAPTER IV. DESIGN AND OPTIMIZATION OF ACTIVE UNIT-CELLS FOR
ELECTRONICALLY RECONFIGURABLE TRANSMITARRAYS

ground plane (M3, Figure IV-28 (d)). The two diodes on the Tx or Rx layers are polarized in opposite states using a single bias line with a positive or negative current. This leads to 0° and 180° phase states in the Tx side, while 0° and 90° phase states are obtained in the Rx side thanks to the delay line printed on the opposite side of its substrate. As a result, four phase-shifts (0° , 90° , 180° , and 270°) are obtained in transmission by combining different states of the receive and transmit layers.

Table IV-5: Simulated performances of the 2-bit circularly-polarized unit-cell.

Parameter	Value (mm)	Parameter	Value (mm)	Parameter	Value (mm)
l_{Tx}	2.3	l_{dc-gnd}	3.4	l_s	0.1
w_{Tx}	2.8	w_c	0.5	w_B	0.1
t_{1-Tx}	1.6	l_c	2.5	l_{Rx}	2.4
t_{2-Tx}	0.75	t_{1-Rx}	0.56	w_{Rx}	2.7
ϕ_{dB}	0.15	t_{2-Rx}	0.1	l_{line}	0.6

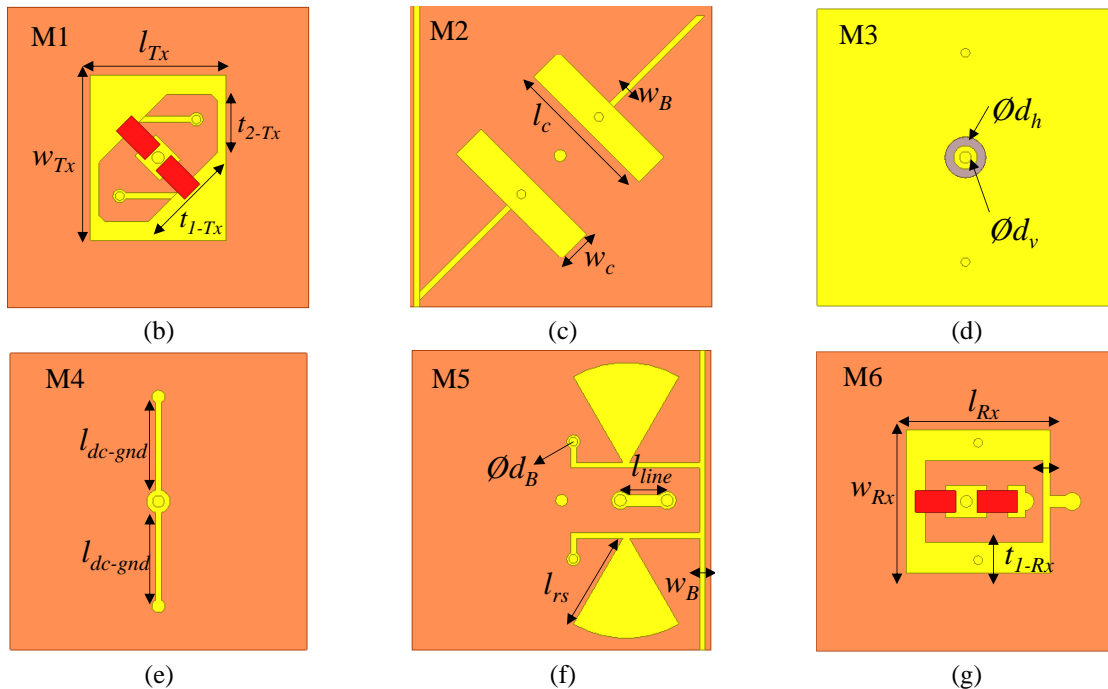
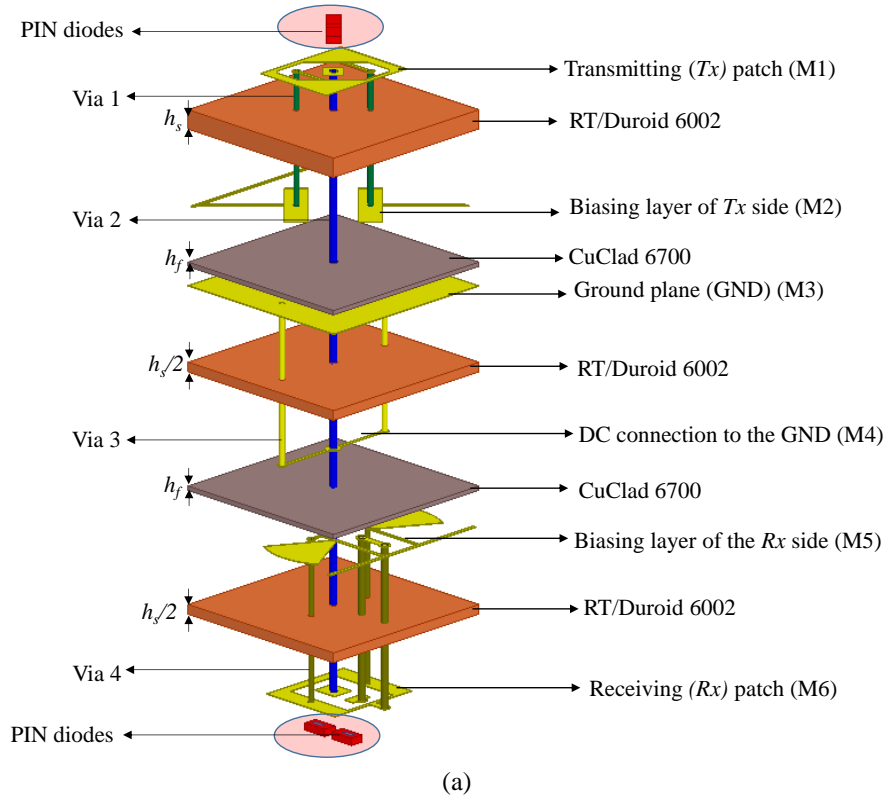


Figure IV-28: Proposed circularly-polarized unit-cell: (a) Schematic view, (b) transmitting layer, (c) biasing layer of the transmit side, (d) ground plane, (e) DC connection to the ground layer, (f) biasing layer of the receive side, and (g) receiving layer.

4.3.2. Simulated frequency response

Numerical simulations have been performed using the commercial software Ansys-HFSS in order to investigate the frequency responses of the proposed 2-bit unit-cell. Periodic

boundary conditions are applied on the unit-cell lateral faces to model an infinite array and Floquet port excitations are placed on both sides of the unit-cell. The scattering parameters of the circularly-polarized unit-cell have been calculated with the appropriate combination of the TE (Transverse-Electric) and TM (Transverse-Magnetic) orthogonal modes excited in the structure.

The parameters S_{11} and S_{22} indicate the reflection coefficients referred to ports 1 (R_x side) and 2 (T_x side), respectively. The relative 10-dB return loss (S_{11}) bandwidth is equal to 6.5%, 9.3%, 7.9%, 8.6% for the 0° , 90° , 180° , and 270° states as shown in Figure IV-29(a). The relative -10 dB matching (S_{22}) bandwidth corresponds to 10.3%, 13.8%, 12.1%, and 12.7% for the 0° , 90° , 180° , and 270° states, respectively (see Figure IV-29(b)).

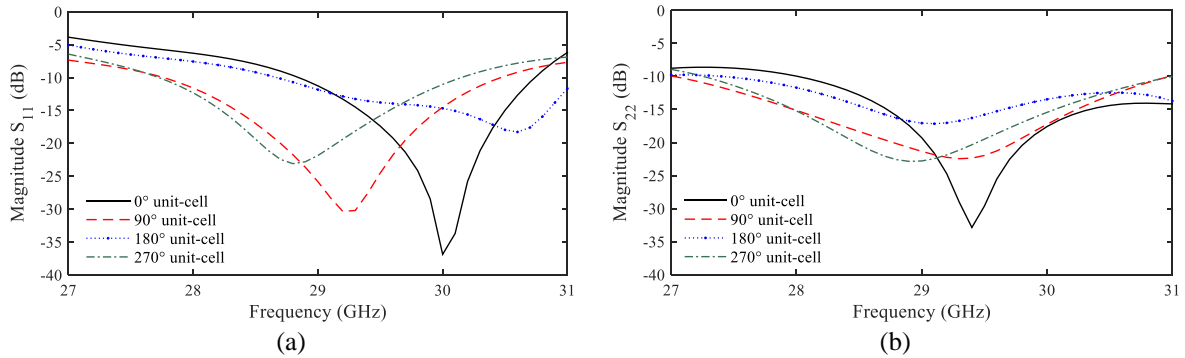


Figure IV-29: Reflection coefficient (a) S_{11} and (b) S_{22} referred to the Rx and Tx sides, respectively, of the proposed 2-bit circularly polarized unit-cell.

The magnitudes of the transmission coefficients associated to the left-handed and the right-handed circular polarizations are labelled S_{21-L} , and S_{21-R} , respectively, as indicated in Figure IV-30(a) and Figure IV-30(b). The relative 3-dB transmission bandwidth (S_{21-L}) is 10.3%, 12.4%, 12.4%, and 12.1% for the 0° , 90° , 180° , and 270° phase states, respectively. The minimum insertion loss equals 1.3 dB for both the 0° and 180° states, 1.1 dB for the 90° state and 1.2 dB for the 270° state. The cross-polarized transmission coefficient (S_{21-R}) is lower than -15 dB at 29 GHz, the broadside axial ratio 3-dB bandwidth is 4.5%, 3.8%, 4.1%, and 4.5% for the 0° , 90° , 180° , and 270° states, respectively.

CHAPTER IV. DESIGN AND OPTIMIZATION OF ACTIVE UNIT-CELLS FOR ELECTRONICALLY RECONFIGURABLE TRANSMITARRAYS

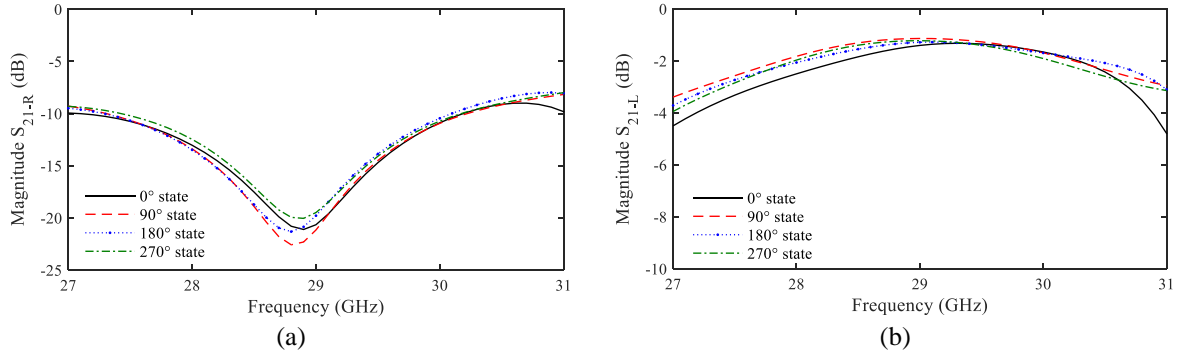


Figure IV-30: Magnitude of the transmission coefficients associated to the (a) right-, and (b) left-handed circular polarization.

The transmission phase of the four states of the 2-bit left-handed circularly-polarized unit cell and the phase-shift between the 0° state and the other states are plotted in Figure IV-31(a) and Figure IV-31(b). The phase difference between two consecutive states is around 90° with a maximum error of 23° in the 27-31 GHz frequency band.

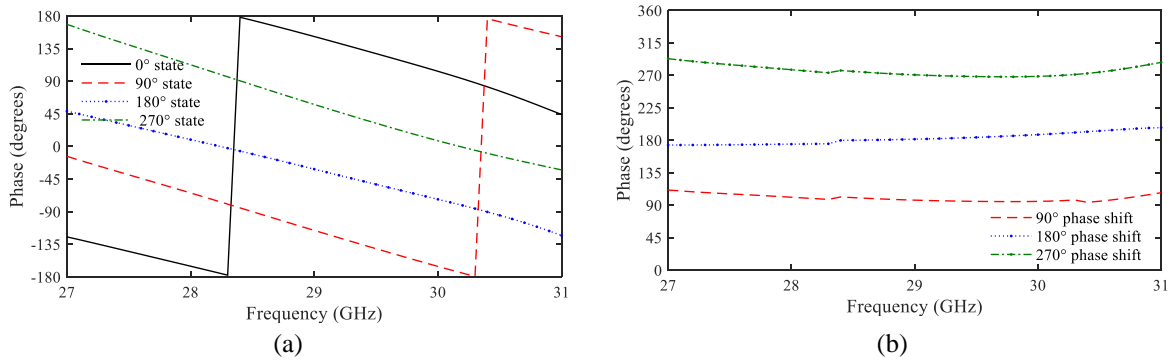


Figure IV-31: (a) Transmission phase and (b) phase-shift between the 0° state and the other states.

An active circularly-polarized unit-cell with 2 bits of phase quantization working at Ka-band has been presented in this section. It exhibits good performances as summarized in Table IV-6.

Table IV-6: Summary of the 2-bit circularly-polarized unit-cell performances.

	0°	90°	180°	270°
S₁₁				
10-dB bandwidth	28.8 - 30.7 GHz	27.8- 30.5 GHz	28.7 - 31.0 GHz	27.8 - 30.1 GHz
Minimum insertion loss	1.3 dB	1.1 dB	1.3 dB	1.2 dB
S_{21-L}				
3-dB bandwidth	27.7 - 30.7 GHz	27.3 – 30.9 GHz	27.3 - 30.9 GHz	27.4 – 30.9 GHz

4.4. Conclusion

In this chapter, we described in detail the design of electronically reconfigurable unit-cells with 2 bits of phase resolution (4 phase states) in both linear and circular polarization and working at Ka-band.

We first presented the active linearly-polarized unit-cell which is composed of six metal layers, three substrates and two bonding films. Two p-i-n diodes are used both on the receiving and transmitting layers to control the phase-shift. The proposed unit-cell has been simulated using the commercial software Ansys HFSS with infinite periodic boundary conditions and Floquet port excitations and also in waveguide simulator to mimic the real condition of characterization. It exhibits a minimum insertion loss of about 1dB and a 3-dB transmission bandwidth of 9.6%, 16.5%, 12.1%, and 15.5% at 29 GHz, for the 0° , 90° , 180° , and 270° phase states, respectively. We have shown that the insertion of several bias lines has no impact on the performances of the proposed linearly-polarized unit-cell. Then, the unit-cell was fabricated and characterized in a WR-28 waveguide simulator. It has presented higher insertion losses than predicted. The measured minimum insertion loss is about 2 dB with a relative 3-dB transmission bandwidth corresponding to 11.7%, 10.0%, 12.1%, and 10.3% at 29 GHz for the 0° , 90° , 180° , and 270° states, respectively. This difference between simulated and measured results is certainly due to manufacturing errors. It is difficult to find this error because of the complexity of the unit-cell (six metal layers). Despite this disagreement between the simulations and measurement results, we have nevertheless validated the working principle of an active unit-cell with four phase states.

The final section of this chapter was dedicated to the design of a 2-bit circularly-polarized unit-cell. It is based on the same stack up as the linearly-polarized unit-cell, only the bonding film is different (the CuClad 6700 is used here). Simulation results of the proposed 2-bit unit-cell have shown a minimum insertion loss of about 1.2 dB for all phase states of the unit-cell. The 3-dB transmission bandwidth is equal to 10.3%, 12.4%, 12.4%, and 12.1% for the 0° , 90° , 180° , and 270° states, respectively. The 3-dB axial ratio corresponds to 4.5%, 3.8%, 4.1%, and 3.8% for the 0° , 90° , 180° , and 270° states, respectively.

The proposed unit-cell was not prototyped due to lack of time, but it is possible to characterize it in a waveguide by using the characterization technique developed in Luca di Palma's thesis for circularly-polarized unit-cells [113].

Chapter V. Linearly-polarized electronically reconfigurable transmitarray antenna with 2-bit phase resolution in Ka-band

In this chapter, we present the design and experimental demonstration of an electronically reconfigurable transmitarray based on the 2-bit linearly-polarized unit-cell demonstrated in Chapter IV. Firstly, the design and optimization of the proposed TA is detailed. Then, the prototype architecture of the TA and the electronic control board are described. Finally, the experimental results compared to numerical ones are presented.

5.1. Design and optimization of the active linearly-polarized transmitarray

The 2-bit linearly-polarized unit-cell described in Chapter IV is used as a building block of a square transmitarray. The size of the transmitarray is fixed to 14×14 unit-cells, so the length (D) of the array side equals 71.4 mm ($7 \times \lambda_0$). The TA contains in total 784 PIN diodes in order to control the phase of the transmitted wave and allow the electronic reconfiguration of the radiation pattern. The performance of the transmitarray has been simulated with the ad-hoc simulation tool. It is illuminated by a linearly-polarized waveguide horn (WR-34) [111] with a nominal gain of 10 dBi placed at the focal distance $F = 48$ mm ($4.7 \times \lambda_0$, $F/D = 0.67$), as shown in Figure V-1. The focal distance and the phase distribution were chosen to maximize the aperture efficiency.

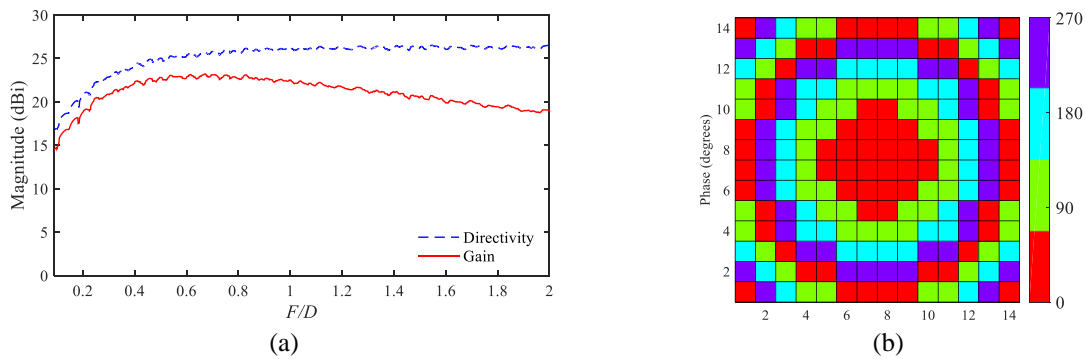


Figure V-1: Optimization of the proposed 196-element transmitarray. (a) Directivity and gain as a function of the focal ratio (F/D). (b) Optimal phase distribution for a broadside beam.

The radiation characteristics of the reconfigurable TA extracted from the ad-hoc simulator are compared to those obtained by a full-wave simulation using Ansys HFSS. The latter is done using the finite element-boundary integral (FE-BI) solver in order to reduce the computation time. The theoretical and simulated frequency response of the 196-element transmitarray in terms of gain are plotted in Figure V-2.

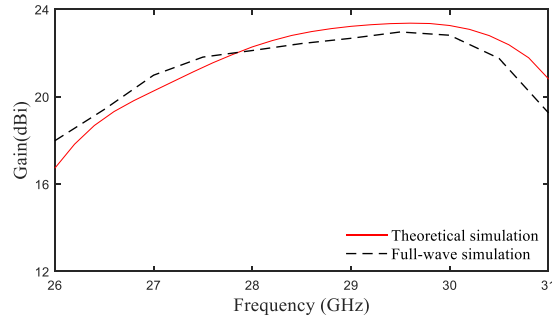


Figure V-2: Theoretical and full-wave simulated broadside gain of the 2-bit transmitarray as a function of frequency.

The 3-dB gain bandwidth goes from 26.7 GHz to 31 GHz, which corresponds to a fractional bandwidth of 14.8% at 29 GHz. A maximum difference of 1 dB is observed between the theoretical result and the full-wave simulation.

The radiations patterns of the array (E-, and H-planes) have been evaluated numerically by our ad-hoc simulator and also by full-wave simulations using Ansys HSS. A good agreement is obtained between the two numerical methods as shown Figure V-3. The higher side-lobe levels observed in the two cut-planes for the full-wave simulation are due to the spillover radiation that is not taken into account in the ad-hoc simulation. The ground plane could be extended around the TA to solve this problem.

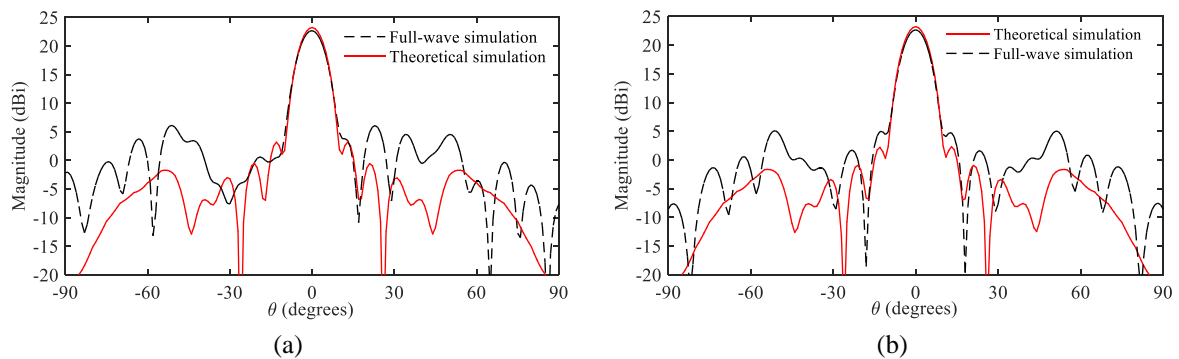


Figure V-3: Theoretical and simulated radiation patterns of the 196-element transmitarray at 29 GHz: (a) E, and H planes.

The transmitarray antenna demonstrates a maximum gain of 23.2 dBi, corresponding to an aperture efficiency of 35%, and a side-lobe level equal to -20.0 dB at 29 GHz. A difference of 0.5 dB is observed between the full-wave and theoretical maximum gains at 29 GHz. The

cross-polarization level is lower than -12.6 dBi. Beam-steering in any cut-plane can be achieved by changing properly the phase-shift distribution across the array. The ad-hoc radiation patterns in E- and H-planes for θ_0 ranging from -60° to $+60^\circ$ in 10° steps are plotted in Figure V-4. Some cases of phase distribution (beam pointing at 20° , 40° , and 60°) in both E-, and H- planes are shown in Figure V-5, and Figure V-6, respectively. The maximum gain decreases from 23.2 dBi to 17.6 dBi from broadside to a 60° scan angle in both E-, and H-planes as depicted in Figure V-4(a,b).

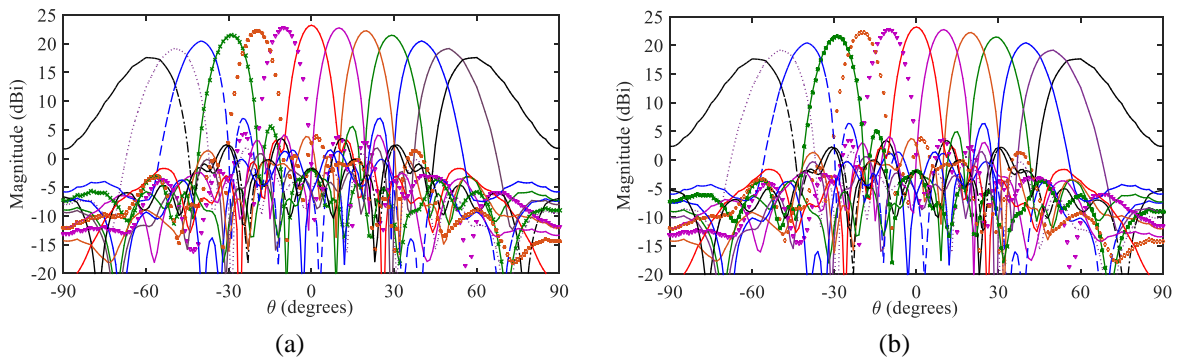


Figure V-4: Co-polarized radiation patterns computed at 29 GHz for a beam scanned from -60° to $+60^\circ$ in (a) E, and (b) H planes.

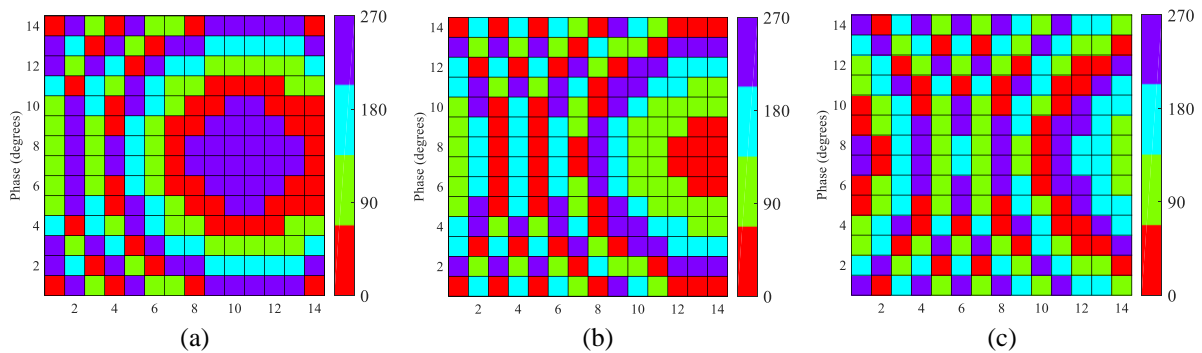


Figure V-5: Optimal phase distributions computed at 29 GHz for a beam pointing at (a) 20° , 40° , and 60° in E plane.

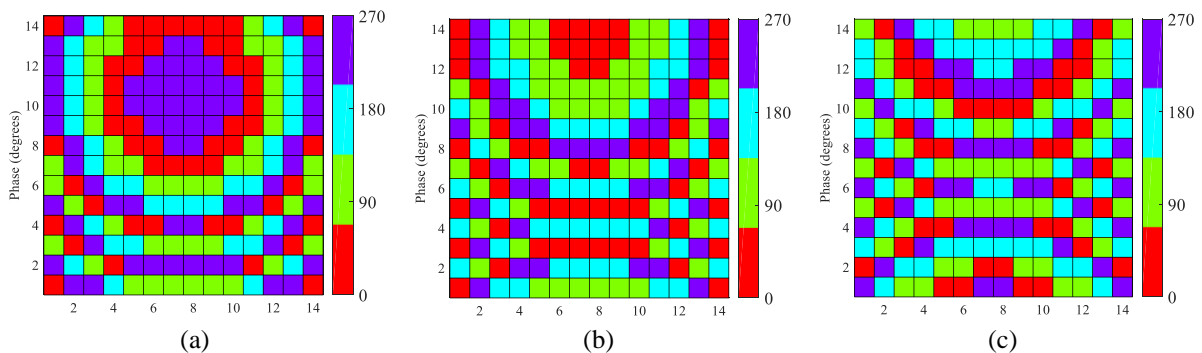


Figure V-6: Optimal phase distributions computed at 29 GHz for a beam pointing at (a) 20° , 40° , and 60° in H plane.

5.2. Architecture of the prototype board

As regards to the numerical good performances demonstrated by the transmitarray antenna (relatively high gain and beam scanning capability up to $\pm 60^\circ$ in both E and H planes) (section 5.2), we decided to fabricate a prototype of the active transmitarray. The TA comprises 14×14 unit-cells in which 784 PIN diodes are integrated in receiving and transmitting sides to control the transmission phase for electronic beam scanning capability. The prototype architecture for realization of the proposed transmitarray is addressed in this section.

The transmitarray antenna is divided in four sub-arrays to bias the PIN diodes. The bias lines arrangement of the full TA is realized by symmetries in both receiving and transmission sides. A total number of 98 bias lines are necessary to polarize the 196 PIN diodes located in the transmitting and receiving layers of a sub-array. Bias lines are distributed on the two outermost layers and the two inner layers closest to the ground plane to respect the line spacing constraints (a minimum spacing of 1 mm is required between two adjacent bias lines on the circuit board). The routing of the bias lines for the diodes on the transmission side in the external and inner layers is shown in Figure V-7(a) and Figure V-7(c), respectively, for the 7×7 subarray. Close-up views on one line of 7 unit-cells are presented in Figure V-7(b) and Figure V-7(d). Figure V-8 shows similar views for the bias line arrangement of the receiving side (external and inner layers). Figure V-8(a) shows also on the left side the footprint of the 100-pin connector used to interface the array with the electronic control boards.

The set-up for electronic control of the diodes states in the array is composed of a computer with the control code implemented in Matlab, a digital input/output interface module, two independent DC supplies to generate negative and positive bias currents, and four control boards [42] (more details are given in Appendix B). Each control board is able to control up to 100 bias lines. It contains 13 shift registers, 25 4×4 switches, and 100 resistors. The resistors are used to set the current at ± 10 mA on each bias line at the output of the switches. Each switch is provided with a negative ($-V_{cc}$) and positive ($+V_{cc}$) voltage ($V_{cc} = 5\text{V}$). Both polarization states (ON/OFF) are obtained by changing the direction of the bias current in the bias line.

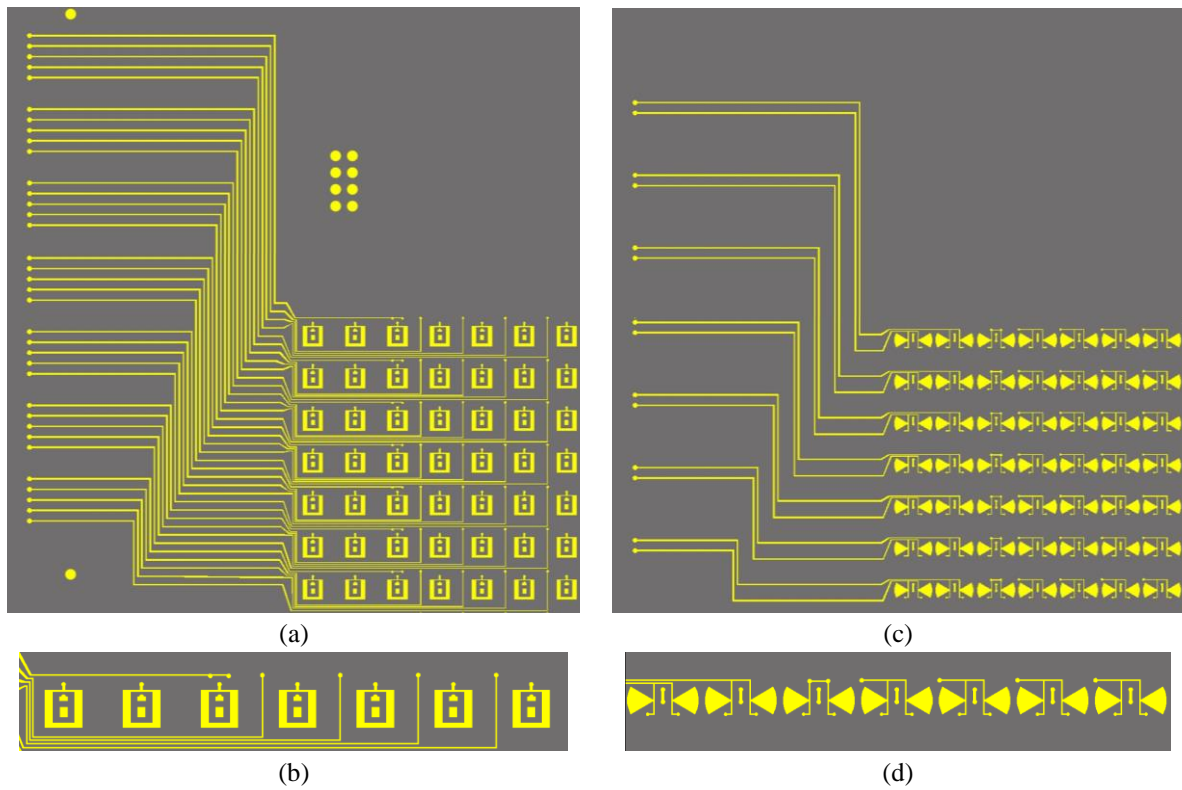


Figure V-7: Arrangement of the bias lines in the external layer for diodes on the transmission patches: (a,b) sub-array of 7×7 unit-cells, (c,d) a line of 7 unit-cells of the sub-array.

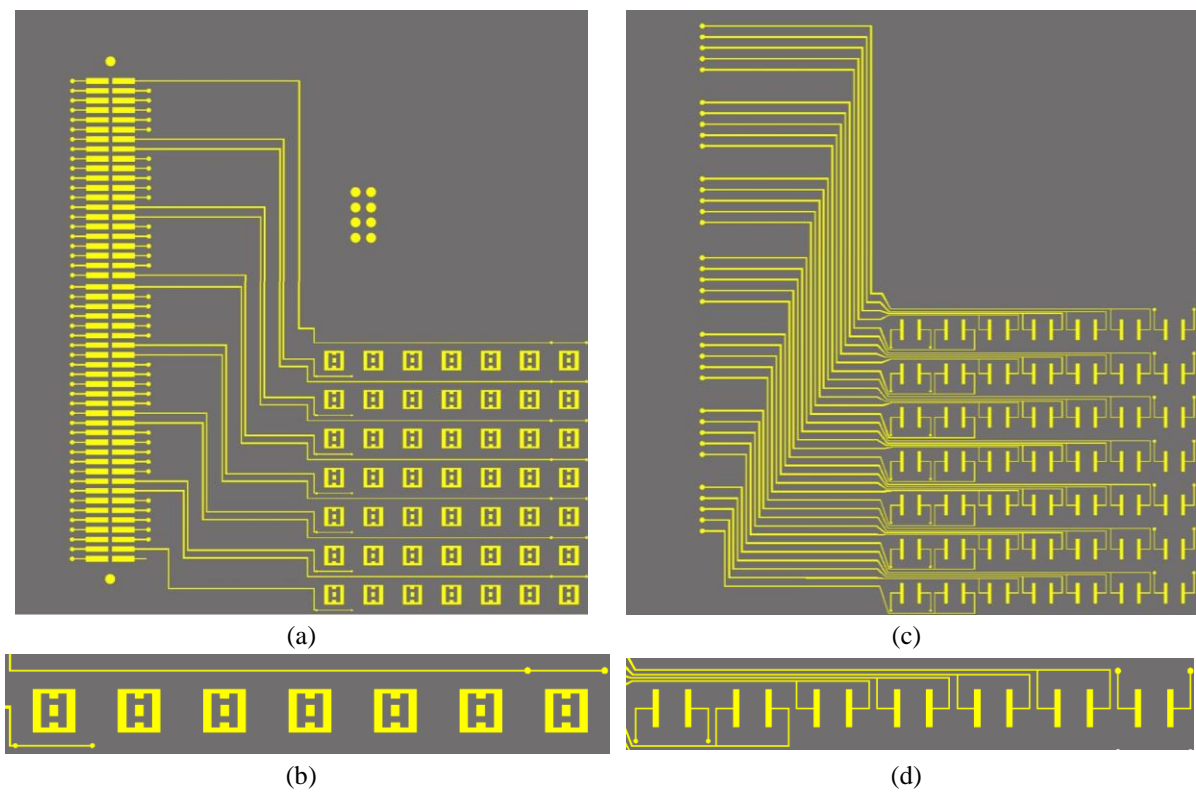


Figure V-8: Arrangement of the bias lines in the external layer for diodes on the receiving patches: (a,b) sub-array of 7×7 unit-cells, (c,d) a line of 7 unit-cells of the sub-array.

After the routing step, the 14×14 unit-cells transmitarray was fabricated based on PCB board technology. The 784 PIN diodes have been soldered on the two outermost layers of the TA. A 2×50 -pin 1.27-mm connector (TFM 150 02 LD), and a 2×4 -pin 2-mm connector (SQT 104 01 LD) from SAMTEC [114] are used to interconnect each sub-array to the electronic control boards and to get the connection to the ground plane. Four holes are drilled in the corners to mount the TA prototype on the mechanical support. The top (transmission layer) and bottom (receiving layer) views of the TA prototype are illustrated in Figure V-9 and Figure V-10, respectively

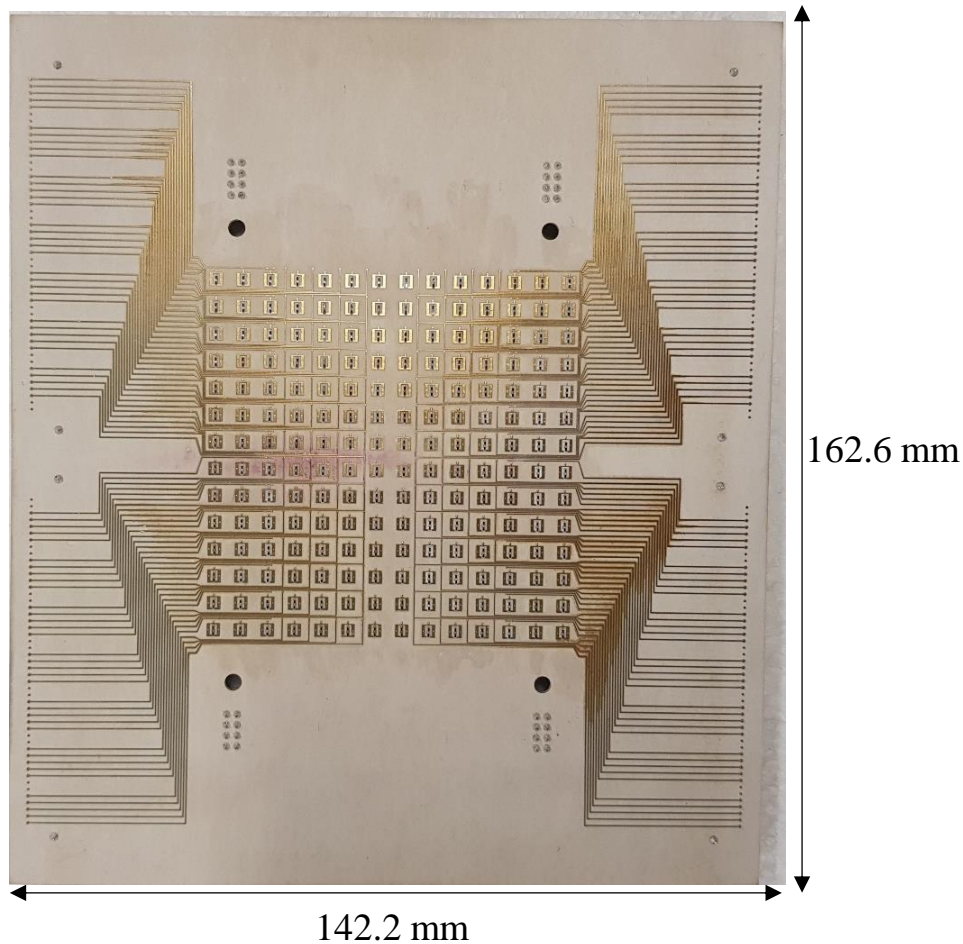


Figure V-9: Prototype of the 2-bit electronically reconfigurable transmitarray: top view (transmitting layer).

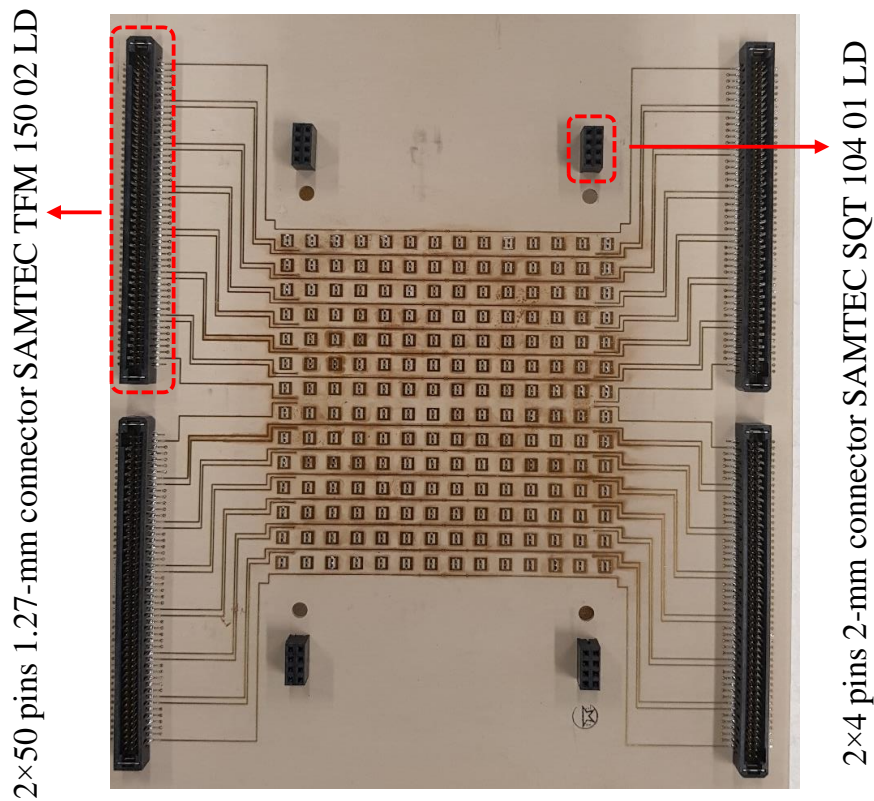


Figure V-10: Prototype of the 2-bit electronically reconfigurable transmitarray: bottom view (receiving layer).

5.3. Experimental results

The fabricated prototype of the transmitarray has been characterized in the anechoic chamber of CEA-Leti. There is 3m between the measuring antenna and the antenna under test; this distance is much greater than the far field zone of the antenna. The setup of electronically reconfigurable TA prototype mounted in the anechoic chamber is presented in Figure V-11.

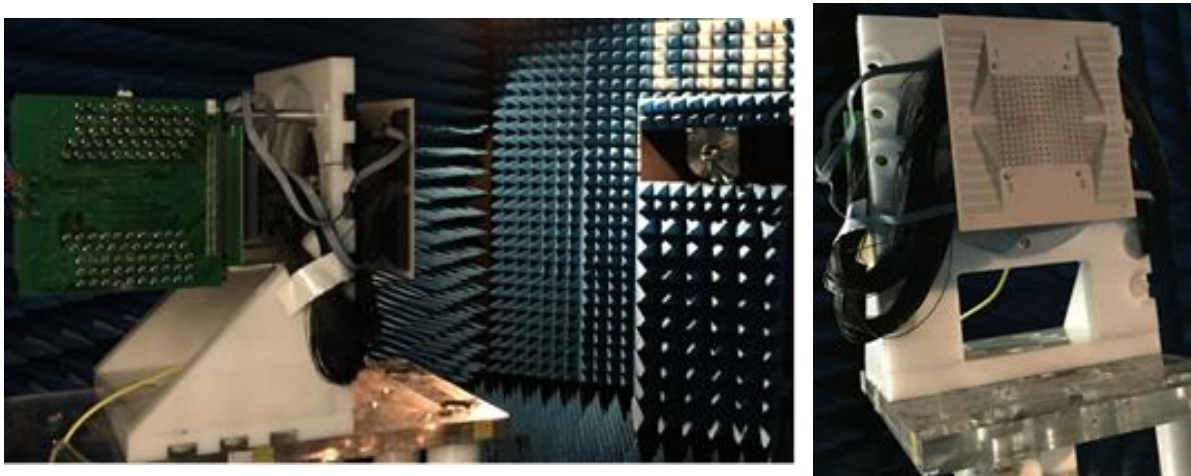


Figure V-11: Setup of the TA prototype mounted in the anechoic chamber for characterization.

The broadside gain was measured with the prototype mounted both for vertical and horizontal polarization. The gain measurements are compared to the theoretical one as a function of frequency in Figure V-12. A lower measured gain than predicted by theoretical and full-wave simulation is observed. The measured and simulated broadside gain at 29 GHz are 19.8 dBi and 23.2 dBi, showing a difference of 3.4 dB.

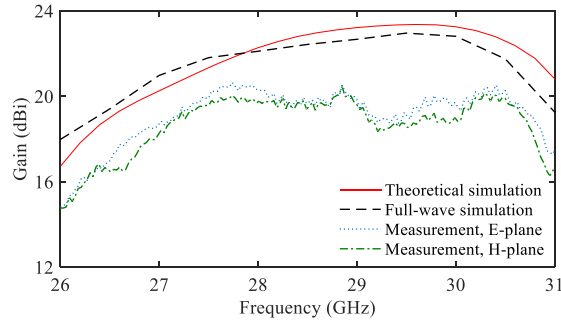


Figure V-12: Broadside gain: theoretical simulation (solid line), full-wave simulation (dashed line), and measurement in vertical (dot line) and horizontal polarization (dash-dot line).

The simulated and measured radiation patterns (normalized) at broadside in both E-, and H-planes are presented in Figure V-13. The main beam is well formed with the correct beam width, even though the side-lobe levels are higher than expected.

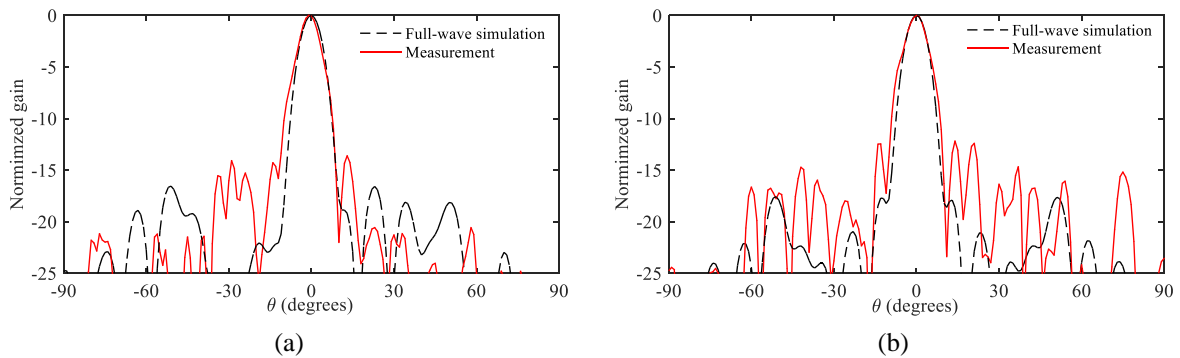


Figure V-13: Normalized radiation patterns computed at 29 GHz in (a) E and (b) H planes. Measured results (solid lines) and simulated results (dash lines).

An important disagreement is observed between the measurements and the simulations, in particular on the gain level (Figure V-12).

Firstly, we have precluded that diodes are failed by testing them individually with a multimeter. Then, we checked the state of each diode under bias and we observed DC (Direct Current) short circuits between some bias lines and the ground plane. In these unit cells, the diodes are to 0V and consequently their state is close to the blocked state. Thereafter, these faulty diodes were removed as indicated in the Figure V-14. A total of 51 faulty bias lines were found probably due to some fabrication errors.

Next, we have listed the positions of the faulty unit-cells as shown in Figure V-14, and we have carried out a new full-wave simulation where we removed the faulty PIN diodes.

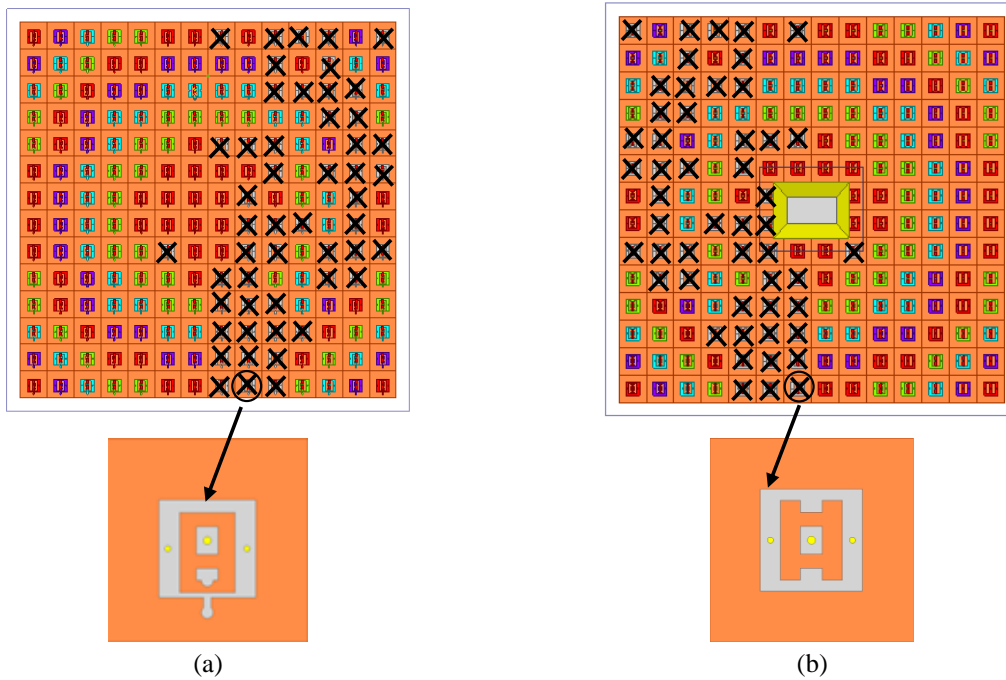


Figure V-14: Location of the faulty unit-cells (in cross) in the prototype: (a) Top and (b) bottom views.

The measured frequency responses of the 196-element transmitarray in terms of gain for the broadside beam in both E and H planes are compared to full-wave simulation and theoretical results, as illustrated in Figure V-15. A good agreement is obtained now between the numerical and measured results in both planes. The 3-dB measured gain-bandwidth at broadside is 4.7 GHz (26.2-30.9 GHz), which is a fractional bandwidth of 16.2% at 29 GHz. The measured, theoretical, and full-wave simulated gains at 29 GHz correspond to 19.8, 20.5, and 19.2 dBi, respectively. A maximum gain difference of 0.7 dB at 29 GHz is observed between the theoretical and measured results, which is in accordance with measurement accuracy at Ka-band, as shown in Figure V-15.

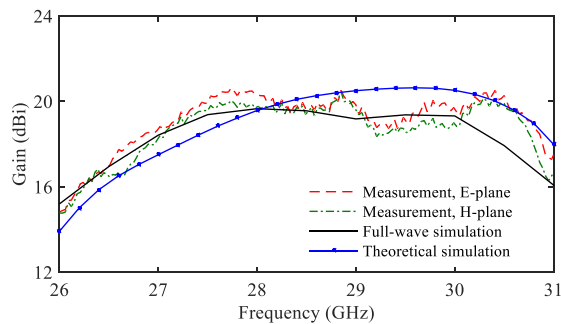


Figure V-15: Measured gain as a function of frequency in E (dash lines), and H (dash-dot lines) planes of the prototype compared to the full-wave and theoretical results.

The beam-scanning capability of the manufactured transmitarray has been characterized considering the ad-hoc calculated phase distribution as shown for some cases of beam steering in Figure V-5, and Figure V-6. The co-, and cross-polarized radiation patterns of the TA prototype considering steering angles between -60° to $+60^\circ$ by 10° steps in both E and H planes are shown in Figure V-16 and Figure V-17, respectively.

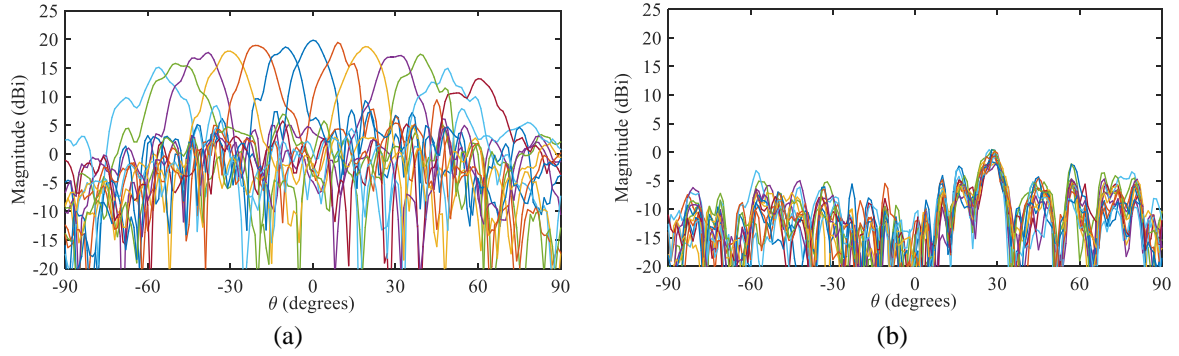


Figure V-16: (a) Co-, and (b) cross-polarized measured radiation patterns at 29 GHz in E plane for different steering angles from -60° to $+60^\circ$.

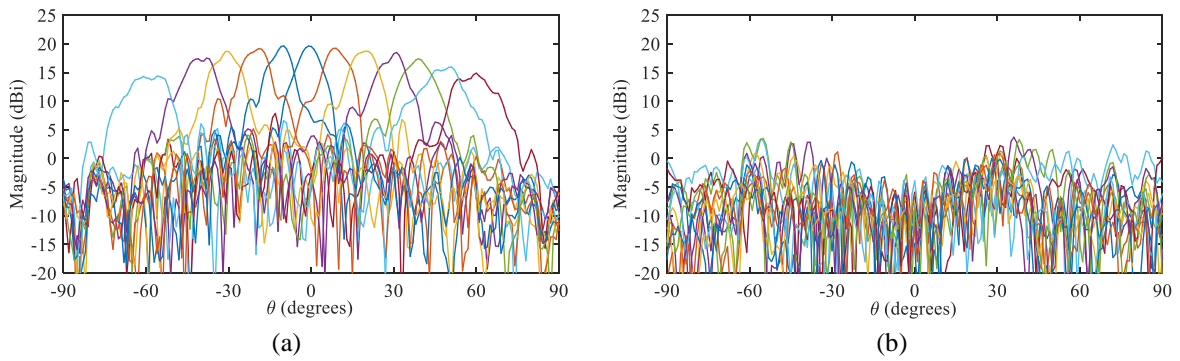


Figure V-17: (a) Co-, and (b) cross-polarized measured radiation patterns at 29 GHz in H plane for different steering angles from -60° to $+60^\circ$.

The maximum gain at broadside is equal to 19.8 dBi. The maximum gain measured in E plane at steering angles of -60° and 60° equal 15.1 dBi and 13.1 dBi, respectively, and 14.4 dBi and 14.9 dBi in H plane. In the case of beam scanning at -40° and 40° , the measured maximum gain in E plane is 17.7 dBi and 17.4 dBi, respectively, and 17.1 dBi and 17.4 dBi in H-plane, respectively. For steering angles of -20° , and 20° , we have measured a maximum gain in E plane of 18.9 dBi and 18.7 dBi, respectively, and 19.1 dBi and 18.7 dBi in H plane, respectively. The results show that the radiations are asymmetrical on both E and H planes due to the distribution of the defective unit-cells, which is more important on one side than the other.

The measured and simulated radiation patterns of the proposed transmitarray have been investigated in both E and H planes for steering angles of -40° , -20° , 0° , 20° , 40° at 29 GHz as shown in Figure V-18, Figure V-19, Figure V-20, Figure V-21, and Figure V-22, respectively.

Good agreement in terms of gain level is obtained between the simulated and measured results. The measured and simulated gains at broadside correspond to 19.8 dBi, and 20.5 dBi, respectively, with an aperture efficiency of 15.9%, and 18.7%.

The performances (directivity, gain, side-lobe levels (SLL), and half-power beam widths (HPBW)) of the proposed 2-bit electronically reconfigurable transmitarray in E and H planes are summarized in Table V-1 and Table V-2, respectively.

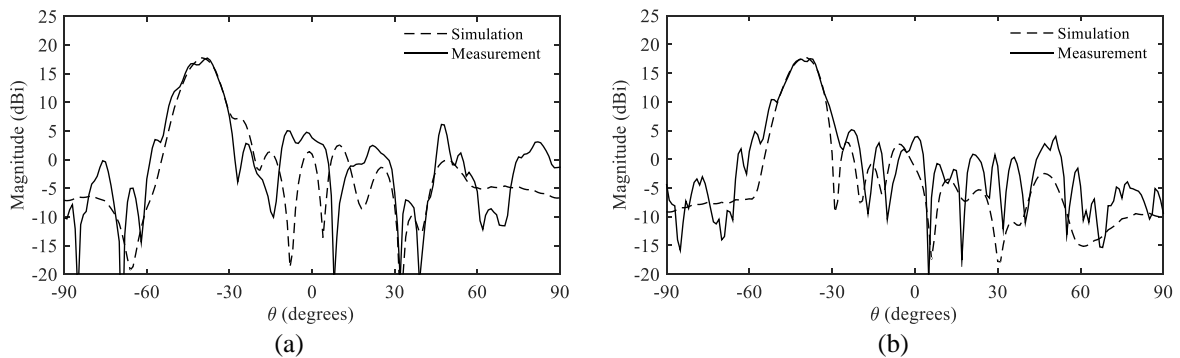


Figure V-18: Measured and simulated radiation patterns at 29 GHz in (a) E and (b) H planes for a steering angle of -40° .

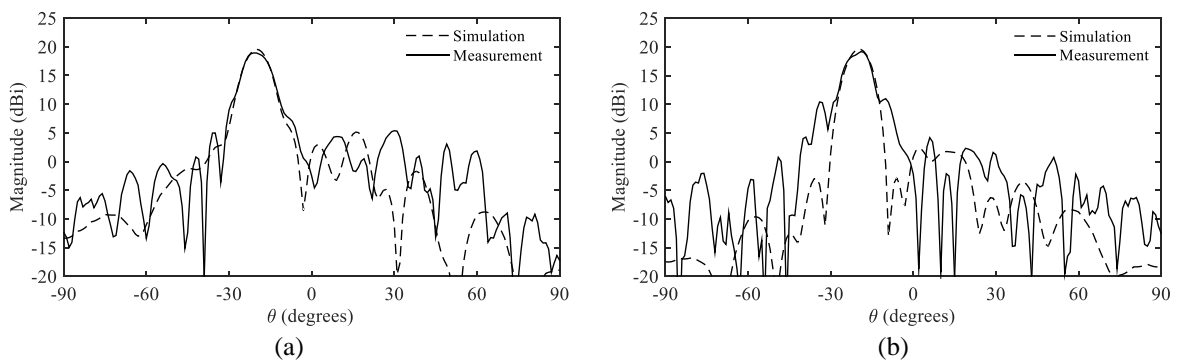


Figure V-19: Measured and simulated radiation patterns at 29 GHz in (a) E and (b) H planes for a steering angle of -20° .

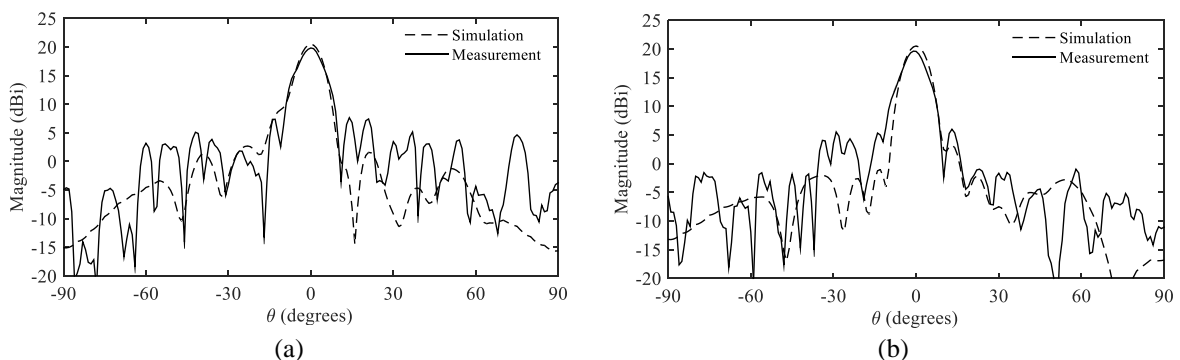


Figure V-20: Measured and simulated radiation patterns at 29 GHz in (a) E and (b) H planes at broadside.

CHAPTER V. LINEARLY-POLARIZED ELECTRONICALLY RECONFIGURABLE TRANSMITARRAY ANTENNA WITH 2-BIT PHASE RESOLUTION IN KA-BAND

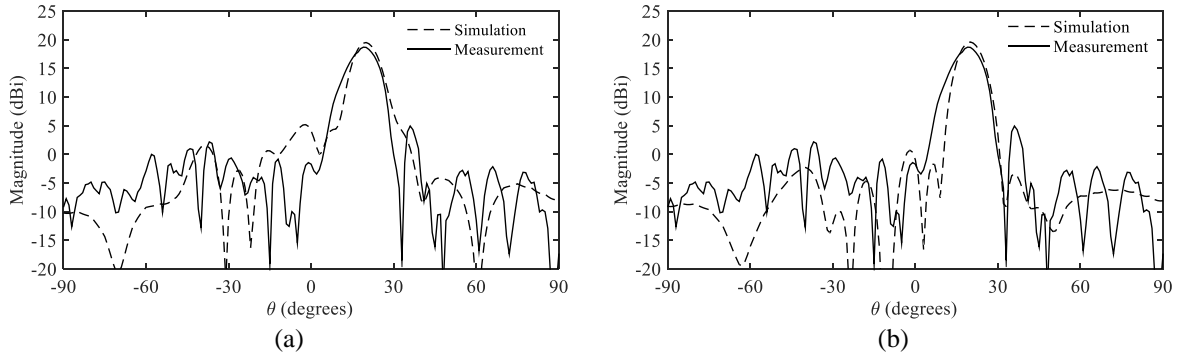


Figure V-21: Measured and simulated radiation patterns at 29 GHz in (a) E and (b) H planes for a steering angle of 20°.

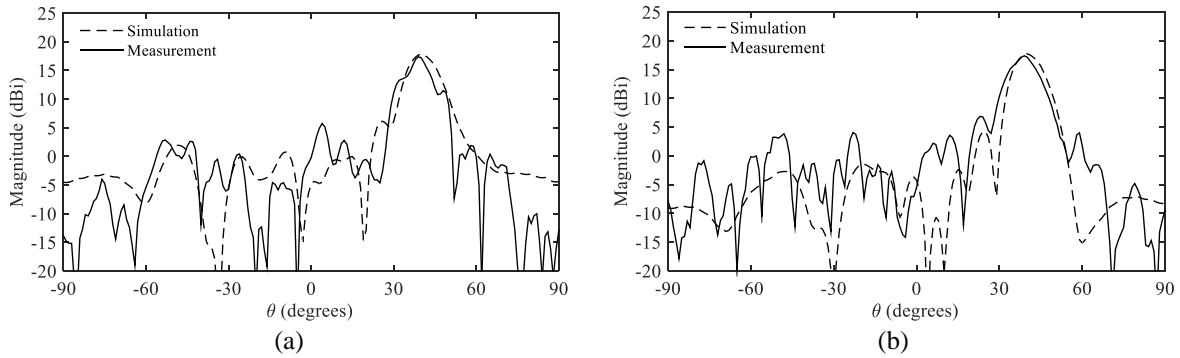


Figure V-22: Measured and simulated radiation patterns at 29 GHz in (a) E and (b) H planes for a steering angle of 40°.

Table V-1: Summary of the 2-bit electronically reconfigurable transmitarray performances in E plane at 29 GHz.

Steering angle	Directivity (dBi)		Gain (dBi)		HPBW (degrees)		SLL (dB)	
	Sim.	Meas.	Sim.	Meas.	Sim.	Meas.	Sim.	Meas.
-60°	18.8	14.8	15.1	17	9.1	14.1	5.3	
-50°	20.4	16.5	15.8	13	14.5	11.8	11.4	
-40°	21.7	17.7	17.7	11.0	12.7	10.7	14.3	
-30°	22.7	18.8	17.9	10.0	10.6	18.1	14.1	
-20°	23.5	19.6	18.9	10.0	10.6	16.7	14.0	
-10°	24.0	20.1	18.6	10.0	10.2	16.8	12.8	
0°	24.4	20.5	19.8	9.0	9.5	18.9	12.5	
10°	24.0	20.0	19.4	9.0	6.4	14.8	11.4	
20°	23.5	19.5	18.7	9	11.2	14.4	13.8	
30°	22.7	18.7	17.2	9.5	12.6	16.7	12.6	
40°	21.8	17.9	17.4	11.5	8.6	11.8	6.4	
50°	20.4	16.5	14.9	14.6	11.5	15.2	5.9	
60°	19.0	15.0	13.1	16.9	10.9	14.8	2.7	

CHAPTER V. LINEARLY-POLARIZED ELECTRONICALLY RECONFIGURABLE TRANSMITARRAY ANTENNA WITH 2-BIT PHASE RESOLUTION IN KA-BAND

Table V-2: Summary of the 2-bit electronically reconfigurable transmitarray performances in H plane at 29 GHz.

Steering angle	Directivity (dBi)		Gain (dBi)		HPBW (degrees)		SLL	
	Sim.	Meas.	Sim.	Meas.	Sim.	Meas.	Sim.	Meas.
-60°	19.0	15.0	14.4	16.1	16.3	18.3	9.9	
-50°	20.4	16.5	16.2	13.3	10.9	20.0	9.7	
-40°	21.7	17.8	17.5	11.0	11.0	14.8	12.6	
-30°	22.7	18.8	18.6	10.2	9.8	15.8	8.9	
-20°	23.6	19.6	19.2	9.0	11.4	16.6	8.8	
-10°	24.0	20.0	19.6	10.0	8.1	19.6	9.3	
0°	24.4	20.5	19.7	9.1	12.8	17.7	14.3	
10°	23.9	20.0	19.2	9.5	9.4	18.9	18.5	
20°	23.6	19.6	18.7	9.6	10.8	21.2	11.9	
30°	22.7	18.8	18.5	9.9	9.4	16.8	9.6	
40°	21.7	17.8	17.4	11.9	11.2	13.6	10.5	
50°	20.4	16.5	15.9	12.4	12.8	19.3	10.6	
60°	18.8	14.8	14.9	16.7	14.2	13.8	11.7	

The measured gain as a function of the frequency and elevation angle in both vertical and horizontal planes at broadside and for steering angles of -20°, 20°, -40°, 40°, -60°, and 60° are presented in Figure V-23, Figure V-24, Figure V-25, Figure V-26, Figure V-27, Figure V-28, and Figure V-29, respectively. The broadband characteristic and the beam scanning capability of the fabricated transmitarray is preserved despite the fact that there are faulty cells. A beam squint phenomenon is observed in the frequency band of interest for all cases of beam scanning.

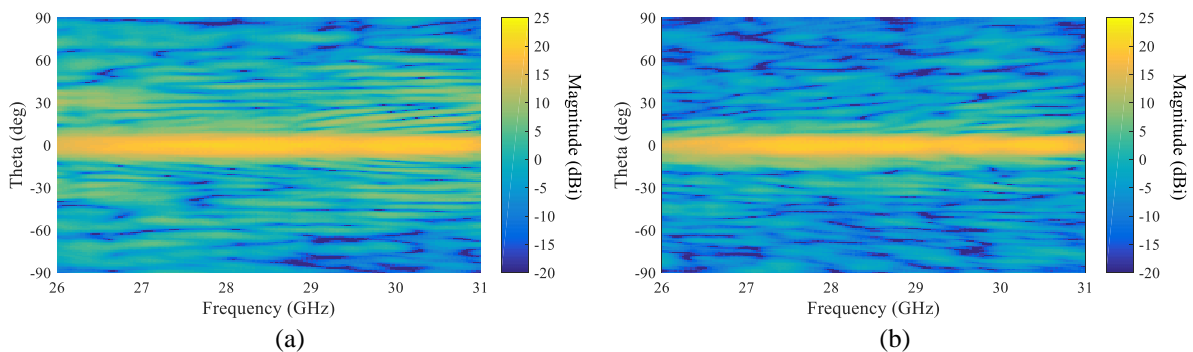


Figure V-23: Measured gain as a function of the frequency and elevation angle at broadside in (a) E and (b) H planes.

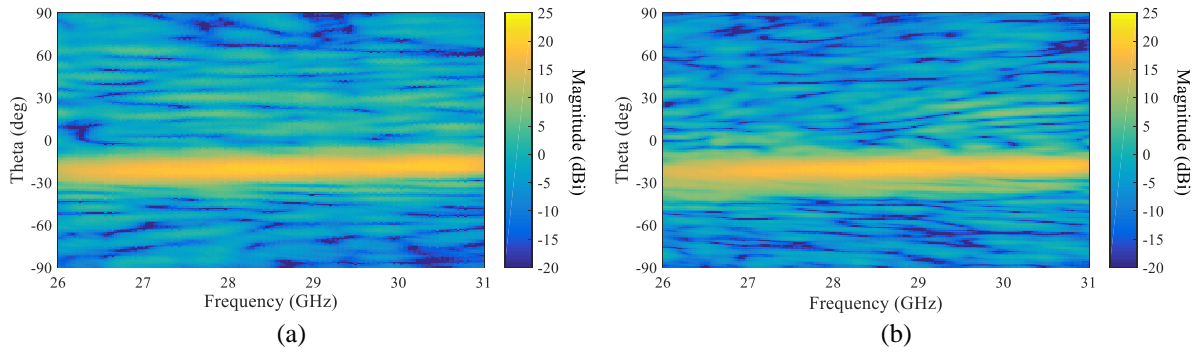


Figure V-24: Measured gain as a function of the frequency and elevation angle for a steering angle of -20° in (a) E and (b) H planes.

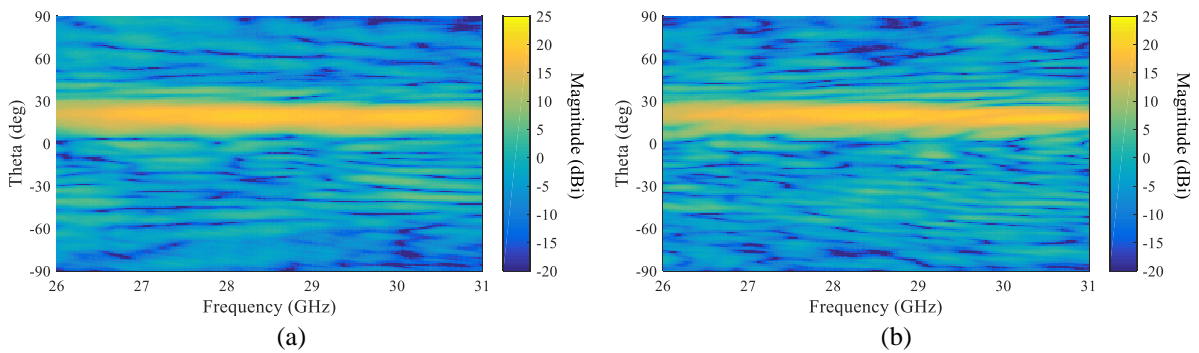


Figure V-25: Measured gain as a function of the frequency and elevation angle for a steering angle of 20° in (a) E and (b) H planes.

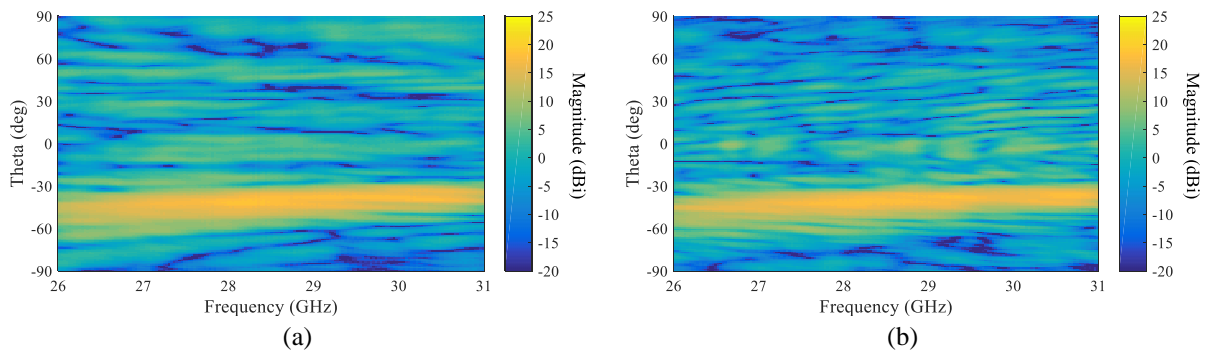


Figure V-26: Measured gain as a function of the frequency and elevation angle for a steering angle of -40° in (a) E and (b) H planes.

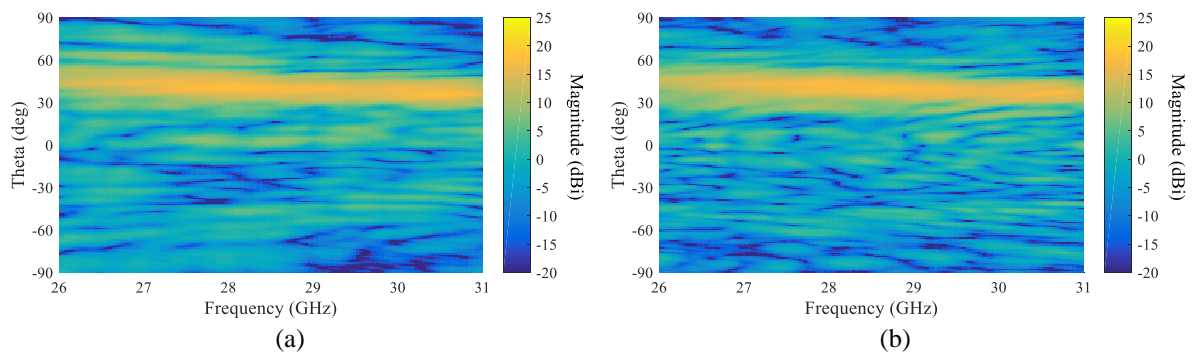


Figure V-27: Measured gain as a function of the frequency and elevation angle for a steering angle of 40° in (a) E and (b) H planes.

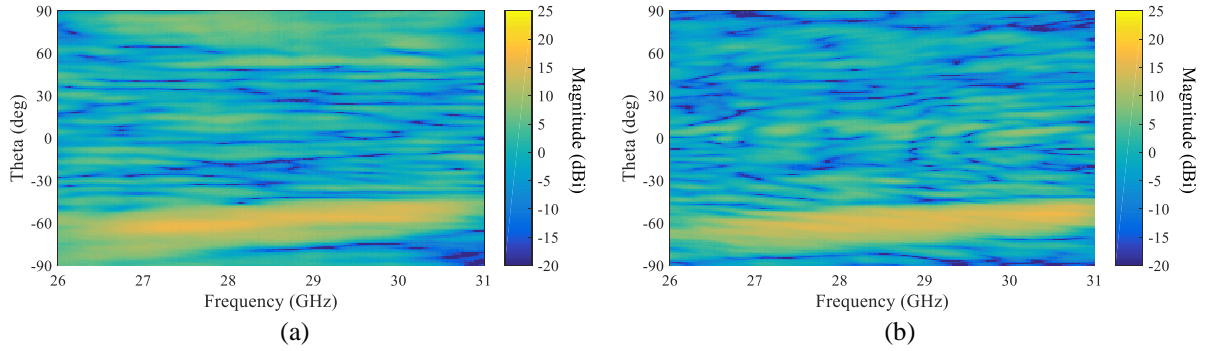


Figure V-28: Measured gain as a function of the frequency and elevation angle for a steering angle of -60° in (a) E and (b) H planes.

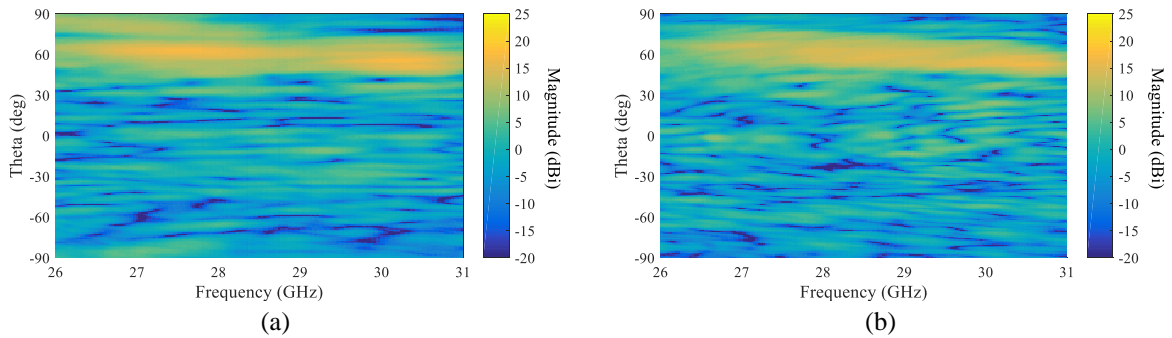


Figure V-29: Measured gain as a function of the frequency and elevation angle for a steering angle of 60° in (a) E and (b) H planes.

5.4. Conclusion

The study presented in this chapter focuses on the design, simulation, and prototyping of a 2-bit electronically reconfigurable transmitarray working at Ka-band. The prototype contains 14×14 elements and is based on the active linearly-polarized unit-cells presented in Chapter IV. 784 PIN diodes have been integrated in the TA to control the transmission phase of each unit-cell. In view of the good theoretical results (3-dB gain bandwidth of 14.8% at 29 GHz, an aperture efficiency of 35%, and beam scanning capability of $\pm 60^\circ$ in both E and H planes), we fabricated a prototype of this transmitarray on a panel of $162.2 \times 142.2 \text{ mm}^2$ and characterized its performances in the anechoic chamber.

The working principle of the proposed transmitarray is demonstrated despite some defective unit-cells, which is a positive outcome from the application point of view showing the graceful degradation of the performances in presence of defective devices. Despite the faulty unit-cells, the radiation patterns remain relatively good with moderate side-lobe levels. It is believed that this work represents a progress in the current state of the art since there is no other example of a 2-bit active Ka-band transmitarray with such good results.

**CHAPTER V. LINEARLY-POLARIZED ELECTRONICALLY RECONFIGURABLE
TRANSMITARRAY ANTENNA WITH 2-BIT PHASE RESOLUTION IN KA-BAND**

The measured performances, the theoretical with, and without manufacturing errors results (in broadside) of the proposed electronically reconfigurable transmitarray are summarized in Table.

Table V-3: Summary of the 2-bit electronically reconfigurable transmitarray performances at broadside (Measurement, theoretical results with and without errors).

Performances of the proposed 2-bit electronically reconfigurable transmitarray at broadside			
	Theoretical results without errors	Theoretical results with errors	Measurement
Directivity	25.7 dBi	-	-
Gain	23.2 dBi	20.5 dBi	19.8 dBi
Aperture efficiency	35%	18.7%	15.9%
3-dB bandwidth	26.7-31 GHz	27-31 GHz	26.2-30.9 GHz
	14.8% @29GHz	13.8% @29GHz	16.2% @29 GHz

General conclusion and perspectives

Nowadays, discrete lenses or transmitarrays are demonstrated as an excellent alternative to reflectors, reflectarrays, and phased arrays in several applications at microwave and millimeter-wave frequencies. These frequency bands are increasingly used for their wide available bandwidth and better security and privacy due to the strong propagation attenuation.

The aim of the thesis was to implement high-gain fixed beams and electronically reconfigurable transmitarrays for point-to-point or wireless backhauling/fronthauling for 5G mobile networks, civil and military radars, and imaging systems. The antennas developed in this thesis operate in Ka-band (27-40 GHz) and are based on standard PCB manufacturing technology.

Chapter I was dedicated to a general overview of mm-wave applications and also the recent state of the art covering fixed beam, switched beam and electronically reconfigurable transmitarray antennas. This study showed the large number of applications for mm-wave antennas, particularly in Ka-band, for 5th generation networks and SatCom systems. The state of the art highlighted several types of passive and electronically reconfigurable transmitarrays working from C- to mm-bands. Good performances in terms of bandwidth, gain, single or multi-band response, and dual polarization properties have been shown. As a result of this literature study, areas for improvement have been identified such as the design of low loss transmitarray structures with high aperture efficiency and low-profile in Ka band.

A detailed analysis of phase compensation impacts on the transmitarray performance and the working principle of a faceted transmitarray have been reported in Chapter II. These studies are based on analytical formulations and numerical simulations performed in Matlab. True-Time Delay compensation has been demonstrated as a solution to avoid both bandwidth and beam-squint limitations. The performance improvement introduced by TTD compensation, in terms of peak gain, gain-bandwidth, and side lobe levels for large size transmitarrays operating over a 17% frequency band, has been quantified. The principle of faceted transmitarray has been implemented in Matlab and validated through 3-D electromagnetic simulations. We have illustrated that for a certain faceting angle, the bandwidth and the scanning performance are improved at the cost of a gain reduction.

In 0, the design, optimization, and sensitivity analysis of linearly-polarized unit-cells based on patch antennas have been done. From this analysis, a 3-bit unit-cell implementing both phase-shifting and linear-to-circular polarization conversion functions has been developed. A collimated-beam transmitarray and a quad-beam transmitarray based on these unit-cells have been realized and measured. A measured gain of 33.8 dBi, an aperture efficiency of 51.2%, and 3-dB gain bandwidth better than 15.9% have been obtained for the focused-beam transmitarray. The quad-beam transmitarray demonstrated four simultaneous beams at $\theta_0 = \pm 25^\circ$ in two orthogonal planes with a gain around 18 dBi in good agreement with simulations.

In Chapter IV, linearly- and circularly-polarized reconfigurable unit-cells in Ka-band with 2-bit phase quantization have been presented. Two PIN diodes are flip-chipped on each patch antenna to tune the transmission phase; they are controlled by two bias lines printed on the opposite side of each patch substrate. The bias networks include microstrip radial stubs and capacitors to isolate the RF signals in transmission and receive sides, respectively. A prototype of the active linearly-polarized unit-cell has been realized and characterized in standard WR-28 waveguide including ad-hoc adaptors in order to reduce the impedance mismatch. The measured minimum insertion loss is about 2 dB with a relative 3-dB transmission bandwidth corresponding to 11.7%, 10.0%, 12.1%, and 10.3% at 29 GHz for the 0° , 90° , 180° , and 270° states, respectively. Some differences between simulated and measured results were observed and we investigated through simulations several possible causes related to manufacturing uncertainties; although a final conclusion on this issue was not possible due to the complexity of the unit-cell (six metal layers), the discrepancies are mainly attributed to manufacturing errors. Nevertheless, the simulations and measurement results validated the working principle of the active unit-cell with four phase states. Next, a 2-bit circularly-polarized unit-cell was proposed and investigated through 3-D simulations. The results showed a minimum insertion loss of about 1.2 dB for all phase states of the unit-cell. The 3-dB transmission bandwidth is equal to 10.3%, 12.4%, 12.4%, and 12.1% for the 0° , 90° , 180° , and 270° states, respectively. The 3-dB axial ratio corresponds to 4.5%, 3.8%, 4.1%, and 3.8% for the 0° , 90° , 180° , and 270° states, respectively. Due to lack of time, this circularly-polarized unit-cell was not prototyped.

Chapter V is dedicated to the design of a reconfigurable 196-element transmitarray working in linear polarization in Ka-band. This TA is based on the 2-bit linearly-polarized unit-cell of Chapter IV. The measured and simulated broadside gains at 29 GHz are 19.8 dBi and 23.2 dBi, showing a difference of 3.4 dB. This gain difference is due to the presence of defective unit-cells in the prototype. A total of 51 faulty bias lines were found probably due to some fabrication errors. Despite the faulty unit-cells, the radiation patterns remain relatively good

with moderate side-lobe levels and beam steering capabilities of $\pm 60^\circ$ in both E and H planes were demonstrated. It is believed that this work represents a progress in the current state of the art since there is no other example of a 2-bit active Ka-band transmitarray with such good results.

This thesis opens several perspectives for further research in the field of millimeter-wave transmitarray antennas. With the increasing demand for broadband and wide scanning angle antennas, a transmitarray based on TTD unit-cells with delay lines can be designed, optimized, and prototyped to validate the theoretical analysis done in the thesis (Chapter II). Implementing a TTD unit-cell is very complex because of the need for very long delay lines, which are difficult to integrate within the area of a unit-cell.

Another axis of research is the prototyping of a 3-facet transmitarray based on the linearly-polarized unit-cell optimized in 0. Other typologies of faceting or conformal aperture can be also considered. In fact, these topologies will be more and more requested in the upcoming years for enhancing the aerodynamics of aircrafts' fuselage or reducing the visual impact of the antenna.

Ultra-low-profile and lightweight transmitarrays with advanced functions, such as dual polarization, multi-beam and electronic reconfiguration can be introduced. In fact, satellite applications require such topologies to be mounted on an aircraft, a ship or a terrestrial vehicle for getting a wider or a global coverage.

The working principle of a 2-bit reconfigurable transmitarray was demonstrated in Chapter V despite some defective unit-cells, which have degraded the expected performances. More analysis are needed on the sensitivity of the structure to the constraints and probable manufacturing errors. Other robust architectures with higher phase resolution can also envisaged to further reduce the insertion losses

Electronically reconfigurable transmitarrays working at higher frequency bands such as V-, or E-band are another perspective. Such designs present challenging requirements in terms of complexity and cost of the antenna.

Appendix A - Scattering parameters in circular polarization of a unit-cell with periodic boundary conditions

In this appendix, the scattering parameters associated to a unit-cell with a circular polarization is presented. The proposed formulations are applied to unit-cells with a linear polarization on the side of the focal source (receiving layer) and a circular polarization on the free space side (transmitting layer), as in the case of the unit-cells designed in 0, and Chapter IV.

The electromagnetic simulation provides the scattering parameters of the unit-cell expressed in linear polarization for receiving and transmitting waves. The relation between the incoming (vector \underline{e}) and the outgoing waves (vector \underline{f}) is:

$$\underline{f} = \underline{S}_{LC} \cdot \underline{e}$$

With:

$$\underline{e} = \begin{bmatrix} e_{1_x} \\ e_{1_y} \\ e_{2_l} \\ e_{2_r} \end{bmatrix}, \quad \underline{f} = \begin{bmatrix} f_{1_x} \\ f_{1_y} \\ f_{2_l} \\ f_{2_r} \end{bmatrix}, \quad \text{and} \quad \underline{S}_{LC} = \begin{bmatrix} S_{11_xx} & S_{11_xy} & S_{12_xl} & S_{12_xr} \\ S_{11_yx} & S_{11_yy} & S_{12_yl} & S_{12_yr} \\ S_{21_lx} & S_{21_ly} & S_{22_ll} & S_{22_lr} \\ S_{21_rx} & S_{21_ry} & S_{22_rr} & S_{22_rr} \end{bmatrix}$$

The incoming (\underline{e}) and outgoing (\underline{f}) wave vectors are composed of linearly-polarized components (port 1) and circularly-polarized components (port 2). They are expressed as a function of the vectors \underline{a} , and \underline{b} of the incoming and outgoing waves, respectively:

$$\underline{e} = \underline{H} \cdot \underline{a}, \quad \underline{f} = \underline{H} \cdot \underline{b}$$

Where:

$$\underline{a} = \begin{bmatrix} a_{1_x} \\ a_{1_y} \\ a_{2_x} \\ a_{2_y} \end{bmatrix}, \quad \underline{b} = \begin{bmatrix} b_{1_x} \\ b_{1_y} \\ b_{2_x} \\ b_{2_y} \end{bmatrix}, \quad \text{and} \quad \underline{H} = \frac{1}{\sqrt{2}} \begin{bmatrix} \sqrt{2} & 0 & 0 & 0 \\ 0 & \sqrt{2} & 0 & 0 \\ 0 & 0 & 1 & i \\ 0 & 0 & 1 & -i \end{bmatrix}$$

The vector of the incident waves \underline{a} , and the vector of the transmitted waves \underline{b} are related as follows:

$$\underline{b} = \underline{S}_{xy} \cdot \underline{a}$$

Where

$$\underline{S}_{xy} = \begin{bmatrix} S_{11_xx} & S_{11_xy} & S_{12_xx} & S_{12_xy} \\ S_{11_yx} & S_{11_yy} & S_{12_yx} & S_{12_yy} \\ S_{21_xx} & S_{11_xy} & S_{22_xx} & S_{22_xy} \\ S_{21_yx} & S_{11_xy} & S_{22_yx} & S_{22_yy} \end{bmatrix}$$

Then, the matrix of the scattering parameters in circular polarization \underline{S}_{LC} is expressed as:

$$\underline{S}_{LC} = \underline{H} \cdot \underline{S}_{xy} \cdot \underline{H}^{-1}$$

Finally, the components of \underline{S}_{LC} are given by the following expressions:

$$S_{22_ll} = \frac{S_{22_xx} + iS_{22_xy} + iS_{22_yx} - S_{22_yy}}{2} \quad S_{22_lr} = \frac{S_{22_xx} - iS_{22_xy} + iS_{22_yx} + S_{22_yy}}{2}$$

$$S_{22_rl} = \frac{S_{22_xx} + iS_{22_xy} - iS_{22_yx} + S_{22_yy}}{2} \quad S_{22_rr} = \frac{S_{22_xx} - iS_{22_xy} - iS_{22_yx} - S_{22_yy}}{2}$$

$$S_{12_xl} = \frac{S_{12_xx} + iS_{12_xy}}{\sqrt{2}}$$

$$S_{12_yl} = \frac{S_{12_yx} + iS_{12_yy}}{\sqrt{2}}$$

$$S_{12_xr} = \frac{S_{12_xx} - iS_{12_xy}}{\sqrt{2}}$$

$$S_{12_yr} = \frac{S_{12_yx} - iS_{12_yy}}{\sqrt{2}}$$

$$S_{12_lx} = \frac{S_{21_xx} + iS_{21_yx}}{\sqrt{2}}$$

$$S_{21_ly} = \frac{S_{21_xy} + iS_{21_yy}}{\sqrt{2}}$$

$$S_{12_rx} = \frac{S_{21_xx} - iS_{21_yx}}{\sqrt{2}}$$

$$S_{21_ry} = \frac{S_{21_xy} - iS_{21_yy}}{\sqrt{2}}$$

Appendix B - Description of electronic control boards for reconfigurable transmitarray antenna

As mentioned in Chapter V, four boards (developed in [42]) are used to control the p-i-n diodes located on the unit-cells of the 2-bit reconfigurable transmitarray. Each board provides the DC current to control a total of 100 bias lines in a quarter of the transmitarray. The four boards are placed behind the focal source and connected to the transmitarray through ribbon cables, as indicated in Figure B-2. The programmable sequence is generated by the Matlab code developed in [42] and sent to the boards serially.

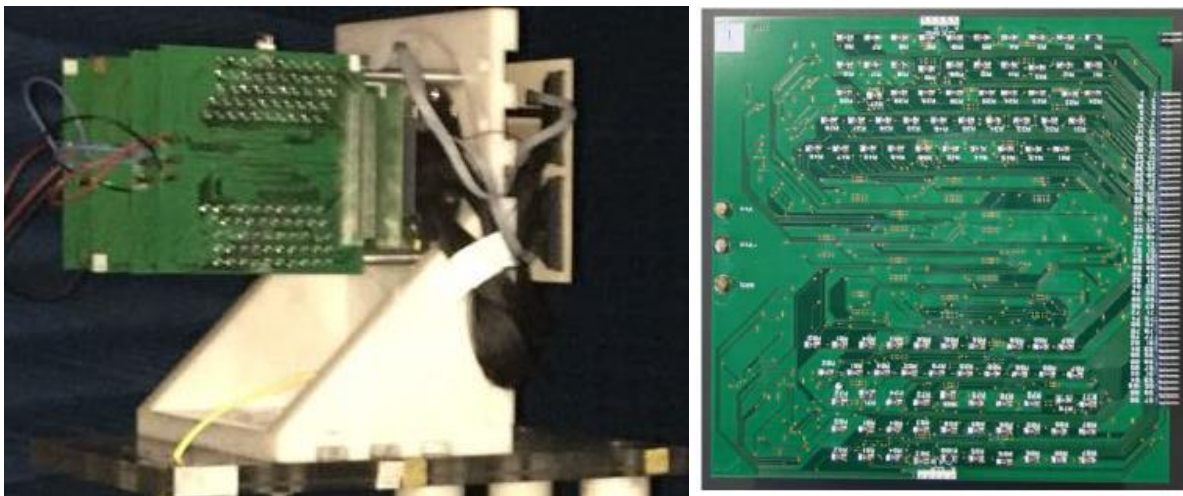
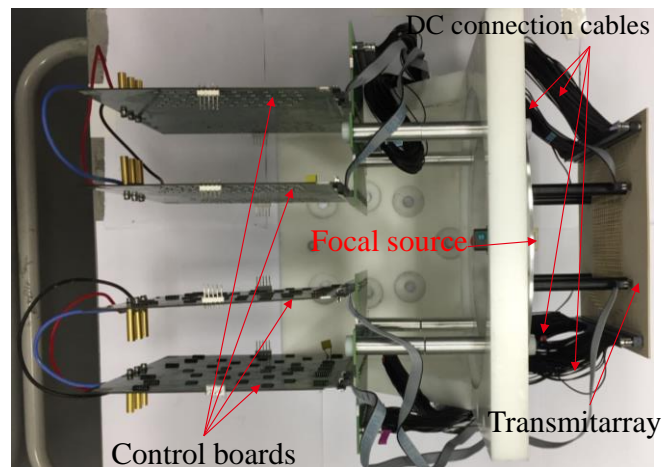


Figure B-1: The 2-bit linearly-polarized transmitarray with the four control boards.

As shown in Figure B-2, each control board is composed of 13 8-bit shift registers, which are connected to switches (25 4×4 switches). Each switch controls a bias line of the transmitarray and provides a negative or positive voltage of $\pm 5V$. 100 chip resistors of 360Ω are used in order to set the current to $\pm 10 \text{ mA}$ on each bias line.

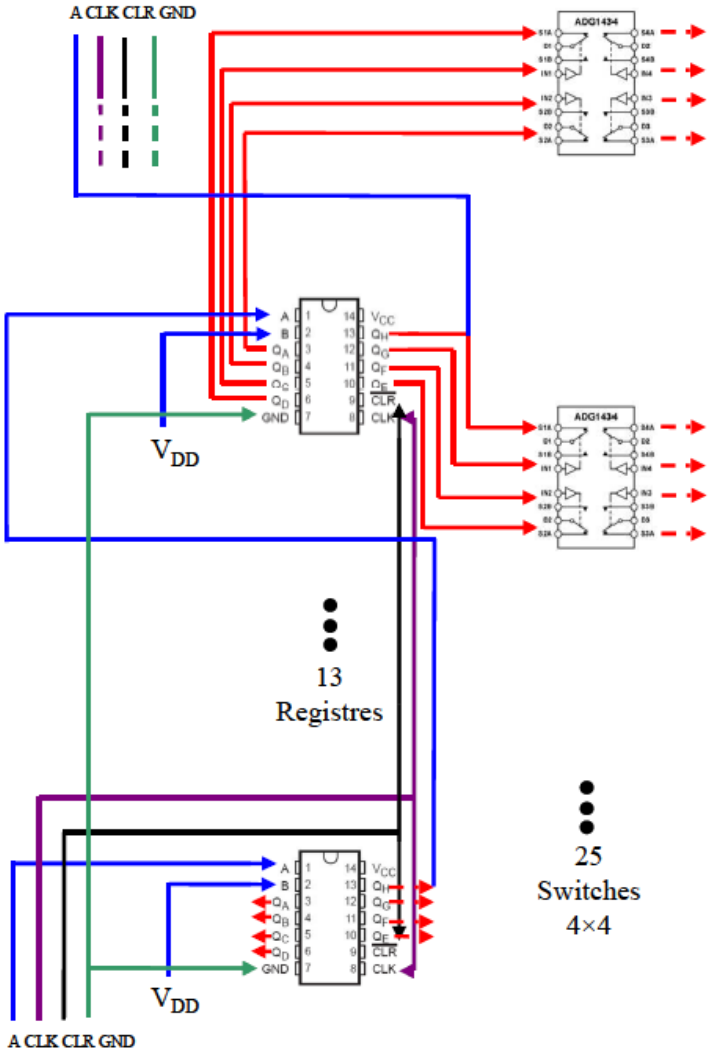


Figure B-2: Description of the architecture of the control board.

Bibliography

- [1] IEEE Std 521-2002 Standard Letter Designations for Radar-Frequency Bands, 21 Jan. 2003.
- [2] A. Boriskin and R. Sauleau (Ed.), “Aperture Antennas for MM and Sub-MM Wave Applications ,” Springer, Sept. 2017.
- [3] D. Sheen, D. McMakin, and T. Hall, “Three-dimensional millimeter-wave imaging for concealed weapon detection,” *IEEE Transactions on Microwave Theory and Techniques*, vol. 49, no. 9, pp. 1581 –1592, Sep. 2001.
- [4] S. Ahmed, A. Schiessl, and L.-P. Schmidt, “A novel fully electronic active real-time imager based on a planar multistatic sparse array,” *IEEE Transactions on Microwave Theory and Techniques*, vol. 59, no. 12, pp. 3567 –3576, Dec. 2011.
- [5] ETSI EN 302 288-1, “Electromagnetic compatibility and Radio spectrum Matters (ERM); short range devices; Road Transport and Traffic Telematics (RTTT); short range radar equipment operating in the 24 GHz range; part 1: technical requirements and methods of measurement,” 2012.
- [6] ETSI EN 302 264-1, “Electromagnetic compatibility and Radio spectrum Matters (ERM); short range devices; Road Transport and Traffic Telematics (RTTT); Short Range Radar equipment operating in the 77 GHz to 81 GHz band; Part 1: Technical requirements and methods of measurement,” 2009.
- [7] ETSI EN 301 091, “Technical characteristics and test methods for radar equipment operating in the 76 GHz to 77 GH band,” 1998.
- [8] G.A Isted, “Guglielmo Marconi and the history of radio-part II,” *GEC review*, vol.7, n^o 2, pp. 110- 122, 1991.
- [9] P-H. Kuo, and A. Mourad, “Millimeter wave for 5G Mobile Fronthaul and Backhaul,” *Networks and Communications (EuCNC) 2017 European Conference on*, Oulu, Finland, Jun. 2017.
- [10] Y. Niu, Y. Li, D. Jin, L. Su, and A. V. Vasilakos, “A Survey of millimeter Wave (mmWave) Communications for 5G: opportunities and challenges,” *Wireless Networks*, pp. 1-17, Apr. 2015.
- [11] FCC, “Notice of Inquiry 14-154,” Oct. 2014.
- [12] K.Sakaguchi et al., “Where, when, and how mmWave is used in 5G and beyond,” *IEICE Trans. Electron.*, vol. E100-C, no. 10, pp. 790–808, Oct. 2017.

- [13] W. Roh, J.-Y. Seol, J. Park, B. Lee, J. Lee, Y. Kim, J. Cho, K. Cheun, and L. Aryanfar, "Millimeter-wave beamforming as an enabling technology for 5G cellular communications: theoretical feasibility and prototype Results," *IEEE Communications Magazine*, 2012.
- [14] K. Kibaroglu, M. Sayginer, and G. M. Rebeiz, "An ultra-low-cost 32-element 28 GHz phased-array transceiver with 41 dBm EIRP and 1.0-1.6 Gbps 16-QAM link at 300 meters," *Radio Frequency Integrated Circuits Symposium (RFIC)*, 2017 IEEE, pp. 73-76, Honolulu, USA, Jun. 2017.
- [15] R. Elsharkawy, A.-R. Sebak, M. Hindy, Osma. M. Haraz, A. Saleeb, and El-Sayed M. Rabaie, "Single layer polarization independent reflectarray antenna for future 5G cellular applications," *2015 International Conference on Information and Communication Technonolgy Research (ICTRC2015)*, Surabaya, Indonesia , Sep. 2015.
- [16] Y. Shen, S. Hu, and W. Dou, "38 GHz Folded Reflectarray Antenna for Point-to-Point 5G Communications," *2016 IEEE 5th Asia-Pacific Conference on Antennas and Propagation (APCAP)*, pp. 369-370, Kaohsiung, Taiwan, Jul. 2016.
- [17] T. Visentin, W. Keusgen, and R. Weiler, "Dual-polarized square-shaped offset-fed reflectarray antenna with high gain and high bandwidth in the 60 GHz domain," *9th European Conference in Antennas and Propag. (EuCAP 2015)*, Lisbon, Portugal, Apr. 2015.
- [18] ETSI EN 302 217, "Fixed Radio Systems; characteristics and requirements for point-to-point equipment and antennas," Jan. 2010.
- [19] http://www.thinkom.com/wp-content/uploads/2018/04/ThinAir-Falcon-Ka2517-Data-Sheet_Rev02-18.pdf.
- [20] R. Stevenson, M. Sazegar, A Bily, M. Johnson, and N. Kundtz, "Metamaterial surface antenna technology: commercialization trough diffractive metamaterials and liquid crystal display manufacturing," *10th International Congress on Advanced Electromagnetic Materials in Microwaves and Optics – Metamaterials 2016*, Crete, Greece, 17-22 Sep. 2016.
- [21] W. H. Henderson, and W. W. Milroy, "Wireless communication applications of the Continuous Transverse Stub (CTS) array at microwave and millimeter Wave Frequencies," *IEEE/ACES International Conference on Wireless Communications and Applied Computational Electromagnetics*, Honolulu, HI, USA 3-7 Apr. 2005.
- [22] S. Otto, I. Nistal, S. Holzwarth, O. Litschke, and R. Baggen, "Planar Satcom antenna systems in Ka-band", *ESA Antenna Workshop*, Noordwijk, Hollande, Oct. 2012.

- [23] Integrated X/Ka-Band SATCOM On-the-Move, <http://www.thinkom.com/wp-content/uploads/2013/11/TK-TSatCommander-Data-Sheet.pdf>.
- [24] Thin Air eagle-Ka 2000, http://www.thinkom.com/wp-content/uploads/2014/03/TK-ThinAirEagleKa2000-Data-Sheet_Rev03-14.pdf.
- [25] T. Smith, U. Gothelf, O. S. Kim, and O. Breinbjerg, "An FSS-Backed 20/30 GHz circularly polarized reflectarray for a shared aperture L- and Ka-band satellite communication antenna," *IEEE Transactions on Antennas and Propag.*, vol. 62, no. 2, pp. 661-668, Feb. 2014.
- [26] W. An, S. Xu, F. Yang, and J. Gao, "A Ka-band reflectarray antenna integrated with solar cells," *IEEE Transactions on Antennas and Propag.*, vol. 62, no. 11, pp. 5539-5546, Nov. 2014.
- [27] Q. Luo, S. Gao, C. Zhang, D. Zhou, T. Chaloun, W. Menzel, V. Ziegler, and M. Sobhy, "Design and analysis of a reflectarray using slot antenna elements for Ka-band SatCom," *IEEE Transactions on Antennas and Propag.*, vol. 63, n^o4, pp. 1365-1374, Apr. 2015.
- [28] E. Martinez-de-Rioja, J. A. Encinar, M. Barba, R. Florencio, R. R. Boix, and V. Losada, "Dual Polarized Reflectarray Transmit Antenna for Operation in Ku- and Ka-Bands With Independent Feeds," *IEEE Transactions on Antennas and Propag.*, vol. 65, no. 6, pp. 3241- 3246, Jun. 2017.
- [29] ECC report 152, "The use of the frequency bands 27.5 – 30 GHz and 17.3- 20.2 GHz by Satellite Networks," Gothenburg, Sept. 2010.
- [30] ETSI TR 103 263, "Electromagnetic compatibility and radio spectrum matters (ERM); system reference document (SRdoc); cognitive radio techniques for satellite communications operating in Ka band," Jul. 2014.
- [31] R. Pearson, "Next generation mobile SATCOM terminal antennas for transformed world," in *Proc. European Conf. Antennas Propagation (EUCAP 2011)*, Rome, Italy, 11-15 Apr. 2011.
- [32] E. Feltin, J. Freixe, E. Weller, "Mobility in Ku and Ka bands: the Eutelsat's point of view," *European Conf. Antennas Propagation (EuCAP 2011)*, Rome, Italy, 11-15 Apr. 2011.
- [33] O. Rostbakken, "Inmarsat global Xpress: bringing global mobility to Ka-band satellite communications," *ESA Antenna workshop*, Noordwijk, Hollande, Oct. 2012.
- [34] ETSI EN 301 360, "Satellite Earth station and systems (SES); harmonized EN for satellite interactive terminals (SIT) and satellite user terminals (SUT) transmitting towards

- geostationary satellites in the 27.5 GHz to 29.5 GHz frequency bands covering essential requirements under article 3.2 of the R&TTE directive,” 2006.
- [35] ITU-R s.465.6, “Reference radiation pattern for Earth station antennas in the fixed-satellite service for use in coordination and interference assesment in the frequency range from 2 to 31 GHz,” 2010.
- [36] FCC regulations, [Online]. Available: www.fcc.gov.
- [37] ETSI EN 303 978, “Satellite Earth stations and Systems (SES); harmonized EN for Earth stations on mobile platforms transmitting towards satellites in geastationary orbit in the 27.5 GHz to 30.0 GHz frequency bands covering the essential requirements of article 3.2 of the R&TTE directive,” Feb. 2013.
- [38] B. Hamdi, T. Aguilí, N. Raveu, and H. Baudrand, “Floquet modal analysis to modelize and study 2-D planar almost periodic structures in finite and infinite extent with coupled motifs,” *Progress In Electromagnetics Research B*, Vol. 62, pp. 63–86, 2015.
- [39] H. Kaouach, L. Dussopt, R. Sauleau, and T. Koleck, Design and demonstration of 1-bit and 2-bit transmit-arrays at X-band frequencies,” in *European Microw. Conf.*, 2009.
- [40] A. Clemente, L. Dussopt, R. Sauleau, P. Potier and P. Pouliguen, "Wideband 400-element electronically reconfigurable transmitarray in X Band," *IEEE Trans. Antennas and Propag.*, vol. 61, no. 10, pp. 5017-5027, Oct 2013.
- [41] L. Di-Palma, A. Clemente, L. Dussopt, R. Sauleau, P. Potier, and P. Pouliguen, “Circularly polarized transmitarray with sequential rotation in Ka-band,” *IEEE Transaction on Antennas and Propagation*, vol. 63, no. 11, pp. 5118-5124, Nov. 2015.
- [42] A. Clemente, “Conception d’antennes à réseaux transmetteurs à dépointage et formation de faisceau,” *University of Rennes*, 2012.
- [43] L. Schwartzman and L. Topper, "Analysis of phased array lenses," *IEEE Trans. Antennas Propag.*, vol. 16, no. 6, pp. 628-632, Nov 1968.
- [44] D. M. Pozar, “Flat lens antenna concept using aperture coupled microstrip patches,” *Electron. Lett.*, vol. 32, no. 23, pp. 2109–2111, 1996.
- [45] P. Padilla, M. Sierra-Castaner, and M. Sierra-Perez, “Design of a double array lens,” *European Conf. Antennas and Propag.*, 2006.
- [46] M. Barba, E. Carrasco, and J. A. Encinar, “Suitable planar transmit-arrays in X-band,” *European Conf. Antennas and Propag.*, 2006.
- [47] H. Kaouach, L. Dussopt, J. Lanteri, T. Koleck, and R. Sauleau, “Wideband low-loss linear and circular polarization transmit-arrays in V-band,” *IEEE Trans. Antennas Propag.*, vol. 59, no. 7, pp. 2513–2523, Jul. 2011.

- [48] C.-C. Cheng and A. Abbaspour-Tamijani, "Study of 2-bit antenna-filter-antenna elements for reconfigurable millimeter-wave lens arrays," *IEEE Trans. Microw. Theory Tech.*, vol. 54, no. 12, pp. 4498–4506, 2006.
- [49] C.-C. Cheng, B. Lakshminarayanan, and A. Abbaspour-Tamijani, "A programmable lens-array antenna with monolithically integrated MEMS switches," *IEEE Trans. Microw. Theory Tech.*, vol. 57, no. 8, pp. 1874–1884, 2009.
- [50] P. Padilla, A. Munoz-Acevedo, M. Sierra-Castaner, and M. Sierra-Perez, "Electronically reconfigurable transmitarray at Ku band for microwave applications," *IEEE Trans. Antennas Propag.*, vol. 58, no. 8, pp. 2571–2579, 2010.
- [51] R.H. Phillion, "Flat lenses for circularly polarized electromagnetic waves," *PhD Thesis*, University of Calgary, AL, Canada, Dec 2010.
- [52] J.Y. Lau, "Reconfigurable Transmitarray Antennas," *PhD. Thesis*, University of Toronto, 2012.
- [53] L. Di Palma, "Reconfigurable transmitarray antennas at millimeter-wave frequencies," *PhD. Thesis*, University of Rennes, 2015.
- [54] F. Yang, R. Deng, S. Xu, and M. Li, "Design and experiment of a near-zero-thickness high-gain Transmit-Reflect-Array antenna using anisotropic metasurface," *IEEE Transactions on Antennas and Propagation*, vol. 66, no. 6, pp. 2853 – 2861, Jun. 2018.
- [55] S. H. Ramazannia Tuloti, P. Rezaei, and F. Tavakkol Hamedani, "high-efficient wideband transmitarray antenna," *IEEE Antennas and Propagation Letters*, vol. 17, no. 5, pp. 817–820, May. 2018.
- [56] M. O. Bagheri, H. R. Hassani, B. Rahmati, "Dual-band, dual-polarised metallic slot transmitarray antenna," *IET Microwaves Antennas and Propag.*, vol. 11, no. 3, pp. 402-409, Apr. 2017.
- [57] Q. Luo, S. Gao, M. Sobhy, and X. Yang, "Wideband transmitarray with reduced profile," *IEEE Antennas and Wireless Propagation letters*, vol. 17, n°3, pp. 450 – 453, Mar. 2018.
- [58] W. An, S. Xu, F. Yang, and M. Li, "A Double-Layer Transmitarray Antenna Using Malta Crosses with Vias," *IEEE Transaction on Antennas and Propagation*, vol. 64, n°, pp. 1120 –1125, Mar. 2016.
- [59] C. Fan, W. Che, W. Yang, and S. He, "A novel PRAMC-based ultralow-profile transmitarray antenna by using Ray Tracing Principle," *IEEE Transactions on Antennas and Propog.*, vol. , no. 4, pp. 1779-1787, Apr. 2017.

- [60] Y. Hou, X. Liu, Y. Li, Z. Zhang, and Z. Feng, "Circular polarization transmitarray element with linear polarization feed," *IEEE International Conference on Microwave and Millimeter Wave Technology (ICMMT 2016)*, Beijing, China, 2016.
- [61] H. Hasani, J. S. Silva, J. R. Mosig, and M. Garcia-Vigueras, "Dual-band 20/30 GHz circularly-polarized transmitarray for SOTM applications," *10th European Conference on Antennas and Propagation (EuCAP 2016)*, Davos, Switzerland, 2016.
- [62] K. Pham, R. Sauleau, E. Fourn, F. Diaby, A. Clement, and L. Dussopt, "Dual-band transmitarrays with dual-linear polarization at Ka-band," *IEEE Transactions on Antennas and Propag.*, vol. 65, no. 12, pp. 7009-7018, Dec. 2017.
- [63] P. Naseri, S. A. Matos, J. R. Costa, and C. A. Fernandes, "Phase-Delay versus Phase-Rotation cells for circular polarization transmit arrays - application to Satellite Ka-Band beam steering," *IEEE Transactions on Antennas and Propagation*, vol. 66, no. 3, pp. 1236- 1246, Mar. 2018.
- [64] C. Jouanlanne, A. Clemente, M. Hucharda, J. Keignart, C. Barbier, T. Le Nadan, and L. Petit, "Wideband Linearly Polarized Transmitarray Antenna for 60 GHz Backhauling," *IEEE Transactions on Antennas and Propagation*, vol. 65, no. 3, pp. 1440-1445, 2017.
- [65] Z-W. Miao, Z-C. Hao, G. Q. Luo, L. Gao, J. Wang, X. Wang, and W. Hong, "140 GHz high gain LTCC-integrated transmit-array antenna using a wideband SIW aperture-coupling phase delay structure," *IEEE Transactions on Antennas and Propag.*, vol. 66, no. 1, pp. 182-190, Nov. 2017.
- [66] H. Yi, S-W. Qu, and C. H. Chan, "Low-cost two-layer terahertz transmit array," *Electronics Letters*, vol. 53, no. 12, pp. 789-791, Jun. 2017.
- [67] S. A. Matos, E. B. Lima, J. S. Silva, J. R. Costa, C. A. Fernandes, N. J. G. Fonseca, and J. R. Mosig, "High gain dual-band beam-steering transmit-array for Satcom Terminals at Ka-band," *IEEE Transactions on Antennas and Propag.*, vol. 65, no. 7, pp.3528-3539, Jul. 2017.
- [68] M. Jiang, Z. N. Chen, Y. Zhang, W. Hong, and X. Xuan, "Metamaterial-based thin planar lens antenna for spatial beamforming and multibeam massive MIMO," *IEEE Transactions on Antennas and Propag.*, pp. 464- 472, vol. 65, no. 2, Feb. 2017.
- [69] L. Dussopt, A. Moknache, J. Säily, A. Lamminen, M. Kaunisto, J. Aurinsalo, T. Bateman, and J. Francey, "A V-Band Switched-Beam Linearly-Polarized Transmit-Array Antennafor Wireless Backhaul Applications,," *IEEE Transactions on Antennas and Propagation*, vol. 65, no. 12, , pp. 6788–6793, 2017.

- [70] S.B. Yeap, X. Qing, and Z.N. Chen, “77-GHz dual-layer transmit-array for automotive radar applications,” *IEEE Trans. Antennas Propag.*, vol. 63, no. 6, pp. 2833–2837, 2015.
- [71] J.Y. Lau, and S.V. Hum, “Reconfigurable transmitarray design approaches for beamforming applications”, *IEEE Trans. Antennas Propag.*, vol. 60, no. 12, pp. 5679–5689, 2012.
- [72] C. Huang, W. Pan, X. Ma, B. Zhao, J. Cui, and X. Luo, “Using reconfigurable transmitarray to achieve beam-steering and polarization manipulation applications,” *IEEE Transactions on Antennas and Propagation*, vol. 63, no. 11, pp. 4801-4810, Nov. 2015.
- [73] C. Huang, W. Pan, and X. Luo, “Low-loss circularly-polarized transmitarray for beam steering application,” *IEEE Transactions on Antennas and Propag.*, vol. 64, n°10, pp. 4471- 4476, Oct. 2016.
- [74] J. G. Nicholls, and S. V. Hum, “Full-space electronic beam-steering transmitarray,” *IEEE Transactions on Antennas and Propag.*, vol. 64, no. 8, pp. 3410-322, Aug. 2016.
- [75] J. R. Reis, R. F. S. Caldeirinha, A. Hammoudeh, and N. Copner, “Electronically reconfigurable FSS-Inspired transmitarray for 2-D beamsteering,” *IEEE Transactions on Antennas and Propag.*, vol. 65, n°9, pp. 4880-4885, Sep. 2017.
- [76] W. Pan, C. Huang, X. Ma, and X. Luo, “An amplifying tunable transmitarray element,” *IEEE Antennas and Wireless Propagation Letters*, vol. 13, no. 10, pp. 702-705, Mar. 2014.
- [77] A. Clemente, L. Dussopt, R. Sauleau, P. Potier, and P. Pouliguen, “Wideband 400-element electronically reconfigurable transmitarray in X-band,” *IEEE Transaction on Antennas and Propagation*, vol. 61, no.10, pp. 5017-5027, Oct. 2013.
- [78] C. Huang, W. Pan, X. Ma, and X. Luo, “1-Bit Reconfigurable Circularly Polarized Transmitarray in X-Band,” *IEEE Antennas and Wireless Propagation Letters*, vol. 15, pp. 448-441, Jul. 2015.
- [79] W. Pan, C. Huang, X. Ma, B. Jiang, and X. Luo, “A dual linearly polarized transmitarray element with 1-bit phase resolution in X-band,” *IEEE Antennas and Wireless Propagation Letters*, vol. 14, pp. 167-170, 2015.
- [80] E. Erdil, K. Topalli, N. S. Esmailzad, Ö. Zorlu, H. Kulah, and O. A. Civi, “Reconfigurable Nested Ring-Split Ring Transmitarray Unit Cell Employing the Element Rotation Method by Microfluidics,” *IEEE Transactions on Antennas and Propagation*, vol. 63, no. 13, pp. 1163- 1167, 2015.

- [81] M. Wang, S. Xu, F. Yang, and M. Li, "Design of a Ku-band 1-bit reconfigurable transmitarray with 16×16 slot coupled elements," *Antennas and Propagation & USNC/URSI National Radio Science Meeting, 2017 IEEE International Symposium*, San Diego, CA, USA, Jul. 2017.
- [82] M. Frank, R. Weigel, and A. Koelpin, "Multilayer reconfigurable transmitarray in K-band for beam steering applications," *Electromagnetics in Advanced Applications (ICEAA), 2017 International Conference*, Verona, Italy, Sep. 2017.
- [83] M. Frank, R. Weigel, and A. Koelpin, "Design of a 24 GHz reconfigurable transmitarray element with continuous phase range," in *2017 11th European Conference on Antennas and Propagation (EUCAP)*, Paris, France, March 2017.
- [84] C.-C. Cheng, B. Lakshminarayanan, and A. Abbaspour-Tamijani, "Programmable lens-array antenna with monolithically integrated MEMS switches," *IEEE Trans. Microwave Theory Techn*, vol. 57, no. 8, pp. 1874-1884, Aug. 2009.
- [85] L. Di-Palma, A. Clemente, L. Dussopt, R. Sauleau, P. Potier, and P. Pouliguen, "Circularly- Polarized Reconfigurable Transmitarray in Ka-Band With Beam Scanning and Polarization Switching Capabilities," *IEEE Transactions on Antennas and Propagation*, vol. 65, no. 12, pp. 529-540, Feb. 2017.
- [86] T. Chaloun, C. Hillebrand, C. Waldschmidt, and W. Menzel, "Active transmitarray submodule for K/Ka band satcom applications," *2015 German Microwave Conf. (GeMiC 2015)*, pp. 198-201, Mar. 16–18, 2015.
- [87] M. Longbrake, "True time-delay beamsteering for radar," *Aerospace and Electronics Conference (NAECON), 2012 IEEE National*, pp. 246-249, Jul. 2012.
- [88] L. Yang, C. W. Domier, and N. C. Luhman, "Ka-band true time delay E-plane beam scanning and broadening phased array system using antipodal elliptically-tapered slot antennas," *IEEE Antennas Propag. Society International Symposium*, Albuquerque, NM, USA, pp. 2213-2216, 2006.
- [89] Z. Ji, W. Zhu, Z. Li, Y. Sun, and Q. Wang, "A novel method of optical true time delay in phased array antenna," *9th European Radar Conference (EuRAD 2012)*, Amsterdam, Netherlands, pp. 492-495, 2012
- [90] E. Carrasco, J.A. Encinar, and M. Barba, "Bandwidth improvement in large reflectarrays by using true-time delay," *IEEE Trans. Antennas Propag.*, vol. 56, no. 8, pp. 2496-2503, Aug. 2008.

- [91] M. Li and N. Bedhad, "Broadband true time delay microwaves lenses based on minaturized element frequency selective surfaces," *IEEE Trans. Antennas Propag.*, vol. 61, no. 3, pp. 1166-1177, Mar. 2013.
- [92] M. Li and N. Bedhad, "Wideband true-time-delay microwave lenses based on metallo-dielectric and all dielectric lowpass frequency selective surfaces," *IEEE Trans. Antennas Propag.*, vol. 61, no. 8, pp. 4109-4119, Aug. 2013.
- [93] P. Nayeri, F. Yang, and A.Z. Elsherbeni, "Radiation analysis and characteristics of conformal reflectarray antennas," *Int. Journal Antennas Propag.*, pp. 1-6, 2012.
- [94] M. Beccaria, P. Pirinoli, and M. orifice, "On the bandwidth of convex conformal reflectarray antennas," in *Proc. Intern. Workshop Antenna Tech. (iWat 2016)*, Cocoa Beach, FL, USA, 29 Feb. – 2 Ma. 2016.
- [95] J-M. Fleuriaux, "Synthèse du diagramme de rayonnement d'un réseau de source," *Thèse de Doctorat, Université de Rennes I*, Jun. 1996.
- [96] W. Bu-hong, M. Ling-qin, and G. Ying, "Pattern synthesis of double curved conformal paraboloidal array," *IEEE Antennas Propag. Society International Symposium (AP-S 2008)*, San Diego, CA, Jul. 2008.
- [97] Recommendation ITU-R BO.79, "Choice of polarization for the broadcasting-satellite service", pp. 1-9, 1992.
- [98] D. Chang, J. Lee, and T-H. Lin, "Service provision for incompatible polarization satellite assets via wavefront multiplexing techniques," *IEEE Global Communications Conference*, pp. 1370- 1375, Texas, USA, 2014.
- [99] G. Kumar, K.P Ray, "Broadband Microstrip Antenna," *Artech House Publication*, pp.1-291, 2003.
- [100] R. L. Haupt, "Antennas Arrays: A Computational Approach," *John Wiley & Sons, Inc.*, Hoboken, NJ, USA, 9 Sept. 2010.
- [101] J. R James and P.S Hall, "Handbook of Microstrip Antennas", *Peter Peregrinus Ltd.*, London, UK, 1989.
- [102] Y. Li, and K-M. Luk, "A 60-GHz wideband circularly polarized aperture-coupled magneto-electric dipole antenna array," *IEEE Trans. Antennas Propag.*, vol. 6, no. 4, pp. 1325-1332, Apr. 2016.
- [103] J. Garcia, A. Arriola, F. Casado, X. Chen, J. I. Sancho, and D. Valderas, "Coverage and read range comparison of linearly and circularly polarized radio frequency identification

- ultra-high frequency tag antennas”, *IET Microwaves, Antennas and Propagation*, vol. 6, no. 9, pp. 1070–1078, 2012.
- [104] B. Schoenlinner, and G. M. Rebeiz, “Compact multi-beam imaging antenna for automotive radars”, *2002 IEEE MTT-S International Microwave Symposium Digest*, vol. 2, pp. 1373-1376, 2002.
- [105] P.Nayeri, F. Yang, and A. Z. Elhersbeni, “Design and experiment of single-feed quad-beam reflectarray antenna”, *IEEE Transaction on Antennas and Propagation*, vol.12, pp. 1166-1171, 2012.
- [106] I. Slomian, P. Kaminski, J. Sorocki, I. Piekarcz, and K. Wincza, and S. Gruszczynski, “Multi-beam and multi-range antenna array for 24 GHz radar Applications,” *20th International Conference on Microwaves, Radar and Wireless Communications (MIKON)*, 16-18 Jun., Gdansk, Poland, 2014.
- [107] A. H. Abdelrahman, P. Nayeri, A. Z. Elsherbeni, and Fan Yang, “Single-Feed Quad-Beam Transmitarray Antenna Design,” *IEEE Transaction on Antennas and propagation*, vo. 64, no. 3, pp. 953-957, March. 2016.
- [108] Trung-Kien Pham, “Etude et conception de réseaux transmetteurs reconfigurables en bande Ka,” *PhD. Thesis*, University of Rennes, Rennes, 2017.
- [109] A. Clemente, L. Di Palma, L. Dussopt, "Elementary cell of a network transmitter for a reconfigurable antenna," *patent FR3065329*, 14/04/2017.
- [110] PIN diodes, MACOM technologies, www.macom.com.
- [111] Rectangular Waveguide, <http://www.millitech.com/pdfs/recspec.pdf>.
- [112] P. Hannan and M. Balfour, “Simulation of a phased-array antenna in waveguide,” *IEEE Transaction on Antennas and Propagation*, vol. 13, pp. 342-353, May. 1965.
- [113] L. Di Palma, A. Clemente, L. Dussopt, R. Sauleau, P. Potier, P. Pouliguen, "Experimental Characterization of a Circularly-Polarized 1-Bit Unit-Cell for Beam Steerable Transmitarrays at Ka-Band," *IEEE Trans. on Antennas and Propagation*, vol. 67, no. 2, Feb. 2019, pp. 1300-1305.
- [114] SAMTEC Inc.: www.samtec.com.

List of Publications

Journals

- K. Pham, R. Sauleau, E. Fourn, F. Diaby, A. Clemente, L. Dussopt, “Dual-band transmitarrays with dual-linear polarization at Ka-band,” *IEEE Transaction on Antennas and Propagation*, vol. 65, no. 12, pp. 7009-7018, Dec. 2017.
- F. Diaby, A. Clemente, K. Pham, R. Sauleau, and L. Dussopt, “Circularly-polarized transmitarray antennas at Ka-band,” *IEEE Antennas Wireless Propagation Letters*, vol. 17, no. 7, pp. 1204 - 1208, July 2018.
- K. Pham, R. Sauleau, E. Fourn, F. Diaby, A. Clemente, and L. Dussopt, “Low-cost metal-only transmitarray antennas at Ka-band,” *IEEE Antennas and Wireless Propagation Letters*, under review.
- F. Diaby, A. Clemente, R. Sauleau, K. Pham, and L. Dussopt, “2-bit tunable unit-cell and electronically steerable transmitarray at Ka-band,” *IEEE Transaction. Antennas and Propagation*, under review.

Conferences

- F. Diaby, A. Clemente, L. Di Palma, L. Dussopt, and R. Sauleau, “Impact of Phase Compensation Method on Transmitarray Performance,” *11th European Conference on Antennas and Propagation (EuCAP) 2017*, March 2017, Paris, France.
- K. Pham, R. Sauleau, E. Fourn, F. Diaby, A. Clemente, and L. Dussopt, “Dual-band dual polarized transmitarrays at Ka-band,” *11th European Conference on Antennas and Propagation (EuCAP 2017)*, March 2017, Paris, France.
- F. Diaby, A. Clemente, L. Di Palma, L. Dussopt, K. Pham, E. Fourn, and R. Sauleau, “Wideband circularly-polarized 3-bit transmitarray antenna in Ka-Band,” *11th European Conference on Antennas and Propagation (EuCAP) 2017*, March 2017, Paris, France.
- F. Diaby, A. Clemente, L. Di Palma, L. Dussopt, K. Pham, E. Fourn, and R.Sauleau, “Impact de la méthode de compensation de phase sur les performances des réseaux transmetteurs,” *20^{ème} Journée Nationale des Micro-ondes (JNM)*, May 2017, Saint-Malo, France.
- F. Diaby, A. Clemente, L. Di Palma, L. Dussopt, K. Pham, E. Fourn, and R.Sauleau, “Design of 2-bit unit-cell for electronically reconfigurable transmitarray at Ka-band,” *47th European Microwave Week*, October 2017, Nuremberg, Germany.
- K. Pham, R. Sauleau, E. Fourn, F. Diaby, A. Clemente, and L. Dussopt, “Characterization of dual-band dual-linearly polarized transmitarray antennas,” *47th European Microwave Conference (EuMC 2017)*, October 2017, Nuremberg, Germany.

- F. Diaby, A. Clemente, L. Di Palma, L. Dussopt, K. Pham, E. Fourn, and R. Sauleau, “Linearly-polarized electronically reconfigurable transmitarray antenna with 2-bit phase resolution in Ka-band,” *9th Int. Conf. on Electromagnetics in Advanced Applications (ICEEA)*, September 2017, Verona, Italy.
- F. Diaby, A. Clemente, L. Dussopt, K. Pham, E. Fourn, and R. Sauleau, “Design of a 3-faceted linearly-polarized transmitarray at Ka-band,” in *Proc. Antennas Propag. Intern. Symp. (APS-URSI)*, July 2018, Boston (MA), USA.
- F. Diaby, L. Di Palma, A. Clemente, L. Dussopt, E. Fourn, and R. Sauleau, “2-bit Reconfigurable Circularly-Polarized Unit-Cell at Ka-band,” *12th European Conference on Antennas and Propagation (EuCAP) 2018*, April 2018, London, UK.
- K. Pham, R. Sauleau, E. Fourn, F. Diaby, A. Clemente, and L. Dussopt, “K/Ka-band transmitarray antennas based on polarization twisted unit cells,” *12th European Conference on Antennas and Propagation (EuCAP 2018)*, April 2018, London, UK.
- F. Diaby, A. Clemente, R. Sauleau, K. Pham, and L. Dussopt, “Electronically-steerable transmitarray at Ka-band with 2 bits of phase quantization,” in *Proc. 39th ESA Antenna Workshop*, Oct. 2018, Noordwijk, The Netherlands.
- F. Diaby, A. Clemente, K. Pham, R. Sauleau, and L. Dussopt, “Synthesis and experimental characterization of a single-feed quad-beam circularly-polarized transmitarray at Ka-band,” *39th ESA Antenna Workshop*, 2018.
- K. Pham, R. Sauleau, E. Fourn, F. Diaby, A. Clemente, and L. Dussopt, “Ka-band metal-only transmitarrays for low-cost Satcom terminals,” *39th ESA Antenna Workshop*, 2018.
- A. Clemente, R. Sauleau, L. Dussopt, L. Di Palma, K. Pham, and F. Diaby, “Electronically-steerable transmitarray antennas for Ka-band,” *EuCAP 2019*, Convened Paper, accepted.